UNIVERSITY OF MESSINA

Department of Chemical, Biological, Pharmaceutical and Environmental Science
Doctoral course in
Advanced Catalytic Processes for using Renewable Energy Sources (ACCESS)

DIRECT SYNTHESIS OF NH_3 FROM N_2 BY RENEWABLE ENERGY FOR PRODUCTION OF FERTILIZERS AND AS A GREEN H_2 VECTOR

PhD thesis of:

Matteo Miceli

Supervisor:

Prof. Claudio Ampelli

Co-supervisor:

Dr. Pierdomenico Biasi

The coordinator of the Doctoral Course:

Prof. Gabriele Centi

Academic Year 2022-2023- XXXVI cycle

S.S.D. ING-IND/25
S.S.D. CHIM/04

INDEX

i. | Abstract

Nitrogen Reduction Reaction (NRR) in mild conditions is an alternative and attractive way to produce (green) ammonia, but greatly challenging, due to the major difficulty of activating the inert dinitrogen molecule (N_2), having a stable N-N triple bond. In this context, the three-year PhD research activities focused on the conversion of N_2 to ammonia (NH_3) by electrocatalytic-plasma routes through the development of advanced electrodes/cells to improve catalytic performance. Ammonia (NH_3) is currently one of the most important industrial chemicals, serving as a vital precursor for fertilizers, and a potential carbon-free energy carrier. At present, NH_3 is mainly synthesized by the Haber-Bosh (HB) process, which involves the reaction between dinitrogen (N_2) and hydrogen (H_2). However, this method operates at high temperature and pressure (400−600 °C, 20−40 MPa), consuming over 1% of the world's energy supply. Unfortunately, the conventional hydrogen production routes from *Steam Methane Reforming* (SMR) and *Water Gas Shift* (WGS) processes emit a large amount of CO_2, causing serious environmental damage. The European Union (EU) has set the goal of reducing greenhouse gas (GHG) emissions within 2050, and using renewable energy sources is thus a mandatory step to achieve this goal. For these reasons, many efforts have been made to mitigate the GHG emission, e.g. process electrification (with electricity coming from renewable sources), or moving to a (green) H_2 economy and developing novel hydrogen or energy carriers (like ammonia).

Nitrogen Reduction Reaction (NRR) in mild conditions is an alternative and attractive way to produce (green) ammonia, but greatly challenging, due to the major difficulty of activating the inert dinitrogen molecule (having a stable N-N triple bond). In this context, this PhD thesis focuses on the electrocatalytic

reduction of N_2 to NH_3 through the development of advanced electrodes/cells to improve electrocatalytic performance. The research activities have been carried out in the framework of the *PON project (**Programma Operativo Nazionale – Italy**), financing "Innovative Doctorates with Industrial Characterization (DOT20JCJJA)" (cycle 36th)*, which involves the collaboration of three institutions (University of Messina, Technical University of Eindhoven TU/e, and Casale SA).

Specifically, during the period spent at the Home Institution (**University of Messina,** Messina - Italy), a home-made electrochemical cell operating in different configurations (gas and liquid phase, or combined gas-liquid phase) was developed and optimized. This innovative device enhances the interaction between gas nitrogen and the active surface area of the electrode through the utilization of a gas-diffusion layer (GDL) that physically separates the gas and liquid chambers. In order to fabricate the electrodes, different electrocatalysts have been synthesized and characterized, consisting of metals (Iron, Ruthenium) loaded on two different supports *i.e.* α-Alumina (Al_2O_3) and Carbon Nanotubes (CNTs), then deposited/layered over the GDL. A wide range of potentials were investigated, to evaluate the NRR conditions in relation to the competitive hydrogen evolution reaction (HER). The activity of the different metals and the role of the support have been highlighted. Many efforts were also made to improve the analytical methodology for ammonia detection and to avoid contamination. In addition, through a study in collaboration with the University of Trieste, a direct comparison between two cell setups (gas-phase approach, and gas/liquid-phase approach) has been made. For all the tests, advanced electrochemical characterization techniques such as Electrochemical Impedance Spectroscopy (EIS), Active Electrochemical Surface Area (AESA), Electrochemical Surface Area (ECSA), and Double-layer capacitance (C_{DL}) calculations were performed, in order to support the experimental data.

Abstract

During a six-month period of research stay at the **Eindhoven University of Technology** (TU/e, Eindhoven - Netherlands) the synergy between plasma and catalysis in ammonia production was evaluated. Specifically, the synthesis of ammonia was investigated by experiments in a Dielectric Barrier Discharge (DBD) reactor by non-thermal plasma route in combination with catalysis. The different electrocatalysts mentioned before, having different chemical, physical, and electronic characteristics, were tested. Operational parameters such as feed gas ratio (N_2:H_2), flow rate, and power input were investigated to optimize the process. The feed gas ratio (N_2: H_2) was varied from 3:1 to 1:3 showing that the catalyst plays a key role in shifting the feed gas ratio to higher ammonia production. Differences between the empty reactor and the packed reactor were discussed, highlighting the internal differences between the two subgroups of catalysts, *i.e.*, supported on AL_2O_3 or CNTs.

Furthermore, the six-month period spent at **Casale SA** company (Lugano - Switzerland) was dedicated to the technical economic assessment (TEA) of current and novel processes for industrial ammonia production. The exploration of the different options for ammonia production started by examining both traditional and innovative methods. The well-established Haber-Bosh (HB) and green HB processes served as the initial references. Additionally, this research activity highlighted the potential for industrial application, albeit on a smaller scale, of emerging technologies like electrocatalysis (in aqueous, organic, and ionic liquid environments) and plasma-assisted catalysis (including thermal plasma, TP-SOEC, and non-thermal plasma, DBD). It is also considered a hybrid technique of Plasma-Electro catalysis where dinitrogen molecule is activated by plasma under NO_x form, and also electrification possibilities for the HB method using magnetic induction heating. Following this, comprehensive data on plant and operating parameters were gathered to facilitate a thorough technical-economic evaluation. The main part of this work has been devoted to understanding what the current ammonia production scenario (scenario 0) is and

what the critical issues are. For this reason, three scenarios have been assumed, covering all the ammonia production needs on multiple scales. In scenario 1, we explored the possibility of using a portable device (stand-alone) for ammonia production powered only by photovoltaic panels. Scenario 2 entails a medium-sized, decentralized facility capable of utilizing various renewable sources. Scenario 3 implements magnetic induction heating for pre-existing HB plants (electrification process).

Closely related to the Scenario 1, solar energy is a sustainable and abundant source of energy, obtained by converting sunlight into electricity. This process takes place through the use of photovoltaic cells, commonly known as solar panels, or through the excitation of photo-cathode or photo-anode materials. In this context, *artificial leaves* (ALs) are devices designed to mimic the process of photosynthesis in plants, capturing solar energy to produce chemicals with higher added value or electricity. Applicable in the case of CO_2 reduction reaction (CO_2RR, as will be discussed in Chapter 6), NRR, and in electrolysers for the production of green hydrogen. Coupling photovoltaic cells with electrochemical (PV-EC) cells is a strategy to store solar energy in chemical form using electrochemical processes. These approaches contribute to the search for sustainable solutions for energy production and storage, reducing dependence on nonrenewable energy sources and mitigating associated environmental impacts. Below a brief summary of the single chapters is reported.

Chapter 1 is a general introduction to the global landscape of current ammonia production technologies. It begins with an introduction to how the historical problem of nitrogen fixation was approached up to the process devised by German chemists Fritz Haber and Carl Bosch. Then, the focus is shifted to emerging technologies designed to meet global emission requirements. Moreover, the ultimate goal is to provide all preliminary information as the state of the art.

Chapter 2 contains a detailed explanation of the chemical and physical properties of the substrate materials used (alumina and CNTs) in both electrocatalytic and plasma catalytic applications. The type of synthesis adopted in comparison with other techniques (Impregnation, co-precipitation, Atomic Layer Deposition) and experimental details (weight, loading, volumes, weight ratios, precursors, assays, and so on) are provided. In addition, material characterizations through X-Ray diffraction (XRD), Brunauer-Emmett-Teller (BET) calculations, Scanning Electron Microscope (SEM), and Energy Dispersive X-Ray (EDX) analysis, are discussed.

In **Chapter 3**, the electrochemical approach by unconventional techniques using heterogeneous catalysts (in aqueous environment under mild conditions, i.e. room temperature and ambient pressure) is discussed. The comparison between two chemically and physically different media, investigated by doping with metals such as Ru, Fe, or a mix of them, is reported. The results show a higher tendency of Ru-Fe/Al_2O_3 to catalyse the reaction due to the higher productivity (1.05 μg mg_{cat}^{-1} h^{-1}) with a Faradic efficiency of 0.5% and a current density of 294 μA cm^{-2} at -0.3V vs RHE. Cell design is also crucial as it affects the electrocatalytic performances. The gas-phase (electrochemical cell 1) and gas-liquid-phase (electrochemical cell 2) approaches have strengths and weaknesses related to the presence of the membrane electrode assembly (MEA), as evidenced by the rGO-Mn_xO_y-Fe and rGO-Mn_xO_y comparison. The latter catalysts (in collaboration with the University of Trieste) are here reported especially to emphasize the different behaviour depending on the cell configuration, as expounded in Chapter 3.

The approach to plasma catalysis in **Chapter 4**, expresses the connubial approach between plasma and catalysis. The experimental behaviour of a dielectric barrier discharge (DBD) reactor is reported, monitoring the ammonia performance by varying several operating parameters, including the N_2:H_2 ratio and the flow rate, by keeping the frequency constant at 20 kHz and maintaining a constant power of

27 W. The comparison shows that the ruthenium-based catalyst doped on alumina (Ru/Al_2O_3) achieved the best performance of 4725.7 ppm (22.7 μmol min^{-1}) with an N_2:H_2 ratio of 2:1 and an energy consumption of 70.1 MJ mol^{-1}. The value, unbalanced toward higher nitrogen contents, shifts the reaction ratio from 1:3 to 2:1.

Chapter 5 reports the techno-economic evaluation of ammonia production processes. Specifically, a study related to the energy consumption - costs of all the technologies mentioned in Chapter 1, and other particular technologies found in the literature, such *Thermal Plasma- Solid Oxide Electrolyser Cell (TP-SOEC)* and a *Hybrid Plasma-Electrocatalitic (HPE)* reactor, are discussed. Then, after evaluating the scenarios, the energy consumption related to the individual reactor is compared as a boundary condition. This preliminary TEA serves to emphasize the possibility of using the technologies synergistically.

Finally, **Chapter 6** is dedicated to the electrochemical-photovoltaic coupling, also discussed in Chapter 5 - scenario 1, but used here for the carbon dioxide reduction reaction (CO_2RR). The reaction under investigation is different from the Nitrogen Reduction Reaction (NRR) but the issues are quite similar, thus it is possible to translate these results (including the design of the PV-EC cell working as an artificial leaves) the to a potential solar-driven NRR for future purposes.

Chapter 7 draws general conclusions and discuss future outlooks. This thesis aims to provide an understanding of the current global overview of technologies and for developing sustainable energy solutions. These approaches could revolutionize energy production and storage, helping to mitigate climate change and promote the transition to clean energy sources. Future implications include the possibility of a more efficient energy supply with less impact on the environment.

Keywords: Electro-catalysis, nitrogen reduction reaction (NRR), plasma catalysis, dielectric barrier discharge (DBD) reactor, nitrogen fixation, ammonia

synthesis, iron oxide, ruthenium, α-Al_2O_3, carbon nanotubes (CNTs), gas-phase reactors, technical economic assessment (TEA), artificial leaf, electrochemical impedance spectroscopy (EIS), double layer capacitance.

1. | Introduction

1.1. | Background: Nitrogen Fixation

Nitrogen plays a fundamental role in life on Earth, from the growth of plants, composition of enzyme proteins, and amino acids, to the major part of nucleic acid (DNA and RNA) [1,2], as well as in today's society, as a building block for chemicals, fuels, explosives, and fertilizers, for most of the global production (around 80%) [3].

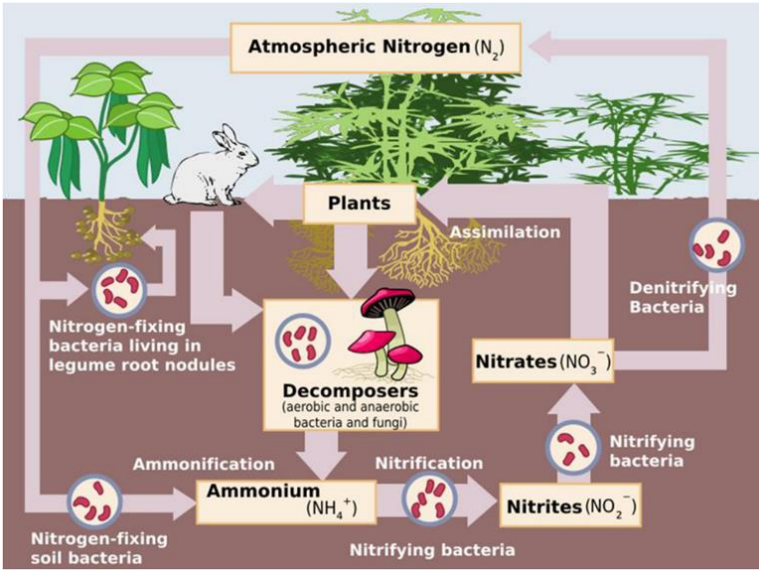

Figure 1.1 *– Ecosystem's Nitrogen Cycle [4]*

The first important step of nitrogen cycle is breaking the extremely strong triple bond (945 kJ mol^{-1}) and nonpolar stable electron configuration[5] in dinitrogen molecule (N_2), thus activating the molecule and producing derivate nitrogen compounds with more added value. Some aerobic, free-living soil microbes called *Azotobacter*, biologically fix the nitrogen and release it in the form of ammonium ions into the soils [6,7] (**Figure 1.1**). Practically, *dinitrogenase* binds and actives the N_2 molecule, and the *reductase* enzyme reduces it into ammonia (eq.1.1);

$$N_2 + 8H^+ + 8e^- \rightarrow 2NH_3 + H_2 \qquad \text{(eq. 1.1)}$$

One catalytic cycle involves eight electrons, two of which are used for the formation of hydrogen. The active site of the biological nitrogen fixation is a $MoFe_7S_9N$ cluster[8]. About 16 adenosine triphosphate (26-30 GJ/t_{NH3}) are required for the fixation[9]. However, an efficiency of about 10-15% is estimated for the nitrogenase enzyme (150-225 GJ/t_{NH3})[10].

At the beginning of the last centuries, the exploding global population and subsequent growing global demand for agricultural chemicals led society to investigate other ways apart from the biological fixation to supply the human demand. Many artificial processes have been developed for fixing atmospheric dinitrogen.

1.2. | Development of processes for nitrogen fixation

The first significant exploration of ammonia was in the 18th century when the English chemist Joseph Priestley discovered ammonia gas [11] (NH_3) obtained by heating various substances, including salt ammoniac (ammonium chloride – NH_4Cl). This discovery was crucial in understanding one form of nitrogen compounds. Other milestones in nitrogen fixation field are reported in **Figure 1.2**.

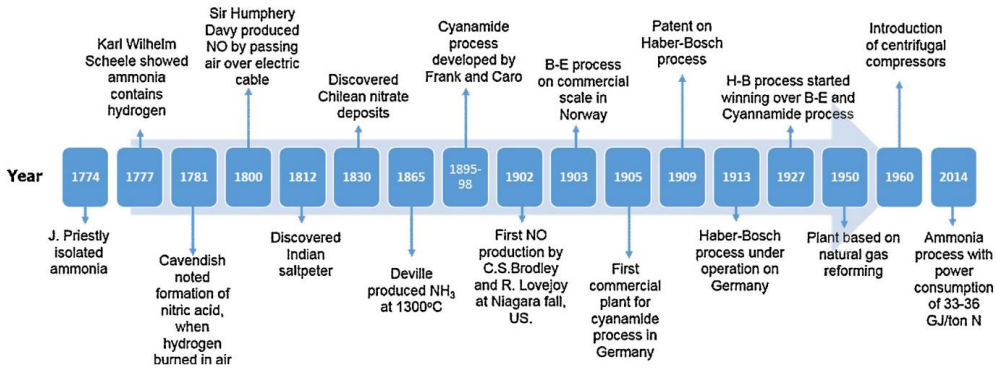

Figure 1.2 *– Main milestones in the nitrogen fixation processes [12,13]*

The first method of nitrogen fixation was described by Henry Cavendish in 1784 using nitrogen and oxygen contained in the air under electric arc discharge producing nitrogen oxides [14]. This method was implemented in 1903 into Birkeland-Eyde process, from nitric oxide sequentially converted, in H_2O, into nitric acid (HNO_3) as the final product [15,16]. During 1895-1899 two German chemists, Adolph Frank and Nikodem Caro, developed a process of nitrogen fixation that consisted of the reaction of calcium carbide with nitrogen in a heated reactor around 1.000 °C [17,18,19]. The exothermic reaction self-sustained the process when the temperature was reached. The synthesis produced a solid mixture of calcium cyanamide ($CaCN_2$) and carbon. The concept of nitrogen fixation has been refined in the early 20th century [20], when the German chemists Fritz Haber and Carl Bosch developed the Haber-Bosch process, a method for synthesizing ammonia from atmospheric dinitrogen and hydrogen gas (from fossil fuels), under high pressure and temperature. Nowadays, Haber-Bosch is still the widely used industrial process for producing ammonia in a large-scale, in a centralized plant and transporting ammonia over long distances, as discussed in detail in the next section.

1.3. | Haber-Bosh process: Traditional approach

Almost the totality of nitrogen fixed on a large scale is made with the "Haber-Bosh process", using high temperature (400-600°C) and high pressure (150-350 bar) in presence of an *iron-based* catalyst [21]. As mentioned before, the starting point for this process is the fossil fuel (CH_4) that takes part in the Steam Methane Reforming (SMR), an endothermic reaction described in eq. 1.2:

$$CH_4(g) + H_2O(g) \rightarrow CO(g) + 3H_2(g) \qquad \Delta H° = +206\ kJ \qquad \text{(eq. 1.2)}$$

The CO produced is used in another subsequent reaction called Water Gas Shift (WGS), lightly exothermic (eq. 1.3).

$$CO(g) + H_2O(g) \rightarrow CO_2(g) + H_2(g) \qquad \Delta H° = -41\ kJ \qquad \text{(eq. 1.3)}$$

Hydrogen produced in this way (derived from fossil fuels) is known as "grey hydrogen" [23]. Nitrogen is instead obtained from the air through its condensation at low temperature. The supplied hydrogen to Haber-Bosch could also be called "blue hydrogen" if CO_2 produced by eq. 1.2 is stored by Carbon Capture and Storage (CCS) technology present in the steam reforming plant, thus reducing the greenhouse gas (GHG) emissions [22,23].

High temperature and pressure are needed to overcome the sluggish kinetics of the reaction; moreover, the thermodynamics of this process favours ammonia decomposition to N_2 and H_2 , and for this reason high pressures are needed. The energy required to obtain pure feed gases, to pressurize the reactor, and so on, is typically around 485 kJ mol^{-1} [24].

The overall Haber-Bosch reaction of fixation is reported as follows (eq. 1.4):

$$N_2(g) + 3H_2(g) \rightarrow 2NH_3(g) \qquad \Delta H° = -92.4 \text{ kJ} \qquad \text{(eq. 1.4)}$$

This reaction is exothermic and auto-sustained, and does not require any supplementary heating once the reaction temperature is reached in the reactor. However, the start-up and shutdown of the plant require days or even weeks for the heating (or cooling) for maintenance, due to the activation of the catalyst.In Haber-Bosh process, the catalyst is usually made of magnetite (Fe_3O_4)[25], which is doped with potassium (K_2O), aluminium (Al_2O_3), and calcium (CaO). The pre-reduction initiates the formation of empty spaces and establishes points for the primary reduction, typically starting around 550 K. The inclusion of promoter oxides serves to hinder the growth of iron oxide crystallites into sizable, uniform structures, preventing them from becoming unreactive[26]. Often, in order to protect the catalyst, companies ship the catalyst in a pre-reduced form.

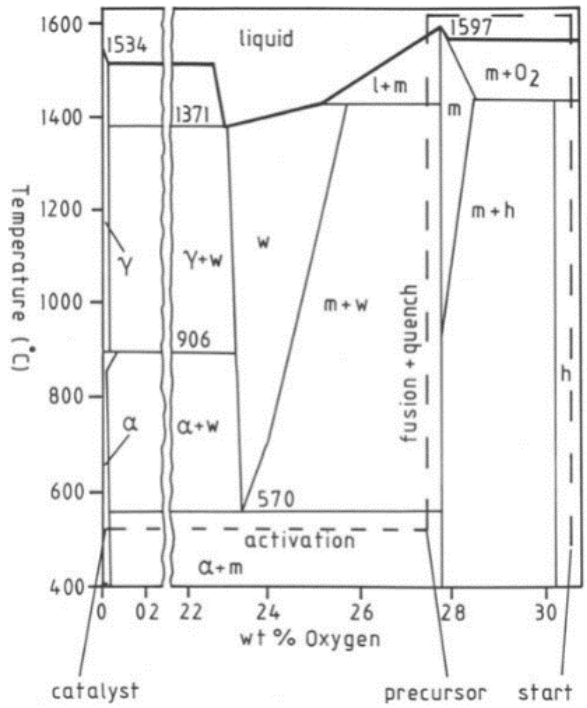

***Figure 1.3** - Section of the iron-oxygen phase diagram: "m" denotes magnetite, "h" hematite, and "w" wustite; α and γ stand for these modifications of iron metal. The dashed line describes the path of synthesis of the ammonia catalyst in the phase diagram[26]*

A controlled oxide layer generated by controlled oxidation at around 400 K state, is purposely made to form and then treated in dry hydrogen. At the end of the reduction process, the ratio of iron-to-oxygen on the surface is 1.85 with dry-reduction, while it reaches 1.75 if the wet-reduction is performed [26]. The active part of the HB catalyst is the metallic α-Fe spot (**Figure 1.3**).

As part of the synthesis process, contaminants can alter catalytic activity, such as impurities in the syngas that poison the catalyst, such as sulfur, phosphorus, chlorinated and oxygenated compounds like H_2O, CO, and O_2 [27].

1.4. | Haber-Bosh process: Green Haber-Bosh

The issues of global warming and energy transition require that hydrogen to power the Haber-Bosch process cannot longer be derived from fossil fuels (grey H_2 or blue H_2 if CCS is included) [22,23] but it should be formed by renewable and

sustainable ways. In this direction, the "green hydrogen" is provided from electrolysers by water splitting (WS). In comparison to the conventional ammonia process, the sustainable future of the Haber Bosch process (and chemical industry in general) is dependent on the utilization of renewable energy as part of chemical industry's electrification [28].

In Haber-Bosch process, renewable energy has the potential to meet all the energy needs, replacing methane as both the feedstock and fuel. Hydrogen is generated by water electrolysis and then transformed to ammonia in a Haber-Bosch reactor, as mentioned above. Overall Haber-Bosh reactor and technology are basically the same, and it is possible to identify similitudes and differences between the two technologies (**Figure 1.4**).

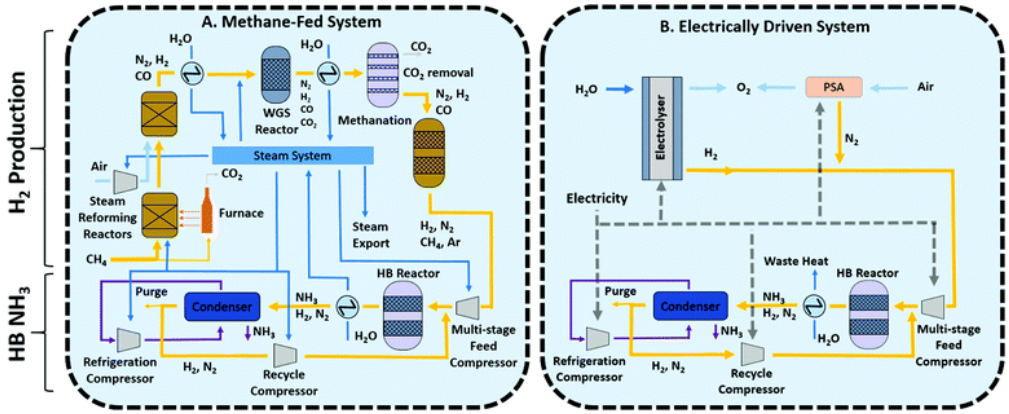

***Figure 1.4** - Schematic diagram of a) methane-fueled Haber-Bosh process and b) electrified process, in which H_2 comes from an electrolyzer to produce ammonia; process gas is shown in yellow, water and steam in dark blue, air in light blue, ammonia in purple, and electricity in dashed lines [29]*

The concept of electrically driven ammonia synthesis is not new, but it has never gained widespread acceptance as an alternative to coal or methane-fed processes because the vast majority of electricity is already derived from fossil fuels, with hydroelectric power [30] being an exception. **Figure 1.5**, which demonstrates the products derived from ammonia, illustrates the irreplaceable role of ammonia in chemical industry.

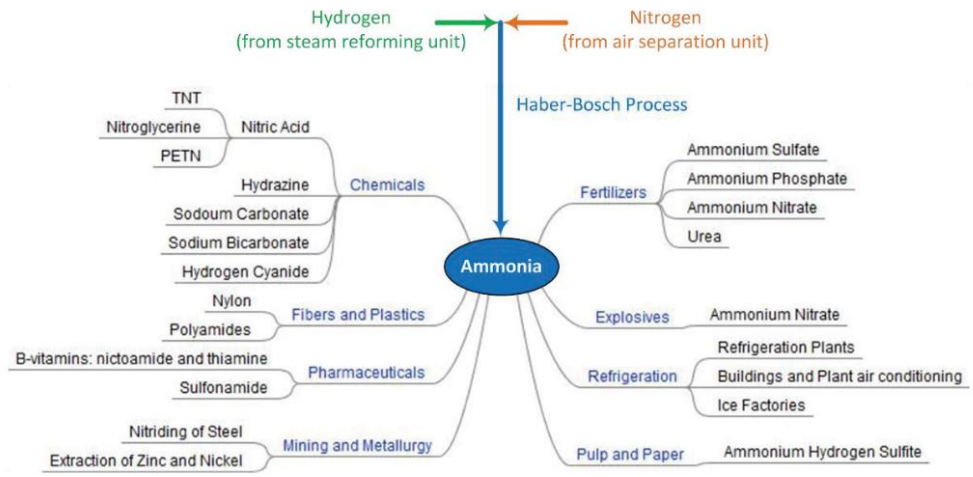

Figure 1.5 *- Compounds containing nitrogen and their applications in general* [18,31]

However, it should be remembered that the massive use of fertilizers, both nitrogenous and phosphorylated, leads to the problem of eutrophication [32], and thus for every action there is an anthropological effect on a global scale to be taken into account.

1.5. | Why look for alternatives?

The Haber-Bosh process consumes 1% of global energy demand and the use of 3-5% natural gas which produces over 300 million metric tons of CO_2 [33,34] in the atmosphere. Therefore, it is important to move from fossil fuel production to a more sustainable pathway in order to decarbonize the process as much as possible[35] with renewable energy sources. Furthermore, ammonia could be used as a potential hydrogen carrier, reducing the risks and costs related to transporting H_2 in its gaseous state. More sustainable pathways are needed to achieve the target of net zero GHG emissions by 2050 [35,36]. Due to the thermal inertia of the planet, it may take some time before the impact of our current efforts to mitigate global warming becomes evident. Accelerating the development of processes leading to green ammonia is beneficial to begin the energy transition as quickly as possible [37].

1.5.1. | Magnetic Induction Heating

Magnetic Induction Heating is a highly efficient and precise method for heating electrically conductive materials. This technique of heating could be perfectly integrated into the current Haber-Bosh process as an electrification process, acting to reduce the start-up times, with the benefit of a localized and tuneable temperature (300-600°C) and, as mentioned before, as a fast start-up for the initial ignition of the reaction. On the other hand, the metal catalyst or metal support has to stay under Curie temperature for working as a non-magnetic reactor [38,39] (or by putting a coil inside the reactor). The temperature is also limited by the depth of the metal catalyst pellets in the reactor.

1.5.2. | Electrocatalysis

In the view of using renewable energy sources and producing electricity in a more sustainable way, electro-catalytic processes are a promising way to produce ammonia. Redox reactions could be driven by electricity, through appropriate reactors, so that N_2 can be reduced at the cathode (and water oxidized at the anode) by heterogeneous catalysts. Ammonia production is a hot topic, and recently many efforts have been made by the scientific community to develop efficient electrocatalytic processes for ammonia production and find a sustainable alternative to the HB process, which has been widely used for more than one century. *Chen et al.*[40,41] tested activated carbons, functionalized and decorated with different amounts of iron/iron oxides nanoparticles[42], in different cell configurations to increase nitrogen solubility/reactivity[43,44]. *Wei et al.* also obtained interesting results using modified metal-organic frameworks (MOF-based) with a structural morphology modification that improves nitrogen conversion[45]. Molybdenum-based catalysts have recently been developed to mimic the behaviour of the *dinitrogenase* enzyme mentioned in **section 1.1**. Interestingly, *Chu et al.*[46] have obtained a productivity of 95.8 μg mg_{cat}^{-1} h^{-1} of ammonia at -0.4 V vs RHE (MoO_{3-x}/MXene). *Fei et al.*[47], on the other hand,

prepared a molybdenum sulphide (MoS_2) modified by incorporation of phosphorus obtaining a yield of 60.27 μg mg_{cat}^{-1} h^{-1} at -0.6 V RHE and a Faradaic efficiency of 12.22%. Another interesting research conducted by *Jiang et al.*[48] reported that a distorted ferrite-based spinel heterostructure ($Sr_{0.3}Co_{0.7}Fe_2O_4$) , resulted in a high Faradaic efficiency of 76.7% and a productivity of 36.4 μg mg_{cat}^{-1} h^{-1}, at -0.3 V vs. RHE.

Electrocatalytic approach is highly implementable with renewable energy sources and allows a possible electrocatalytic plant to start or stop an ammonia production in a short time (minutes).

Theoretical studies by DFT (Density Functional Theory) on N metal-surface catalysts (**Figure 1.6**) have been widely reported in the literature[49,50]. The volcano plot diagrams, obtained by plotting the limiting potential chemisorption energy on nitrogen adsorbed atoms (on flat or step surface for dissociative and associative pathways [50]), indicate the metals on top of volcano that should provide the highest catalytic activity for ammonia formation, i.e. Mo, Fe, Rh, Ru.

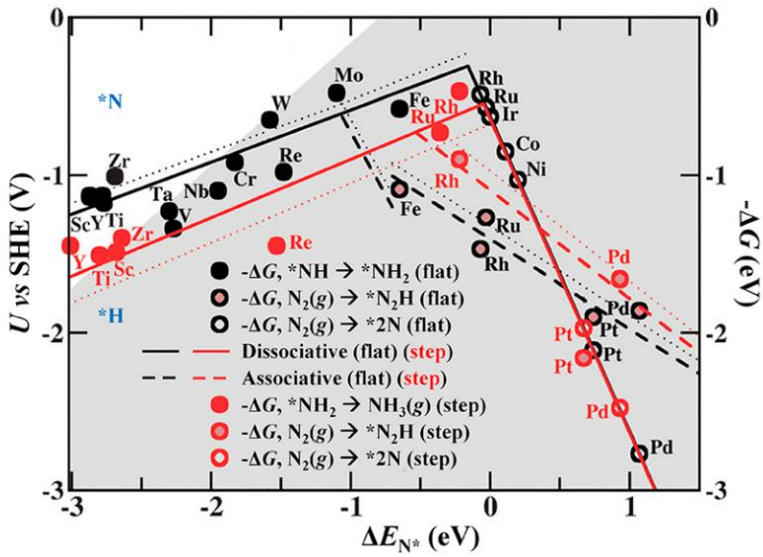

Figure 1.6 *- Volcano diagrams: dotted lines indicate the effect of hydrogen- bonding stabilization of the adsorbates when water is present. Following the scaling relations, only one descriptor, ΔE_{N*}, is needed to describe the catalysts for N_2 reduction. Reproduced with permission [50]*

1.5.2.1 | Nitrogen Reduction Reaction (NRR) mechanism

The way the nitrogen molecule reacts can be classified into different mechanisms reported in **Figure 1.7**: the first and the second mechanisms are called the "dissociative" and "associative" pathways, respectively[51]. In the "dissociative" one, the triple bond is broken before the addition of H atoms to a nitrogen atom, as represented by steps 2, 3, and 4 (**figure 1.7a**). The "associative" mechanism consists of the simultaneous release of two NH_3 molecules, which can occur in two ways: the acquisition of three H atoms on the nitrogen molecule that is bound to the metal support, in fact (acquisition of steps 2, 3, and 4), occurs i) "distally", i.e., on the same nitrogen atom, or ii) "alternately", i.e., the acquisition of H atoms alternately on the two nitrogen atoms (**Figure 1.7b**)[52]. Note that the "enzymatic" mechanism also follows the associative model, which, however, involves lateral adsorption of the molecule (**Figure 1.7c**).

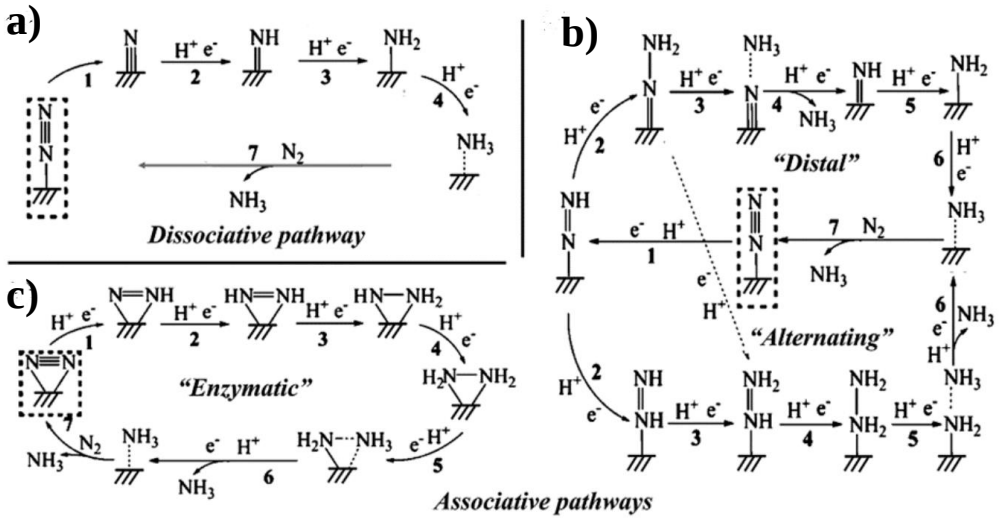

***Figure 1.7** - An illustration of the a) dissociative and b) associative pathways (alternating, and distal) including c) associative enzymatic pathway, for catalysing N_2 to NH_3*

1.5.2.2 | Aqueous Environment

Water is a safe and environmental-friendly solvent for electrochemical reactions, but pure water is not conductive; thus, it is mandatory to add an electrolyte that

does not interfere with the Nitrogen Reduction Reaction (NRR). Electrocatalysis in an aqueous environment consists of two reactions, in cathodic and anodic chambers separated by a proton exchange membrane. Ammonia is produced in the cathodic part, where i) proton sources are supplied by H_2O applying a potential difference closing the electrical circuit, ii) electrons move from anode to cathode. The role of the salt in H_2O is to supply the charge and maintains the current. Oxygen Evolution Reaction (OER) occurs at the anode side as the counter-reaction. It is also possible to study the anodic Nitrogen Oxidation Reaction (NOR), where the conversion is from N_2 to oxygenated N-compounds (NO_x^-) [53]. NO_x^- from NOR could be further reduced by second electrocatalytic step to NH_3 with high faradic efficiencies[54,55,56] (55.0-99.7%).

The NRR by electrocatalytic route under mild conditions at small scale could provide a delocalized production of ammonia with respect to the large scale of HB and supply a safer environment. However, i) N_2 has a low solubility in water as a first drawback, and ii) the second drawback is the Hydrogen Evolution Reaction (HER) as a competitive cathodic reaction.

One of the first tests in aqueous system of NRR goes back to 1983 by *Sclafani et al.*[57], who investigated the reaction in 6M KOH, using an iron catalyst and a stainless steel anode at different temperatures (25, 35, and 45°C), producing a range of ammonia from 0.1 to 0.5 μmol h^{-1} (tested potentials from 0.9 to 1.2 V vs. SCE) with a Faradaic Efficiency (FE) of 1%. *Liu et al.*[58] prepared and tested Rh-nanosheets in a 0.1M KOH aqueous solution, with the highest ammonia formation rate of 23.9 $\mu g_{NH3}\ g_{cat}^{-1}\ h^{-1}$ at an applied voltage of -0.2 V vs. RHE and a FE of 0.22%, in a two-compartment cell. Ag-nanosheets were also studied and tested by *Huang et al.*[59] for this reaction in acidic media (0.1M HCl) where a FE of 4.8% at -0.6 V vs. RHE and a yield of 4.6×10^{-11} mol $s^{-1}\ cm^{-2}$ were reached.

Overall, the FE found in the literature ranges from 0.1 to 29.6% (1-100 $\mu g_{NH3}\ g_{cat}^{-1}\ h^{-1}$) [60,61]. The conditions are milder than HB, i.e. room temperature and ambient pressure, with a possibility to scale medium and small plants.

1.5.2.3 | Organic Environment

The non-aqueous electrolyte is a challenging technique with respect to the water-based, with a potential window that allows the NRR without producing substantial amounts of H_2.

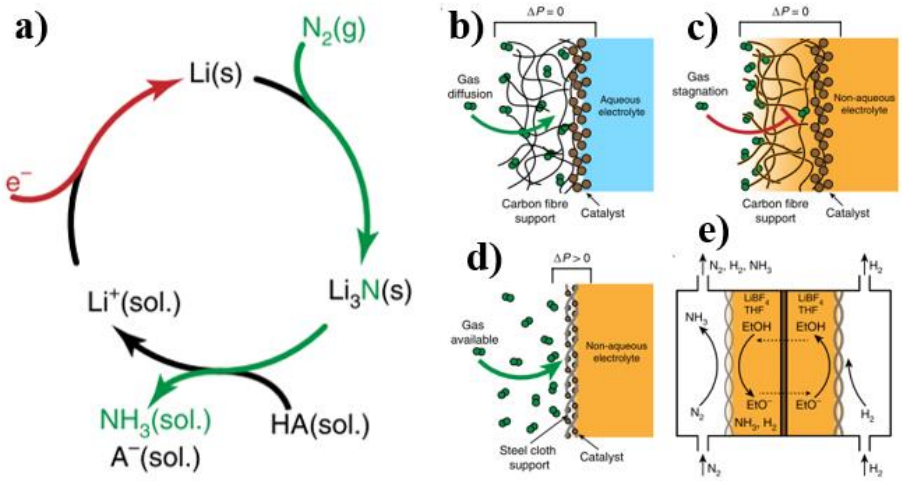

Figure 1.8 *– a) simplified reaction mechanism for the Li-catalysed cycle for Nitrogen Reduction Reaction (sol., solvatated). b) hydrophobic GDE with aqueous solvent. c) hydrophobic GDE with non-aqueous solvent, effectively flooding the catalyst d) Catalyst on stainless steel in presence of non-zero pressure (P) gradient across the cloth preventing the flooding. e) Proton donor cycling; adapted from ref* [62]

Electrocatalysis in organic solvent takes advantage of the Li-cycle. The feed gases are H_2 and N_2 (for example coming from water electrolysis and air separation, respectively), while the tetrahydrofuran (THF) inside the reactor is the solvent, EtOH is the proton source (**Figure 1.8e**). A pressure gradient (**Figure 1.8d**) is used for avoiding flooding in the gas compartment (**Figure 1.8c**), as the use of organic solvents has the disadvantage of penetrating through the electrode support (i.e. a porous material acting as a gas-diffusion layer -GDL- or a stainless steel mesh) more than an aqueous electrolyte (**Figure 1.8b**. Lithium favours the breakage of the N_2 triple bond through the formation of Li_3N[63] (**Figure 1.8a**).

In the work made by *Lazouski et al.*[62], the maximum FE to ammonia formation was of 47.5 ± 4%; furthermore, the highest rate of production (30 ± 5 nmol cm^{-2}

s^{-1}) was obtained with a FE of 30 ± 2%. The work demonstrates the possibility of using metal cloth-based supports for NRR, with H_2 supplied by a water-splitting electrolyser.

1.5.2.4 | Ionic Liquids Environment

Ionic Liquids (ILs) are defined as compounds composed totally of cations and anions, in liquid state near room temperature. Compared to conventional solvents, ILs have the advantages of a wide electrochemical window and large absorption capacity of gases, they are non-volatile, non-flammable and stable, but toxic, not environmentally friendly, difficult to separate from the products, and expensive. Electrocatalysis mediated by ILs is a technique where N_2 and H_2 were flowed into a batch reactor, with ILs, a catalyst (cathode), a reference, and a counter-electrode (anode). Gaseous products are easily separated (H_2 and N_2 recycled), but NH_3 in IL needs to be separated and IL recycled.

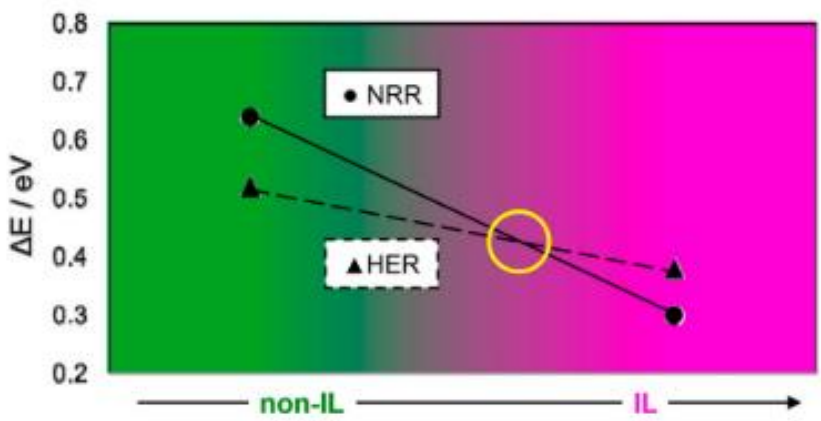

Figure 1.9 *– relative energy differences for HER and NRR, with and without IL*

ILs improve the solubility of nitrogen and make available more nitrogen for conversion; furthermore, the HER is suppressed due to less availability of protons. With ILs, NRR energy is only 0.30 eV compared to the 0.64 eV value calculated with a non-IL solvent (**Figure 1.9**). Similarly, HER was 0.38 eV with respect to 0.52 eV; this means an improved activity and selectivity for the NRR [65]. *Li et al.*

[64] used ILs as templates or precursors for tuning particular morphology and properties, using *tetrabutylammonium hydroxide* (TBAH). The combination of ILs with electrocatalysis allowed to reach FE of 30-60% [65].

1.5.2.5 | Artificial Leaf reactor

Electrocatalytic methods mentioned above (aqueous, organic, ionic liquids) can be perfectly integrated with renewable energy and used from small to medium scale for delocalized supplies, compared with current industrial processes.

In this context, Artificial Leaves (ALs) are small-scale reactors that use renewable energy sources like solar power to catalyse different reactions widely studied in the literature, including water splitting, carbon dioxide reduction reaction (CO_2RR), diatomic nitrogen reduction reaction (NRR), and so on [66].

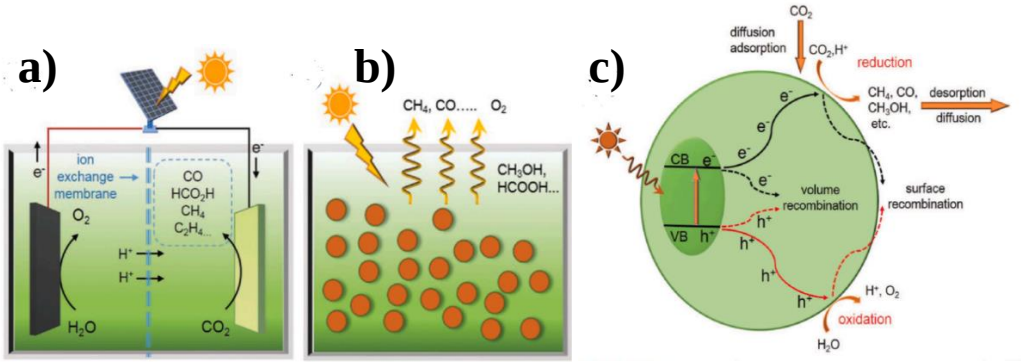

***Figure 1.10** - Schematic representation of a) an electrochemical cell driven by an external photovoltaic panel and b) an electrochemical reaction supported by a photocatalyst; c) Simplified diagram of the photocatalyst activation mechanism*

ALs can be configured in a variety of ways: a wired or wireless configuration[67] in which the photoactive element is in touch with the electrolyte (**Figure 1.10b**), or a configuration in which the photoactive element (a photovoltaic – PV – cell) is not in contact with the electrolyte, despite being integrated into the device (**Figure 1.10a**). In **Figure 1.10c** is represented the photo-activation of the catalyst due to the transfer of an electron from the valence band to the conduction band.

1.5.3. | Plasma catalysis

Plasma is also known as the fourth state of matter, consisting of an ionized gas, composed of ions (positive and negative), free electrons, and radicals that make plasma formally neutral. Typically, plasma is generated by applying an external electric field between two electrodes. The minimum applied voltage required to generate plasma is called breakdown voltage (V_b) and depends on the gas pressure, the distance between the electrodes, and from the applied electric field, as described by *Paschen's law* (eq. 4), where *d* is the distance from electrodes, *p* is the gas pressure, *a* is the saturation ionization in a particular electric field/pressure ratio, and *b* is related to the excitation energies.

$$V_b = \frac{a(pd)}{\ln(pd)+b} \qquad \text{(eq. 1.4)}$$

Plasma mixed with catalysis (sometimes called plasma-enhanced catalysis) is a hybrid technique where a catalytic material is used to improve the conversion from reactants to products, and is used from food factories to cleaning, for removing pollutants such as NO_x, SO_x and removing volatile organic compounds (VOCs). Plasma is a multidisciplinary phenomenon, that touches fields like chemistry, physics, electrical engineering, and so on.

Plasma generally could be classified on the basis of the temperature, a higher temperature meaning a highly ionized species, and every particle in the plasma stream has a high temperature. The criterion for considering the Thermal Plasma (TP) as it is, is $T_e \approx T_i \approx T \leq 2\times10^4 K$, where T_e is the temperature of electrons, T_i is the temperature of ions and T is the temperature of the surrounding environment[68]. On the other hand, Non-Thermal Plasma (NTP) has a lower temperature of ions, near room temperature ($T_i \approx T \approx 300K$), and a temperature of electrons much higher $T_i << T_e \leq 10^5 K$[68].

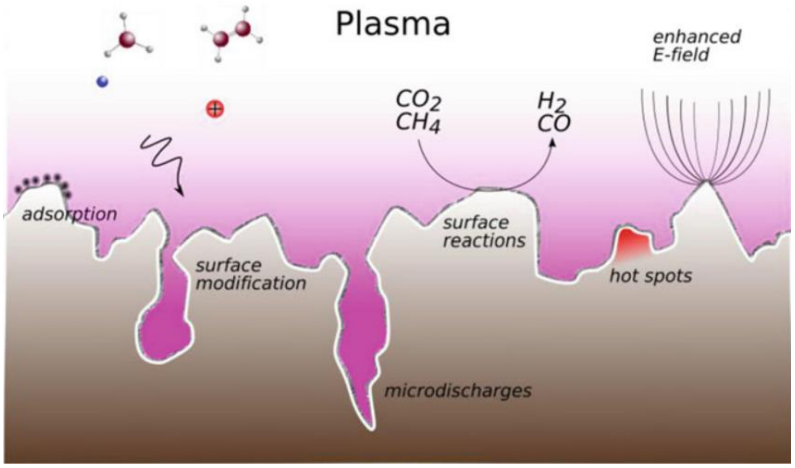

Figure 1.11 *– Catalysis on a nano-scale surface*

With a synergistic approach to plasma and catalysis, new routes can be explored (**Figure 1.11**), enhancing productivity thanks to the high catalytic surface, as well as the confinement of molecules on the surface, which are activated by the support and plasma.

The nitrogen fixation reaction necessitates the direct reaction of nitrogen and hydrogen in the reactor under plasma conditions. The addition of oxygen (e.g., straight from the air) in the reactant gas mixture would primarily result in the synthesis of NO_x, which, being not the principal product gas here, is a good intermediate because nitrogen is already activated in the form of an oxide. Because of the enormous energy involved, the plasma reaction is a process with minimal control over the products.

1.5.3.1 | Thermal Plasma

As previously indicated, plasma processing is distinguished by its capacity to produce electrical discharges that result in highly reactive active species and a fully ionized high-temperature gas. This type of plasma is used to create an engineering material as fine powder[69]. However, because of the high temperature, it was frequently unable to use a catalyst; therefore, in the catalytic process of ammonia production, the reactive gases (nitrogen and hydrogen) either

flow directly into the reaction or are introduced onto the flame, as outlined in the work by *van Helden et al*.[70]

1.5.3.2 | Non-Thermal Plasma

The electron temperature in non-thermal or non-equilibrium plasma (NTP) is substantially greater than the heavier species (e.g., ions and neutral species), and this difference offers the ability to surpass the kinetic and thermodynamic restrictions of chemical reactions. Combining chemistry with NTP is complex, and the need to test catalyst in a well-designed reactor system is the method to improve selectivity (and energy efficiency). 300-1000 K are typical Dielectric Barrier Discharge (DBD) reactor temperatures[71]. In fact, the activations of the vibrational movements of the interacting gases are of particular importance.

1.6. | Energetic challenges

The Haber-Bosh process has been utilized for the synthesis of ammonia for more than a century, starting from 1913 at BASF in Ludwigshafen[72]. Numerous attempts were made throughout the years to enhance energy efficiency, with a significant decrease from approximately 100 GJ/t_{NH3} in 1920 to 27 GJ/t_{NH3}[73] in 2015 (**Figure 1.12**).

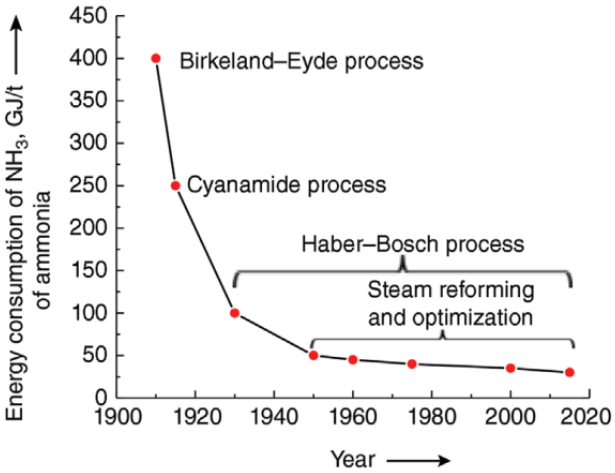

***Figure 1.12** - Historical comparison of energy consumption for different ammonia processes*

Historical advancements include the shift from coal (or lignite) gasification to methane steam reforming, the implementation of compressors, the enhancement of heat and process optimization, and the expansion of plant size. In the 2000s, the plant size was typically 2000 t/d, while currently, the largest plants range from 3000-4000 t/d, with the potential to increase to 5000-6000 t/d [74,75]. These productions are referred to a classical Haber-Bosh (HB). Improving the HB process means reducing the carbon footprint by decreasing both the energy consumption, expressed in GJ/t, and the ratio of metric ton of CO_2 emitted per metric ton of NH_3 produced. **Table 1.1** reports these parameters for the Best Available Technology (BAT) (referred to 2020), for traditional Haber-Bosh, the Haber-Bosh with the Carbon Capture System (Blue-Haber Bosh), and the Green Haber Bosh.

Technology	Energy requirement (GJ/t_{NH3})		CO_2 Footprint (t_{CO2}/t_{NH3})	
	BAT	Potential	BAT	Potential
Traditional/Gray HB	26	26	1.6	1.6
Blue HB	33	26	0.4	0.2
Green HB	33	26	0.1	0.0

Table 1.1 *– Energy requirement and CO_2 footprint for traditional, blue, and green Haber-Bosh*[76]

The blue Haber-Bosh, or blue ammonia, is synthesized in the same way as the gray process but this reduced carbon footprint can be obtained by combining hydrogen production processes with carbon capture storage (CCS). On the other hand, the green ammonia, that comes from green hydrogen, further reduces the emissions by using electrolysers. In the 1920s, the first electrolyser-based process from water and air consumed 46-48 GJ/t_{NH3} and the calculated theoretical minimum energy required for ammonia synthesis is 22.5 GJ/t_{NH3}.

1.6.1 | Electrolysis technology Comparison

The electrolysis technologies available today (**Table 1.2**) are: i) alkaline electrolysis, ii) Proton Exchange Membrane (PEM) electrolysis, and Solid Oxide Electrolysis (SOE), which consume 29-46 GJ/t_{NH3}, 31-46 GJ/t_{NH3}, and 24-27 GJ/t_{NH3}, respectively.

Technology	Energy requirement (GJ/t_{NH3})	Temperature (°C)	Pressure (bar)	Electrolyte	System size	Technology Readiness Level (TRL)
Alkaline	29-46	60-90	1-30	20-40wt.% KOH	Large	9
PEM	31-46	50-80	10-200	Nafion	Compact	8-9
Solid Oxide	24-27	600-1000	1-25	YSZ/SSZ	Compact	5-6

***Table 1.2** – Electrolysis technologies[76]; Technology Readiness Level (TRL) from the European Community[77]: 1 - Considered fundamental principles; 2 - Formulated the technology concept; 3 - Experimental proof of concept; 4 - Technology validated in the laboratory; 5 - Technology validated in an industrially relevant environment; 6 - Technology demonstrated in an industrially relevant environment; 7 - Prototype system demonstrated in an operational environment; 8 - Complete and qualified system; 9 - Real system tested in an operational environment (competitive production, commercialization);*

The green HB has a higher energy consumption, which depends on the electrolysis technology used.

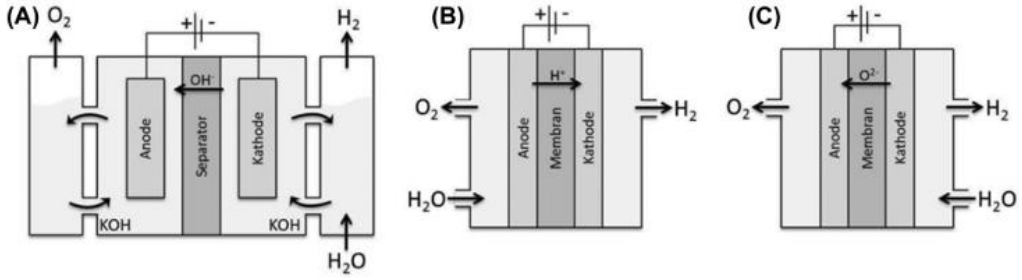

***Figure 1.13** – Schematic representation of the electrolysis system, a) alkaline, b) PEM, and c) Solid Oxide electrolysis [76]*

In the alkaline process (**Figure 1.13a**), the cathode and anode are immersed in an electrolyte solution containing 20-40 wt.% KOH. They are separated by a diaphragm that allows the passage of OH^- species, leading to the generation of hydrogen at the cathode (Ni or Ni alloys) and oxygen at the anode (Ni or Ni-Co). In the case of PEM (**Figure 1.13b**), protons pass through the membrane and

recombine at the cathode (Pt or Pt-Pd), while oxygen is produced at the anode (RuO_2 or IrO_2).

On the other hand, the solid-state electrolyser (**Figure 1.13c**) operates with vapor instead of in the liquid phase. Hydrogen is produced at the cathode (Nickel-based or Iron-Chromium alloy), while oxygen passes through the yttrium or scandium-stabilized zirconia membrane (YSZ or SSZ respectively) and recombines at the perovskite-type anode. One advantage of the solid-state is that it reduces the electrical demand and operates with lower energy input compared to the alkaline and PEM electrolyzers [76]. On the other hand, the operating temperatures of solid state (600-1000°C) are significantly higher than those of alkaline and PEM electrolyzers (60-90 and 50-80°C respectively). Whereas alkaline and solid-state operating pressures are the mildest (1-30 and 1-25 bar) while PEM can also work at higher pressures.

1.6.2 | Conventional and non-conventional technology

Besides providing hydrogen more sustainably, electrolysers (alkaline, PEM and SOEC), can be adapted to other technologies that we mentioned above, which utilize the direct reaction between hydrogen and nitrogen.

Technology	Energy requirement (GJ/t_{NH3})			
	Reported	**Potential**	**TRL**	**Starting Point**
Traditional HB	26	26	9	CH_4/N_2
Electrolysis-based HB	46-50	30-35	8-9	H_2/N_2
Electrochemical	135	27-29	2-4	N_2/H_2O
Non-Thermal Plasma	155	60-70	2-4	N_2/H_2

***Table 1.3** - Summary of different actual and Theoretical energetical requirements[76], and the respective Technology Readiness Level (TRL) for conventional and non-conventional technology for ammonia production; For Technology Readiness Level (TRL) meaning see table 1.2*

In order to produce ammonia in the future by a sustainable alternative NRR route, it is necessary to study the present limitations and evaluate their future potential among the various emerging (or unconventional) technologies (**Table 1.3**). These

technologies will be discussed both experimentally and from a technical-economic perspective in subsequent chapters.

1.7. | Objective of the thesis

The general objective of this thesis is to provide an overview of all the current promising technologies for producing ammonia, showing their strong and weak points compared to the HB process. In particular, in the thesis work some of these technologies were investigated on a laboratory scale, from the **electrocatalytic** process in **aqueous** environment to non-thermal **plasma catalysis** , as will be illustrated in the following chapters.

Electrocatalytic method (investigated at the University of Messina, Italy) and Plasma-catalytic methods (studied at TU/e – Eindhoven, Netherlands) were explored as experimental cases, as they represent some of the most promising and captivating technologies currently being researched by the scientific community, with numerous efforts focused on enhancing productivity. In support of this, a technical economic analysis was carried out (in collaboration with Casale SA – Lugano, Switzerland).

The present **Chapter 1** serves as an introductory section, presenting various technologies commonly employed in industrial settings such as Haber-Bosh, which encompasses energetic and environmental considerations. Additionally, it delves into emerging technologies that are currently under study, aiming to address issues pertaining to localized production. These emerging technologies utilize milder reaction conditions and possess a faster startup or shutdown time, thus exhibiting the potential to evolve into the industrial technologies of tomorrow. Moving on to the next **Chapter 2**, the focus shifts towards methodology, reactors, and materials.

Then, the experimental part of this thesis is structured into three main parts:

- The **electro-catalytic** part in **Chapter 3**, describing the developed electrocatalysts and the designed electrochemical reactor for the nitrogen

reduction reaction, and evaluating the faradic efficiency and the quantification of ammonia (in micromoles per milligram and per hours) as parameters of catalyst schedules, as well as other characterization techniques including electrochemical impedance spectroscopy.

- The **plasma-catalysis-assisted** part in **Chapter 4**, where the same catalytic materials prepared for the electrocatalytic part are tested under plasma condition in a Dielectric Barrier Discharge reactor, acting to study different operational parameters such as feed-gas ratio (N_2 and H_2) and flowrate, in order to have a comparison between electrocatalysis and plasma catalysis. Furthermore, a high-speed camera was used to capture the plasma discharge behaviour during a discharge test session, and an IR camera was also used to detect the temperature reached on the external surface of the reactor;

- The **technical-economical** part in **Chapter 5**, where the techniques for the production of ammonia (conventional and non-conventional) currently used and found in the literature, which were set out in Chapter 1, are compared on an economic level, in order to study their potential and future developments, studying their strengths and weaknesses, divided into system parameters (including scalability, readiness level technology, lifetime of the system/catalyst, etc) and operating parameters (including Pressure, Temperature, Adaptability with renewable energy, safety, etc);

In **Chapter 6**, finally, the possibility of coupling a photovoltaic panel to an electrochemical reactor is questioned, to drive the process by solar energy; in this case, the problem was studied for the reduction of CO_2 to formic acid and hydrogen, because the quantity of ammonia produced does not have a sufficient

quantity to be able to apply the aforementioned technology here. However, the problems faced are the same and therefore a parallel conclusion can be drawn.

1.8. | References

[1] Erisman, J. W., Galloway, J. N., Dise, N. B., Sutton, M. A., Bleeker, A., Grizzetti, B., Leach, A. M., & de Vries, W. (2015). *Nitrogen: too much of a vital resource : Science Brief*. (WWF science brief NL). WWF Netherlands.

[2] Galloway, J. N., & Cowling, E. B. (2002). Reactive nitrogen and the world: 200 years of change. AMBIO: A Journal of the Human Environment, 31(2), 64–71.

[3] Seh, Z. W., Kibsgaard, J., Dickens, C. F., Chorkendorff, I., Nørskov, J. K., & Jaramillo, T. F. (2017). Combining theory and experiment in electrocatalysis: Insights Into Materials Design. *Science, 355*(6321).

[4] Dréo, J. (2009). Nitrogen Cycle. Wikipedia commons. Retrieved from https://commons.wikimedia.org/wiki/File:Nitrogen_Cycle.svg.

[5] Li, D., Zan, L., Chen, S., Shi, Z.-J., Chen, P., Xi, Z., & Deng, D. (2022). Direct conversion of N_2 and O_2: Status, challenge and perspective. *National Science Review*, 9(12).

[6] Gandora V.; Gupta R. D.; Bhardwaj K. K. R. (1998). "Abundance of Azotobacter in great soil groups of North-West Himalayas". *Journal of the Indian Society of Soil Science*. 46 (3): 379–383. Archived from the original on 2012-09-06. Retrieved 2010-08-30.

[7] Martyniuk S.; Martyniuk M. (2003). "Occurrence of Azotobacter Spp. in Some Polish Soils" (PDF). *Polish Journal of Environmental Studies*. 12 (3): 371–374. Archived from the original (PDF) on 2011-07-15. Retrieved 2010-08-30.

[8] Skúlason, E., Bligaard, T., Guðmundsdóttir, S., Studt, F., Rossmeisl, J., Abild-Pedersen, F., Vegge, T., Jónsson, H., & Nørskov, J. K. (2012). A theoretical evaluation of possible transition metal electro-catalysts for N_2 reduction. *Physical Chemistry Chemical Physics*, 14(3), 1235–1245.

[9] Burgess, K. B., & Lowe, D. J. (1996). Mechanism of molybdenum nitrogenase. *Chemical Reviews*, 96(7), 2983–3012.

[10] Appl, M. (1999). *Ammonia: Priciples & Industrial Practice*. Wiley-VCH.

[11] West, J. B. (2014). Joseph Priestley, oxygen, and the enlightenment. *American Journal of Physiology-Lung Cellular and Molecular Physiology*, 306(2).

[12] Brightling, J. (2018). Ammonia and the fertiliser industry: The development of ammonia at Billingham. *Johnson Matthey Technology Review*, 62(1), 32–47.

[13] Partington, J. R. (1929). Review of *Fixation of Atmospheric Nitrogen* by F. A. Ernst. *Industrial Chemical Monographs*, IX + 154. London: Chapman & Hall, Ltd., 1928. Price: 12s. 6d. *Journal of the Society of Chemical Industry, 48*(18), 455–455.

[14] Eyde, H. S. (1909). The manufacture of nitrates from the atmosphere by the electric arc—Birkeland-Eyde process. *Journal of the Royal Society of Arts, 57*, 568–576.

[15] A. Egeland, W. J. Burke (2005). Kristian Birkeland the First Space Scientist, *Springer*, Dordrecht, The Netherlands.

[16] Birkeland, Kr. (1906). On the oxidation of atmospheric nitrogen in electric arcs. *Transactions of the Faraday Society*, *2*(December), 98.

[17] Ernst, F. A. (1928). Market report –april,1928. *Industrial & Engineering Chemistry*, *20*(5), 559–560.

[18] Maxwell, G. R. (2017). Synthetic Nitrogen Products. *Handbook of Industrial Chemistry and Biotechnology*, 1125–1210.

[19] S. Travis, A. (2015). The synthetic nitrogen industry in World War I. *SpringerBriefs in Molecular Science*.

[20] Appl, M. (1997). The Haber-Bosch Heritage: The Ammonia Production Technology. *50th Anniversary of the IFA Technical Conference*, 1–25.

[21] Ott, J., Gronemann, V., Pontzen, F., Fiedler, E., Grossmann, G., Kersebohm, D. B., Weiss, G., & Witte, C. (2012). Methanol. *Ullmann's Encyclopedia of Industrial Chemistry*.

[22] Howarth, R. W., & Jacobson, M. Z. (2021). How green is blue hydrogen? *Energy Science & Engineering*, 9(10), 1676–1687.

[23] Castelvecchi, D. (2022). How the Hydrogen Revolution can help save the planet — and how it can't. *Nature*, 611(7936), 440–443.

[24] Appl, M. (2011). Ammonia, 1. introduction. Ullmann's Encyclopedia of Industrial Chemistry.

[25] Ertl, G. (1983). Zum Mechanismus der Ammoniak-Synthese. Nachrichten Aus Chemie, *Technik Und Laboratorium*, 31(3), 178–182.

[26] Schlog, R., & Jennings, J. R. (1991). Chapter 2. Preparation and activation of the technical ammonia synthesis catalyst. In *Catalytic Ammonia Synthesis: Fundamentals and Practice* (pp. 19–107). Springer Science+Business Media New York.

[27] Højlund Nielsen, P. E. (1995). Poisoning of Ammonia Synthesis Catalysts. Ammonia, 191–198.

[28] Schiffer, Z. J., & Manthiram, K. (2017). Electrification and decarbonization of the chemical industry. Joule, 1(1), 10–14.

[29] Smith, C., Hill, A., & Torrente-Murciano, L. (2020). Current and future role of Haber–Bosch ammonia in a carbon-free energy landscape. Energy and *Environmental Science*, 13(2), 331–344.

[30] Grundt, T. (1982). Hydrogen by water electrolysis as basis for small scale ammonia production. A comparison with hydrocarbon based technologies. *International Journal of Hydrogen Energy*, 7(3), 247–257.

[31] Modak, J. M. (2002). Haber process for ammonia synthesis. *Resonance*, 7(9), 69–77.

[32] Chew, K. W., Chia, S. R., Yen, H. W., Nomanbhay, S., Ho, Y., & Show, P. L. (2019). Transformation of Biomass Waste into Sustainable Organic Fertilizers. *Sustainability*, 11(8), 2266.

[33] Schrock, R. R. (2006). Reduction of Dinitrogen. *Proceedings of the National Academy of Sciences*, 103(46), 17087–17087.

[34] Rafiqul, I., Weber, C., Lehmann, B., & Voss, A. (2005). Energy efficiency improvements in ammonia production—perspectives and uncertainties. *Energy*, 30(13), 2487–2504.

[35] Lanzafame, P., Abate, S., Ampelli, C., Genovese, C., Passalacqua, R., Centi, G., & Perathoner, S. (2017). Beyond solar fuels: Renewable energy-driven chemistry. *ChemSusChem*, 10(22), 4409–4419.

[36] IEA. (2023). *Global Energy and Climate Model*. Paris: IEA. Retrieved from https://www.iea.org/reports/global-energy-and-climate-model. License: CC BY 4.0.

[37] Summary for policymakers. (2022). Global Warming of 1.5°C, 1–24.

[38] Højlund Nielsen, P. E. (2017). Method for Start-up Heating of an Ammonia Synthesis Converter (Patent No. WO2017186613A1). Retrieved from https://patents.google.com/patent/WO2017186613A1/en

[39] Ponikvar, Ž., Likozar, B., & Gyergyek, S. (2022). Electrification of catalytic ammonia production and decomposition reactions: from resistance, induction, and dielectric reactor heating to electrolysis. *ACS Applied Energy Materials*, 5(5), 5457–5472.

[40] Chen, S., Perathoner, S., Ampelli, C., & Centi, G. (2019). Electrochemical Dinitrogen Activation: To find a sustainable way to produce ammonia. *Studies in Surface Science and Catalysis*, 31–46.

[41] Chen, S., Perathoner, S., Ampelli, C., Mebrahtu, C., Su, D., & Centi, G. (2017a). Electrocatalytic synthesis of ammonia at room temperature and atmospheric pressure from water and nitrogen on a carbon-nanotube-based electrocatalyst. *Angewandte Chemie International Edition*, 56(10), 2699–2703.

[42] Chen, S., Perathoner, S., Ampelli, C., Wei, H., Abate, S., Zhang, B., & Centi, G. (2020b). Enhanced performance in the direct electrocatalytic synthesis of ammonia from N_2 and H_2O by an in-situ electrochemical activation of CNT-supported iron oxide nanoparticles. *Journal of Energy Chemistry*, 49, 22–32.

[43] Chen, S., Perathoner, S., Ampelli, C., Mebrahtu, C., Su, D., & Centi, G. (2017b). Room-temperature electrocatalytic synthesis of NH_3 from H_2O and N_2 in a gas–liquid–solid three-phase reactor. *ACS Sustainable Chemistry & Engineering*, 5(8), 7393–7400.

[44] Chen, S., Perathoner, S., Ampelli, C., Wei, H., Abate, S., Zhang, B., & Centi, G. (2020a). Direct synthesis of ammonia from N_2 and H_2O on different iron species supported on carbon nanotubes using a gas-phase electrocatalytic flow reactor. *ChemElectroChem*, 7(14), 3028–3037.

[45] Wei, H., Jiang, Q., Ampelli, C., Chen, S., Perathoner, S., Liu, Y., & Centi, G. (2020). Enhancing N_2 fixation activity by converting Ti_3C_2 MXenes nanosheets to Nanoribbons. *ChemSusChem*, 13(21), 5614–5619.

[46] Chu, K., Luo, Y., Shen, P., Li, X., Li, Q., & Guo, Y. (2022). Unveiling the synergy of O-vacancy and heterostructure over MoO_{3-x}/MXene for N_2 electroreduction to NH_3. *Advanced Energy Materials*, 12(3).

[47] Fei, H., Guo, T., Xin, Y., Wang, L., Liu, R., Wang, D., Liu, F., & Wu, Z. (2022). Sulfur vacancy engineering of MoS_2 via phosphorus incorporation for improved electrocatalytic N_2 reduction to NH_3. *Applied Catalysis B: Environmental*, 300, 120733.

[48] Jiang, Y., Wang, M., Zhang, L., Liu, S., Cao, Y., Qian, S., Cheng, Y., Xu, X., Yan, C., & Qian, T. (2022). Distorted spinel ferrite heterostructure triggered by alkaline earth metal substitution facilitates nitrogen localization and electrocatalytic reduction to ammonia. *Chemical Engineering Journal*, 450, 138226.

[49] Wang, S., Qian, C., & Zhou, S. (2023). Accelerating the development of electrocatalysts for electrochemical nitrogen fixation through theoretical and computational approaches. *Materials Chemistry Frontiers*, 7(19), 4259–4280.

[50] Skúlason, E.; Bligaard, T.; Gudmundsdóttir, S.; Studt, F.; Rossmeisl, J.; Abild-Pedersen, F.; Vegge, T.; Jónsson, H.; Nørskov, J. K. A Theoretical Evaluation of Possible Transition Metal Electro- Catalysts for N_2 Reduction. *Phys. Chem. Chem. Phys.* 2012, 14, 1235− 1245

[51] Cui, X., Tang, C., & Zhang, Q. (2018). A Review of Electrocatalytic Reduction of Dinitrogen to Ammonia under Ambient Conditions. *Advanced Energy Materials*, 8(22).

[52] Van Der Ham, C. J. M., Koper, M. T. M., & Hetterscheid, D. G. H. (2014). Challenges in reduction of dinitrogen by proton and electron transfer. *Chemical Society Reviews*, 43(15), 5183–5191.

[53] Wan, H., Bagger, A., & Rossmeisl, J. (2022). Limitations of electrochemical nitrogen oxidation toward nitrate. *The Journal of Physical Chemistry Letters*, *13*(38), 8928–8934.

[54] Lü, X., Song, H., Cai, J., & Lu, S. (2021). Recent development of electrochemical nitrate reduction to ammonia: A mini review. *Electrochemistry Communications*, *129*, 107094.

[55] Cai, J., Wei, Y., Cao, A., Huang, J., Jiang, Z., Lu, S., & Zang, S.-Q. (2022). Electrocatalytic nitrate-to-ammonia conversion with ~100% faradaic efficiency via single-atom alloying. *Applied Catalysis B: Environmental*, *316*, 121683.

[56] Wang, Y., Xu, A., Wang, Z., Huang, L., Li, J., Li, F., Wicks, J., Luo, M., Nam, D.-H., Tan, C.-S., Ding, Y., Wu, J., Lum, Y., Dinh, C.-T., Sinton, D., Zheng, G., & Sargent, E. H. (2020). Enhanced nitrate-to-ammonia activity on copper–nickel alloys via tuning of intermediate adsorption. *Journal of the American Chemical Society*, *142*(12), 5702–5708.

[57] Sclafani, A., Augugliaro, V., & Schiavello, M. (1983). Dinitrogen electrochemical reduction to ammonia over iron cathode in aqueous medium. *Journal of The Electrochemical Society*, *130*(3), 734–736.

[58] Liu, H.-M., Han, S.-H., Zhao, Y., Zhu, Y.-Y., Tian, X.-L., Zeng, J.-H., Jiang, J.-X., Xia, B. Y., & Chen, Y. (2018). Surfactant-free atomically ultrathin rhodium nanosheet nanoassemblies for efficient nitrogen electroreduction. *Journal of Materials Chemistry A*, *6*(7), 3211–3217.

[59] Huang, H., Xia, L., Shi, X., Asiri, A. M., & Sun, X. (2018). Ag nanosheets for efficient electrocatalytic N_2 fixation to NH_3 under ambient conditions. *Chemical Communications*, *54*(81), 11427–11430.

[60] Qing, G., Ghazfar, R., Jackowski, S. T., Habibzadeh, F., Ashtiani, M. M., Chen, C.-P., Smith, M. R., & Hamann, T. W. (2020). Recent advances and challenges of electrocatalytic N_2 reduction to ammonia. *Chemical Reviews*, *120*(12), 5437–5516.

[61] Tavella, F., Giusi, D., & Ampelli, C. (2022). Nitrogen reduction reaction to ammonia at ambient conditions: A short review analysis of the critical factors limiting electrocatalytic performance. *Current Opinion in Green and Sustainable Chemistry*, *35*, 100604.

[62] Lazouski, N., Chung, M., Williams, K., Gala, M. L., & Manthiram, K. (2020). Non-aqueous gas diffusion electrodes for rapid ammonia synthesis from nitrogen and water-splitting-derived hydrogen. *Nature Catalysis, 3*(5), 463–469.

[63] Ampelli, C. (2020). Electrode design for ammonia synthesis. *Nature Catalysis, 3*(5), 420–421.

[64] Li, Z., Geßner, A., Richters, J.-P., Kalden, J., Voss, T., Kübel, C., & Taubert, A. (2008). Hollow Zinc oxide mesocrystals from an Ionic Liquid Precursor (ILP). *Advanced Materials, 20*(7), 1279–1285.

[65] Tian, Y., Liu, Y., Wang, H., Liu, L., & Hu, W. (2022). Electrocatalytic reduction of nitrogen to ammonia in ionic liquids. *ACS Sustainable Chemistry & Engineering*, *10*(14), 4345–4358.

[66] Martín, A. J., & Pérez-Ramírez, J. (2019). Heading to Distributed Electrocatalytic Conversion of Small Abundant Molecules into Fuels, Chemicals, and Fertilizers. *Joule, 3*(11), 2602–2621.

[67] Dogutan, D. K., & Nocera, D. G. (2019). Artificial photosynthesis at efficiencies greatly exceeding that of natural photosynthesis. *Accounts of Chemical Research, 52(*11), 3143–3148.

[68] Patil, B. S. (2017). *Plasma (catalyst) - assisted nitrogen fixation: Reactor development for nitric oxide and ammonia production* (PhD Thesis No. 1, Research TU/e / Graduation TU/e), Chemical Engineering and Chemistry]. Technische Universiteit Eindhoven.

[69] Taylor, P. R., & Pirzada, S. A. (1994). Thermal plasma processing of materials: A Review. *Advanced Performance Materials, 1*(1), 35–50.

[70] van Helden, J. H., Wagemans, W., Yagci, G., Zijlmans, R. A., Schram, D. C., Engeln, R., Lombardi, G., Stancu, G. D., & Röpcke, J. (2007). Detailed study of the plasma-activated catalytic generation of ammonia in N_2-H_2 plasmas. *Journal of Applied Physics, 101*(4).

[71] Bogaerts, A., Tu, X., Whitehead, J. C., Centi, G., Lefferts, L., Guaitella, O., Azzolina-Jury, F., Kim, H., Murphy, A. B., Schneider, W. F., Nozaki, T., Hicks, J. C., Rousseau, A., Thevenet, F., Khacef, A., & Carreon, M. L. (2020). *The 2020 plasma catalysis roadmap. Journal of Physics D, 53(*44), 443001.

[72] Farber E. From Chemistry to philosophy: the way of Alwin Mittasch (1869 - 1953). *Chymia 1966*;11: 157 – 78.

[73] Patil, B., Hessel, V., Seefeldt, L. C., Dean, D. R., Hoffman, B. M., Cook, B. J., & Murray, L. J. (2017). Nitrogen fixation. *Ullmann's Encyclopedia of Industrial Chemistry*, 1–21.

[74] Brightling, J. R. (2018). Ammonia and the fertiliser industry: The development of ammonia at Billingham. *Johnson Matthey Technology Review*, *62*(1), 32-47.

[75] Fertilizers Europe. (2000). Best Available Techniques for Pollution Prevention and Control in the European Fertilizer Industry: Booklet No. 1 of 8 - Production of Ammonia. Copyright 2000.

[76] Rouwenhorst, K. H. R., Krzywda, P., Benes, N. E., Mul, G., & Lefferts, L. (2021). Ammonia Production Technologies. In Elsevier eBooks (pp. 41–83).

[77] Technology readiness levels (TRL), HORIZON 2020 – WORK PROGRAMME 2018-2020 General Annexes, Extract from Part 19 - Commission Decision C(2017)7124

2. | Materials

2.1 | Preface

This chapter is dedicated to the materials used for manufacturing the catalysts for both the electrocatalytic and plasma-catalysis tests. Synthesis methods of materials will be described in detail: the metal-based catalysts/electrodes, prepared by depositing the materials on different supports (activated nanocarbons or alumina), present different chemical, physical, and electronic properties, which will be discussed through characterization data, while testing results will be provided and discussed in the next chapters.

2.2 | State-of-the-art

The discovery of new catalysts has brought important advances in the chemical industry and opened the way for new applications and technological developments, helping to make chemical processes more sustainable and environmentally friendly. The technological advancement has also led the engineering of these catalysts, with the help of computational calculations (i.e. Density Functional Theory – DFT) on the binding energies between N_2 and the surface of catalysts, going against the trial-and-error approach typically used.
In literature, several catalysts have been explored by ab initio DFT calculations. These catalysts can be subdivided into i) noble-metal based, ii) non-noble-metal based, and iii) metal-free based [1]. Active phases are anchored on supports, where due to the particular geometry they assumes , acting as hot spots for the reaction.

Currently, single-atom catalysts (SACs) are very popular. As reported from *Wang et al.*[2], single Au atoms, prepared by wet impregnation method, were dispersed on g-C_3N_4 for Nitrogen Reduction Raction (NRR) with a resulted Faradaic Efficiency (FE) of 11.1% and an ammonia yield of 1305 μg mg_{Au}^{-1} h^{-1}. Among

other materials prepared by wet impregnation method, Ru-based single atom nanocarbons (Ru SAs/NCs) were synthesised and tested by *Geng et al.*[3], obtaining a FE of 29.6% and an ammonia yield of 120.9 μg mg_{cat}^{-1} h^{-1} at -0.2 V vs RHE. Iron-based SACs on nanocarbons[4] also showed a good performance, i.e. FE of 39.6% and an ammonia yield of 53.12 μg mg_{cat}^{-1} h^{-1} at -0.35 V vs RHE. A recent work from *Liu et al.* [5] shows how a co-doping synergy could help in the nitrogen conversion into ammonia: the bimetallic Ru-Fe anchored on nitrogen doped-carbon nanospheres catalyst exhibited a FE of 29.3% and an NH_3 yield of 43.9 μg mg_{cat}^{-1} h^{-1} at -0.2 V vs RHE. *Hamsa et al.*[1] also made a comparison between the metal SAC and the nanoparticles-doped carbon, suggesting an increase performance (in yield) of the SAC of a ~50% with respect to nanoparticles catalyst.

2.3 | Aim of chapter

In order to make a useful comparison among different ammonia production catalytic systems, the metals at the top of the volcano plot (Fe, Ru) were chosen in terms of the adsorption/desorption bond energies (as discussed in Chapter 1), in term of costs, and also based on what is promising in the literature. In agreement with published articles for the Non-Thermal Plasma catalytic approach, the most discussed supports used in Dielectric-barrier discharge (DBD) reactor are oxide substrates (TiO_2, Al_2O_3 and SiO_2)[6,7,8], different zeolites[9] and rarely activated carbons[10].

Specifically, Alumina (Al_2O_3) was selected as a promising support for this thesis work, very known in the literature for its excellent dielectric properties (useful for plasma applications), as well as functionalized carbon nanotubes (CNTs) were chosen, for their enhanced properties as conductive electrocatalytic substrate. More in detail, we used carbon nanofibers (having a larger diameter than CNTs) as carbon support.

2.3.1 | Techniques for catalyst preparation

(co-)Precipitation, impregnation and atomic layer deposition (ALD) methods are among the most widely used ways to prepare catalysts on a laboratory scale.

Precipitation methods can be divided into three steps i) supersaturation, ii) nucleation and iii) growth. The main advantages of this technique can be summarized as follows: (i) the homogeneity of component distribution, (ii) the relatively low reaction temperature, (iii) the fine and uniform particle size with weakly agglomerated particles, and (iv) the low cost. The disadvantages to take into account refer to the precipitation process, generally not controlled in term of reaction kinetics, and the nucleation and growth processes depending from the reaction conditions[11]. It is also difficult to control the stoichiometry of the precursor, and the reaction time could reach 18-48h.

Impregnation methods consist in a certain volume of solution containing the precursor of the active phase, in contact with the solid (the support), where subsequently the solvent is dried. There are two methods of impregnation: Wet Impregnation (WI) and Incipient Wetness Impregnation (IWI), the latter also called dry impregnation. The substantial difference between these two methods consists in the volume of solvent that is in excess with respect to the pore volume for WI, while in the IWI the volume is equal to the volume of the pore to fill. The mechanism of deposition of the precursor for WI is limited by diffusion, while for IWI is in direct action into the pore for capillarity. Generally, these methods are fast, inexpensive, and allows to achieve the desired final properties and configuration, but it is hard to prepare high-loading catalysts by these impregnation techniques and obtain a homogeneous dispersion on the surface. However, wet impregnation method allows gaining great advantage compared to other techniques, especially attributable to the change of transport phenomena, from a capillary action (IWI) to a diffusion process (WI).

From the other hands, ALD allows controlling the thickness of the film (due to the number of cycles for deposition), high repeatability, but requiring an

expensive setup, material waste, energy-intensive nature of ALD process and nanoparticle emissions [12].

Among the previously discussed methods, and also given their versatility and ease of use, the WI method was chosen for catalyst preparation[13].

2.3.2 | Catalysts metal loading

Regarding the metal loading of catalysts, the loading used by *Chen et al.*[14] was taken as the reference. Among several iron precursors, Fe_2O_3/CNT achieved the best performance (41.6 μg mg_{cat}^{-1} h^{-1}, and a FE of 17%) in three hours at -0.5 V vs RHE. This 30 wt.% Fe_2O_3 loaded catalyst achieved the higher productivity [15] and was thus taken as the reference for the electrochemical experiments of this thesis.

Moreover, *Li et al.*[16] and *van Raak et al.*[17] tested ruthenium under plasma catalytic conditions on different supports, i.e. Al_2O_3, CeO_2 and Ti-CeO_2. The Ru/Al_2O_3 catalyst achieved the best performance especially with a power input of 10 W, flowrate of 120 mL min^{-1}, and an N_2:H_2 ratio of 2:1. The metal loading of the Ru/Al_2O_3 catalyst at 5 wt.% was also taken as a reference for plasma catalytic catalysts because of the ease of preparation (WI).

In addition, in order to decrease critical/expensive materials, hybrid catalysts (based on Ru-Fe) were designed, where 50% of the ruthenium was replaced with iron. Thus, Iron-based (Fe_2O_3), ruthenium-based (Ru), and Ru-Fe hybrid catalysts were synthesized, supported on both α-alumina ($A_{l2}O_3$) and functionalized carbon nanotubes (CNTs), for a total of 6 catalysts from these combinations as reported in **table 2.1**. The aforementioned catalysts were tested under both electrocatalytic and plasma catalytic conditions, and testing results will be described in Chapters 3 and 4, respectively.

Catalysts	Ru /Al_2O_3	Ru-Fe /Al_2O_3	Fe_2O_3 /Al_2O_3	Ru /CNTs	Ru-Fe /CNTs	Fe_2O_3 /CNTs
Theoretical load (wt.%)	5%	2.5% 2.5%	5%	5%	2.5% 2.5%	30%

Table 2.1 *– Summary of theoretical loading*

2.4 | Alumina-based catalysts

Aluminium oxide, commonly referred as alumina (Al_2O_3), is a highly significant aluminium compound extensively utilized in various industrial and scientific applications (for instance, as a material for catalytic support). Its characteristics, such as outstanding chemical inertness, hardness, and resistance, contribute to its popularity. Moreover, it exhibits a high electrical resistivity[18] of 1×10^{14} Ω·cm (with a dielectric constant $\varepsilon = 9.34$)[19]. Notably, the crystalline structure of this substance varies significantly based on temperature and pressure conditions. The primary crystalline phases of alumina are α, β, and γ-alumina. The main difference is the degree of surface area, which is greater in the γ-alumina and follows the trend (γ > β > α-alumina)[20]. Alumina-based materials synthesis is described below.

2.4.1 | Alumina support

Blank α-alumina pellets (MaTeck) with a surface area of 0.18 m^2 g^{-1} were purchased, smashed, and separated by mechanical milling and sieving in the range of 250-355 mm.

2.4.2 | Ru/Al_2O_3

The α-alumina (0.95 g) and Ruthenium(III) chloride hydrate, (0.1316 g, $RuCl_3 \cdot xH_2O$, Ru basis, 38.0-42.0%) were used to make an aqueous suspension (25 mL ultrapure H_2O) for the wet impregnation process. After one hour of impregnation, the sample was dried overnight and then calcined in air at 400 °C for 4h, and finally reduced at 400 °C in a tubular furnace under H_2 and Ar flow

for 4 h. The *fresh*-Ru-Al_2O_3, loaded with Ruthenium at 5% in weight approximatively, was obtained.

2.4.3 | Ru-Fe/Al_2O_3

The α-alumina (1.90 g), Ruthenium(III) chloride hydrate (0.256 g, $RuCl_3 \cdot xH_2O$, Ru basis, 38.0-42.0%) and iron(III) nitrate nonahydrate (0.361 g, $Fe(NO_3)_3 \cdot 9H_2O$, ≥ 99.95% trace metals basis) were used to make an aqueous suspension (25 mL ultrapure H_2O) for the wet impregnation process. After one hour of impregnation, the sample was dried overnight, then calcined in air at 400 °C for 4h, and finally reduced at 400 °C in a tubular furnace under H_2 and Ar flow for 4 h. The *fresh*-FeRu-Al_2O_3, loaded with Iron at 2.5% and Ruthenium at 2.5% in weight approximatively, was obtained.

2.4.4 | Fe_2O_3/Al_2O_3

The α-alumina (0.903 g) and Fe-precursor, iron(III) nitrate nonahydrate nonahydrate (0.253 g, $Fe(NO_3)_3 \cdot 9H_2O$, ≥ 99.95% trace metals basis), were suspended in 25 mL of deionized water with 1 mL of Ethylene Glycol; then the mixture was sonicated for 30 minutes, and the pH was adjusted to 8 with a 5% ammonium hydroxide solution. Afterwards, the solvent was eliminated by drying at 120 °C overnight. The obtained powder was calcined for 2 h at 400°C in a horizontal tubular furnace under Ar flow. The *fresh*-Fe_2O_3-Al_2O_3, loaded with Iron (III) oxide at 5% in weight approximatively, was obtained.

2.5 | Functionalized Carbon Nanotubes (CNTs-o) based catalysts

2.5.1 | Carbon nanoutubes (CNTs)

A novel carbon allotrope was discovered when Japanese scientist Sumio Iijima observed hollow carbon tubules formed by a high current arc discharge process to evaporate graphite in 1991[21]. Carbon nanotubes (CNTs) are difficult to dissolve in water or organic solvents, or even anchor metals on the surface;

therefore, new methods to modify the properties of these nanotubes with appropriate functional group insertion have been studied and devised. The single-walled carbon nanotubes (SWCNTs) with no functional groups attached are quasi-cylindrical macromolecules that tend to be chemically inert [29]. Their nonplanar state induces a curvature of the pyramidalization and a misalignment of the π-orbital of two conjugated atoms (**Figure 2.1b**).

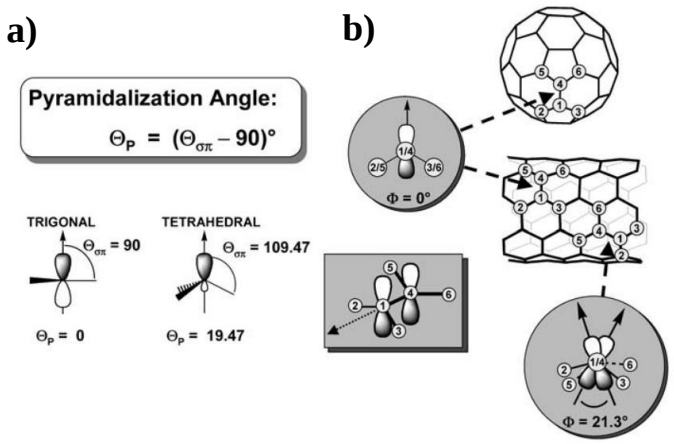

Figure 2.1 *- A representation of the* ***a)*** *pyramidalization angle (Φ_P) and* ***b)*** *of the π-orbital misalignment angles (Φ) along the C1-C4 bond in a (5,5)-SWCNT and a C_{60}* [29]

Due to their cylindrical tube structure composed of sp^2 hybridized carbon atoms, CNTs offer excellent electrical conductivity. Their structure allows electrons to freely move along the tube, making them one of the most conductive materials on Earth. Given their chemical similarity, it is feasible to conduct functionalization on the imperfections present in Multi-Walled Carbon Nanotubes (MWCNTs). The difference is that MWCNTs have a concentrical nested tube-like graphene structures, and other outlet shell having a larger diameter than single walled carbon nanotubes (SWCNTs). For this doctoral thesis, MWCNTs-like carbon support was used, precisely *Pyrograph-III, PR-24XT*. Actually, they are carbon nanofibers, having a bigger diameter (~100-200 nm) with respect to the conventional SWCNTs (1-2 nm diameter and few micrometres in length) or MWCNTs (7-100 nm diameter up to 1 mm in length)[22]. For the sake of clarity

in subsequent discussions, the term "CNTs" will be employed to represent carbon nanofibers.

2.5.2 | Functionalization of CNTs

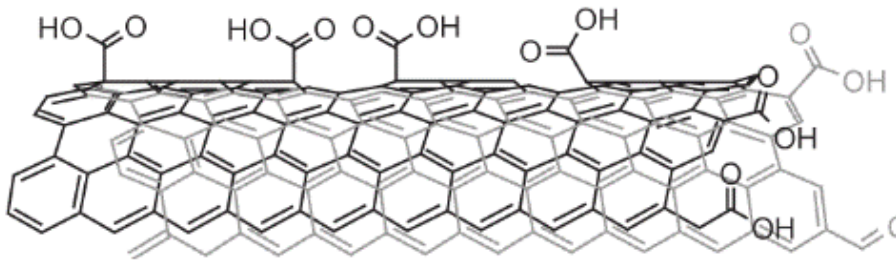

***Figure 2.2** - An oxidized SWCNT section, showing oxidation in the terminal and sidewalls [29]*

Holzinger et al. [23] developed a method for CNTs functionalization through oxidative treatment. The functionalization consists in the insertion of carboxyl groups on the surface of the nanotubes. The oxidative treatment involves the use of concentrated nitric acid, sulfuric acid or a mixture of both. The reaction takes place at reflux at a temperature of 120°C [15]. At the end of the treatment, an indeterminate number of carboxyl groups are introduced, depending on the number of defects on the surface (**Figure 2.2**).

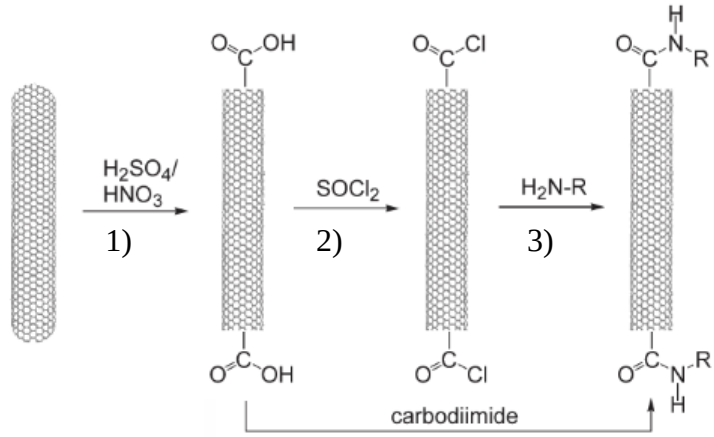

***Figure 3.3** – Schematic representation of different steps of functionalization [29]*

Further functionalization modifications can be made to the functional groups in order to change their properties (hydrophilicity[24], hydrophobicity[25,26], branching[27] and so on[28]), but for our purposes, the reaction will stop at step 1.

CNTs-based material's synthesis and CNT functionalization methods, adopted in this thesis work, are described below.

The functionalization of CNTs consists of a pre-treatment of commercial CNTs (Pyrograph-III, PR-24XT) with Nitric Acid (conc. 65%), 50 mL for 1g of CNTs, in order to create oxygen functionalities [29] (CNTs-o), then treated at 120 °C for 2 h in a reflux apparatus. The suspension was filtered and washed with deionized water until neutral pH. The sample was dried at 80°C overnight.

2.5.3 | Ru/CNTs-o

The CNTs-o (0.425 g) and Ru-precursor, Ruthenium(III) chloride hydrate (0.128 g, $RuCl_3 \cdot xH_2O$, Ru basis, 38.0-42.0%) were dissolved in 25 mL of deionized water, then the mixture was stirred for 1.5h. After that, the solvent was eliminated by drying at 120 °C overnight. The obtained powder was calcined for 4 h at 400°C in a horizontal tubular furnace under H_2 and Ar flows. The *fresh*-Ru-CNTs-o was obtained and loaded with Ruthenium at 5% in weight approximatively.

2.5.4 | Ru-Fe/CNTs-o

The CNT-o (0.95 g) and Ru-precursor, Ruthenium(III) chloride hydrate (0.180 g, $RuCl_3 \cdot xH_2O$, Ru basis, 35.0-40.0%) and iron(III) chloride hexahydrate (0.121 g, $FeCl_3 \cdot 6H_2O$) were dissolved in 25 mL of deionized water, then the mixture was stirred for 1.5h. After that, the solvent was eliminated by drying at 120 °C overnight. The obtained powder was calcined for 4 h at 400°C in a horizontal tubular furnace under H_2 and Ar flows. The fresh RuFe-CNTs-o was obtained and loaded with Iron at 2.5% and Ruthenium at 2.5% in weight approximatively.

2.5.5 | Fe_2O_3/CNTs-o

The CNTs-o (0.7 g) and Fe-precursor, Iron(III) nitrate nonahydrate (1.515 g, $Fe(NO_3)_3 \cdot 9H_2O$, ≥ 99.95% trace metals basis), were dissolved in 25 mL of deionized water with 1 mL of Ethylene Glycol, then the mixture was sonicated for 30 minutes, and the pH was adjusted to 8 with a 5% ammonium hydroxide solution. Afterward, the solvent was eliminated by drying at 120 °C overnight. The obtained powder was calcined for 2 h at 400°C in a horizontal tubular furnace under He flows. The *fresh*-Fe_2O_3-CNT was obtained, and loaded with Iron (III) oxide at 30% in weight approximatively.

2.6 | X-Ray Diffraction

The X-Ray Diffraction (XRD) measurements were performed with a Rigaku MiniFlex600. The instrument was equipped with a Cu(Kα) x-ray radiation source. All samples were analysed in a range from 10° to 90°, step size of 0.02°, speed of 4.0°/min, voltage 40kV, current 15mA.

2.6.1 | Alumina-based catalysts

Catalysts	**Al_2O_3**	**Fe_2O_3/ Al_2O_3**	**FeRu/ Al_2O_3**	**Ru/ Al_2O_3**
Theoretical metal loading (wt.%)	No loaded	5% Fe_2O_3	2.5% Ru 2.5% Fe	5% Ru

Table 2.2 *– Theoretical metal loading for alumina-based catalysts*

Table 2.2 shows the theoretical loadings of metals on the alumina support. For the Al_2O_3 catalyst, the theoretical weight percentage of Fe taken individually (and not as Fe_2O_3) is also given.

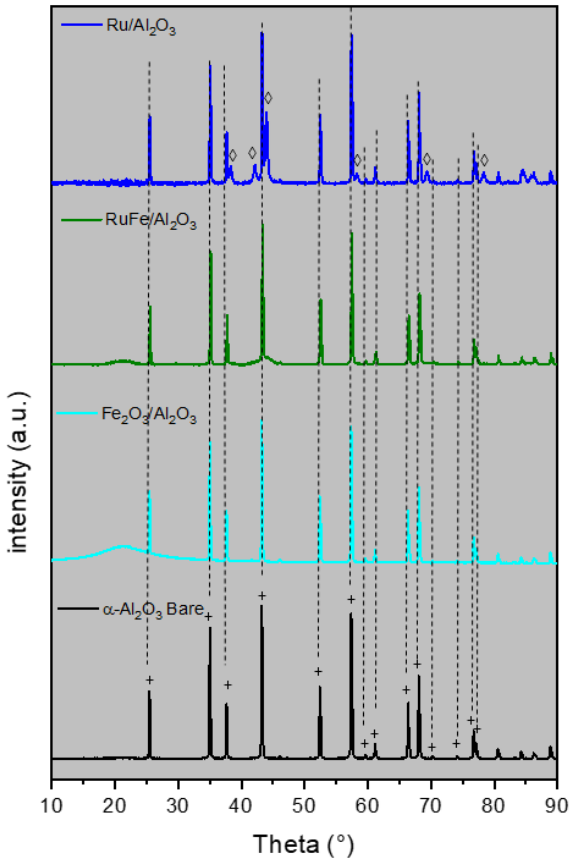

***Figure 2.4** - XRD patterns of the α-Al_2O_3-based samples: (+) α -Al_2O_3, (◊) Ruthenium*

Figure 2.4 shows the XRD patterns of alumina-based catalysts. It is possible to observe that alumina peaks are predominantly for all the α-Al_2O_3-based catalysts. The peaks of Fe_2O_3 and Ru-Fe are not detectable from XRD. As reported by *Kobayashi et al.*[30], the mixed oxide catalyst is not readily visible at XRD due to both the weight loading of Fe_2O_3 (undetectable below 34wt.% on alumina) and the segregation following calcination. The same assumptions can also be made for the Ru-Fe catalyst, as reported by *Liu et al.*[31], both because of the low loading, and the catalyst could be atomically dispersed. Diffraction peaks at 2Θ = 38.41, 42.18, 44.04, 58.36, 69.47, 78.41, for Ruthenium (JCPDS card no. 89-3942) correspond to the (1 0 0), (0 0 2), (1 0 1), (1 0 2), (1 1 0) and (1 0 3) planes, respectively (blue line in **figure 2.4**). Diffraction peaks at 2Θ =25.58, 35.16,

37.78, 43.36, 52.56, 57.51, 59.75, 61.32, 66.53, 68.22, 70.43, 74.32, 76.89, 77.25 for α-Al_2O_3 (International Center of Diffraction Data (ICDD) of card number 00–010–0173 of α-Al_2O_3) correspond to the (0 1 2), (1 0 4), (1 1 0), (1 1 3), (0 2 4), (1 1 6), (2 1 1), (0 1 8), (2 1 4), (3 0 0), (1 2 5), (2 0 8), (1 0 10) and (1 1 9) planes, respectively (black line in **figure 2.4**).

2.6.2 | *CNTs-o-based catalysts*

Catalysts	**CNTs**	**Fe_2O_3/CNTs**	**FeRu/CNTs**	**Ru/CNTs**
Theoretical metal loading (wt.%)	No loaded	30% Fe_2O_3	2.5% Ru 2.5% Fe	5% Ru

Table 2.3 *– Theoretical metal loading for alumina-based catalysts*

Table 2.3 shows the theoretical loadings of metals on the functionalized carbon-nanotubes (CNTs) support. Also in this case for the Fe_2O_3 catalyst, the weight percentage of Fe taken individually (and not as Fe_2O_3) is also given. The theoretical loading of 30%, as mentioned above, was chosen from the best performance loading reported [14,15].

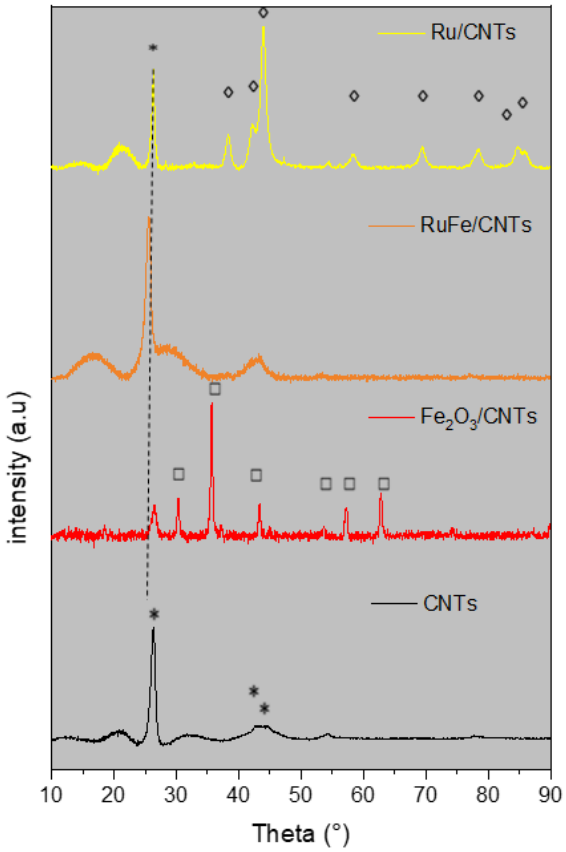

***Figure 2.5** - XRD patterns of the CNTs-based samples: (*) CNTs, (◊) Ruthenium, (□) Fe_2O_3*

The **figure 2.5** shows different diffraction patterns of CNTs-based catalyst. Metal peaks are more intense in comparison with Al_2O_3-based samples, evidencing more clearly the Ruthenium peaks already mentioned above, and in addition, three extra peaks at 2Θ = 82.28, 84.73 and 86.01, corresponding to (2 0 0), (1 1 2) and (2 0 1) planes, respectively (yellow line in **figure 2.5**). For Fe_2O_3, it is possible to see the peaks at 2Θ =30.3, 35.6, 43.3, 53.8, 57.1 and 62.8, corresponding to (2 2 0), (3 1 1), (4 0 0), (4 2 2), (5 1 1) and (4 4 0) planes (red line in **figure 2.5**) and confirming the presence of γ-Fe_2O_3 phase [32] with lattice parameters a= 8.2680, b=8.2680, and c=8.2680. CNTs characteristic peaks at 2Θ = 28°, 42°, and 48° are related to C (002), C (100), and C (101), respectively [33]. The same assumptions as previously stated apply to this case of co-doping Ru-Fe on CNTs as well[31].

2.7 | Brunel-Emmett-Teller analysis

Average pore diameters, BET surface area and total pore volume, were obtained using the Brunauer-Emmett-Teller (BET) equation for fresh samples, analysis performed with Micrometrics TriStar II.

Catalysts	Absorption-Desorption average pore diameter (nm)	BET surface area (m^2/g)	Total pore volume (cc/g)
CNTs	0.965 - 4.023	54.75	$3.564\ 10^{-1}$
Fe_2O_3/CNTs	0.978 - 4.019	61.82	$2.879\ 10^{-1}$
Ru-Fe/CNTs	0.955 - 4.027	63.59	$3.552\ 10^{-1}$
Ru/CNTs	0.956 - 2.533	105.67	$5.975\ 10^{-1}$
Al_2O_3	0.946 - 1.556	0.210	$2.253\ 10^{-4}$
Fe_2O_3/ Al_2O_3	0.949 - 3.613	8.94	$7.199\ 10^{-3}$
Ru-Fe/Al_2O_3	0.949 - 1.935	17.59	$2.055\ 10^{-2}$
Ru/Al_2O_3	0.947 - 1.935	1.841	$1.504\ 10^{-2}$

***Table 2.4** – Surface properties of fresh catalysts*

Table 2.4 compares various properties such as absorption-desorption average pore diameter (nm), BET surface area (m^2/g), and total pore volume (cc/g) of different catalysts and supports.

CNTs show a moderate range of absorption-desorption pore diameters, with a relatively high BET surface area and total pore volume. The addition of metal oxides (Fe_2O_3, Ru) or combinations (Ru-Fe) with CNTs generally leads to increased pore diameters, surface areas, and pore. When considering individual metal oxides (Fe_2O_3, Ru) supported on CNTs, they exhibit higher surface areas and pore volumes compared to CNTs alone. The surface area decreases in the order Ru/CNTs > Ru-Fe/CNTs > Fe_2O_3/CNTs > CNTs.

Al_2O_3, in contrast, displays significantly smaller pore diameters, surface area, and total pore volume compared to CNTs and their combinations with metal oxides. Combinations of metal oxides (Fe_2O_3, Ru) with Al_2O_3 demonstrate improved pore

diameters, surface areas, and pore volumes compared to Al_2O_3 alone, albeit still lower than those observed with CNT combinations. Surface area for Al_2O_3-based catalyst follows the order (Ru-Fe/Al_2O_3 > Fe_2O_3/Al_2O_3 > Ru/Al_2O_3 > Al_2O_3).

Overall, the data highlights the impact of different catalyst compositions on pore characteristics, where combinations involving CNTs generally exhibit larger pore diameters, higher surface areas, and greater pore volumes compared to Al_2O_3-based catalysts.

2.8 | Scanning Electron Microscopy (SEM)

Scanning Electron Microscopy (SEM) and Energy Dispersive X-ray (EDX) Spectroscopy analyses were performed with a Phenom Pro Microscopy with EDX at 15 kV images, confirming the presence of metal not detectable via XRD for Fe_2O_3/Al_2O_3, Ru/Al_2O_3, RuFe/Al_2O_3 and RuFe/CNTs-o. The percentage loading concentration, in atomic concentration (at.%), is shown in section 2.8. For metal tracing, 200 μm images were analysed with EDX (**Figures 2.6** and **2.7**).

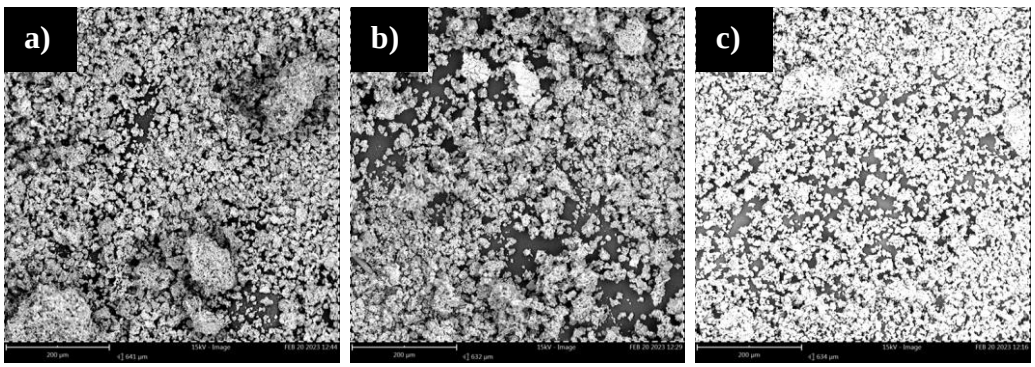

Figure 2.6 *– Catalysts SEM images at 200 μm Al_2O_3-based; a) Ru, b)Ru-Fe c)Fe_2O_3-doped respectively*

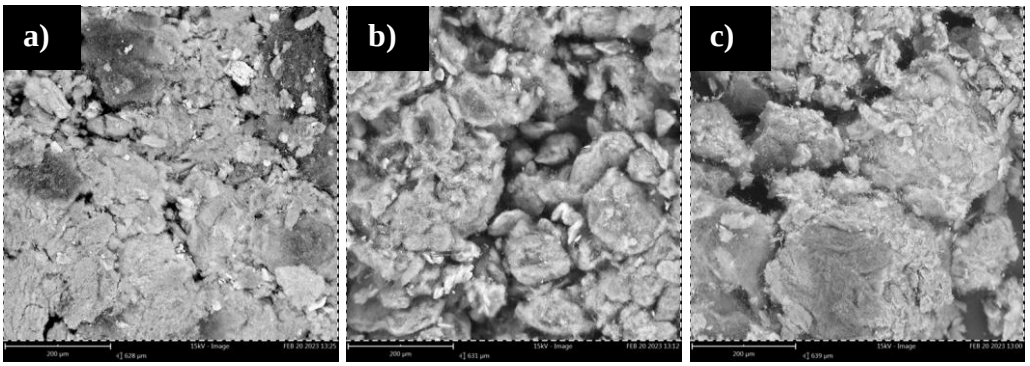

Figure 2.7 *– Catalysts SEM images at 200 μm functionalized CNTs-based; a) Ru, b)Ru-Fe c)Fe_2O_3-doped respectively*

Alumina-based catalysts (as well as functionalized CNTs-based catalysts) are shown at different magnifications, simply to provide a higher degree of detail. As shown by the images, the CNTs filaments in functionalized CNTs-based catalysts can be seen, and metal clusters are visible on their surfaces, whereas alumina-based catalysts have a larger support, and metal clusters are not visible. The sample morphology does not differ significantly (**Figure 2.8** and **2.9**).

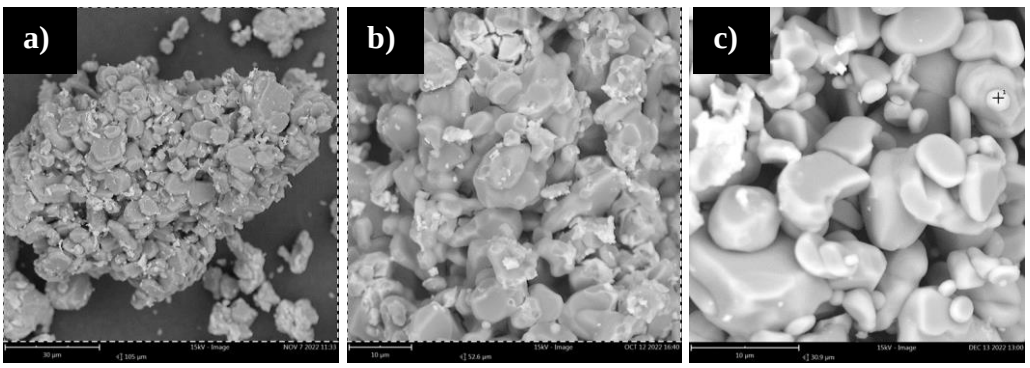

Figure 2.8 *– Catalysts SEM images Al_2O_3-based; a) Ru, b) RuFe c) Fe_2O_3-doped respectively*

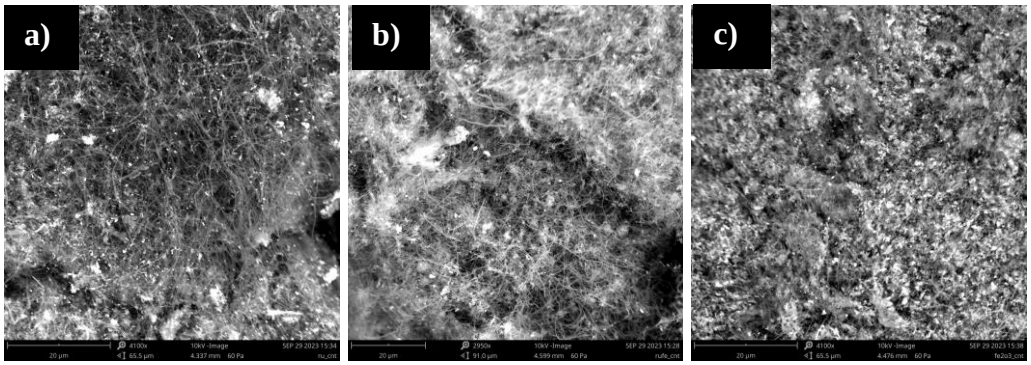

Figure 2.9 *– Catalysts SEM images CNTs-based; a) Ru, b) RuFe c) Fe_2O_3-doped respectively*

2.9 | Energy Dispersive X-ray (EDX) Spectroscopy

As part of the analysis by Phenom Pro with a 15kV source, the EDX spectrum and weight percentages of the individual elements at a focal distance of 200 μm are presented in this section. For a total of three spots, this procedure was repeated at the same focal distance. Among the alumina-based catalysts, the presence of the metals not visible on XRD, were confirmed by EDX analysis. The ruthenium catalyst on alumina, theoretically loaded at 5 wt.%, shows up after EDX analysis, an average loading between spots of 2.55 ± 0.15 at.% (**Table 2.5**). The catalyst with 2.5 wt.% Iron and 2.5 wt.% Ruthenium, shows up with a percentage loading of 2.6 ± 0.3 at.% and 1.2 ± 0.1 at.% respectively (**Table 2.6**), while the alumina loaded with 5 wt.% in Iron (III) oxide, to which corresponds an atomic Iron content of ~3.5% is present at 5.75 ± 1.45 at.% as shown in **Table 2.7**.

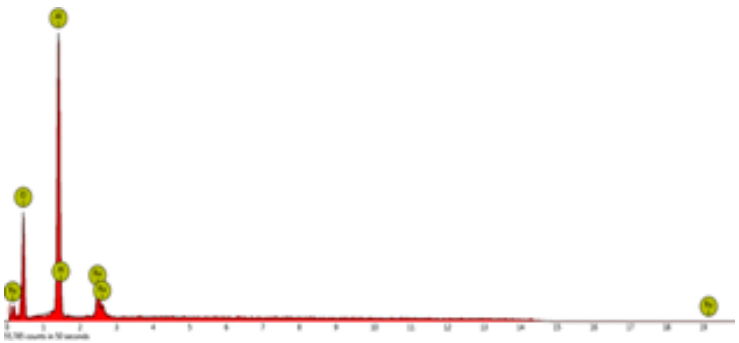

Element Number	Element Symbol	Atomic Concentration (%) Spot #1	Atomic Concentration (%) Spot #2	Atomic Concentration (%) Spot #3
13	Al	30.9	31.1	30.3
8	O	66.6	66.2	67.2
44	Ru	2.5	2.7	2.4

Figure 2.10 *- EDX analysis spectra;* ***Table 2.5*** *- Atomic concentration of elements in* Ru/Al_2O_3

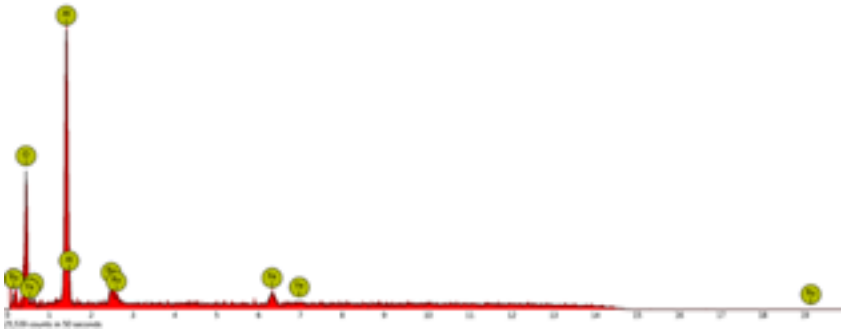

Element Number	Element Symbol	Atomic Concentration (%) Spot #1	Atomic Concentration (%) Spot #2	Atomic Concentration (%) Spot #3
13	Al	29.1	30.2	30.0
8	O	66.3	66.2	66.7
26	Fe	3.2	2.5	2.0
44	Ru	1.3	1.1	1.3

Figure 2.11 *- EDX analysis spectra;* ***Table 2.6*** *- Atomic concentration of elements in* $FeRu/Al_2O_3$

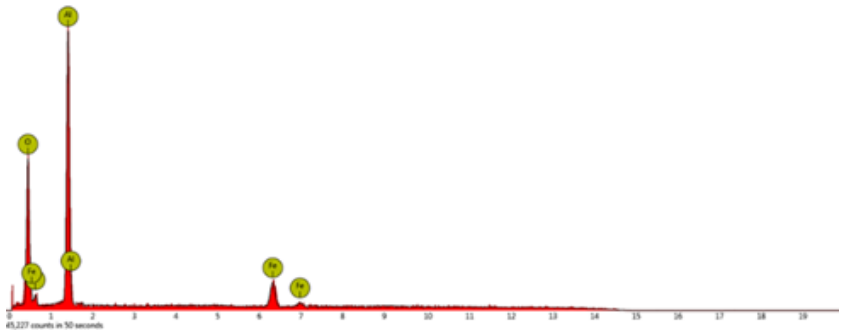

Element Number	Element Symbol	Atomic Concentration (%) Spot #1	Atomic Concentration (%) Spot #2	Atomic Concentration (%) Spot #3
13	Al	30.0	31.1	29.4
8	O	63.6	64.6	63.5
26	Fe	6.3	4.3	7.2

Figure 2.12 *- EDX analysis spectra;* ***Table 2.7*** *- Atomic concentration of elements in* Fe_2O_3/Al_2O_3

On the other hand, for nanotube-based catalysts, the Ruthenium loading which was theoretically assumed to be 5wt.%, was found to be 32.1 ± 3.7 at.% (**Table 2.8**). The theoretical loading of Ruthenium and Iron was 2.5wt.% for both metals, but the resulting loading from the EDXs was found to be 8.3 ± 2.1 at.% and 5.2 ± 1.9 at.% for Ruthenium and Iron, respectively (**Table 2.9**). In the end, the catalyst loaded to the theoretical 30 wt.% with Fe_2O_3 (thus a ~21 wt.% Iron content) was found to be 24.8 ± 4.4 at.% (**Table 2.10**).

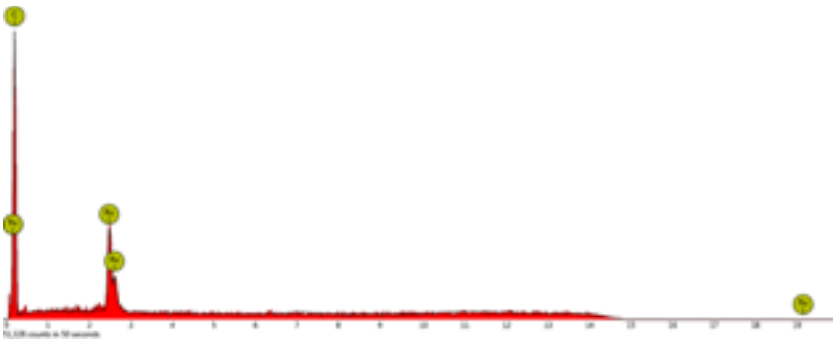

Element Number	Element Symbol	Atomic Concentration (%) Spot #1	Atomic Concentration (%) Spot #2	Atomic Concentration (%) Spot #3
6	C	65.4	65.6	72.8
44	Ru	34.6	34.4	27.2

***Figure 2.13** - EDX analysis spectra; **Table 2.8** - Atomic concentration of elements in Ru/CNTs*

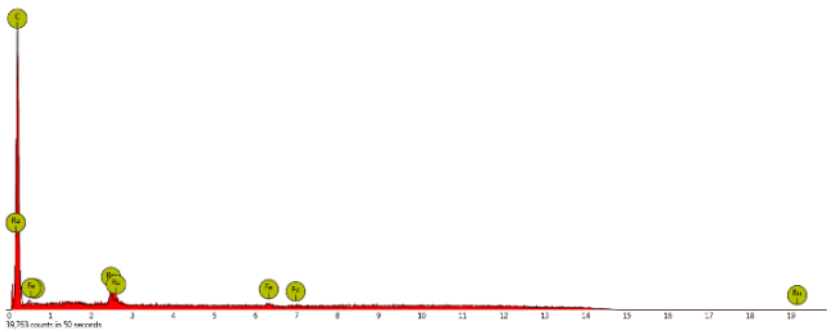

Element Number	Element Symbol	Atomic Concentration (%) Spot #1	Atomic Concentration (%) Spot #2	Atomic Concentration (%) Spot #3
6	C	81.6	87.9	89.9
44	Ru	11.0	7.1	6.7
26	Fe	7.3	5.0	3.4

***Figure 2.14** - EDX analysis spectra; **Table 2.9** - Atomic concentration of elements in Ru-Fe/CNTs*

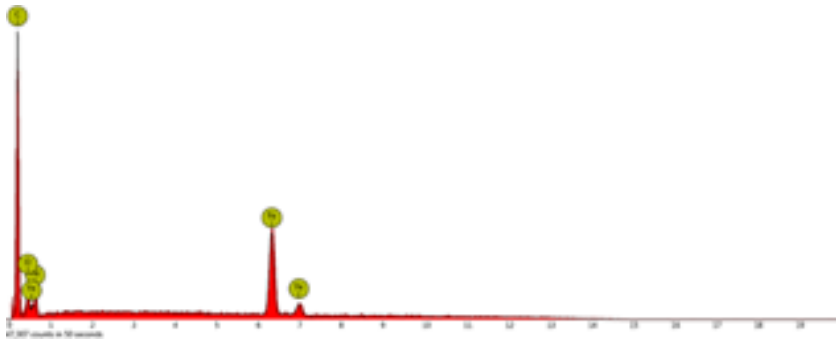

Element Number	Element Symbol	Atomic Concentration (%) Spot #1	Atomic Concentration (%) Spot #2	Atomic Concentration (%) Spot #3
6	C	42.9	42.9	45.8
26	Fe	20.9	29.7	23.7
8	O	36.2	27.4	30.5

Figure 2.15 *- EDX analysis spectra;* ***Table 2.10*** *- Atomic concentration of elements in* Fe_2O_3*/CNTs*

2.10 | Conclusions

This thesis explores the use of different metals (Fe and Ru), or a combination thereof, as an active surface for nitrogen conversion. Experimentally, two techniques were used, electrocatalysis in an aqueous environment (Chapter 3) and plasma catalysis providing H_2 and N_2 as feed gas (Chapter 4). The metals were deposited and immobilized onto the selected supports using the wet impregnation method. The varying load of metals was determined and quantified using Energy Dispersive X-ray Spectroscopy (EDX), which provided the weight percentage of each metal.

Catalysts	Supports	Precursors	Theoretical loading (wt.%)	Atomic concentration (at.%)	Surface area (m^2/g)	Average pore diameter (nm)	Pore volume (cc/g)
Ru	Al_2O_3	$RuCl_3 \cdot xH_2O$	5	2.55	1.841	0.947 - 1.935	$1.504\ 10^{-2}$
Ru-Fe	Al_2O_3	$RuCl_3 \cdot xH_2O$ $FeCl_3 \cdot 6H_2O$	2.5 – 2.5	1.2 – 2.6	17.59	0.949 - 1.935	$2.055\ 10^{-2}$
Fe_2O_3 (Fe)	Al_2O_3	$Fe(NO_3)_3 \cdot 9H_2O$	5 (3.5†)	5.75*	8.94	0.949 - 3.613	$7.199\ 10^{-3}$

Ru	CNTs	$RuCl_3 \cdot xH_2O$	5	32.1	105.67	0.956 - 2.533	$5.975\ 10^{-1}$
Ru-Fe	CNTs	$RuCl3 \cdot xH_2O$ $Fe(NO_3)_3 \cdot 9H_2O$	2.5 – 2.5	8.3 – 5.2	63.59	0.955 - 4.027	$3.552\ 10^{-1}$
Fe_2O_3 (Fe)	CNTs	$Fe(NO_3)_3 \cdot 9H_2O$	30 (21†)	24.8*	61.82	0.978 - 4.019	$2.879\ 10^{-1}$

(*) related to at.% of Fe
(†) related to wt.% of Fe calculated

Table 2.11 *– Summary table of catalysts*

It is well known that EDX analysis is not precise but gives an approximative indication of their presence (**Table 2.11**). Some of the load difference errors are due to differences in the Ruthenium content of the precursors, as reported in sections 2.3 and 2.4.

As discussed at the beginning of the chapter, two distinct supports were selected for this study - an insulating support with a high dielectric constant (alumina), widely studied under plasma conditions, and a highly conductive support like CNTs, for the electrocatalysis. In the upcoming chapters, the performance and characteristics of these catalysts will be elaborated upon, specifically in Chapters 3 and 4.

2.4 | References

[1] Hamsa, A. P., Arulprakasam, M., & Unni, S. M. (2023). Electrochemical nitrogen fixation on single metal atom catalysts. Chemical Communications, 59(72), 10689–10710.

[2] Wang, X., Wang, W., Qiao, M., Wu, G., Chen, W., Yuan, T., Xu, Q., Chen, M., Zhang, Y., Wang, X., Wang, J., Ge, J., Hong, X., Li, Y., Wu, Y., & Li, Y. (2018). Atomically dispersed Au-catalyst towards efficient electrochemical synthesis of ammonia. Science Bulletin, 63(19), 1246–1253.

[3] Geng, Z., Liu, Y., Kong, X., Li, P., Li, K., Liu, Z., Du, J., Shu, M., Si, R., & Zeng, J. (2018). Achieving a record-high yield rate of 120.9 μg_{NH3} mg_{cat}^{-1} h^{-1} for N2 electrochemical reduction over Ru single-atom catalysts. Advanced Materials, 30(40).

[4] Yang, H., Liu, Y., Luo, Y., Lu, S., Su, B., & Ma, J. (2020). Achieving high activity and selectivity of nitrogen reduction via Fe–N_3 Coordination on iron single-atom electrocatalysts at ambient conditions. ACS Sustainable Chemistry & Engineering, 8(34), 12809–12816.

[5] Liu, M., Zhang, S., Chen, M., Zhou, S., & Wu, L. (2023). An isolated bimetallic Fe–Ru single-atom catalyst for efficient electrochemical nitrogen reduction. Journal of Materials Chemistry A, 11(27), 14900–14910.

[6] Zhu, X., Hu, X., Wu, X., Cai, Y., Zhang, H., & Tu, X. (2020). Ammonia synthesis over γ-Al_2O_3 pellets in a packed-bed dielectric barrier discharge reactor. *Journal of Physics D: Applied Physics*, *53*(16), 164002.

[7] Gorbanev, Y., Engelmann, Y., van't Veer, K., Vlasov, E., Ndayirinde, C., Yi, Y., Bals, S., & Bogaerts, A. (2021). Al_2O_3-supported transition metals for plasma-catalytic NH_3 synthesis in a DBD plasma: Metal activity and insights into mechanisms. *Catalysts*, *11*(10), 1230.

[8] Nguyen, H. M., Omidkar, A., Li, W., Meng, S., Li, Z., & Song, H. (2023). Non-thermal plasma assisted catalytic nitrogen fixation with methane at ambient conditions. *Chemical Engineering Journal*, *471*, 144748.

[9] Gorky, F., Lucero, J. M., Crawford, J. M., Blake, B., Carreon, M. A., & Carreon, M. L. (2021). Plasma-induced catalytic conversion of nitrogen and hydrogen to

ammonia over zeolitic imidazolate frameworks zif-8 and zif-67. *ACS Applied Materials & Interfaces*, *13*(18), 21338–21348.

[10] Hu, X., Zhu, X., Wu, X., Cai, Y., & Tu, X. (2020). Plasma-enhanced NH_3 synthesis over activated carbon-based catalysts: Effect of active metal phase. *Plasma Processes and Polymers*, *17*(12).

[11] Deraz, N. M. (2018). The comparative jurisprudence of catalysts preparation methods: I. Precipitation and impregnation methods. *Journal of Industrial and Environmental Chemistry* , *1*(2).

[12] Oviroh, P. O., Akbarzadeh, R., Pan, D., Coetzee, R. A., & Jen, T.-C. (2019). New development of atomic layer deposition: Processes, methods and applications. *Science and Technology of Advanced Materials*, *20*(1), 465–496.

[13] Munnik, P., de Jongh, P. E., & de Jong, K. P. (2015). Recent developments in the synthesis of supported catalysts. *Chemical Reviews*, *115*(14), 6687–6718.

[14] Chen, S., Perathoner, S., Ampelli, C., Wei, H., Abate, S., Zhang, B., & Centi, G. (2020). Enhanced performance in the direct electrocatalytic synthesis of ammonia from N_2 and H_2O by an in-situ electrochemical activation of CNT-supported iron oxide nanoparticles. *Journal of Energy Chemistry*, *49*, 22–32.

[15] Chen, S., Perathoner, S., Ampelli, C., Mebrahtu, C., Su, D., & Centi, G. (2017). Room-temperature electrocatalytic synthesis of NH_3 from H_2O and N_2 in a gas–liquid–solid three-phase reactor. *ACS Sustainable Chemistry & Engineering*, *5*(8), 7393–7400.

[16] Li, S., van Raak, T., & Gallucci, F. (2019). Investigating the operation parameters for ammonia synthesis in dielectric barrier discharge reactors. Journal of Physics D: Applied Physics, 53(1), 014008.

[17] van Raak, T. A. B. J., Li, S., & Gallucci, F. (2023). Prevailing surface reactions in the plasma-catalytic ammonia synthesis with Ru/CeO_2 and $Ru/Ti\text{-}CeO_2$. *Chemical Engineering Journal*, *455*, 140691.

[18] Shackelford, J. F., & Doremus, R. H. (2008). Ceramic and glass materials: Structure, Properties and Processing. Springer Science & Business Media.

[19] Frederikse, H. P. R. (2016). Permittivity (Dielectric Constant) Of Inorganic Solids. In CRC Handbook of Chemistry and Physics (97th ed., pp. 12–48). essay, CRC Press.

[20] Fatimah, T. S., Wahyudi, T., Khaerunisa, H., & Saleh, N. (2021). Characterization of the γ,α-alumina and its adsorption capability to adsorb nickel (II) and magnesium (II) from nickel sulfate as a result of solvent differences. IOP Conference Series: Materials Science and Engineering, 1034(1), 012151.

[21] Iijima, S. (1991). Helical microtubules of Graphitic Carbon. Nature, 354(6348), 56–58.

[22] Filchakova, M., & Saik, V. (2021, May 13). *Single-walled carbon nanotubes: structure, properties, applications, and health & safety*. Carbon nanotube supplier – 97% of the global SWCNT market. https://tuball.com/articles/single-walled-carbon-nanotubes

[23] Holzinger, M., Hirsch, A., Bernier, P., Duesberg, G. S., & Burghard, M. (2000). A new purification method for single-wall carbon nanotubes (SWNTs). Applied Physics A, 70(5), 599–602.

[24] Guo, R., Shi, J., Ma, K., Zhu, W., Yang, H., & Sheng, M. (2023). Superhydrophilicity boron-doped cobalt phosphide nanosheets decorated carbon nanotube arrays self-supported electrode for overall water splitting. *Journal of Colloid and Interface Science*, *651*, 172–181.

[25] Guo, C., Liu, K., Ma, C., Sun, P., & Liang, L. (2024). Constructing a hierarchical coating with photothermal superhydrophobic property by spraying and modification on polyurethane foam for anti-icing and deicing. *Applied Thermal Engineering*, *236*, 121907.

[26] Huang, L., Lau, S. P., Yang, H. Y., Leong, E. S., Yu, S. F., & Prawer, S. (2005). Stable superhydrophobic surface via carbon nanotubes coated with a zno thin film. *The Journal of Physical Chemistry B, 109*(16), 7746–7748.

[27] Li, J., Maazouz, A., & Lamnawar, K. (2023). Unveiling the restricted mobility of carbon nanotubes inside a long chain branched polymer matrix *via* probing the shear flow effects on the rheological and electrical properties of the filled systems. *Soft Matter*, *19*(47), 9146–9165.

[28] De Volder, M. F., Tawfick, S. H., Baughman, R. H., & Hart, A. J. (2013). Carbon nanotubes: Present and future commercial applications. *Science*, *339*(6119), 535–539.

[29] Hirsch, A. & Vostrowsky, O. Functionalization of Carbon Nanotubes. *Topics In Current Chemistry* (2005), 193-237.

[30] Kobayashi, S., Kaneko, S., Ohshima, M., Kurokawa, H., & Miura, H. (2012). Effect of iron oxide on isobutane dehydrogenation over Pt/Fe_2O_3-Al_2O_3 Catalyst. *Applied Catalysis A: General*, *417–418*, 306–312.

[31] Liu, M., Zhang, S., Chen, M., Zhou, S., & Wu, L. (2023). An isolated bimetallic Fe–Ru single-atom catalyst for efficient electrochemical nitrogen reduction. *Journal of Materials Chemistry A*, *11*(27), 14900–14910.

[32] Sahoo, S. K., Agarwal, K., Singh, A. K., Polke, B. G., & Raha, K. C. , Characterization of γ- and α-Fe_2O_3 nano powders synthesized by emulsion precipitation-calcination route and rheological behaviour of α-Fe_2O_3. *International Journal of Engineering, Science and Technology* (2011), *2*(8).

[33] Doroodmand, M. M., Sobhani, S., & Ashoori, A., Sulfonated multiwalled carbon nanotubes (MWCNTs) as a new, efficient, and recyclable heterogeneous nanocatalyst for the synthesis of amines. *Canadian Journal of Chemistry* (2012), *90*(8), 701–707.

3. | Electrochemical-assisted catalysis

3.1 | Preface

Ammonia, which is produced on a large scale by the Haber-Bosch (HB) process, has been in operation for over a century and remains the most widely utilized technology. This process operates under high temperatures and pressures, making it highly energy-intensive (**Section 1.4**).

Electrochemistry, when combined with catalysis, has the potential to offer more moderate reaction conditions (such as ambient temperature and pressure) and can be easily integrated with renewable energies (**Chapter 6**). Considering that this technology is still in the developmental stage, the primary challenges associated with electrocatalysis involve enhancing the catalytic performance for NH_3 (expressed in terms of Faradaic Efficiency, FE, and ammonia yield, $\mu g_{NH3}\ mg_{cat}^{-1}\ h^{-1}$) and optimizing the cell setup by identifying the optimal combination of catalysts, cell geometry, and cell design. This optimization aims to minimize overpotentials, ohmic resistances, and the side Hydrogen Evolution Reaction (HER), while simultaneously maximizing ammonia selectivity. Additionally, it is important to determine the scalability of the system for various applications, which will be discussed in **Chapter 5**.

The kinetics and thermodynamics of the system depend on many factors, such as the applied potential, solvent effect, pH, and N_2 adsorption/desorption on the substrate[1]. This chapter discusses the experimental testing of nitrogen reduction reaction (NRR) in the electrocatalysis-assisted method.

3.2 | State-of-the-art

As previously discussed in **section 1.5.2**, electrocatalysis can occur in various environments such as aqueous, organic, and ionic liquids. However, our focus

will be on electrocatalysis in an aqueous environment. In this context, we will consider the utilization of nitrogen in the cathodic solution and/or gas phase (**Section 3.4.1**), as well as the transformation of H_2O into H_2 on the electrode surface. According to the mechanisms described in **section 1.5.2.1**, this transformation leads to the formation of ammonia under more moderate conditions than the current industrially-used HB operation.

The literature contains numerous metal-containing catalysts that reside at the pinnacle of the volcano plot. These catalysts have also served as inspiration for the current commonly employed catalysts, such as Magnetite in the HB process (**section 1.3**). Catalysts designed for NRR generally possess electrical conductivity. This is precisely why activated carbons are extensively utilized as supportive materials. They exhibit excellent electrical conductivity and possess a high and diverse surface area. The term "activated carbons" encompasses a class of materials that contain amorphous carbon. Carbon nanotubes are a subset of this category, and as stated in **section 2.4.1**; the defects present in the corners of C sp^2 are exploited to facilitate functionalization for metal anchoring.

Chen et al.[2], tested iron oxide nanoparticles supported on carbon nanotubes (CNTs) by wet impregnation method. In an aqueous solution ($KHCO_3$ solution) that showed a maximum formation rate of 2.2 mg h^{-1} m^{-2} achieved at -2.0 V vs Ag/AgCl with a FE of 0.15%, the low performance suggests the major conversion to H_2 as a side reaction. *Cui et al.*[3] prepared an α-Fe_2O_3 Oxygen-vacancies enriched on CNTs in 0.1M KOH, producing 0.459 μg h^{-1} cm^{-2} at -0.9 V vs Ag/AgCl and a FE of 6.0%. *Shi et al.*[4] synthesized anchored palladium and copper nanoclusters on graphene oxides tested in KOH 0.1M, obtaining 2.80 μg mg_{cat}^{-1} h^{-1} at -0.2 V vs RHE and a FE of 0.6%. *Geng et al.*[5] used the Ruthenium single-atoms on Nitrogen-doped carbon to convert N_2 into NH_3 at ambient conditions, at -0.2 V vs RHE with a partial current density of -0.13 mA cm^{-2}, reaching a FE of 29.6% with a production of 120 μg mg_{cat}^{-1} h^{-1}. Recently, both

iron and ruthenium doping (or a bimetallic doping) through the preparation of both Single-atom catalysts (SACs) and nanostructures have been reported in the literature. As described by *Agour et al.*[6] a SAC doped with iron on nitrogen doped carbon, showed a FE of 23. 7% and an ammonia yield of 3.47 μg h^{-1} cm^{-2} in 0.1M KOH. *Wei et al.*[7] reported a method of preparing Fe/Fe_3O_4 nanoparticles on porous carbons, obtaining a surface area of 1004 m^2 g^{-1}. The Fe/Fe_3O_4/PC-800 catalyst obtained the best performance, with a FE of 22.26%, and a yield of 31.15 μg mg_{cat}^{-1} h^{-1} at -0.1 V vs RHE. *He et al.*[8] obtained a coral-shaped structure by doping Iron on molybdenum oxide with oxygen vacancies, supported by activated carbons. The reported performance yields for their catalyst were 15.87 μg mg_{cat}^{-1} h^{-1} in 0.1M Na_2SO_4 at -0.5 V vs RHE. *Sun et al.*[9] reported a one-pot synthesis for the introduction of ruthenium nanoparticles (1.9 nm) on the surface of graphene oxide. The ruthenium-based catalyst reported a yield of 9.14 μg mg_{cat}^{-1} h^{-1}, an efficiency of 2.1% at the working potential of -0.2 V vs. RHE.

At present, there is a lack of literature on the topic of utilizing Al_2O_3 support for direct electrocatalysis from nitrogen to ammonia, mainly due to its tendency to insulate and not conduct electricity (in comparison to CNTs). However, there are articles available that discuss the electrocatalytic reduction of NO_3^- on alumina supports [10,11], the decomposition of NO_x and NH_3 [12], as well as their use as storage systems[13]. Anyway, for alumina, thermal catalysis is the most studied way, as expressed by *Lin et al.*[14] where a transformation of phase from γ-Al_2O_3 to α-Al_2O_3 with Ruthenium and Barium co-doped alumina catalysts, where the best performances were obtained for the catalyst calcined at 980°C, tested at 400°C and 1 MPa, and a formation rate of 7.217 mmol g_{cat}^{-1} h^{-1}.

3.3 | Aim of chapter

The purpose of this chapter is to investigate the electrocatalytic behaviour of different metals (Fe, Ru, or a mixture of them) deposited on two supports showing very different properties (Al_2O_3 and CNTs), in a home-made custom

electrochemical cell, at different potentials in aqueous electrochemical environment. Additionally, electrochemical impedance spectroscopy (EIS) studies have been conducted in order to understand the phenomena occurring at the interface. Moreover, a direct comparison was made between two different cell setups by processing reduced graphene oxide-based catalysts (rGO, rGO-Mn_xO_y, and rGO-Mn_xO_y-Fe) prepared in collaboration with the University of Trieste. This study aims of evaluating the influence of using different cell configurations (gas phase and gas-liquid phase), highlighting strengths and weaknesses, more than studying the behaviour of the catalysts.

3.4 | Conventional and non-conventional electrocatalytic reactors

An electrochemical reaction requires not only a good catalyst but also a proper cell design that takes into account: i) the electrolyte being used, ii) the nanoarchitecture of the catalyst (both cathodic and anodic for the best optimization), iii) the distance between the electrodes. As explained in Chapter 6, these parameters affect overpotentials and cell potentials.

In **Figure 3.1**, various configurations of electrochemical cells are depicted, including both the conventional and commercially prevalent ones. These include (**Figure 3.1a**) the single-chamber cell, which works within a liquid phase in the same environment; the H-Type cell, with a liquid phase separated by a proton/anion exchange membrane, and the back-to-back or zero gap cell, operating in a gaseous phase at both the anode and cathode. In this design, the membrane is positioned between two catalysts deposited on a support known as the gas-diffusion layer (GDL).

In the context of versatility and in response to the aforementioned challenges, numerous unconventional, custom-made cells have been devised (**Figure 3.1b**). These alternative cell designs harness the zero-gap cathode phase with an electrolyte at the anode when studying a cathode reaction, or vice versa, which is referred to the anodic reaction with the gas phase approach.

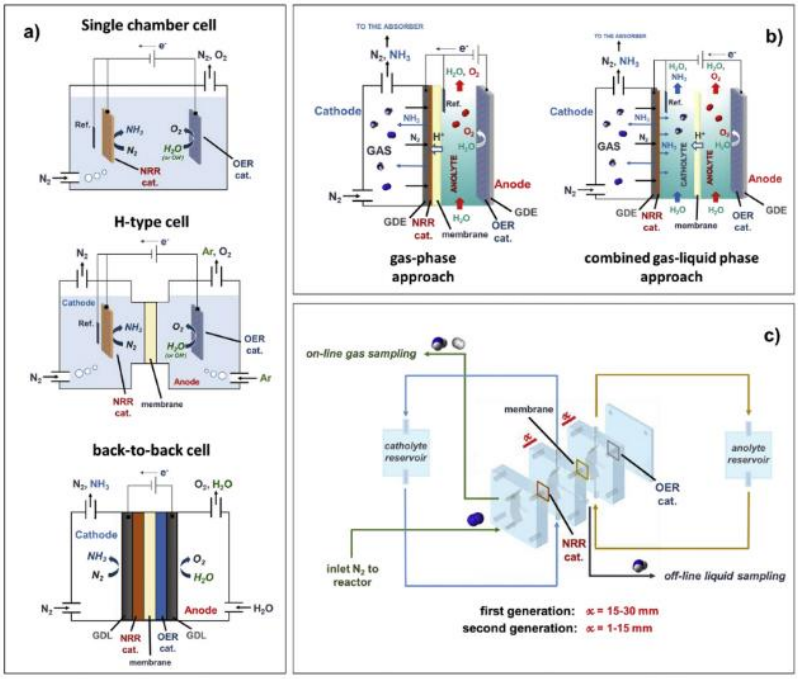

***Figure 3.1** – Classification of electrocatalytic devices a) conventional commonly used configuration for NRR, b) schematic description of unconventional cell configuration gas-phase and gas-liquid phase approach, c) Representation of first and second generation of design reactor for NRR process [15]*

Another approach involves the combination of the gas phase with the liquid phase, primarily at the cathode, offering an innovative solution to address these issues. Minimizing the electrode spacing, as previously discussed, holds significance in enhancing cell performance with the ultimate goal of optimizing the device, and for this reason they can be classified as first- or second-generation cells (**Figure 3.1c**).

3.5 | Electrocatalytic reactor

3.5.1 | Gas-Phase reactor (Electrochemical Cell 1 – EC 1)

In this thesis work, the electrocatalytic tests were conducted using a gas-phase cell reactor (refer to **Figure 3.2**). The flow reactor operates under room temperature and atmospheric pressure.

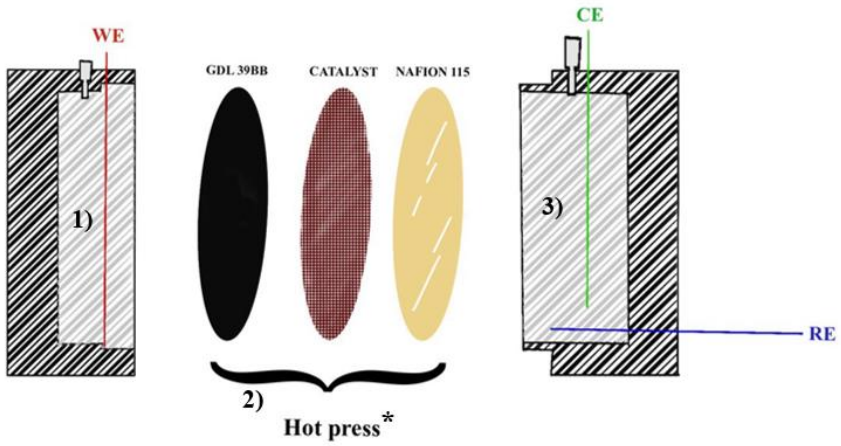

***Figure 3.2** – Schematic sectional representation of the gas phase reactor 1) cathodic gas compartment, 2) composition of working electrode 3) anodic liquid compartment (0.1M Na_2SO_4). (*) see membrane electrode assembly, section 3.6*

In this setup, the counter and reference electrodes are soaked in the anodic semi-cell portion filled with anolyte, while the cathodic semi-cell operates in a gas phase with electrolyte-less conditions, facilitating the NRR process. The main advantage of using a cell in a gas-phase configuration is to overcome the problem associated with the solubility of nitrogen in water, which allows for easier product handling and analysis, as well as to provide greater coverage of reactant gas by limiting diffusive and double charge-layer phenomena. The gas phase works with a continuous flow of nitrogen.

The gas passing through the GDL and reaching the deposited catalyst reacts to form NH_3, which desorbs from the surface according to the mechanisms proposed in **section 1.5.2.1**, and exits continuously from the reactor, then trapped by an absorber containing very dilute sulfuric acid (1mM). Along with ammonia, unreacted N_2 (continuous flow) and the produced hydrogen also exit.

Figure 3.3 – *Exploded depiction of the cell*

The two compartments (cathode and anode) are physically separated by the Membrane Electrode Assembly (Gas Diffusion Layer + Catalyst + Nafion® 115) formed by hot pressing of the catalysts prepared in **section 3.6**.

3.5.2 | Gas-Liquid Phase reactor (Electrochemical cell 2 – EC 2)

In this second cell configuration used, one operates in gas-liquid phase, the working electrode is immersed in the catholyte, and the gas chamber always serving to supply nitrogen to the catalyst (due to the low solubility of nitrogen in an aqueous environment). The Nafion membrane (Nafion 115) is located in the middle of the cell to physically separate anodic and cathodic compartments, allowing protons to pass through. The counter electrode is a bare GDL (Sigracet 39BB). If working in three-electrode configuration, the reference electrode used is based on Ag/AgCl 3.0M KCl (**Figure 3.4** for detail).

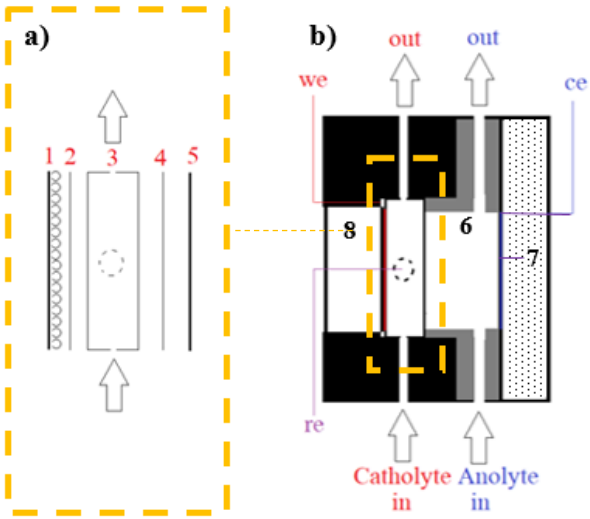

Figure 3.4 *– Gas-liquid phase home-made reactor scheme a) expanse diagram of the section, highlighted in orange, 1) GDL 39BB/Catalyst; 2) Gasket; 3) Central piece (with Reference 3mm enter, and in/out catholyte); 4) Gasket; 5) Nafion® membrane; b) image in section of the cell, 6) Anodic chamber; 7) Counter electrode allocation; 8)Gas Chamber*

3.6 | Working electrode preparation

A commercial gas-diffusion layer (GDL), specifically the Sigracet GDL 39BB, provided by SGL Group, along with a Nafion® membrane 115, and a 10 wt% weight Nafion solution were employed in the electrode fabrication process. All the chemical reagents used in this study were of analytical grade without any further purification.

3.7 | Preparation of Gas-Diffusion Layer

Following the preparation of the ink, which consisted of 50 mg of catalyst, 8 mL of isopropanol, and 50 μL of a perfluorinated Nafion solution (10 wt.%), it underwent a sonication process lasting 30 minutes until a uniform and homogeneous mixture was attained. Subsequently, this ink was applied via spray-coating and deposited across an area measuring 25 cm^2. Once the load has been reached, the catalyst is cut into a round shape (20 mm diameter), and hot-pressed

for 15 s at 130°C with a purified Nafion membrane (Membrane Electrode Assembly - MEA). While, if the EC2 configuration is used, the catalyst will be cut circularly with a diameter of 36mm and arranged as in **Figure 3.4**.

3.8 | Nafion Membrane preparation

Nafion® 115 membrane foils were cut into small pieces and treated with 3 wt. % H_2O_2 water solution for purification at 80 °C for one hour. Next, the membrane pieces were treated in 0.5 mol/L H_2SO_4 solution for activation for one hour at 80 °C under stirring, followed by rinsing until neutral pH. Finally, the treated Nafion membrane was stored in deionized water.

3.9 | Electrochemical experimental set-up

3.9.1 | EC1

Electrochemical experiments were conducted in EC1 at a temperature of 25°C using a potentiostat/galvanostat AMEL 2551. A cation exchange membrane (activated Nafion® 115) was used to prepare the MEA (as reported in Section 3.7), to separate the anode (liquid) and cathode (gas) compartments. A reference electrode (Ag/AgCl 3.0M KCl) was employed, while the catalysts were deposited on a gas diffusion electrode (39 BB) with an active surface area of around 1.7 cm^2 using the spray coating method (0.25 mg cm^{-2}). A platinum wire served as the counter electrode. The anodic compartment was filled with 25 mL of electrolyte (0.1M Na_2SO_4) to facilitate water electrolysis and the generation of protons and electrons. The peristaltic pump was set to a flow rate of 26 mL min^{-1}. Nitrogen (N_2), with a purity of 99.9999%, was continuously supplied at a rate of 20 mL min^{-1}. The effluent from the electrocatalytic reactor outlet, which contained a mixture of N_2 and ammonia, was directed to a liquid absorber containing 1 mL of 1 mM H_2SO_4. The presence of ammonia in the anode electrolyte was also detected using the UV-Vis salicylate method.

3.9.2 | EC2

Electrochemical experiments were conducted in EC2 at a temperature of 25°C using a potentiostat/galvanostat AMEL 2551. A cationic exchange membrane (activated Nafion® 115) was utilized to separate the anodic (liquid) and cathodic (gas-liquid) chambers. A reference electrode (Ag/AgCl 3.0M KCl) was employed, while the catalysts were deposited on a gas-diffusion electrode (GDE, Sigracet 39BB) with an active surface area of around 5.7 cm^2 using the spray coating method (0.25 mg cm^{-2}). A bare GDL 39 BB electrode (active area 5.7 cm^2) served as the counter electrode. The cathodic and anodic compartment was filled with 25 mL of electrolyte (0.1M Na_2SO_4) to facilitate water electrolysis and the generation of protons and electrons. The peristaltic pump was set to a flow rate of 26 mL min^{-1}. Nitrogen (N_2), with a purity of 99.9999%, was continuously supplied into the gas chamber and in the cathodic compartment at a rate of 20 mL min^{-1}. The effluent from the electrocatalytic reactor outlet, which contained a mixture of N_2 and ammonia, was directed to a liquid absorber containing 1 mL of 1 mM H_2SO_4 (absorber only in the gas phase). The presence of ammonia in cathodic and anodic electrolyte was also detected using the UV-Vis salicylate method.

3.9.3 | Calculations

All potentials were converted to RHE (Reversible Hydrogen Electrode) using the equation:

$$\text{E vs RHE} = \text{E vs Ag/AgCl} + 0.210 + 0.059 \times \text{pH} \qquad \text{(eq. 3.1)}$$

Faradaic Efficiency calculation of ammonia was calculated using the following equation:

$$Faradaic\ Efficiency\ (\%) = \frac{ne^- \times 96485\ C \times [NH_3] \times V(L)_{reservoir}}{MW_{Ammonia} \times Q} \qquad \text{(eq. 3.2)}$$

- ne^-: Number of electrons exchanged in the reaction to convert N_2 into NH_3;
- $[NH_3]$: Concentration of Ammonia (in mg/L);
- V: Volume of the reservoir where the withdraw is done (in L);
- MW_{NH3}: Molecular weight of ammonia (in g mol^{-1});
- F: Faraday constant 96485 (in C mol^{-1});
- Q: Total charge supplied to the system (in C).

Ammonia yield calculation was calculated using the following equation:

$$Yield\ (\mu g_{NH3} mg_{catalyst}^{-1} h^{-1}) = \frac{[NH_3] \times V(L)_{absorber}}{load\ (mg_{catalyst}\ cm^{-2}) \times Area_{geo}\ (cm^2) \times time\ (h)} \quad \text{(eq. 3.3)}$$

- $[NH_3]$: Concentration of Ammonia (in mg/L);
- V: Volume of the reservoir where the withdraw is done (in L);
- Load: Quantity of catalyst load on the GDL (in mg_{cat} cm^{-2});
- $Area_{geo}$: Geometric area of the catalyst (in cm^{-2});
- Time: time of analysis (in h).

Advanced electrochemical parameters

AESA (Active Electrochemical Surface Area) was calculated using the following formulas (**eq. 3.7**)[16], while C_{DL} (mF/cm^2) indicates the double layer capacitance, a measure of the charge accumulated on an electrode. C_{DL} was calculated using Cyclic Voltammetry (CV) at different scan rates (2, 5, 10, 15, 20, 30, 40, 50 mV s^{-1}) around the open circuit potential (OCP). The slope of linear regression of the plot scan rate vs ΔJ is the C_{DL}[17] (**eq. 3.4** and **eq. 3.5**).

$$Double\ Layer\ capacitance = C_{DL}(\frac{F}{cm^2}) = from\ different\ scanrate\ around\ OCP \quad \text{(eq. 3.4)}$$

$$\Delta J = \frac{j_{Cat} - j_{An}}{2} \quad \text{(eq. 3.5)}$$

- J_{cat} : Cathodic current of CVs;
- J_{an} : Anodic current of CVs.

C_p *(F/g)* is the specific capacitance, representing the amount of charge that can be stored per unit mass of catalyst. Calculated using the following equation:

$$Specific\ capacity = C_p(\frac{F}{g}) = \frac{Area_{DL}(A \times V)}{2 \times window\ potential\ (V) \times mass_{catalyst}(g) \times scanrate\ (V/s)} \quad \text{(eq. 3.6)}$$

- $Area_{DL}$: Area of last CV cycle with highest scan rate (in A V);
- Window Potential: Window Potential around the OCP (in V);
- $Mass_{catalyst}$: Quantity of catalyst deposited on the GDL (in g_{cat});
- Scan rate: speed of the scan taken into account (in V s^{-1});

AESA (m^2/g): Electrochemically active surface area, a measure of the surface area of material involved in electrochemical reactions[16].

$$AESA(\frac{cm^2}{g}) = \frac{C_p}{C_{DL}} \quad \text{(eq. 3.7)}$$

- C_p : Specific capacity (eq. 3.6);
- C_{DL} : Double Layer Capacitance (eq. 3.4).

ECSA (cm^2) is the Electrochemically active surface area, similar to AESA but expressed in square centimeters[17].

$$ECSA(cm^2) = AESA \times deposited\ weight_{catalyst} \quad \text{(eq. 3.8)}$$

- AESA: Active Electrochemical Surface Area (in $cm^2\ g^{-1}$);
- Deposited weight : deposited catalyst (in g).

3.10 | Methodology

Chronoamperometric (CA) decontamination was performed for 60 minutes by applying a low potential (-0.1V vs RHE) to remove the eventual NH_3 from the membrane or catalysts surface and then performing the actual tests for 1.5 hours at a variety of potentials (from –0.1 to –0.8 V vs RHE), increments have been made taking into account the current of the decontamination test (-0.1V vs RHE) at the end of CA. Ammonia present in the gas phase was trapped and detected by ion chromatography, as previously described, while the ammonia present in the

liquid phase, i.e., the anolyte (EC1) or catholyte and anolyte (in the case of EC2), was detected by the UV-visible spectroscopic method.

3.11 | Ammonia detection

3.11.1 | Ionic chromatography

Chromatographic methods provide valuable information regarding the concentration of ammonium present in a liquid. However, these methods are only applicable when the gaseous flow is conveyed into an absorber filled with 1 mL of trap solution (1mM H_2SO_4); The electrolyte contains a high concentration of Na^+ cations that could mask the ammonium peak. Although ammonium in the electrolyte cannot be detected by ion chromatography, IC is useful for quantifying ammonium produced in the gas phase in a shorter time frame of 20 minutes per analysis, compared with the 60-minute incubation time required for the spectrophotometric method.

To perform the analysis, an ion chromatograph (IC - MetrOhm) equipped with a cationic column (Metrosep C6 - 150/4.0) is utilized. The elution of the ammonium peak occurs at a retention time of 5'42" ± 5". Calibrations were conducted using concentrations of 25, 50, 100, 250, 500, and 1000 ppb (**Figure 3.5**).

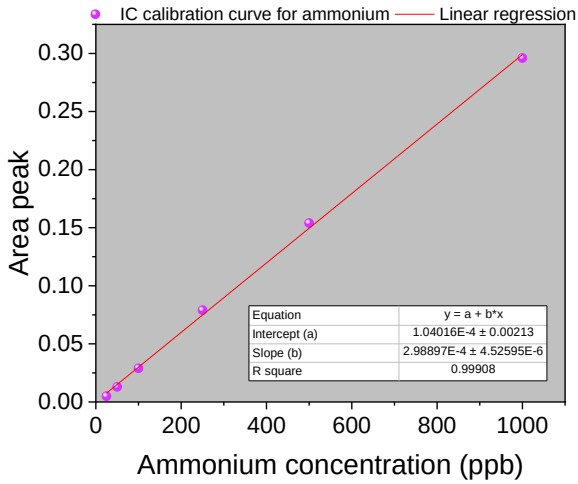

Figure 3.5 *– calibration curve used to calculate the ammonium concentration in gas phase*

3.11.2 | UV-Visible method (Salycilic)

The salicylate method is one of the ammonia quantification methods that has been extensively used in literature for quantifying ammonia in the emerging field of nitrogen (electro)fixation[18].

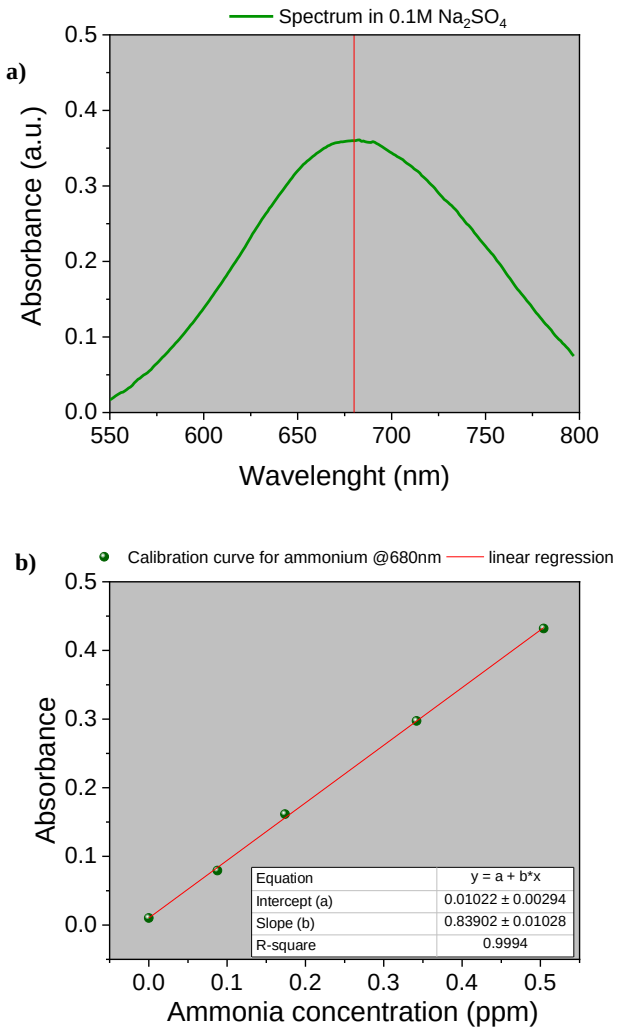

***Figure 3.6** – a) UV-Vis absorption spectra of indophenol-like complex, b) calibration curve used to calculate the ammonia concentration*

A spectrophotometer (Jasco V750) was used at a fixed wavelength. The investigated wavelength of the maximum absorption of radiation is at λ_{max}=680 nm, due to the absorbance of an indophenol-like complex (**Figure 3.6a**), with a light path of 1 cm.

Reagents used:

1. Colouring solution: sodium salicylate (0.4 M) and sodium hydroxide (0.32 M);

2. Oxidizing solution: sodium hypochlorite (ρ_{Cl}=4~4.9) and sodium hydroxide (0.75M);

3. Catalyst solution: 0.1g $Na_2[Fe(CN)_5NO]\bullet 2H_2O$ diluted to 10 mL with deionized water;

4. Standard ammonium solution (0, 0.0877, 0.1739, 0.3419, and 0.5042 ppm).

Standard ammonium solutions were prepared for the calibration at different concentrations by adding 0, 50, 100, 200, and 300 µL respectively from a 10 ppm standard ammonium solution to 5mL of 0.1M Na_2SO_4. Then, 100 µL of oxidizing solution, 500 µL of colouring solution, and 50 µL of catalyst solution were added respectively to the standard solutions. The calibration curve (**Figure 3.6b**) was used to calculate the ammonia concentration after 1h of incubation.

3.12 | Decontamination

While recent literature has proposed rigid protocols employing advanced analytical methods (such as utilizing ^{15}N labelled nitrogen)[19], in this thesis work a simpler methodology to circumvent ammonia contaminations and false positives was adopted. However, it is acknowledged that employing more

sophisticated analyses would be ideal, yet accessibility to such techniques might pose challenges in various laboratory settings.

The sources of contamination that may be encountered in the laboratory during the testing are given below, divided into intra-system and out-system:

Intra-system:

- Catalyst deposition step contamination;
- Catalyst composition (N-doped or N-containing);
- Absorbed ammonia on the Nafion membrane (high capacity)[20];

Out-system:

- Environmental contamination (NH_3/NO_x);
- All the aqueous solution (Electrolyte/Gas phase Trap contamination)[21];
- Setup contamination on the surface equipments;

The countermeasures that have been taken here are given below:

- Chronoamperometric decontamination in a non-faradaic region (60 min, -0.1V vs RHE) before starting;
- Blank analysis on electrolyte and Gas trap before the tests;
- Gas-tight equipment;
- Avoiding soap and other cleaning agents;
- Perform tests in Argon;
- Avoiding N-compounds in the catalyst composition.

Decontamination was conducted by applying a low potential (-0.1V vs RHE) for a duration of 60 minutes. This procedure was essential in eliminating any nitrogen contamination (i.e., adhering to the electrode surface during deposition, adsorbing to the Nafion membrane) not from the supplied Nitrogen present on the reactant

gas. Furthermore, prior to testing, the electrolyte and the sulphuric acid trap were subjected to analysis using the spectrophotometric method and the ion chromatograph, respectively. These analyses were performed to ensure the absence of ammonium.

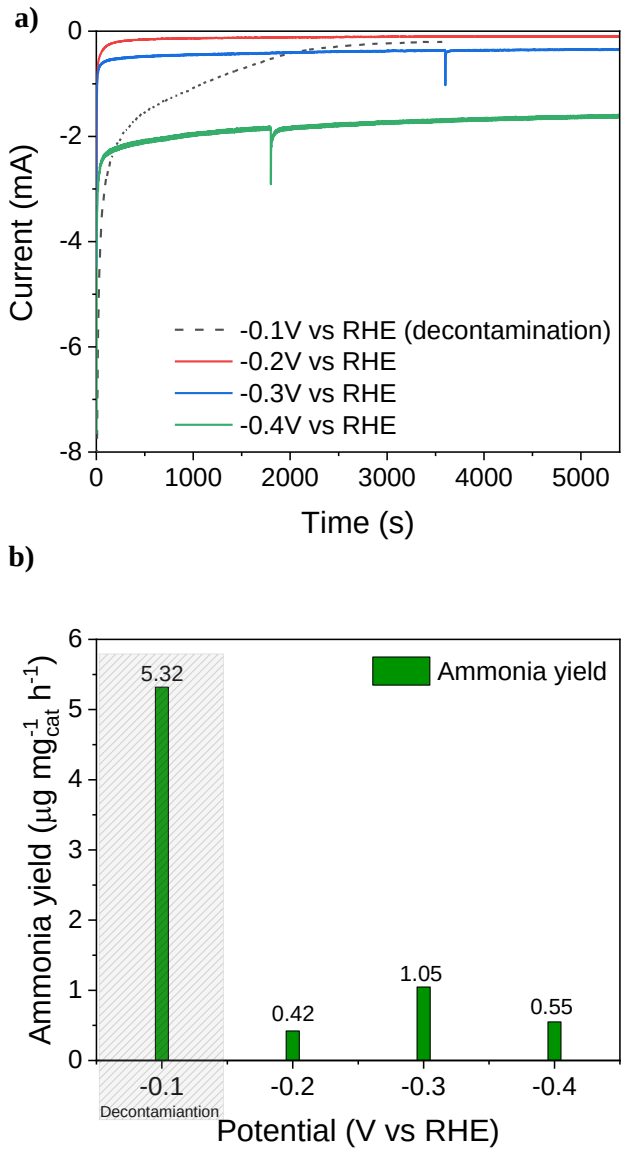

Figure 3.7 *- a) Chrono-amperometries at (dash black line) -0.1V, (solid red line) -0.2V, (solid blue line) -0.3V, (solid green line) -0.4V vs RHE respectively, b) quantification of ammonia yield for Ru-Fe/Al_2O_3.*

In this investigation, an examination was conducted on a catalyst (Ru-Fe co-doped on Al_2O_3) alongside its respective decontaminative test, as illustrated in **Figure 3.7a**. The chronoamperometries presented a comparative analysis. Specifically, the observed current within 0 – 2000 s interval exhibited a declining trend attributed to either adsorbed species on the catalyst surface or those adsorbed on the Nafion membrane. Concurrently, **figure 3.7b** displayed yield values derived from diverse tests, encompassing the decontaminative evaluation (IC + Spectrophotometric). Remarkably, no presence of liquid-phase ammonium was discerned in the subsequent tests conducted.

The entire apparatus employed for the experiment maintained a gas-tight environment and the decontamination value has been voluntarily omitted for subsequent graphs for simplicity.

3.13 | Synthesis of NH_3 via Electrocatalytic method

These electrochemical experiments were conducted in a gas-phase cell labelled as EC1 operating in an aqueous environment with a concentration of 0.1M Na_2SO_4, as described in section 3.9.

Following the decontamination process at fixed potential, -0.1V vs RHE for a duration of 60 minutes, subsequent chronoamperometries were conducted for a period of 1.5 hours at fixed more negative potentials (within the range from -0.1 to -0.8V). The selection of potential increments was based on the preliminary tests, allowing us to operate at optimal currents of 100-300 $\mu A\ cm^{-2}$, which is the range where the onset potential of the reaction occurs, just before the hydrogen evolution reaction (HER) becomes predominant.

3.13.1 | Alumina-based catalysts

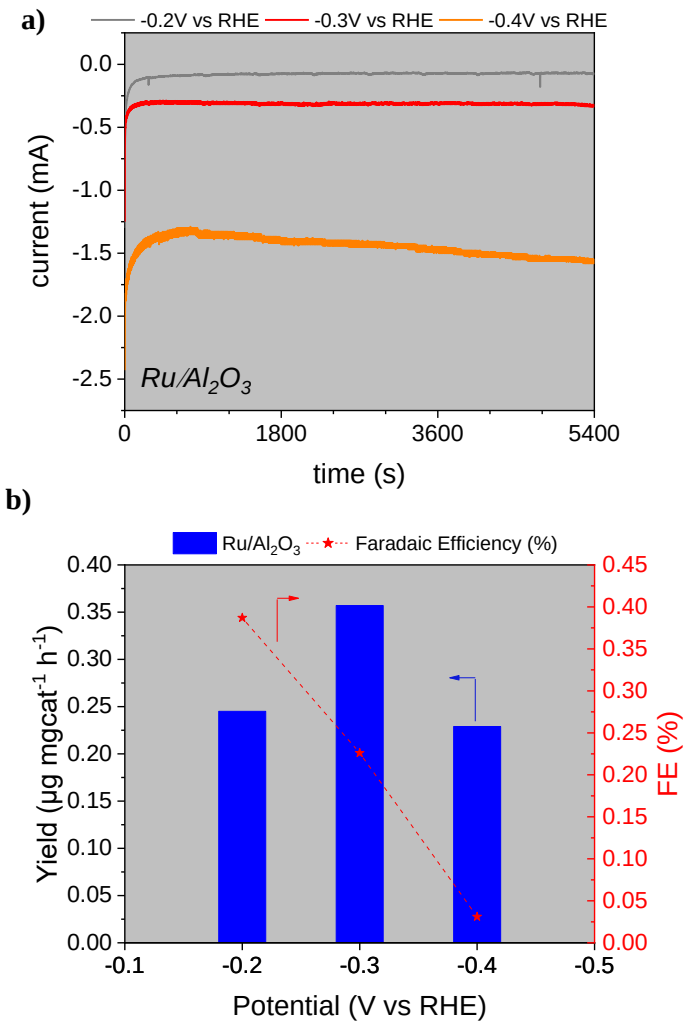

***Figure 3.8** – Different applied potential on Ru/Al_2O_3, a) Chrono-Amperometric detection and b) yield on the left-axis expressed in ($\mu g\ mg_{cat}^{-1}\ h^{-1}$) and Faradaic Efficiency on the right-axis (%)*

Ruthenium on alumina (**Figure 3.8b**) shows its highest productivity at -0.3V vs RHE, and an absolute current density (|J|) at 187 $\mu A\ cm^{-2}$ producing 0.36 $\mu g\ mg_{cat}^{-1}\ h^{-1}$ with a Faradaic Efficiency (FE) of 0.23%. The highest FE achieved by the

catalyst was 0.39% at -0.2V vs RHE, a |J| of 75 μA $cm^{-2,}$ and a productivity of 0.24 μg mg_{cat}^{-1} h^{-1}.

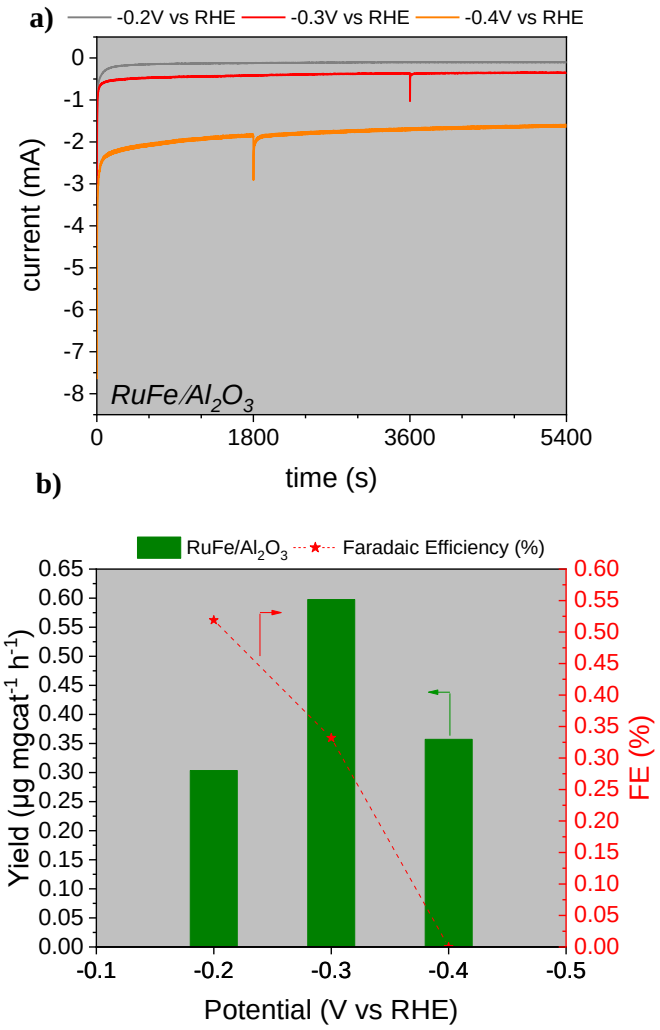

Figure 3.9 *– Different applied potential on $RuFe/Al_2O_3$, a) Chrono-Amperometric detection and b) yield on the left-axis expressed in (μg mg_{cat}^{-1} h^{-1}) and Faradaic Efficiency on the right-axis (%)*

Ruthenium-Iron co-doped on alumina shows (**Figure 3.9b**) its highest productivity at -0.3V vs RHE, and an absolute current density (|J|) at 294 μA cm^{-2}, producing 1.047 μg mg_{cat}^{-1} h^{-1} with a FE of 0.5%. It is also the highest FE achieved by the catalyst. The productivity profile is similar to that of ruthenium

on alumina, but at the same applied potential, the electrocatalytic performances in terms of productivity and efficiencies are higher.

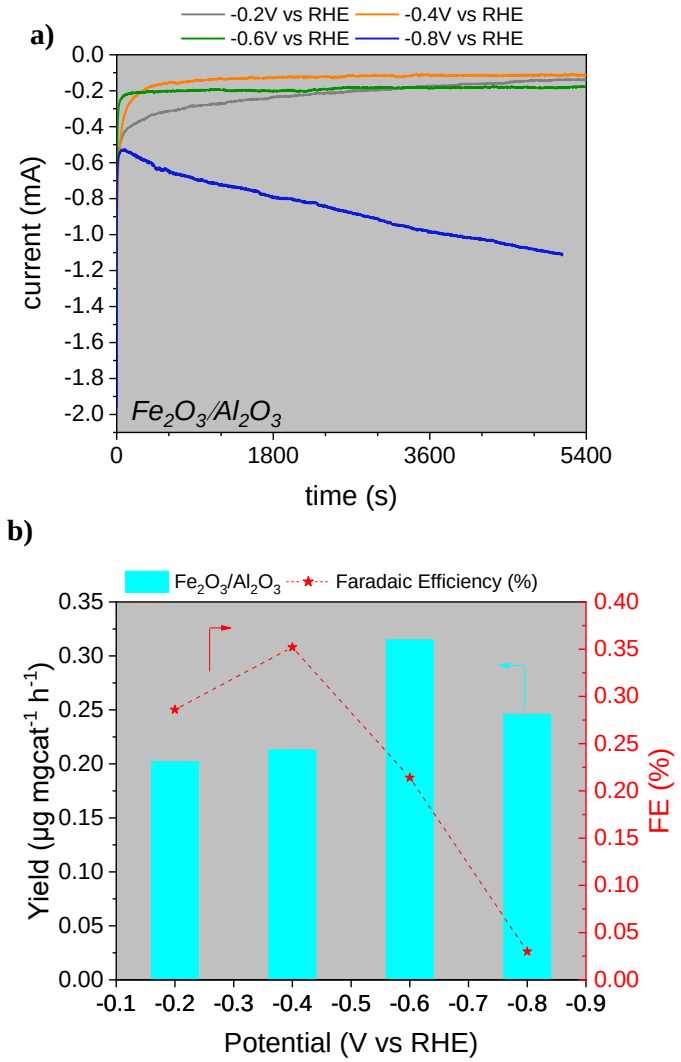

Figure 3.10 *– Different applied potential on Fe_2O_3/Al_2O_3, a) Chrono-Amperometric detection and b) yield on the left-axis expressed in ($\mu g\ mg_{cat}^{-1}\ h^{-1}$) and Faradaic Efficiency on the right-axis (%)*

Iron(III) oxide on alumina shows (**Figure 3.10b**) its highest productivity at -0.6V vs RHE, and an absolute current density (|J|) at 112 µA cm^{-2}, producing 0.31 µg $mg_{cat}^{-1}\ h^{-1}$ with a FE of 0.21%. The highest FE achieved by the catalyst, on the

other hand, was 0.35% at -0.4V vs RHE, with a |J| of 72 μA cm^{-2}, and a productivity of 0.21 μg mg_{cat}^{-1} h^{-1}.

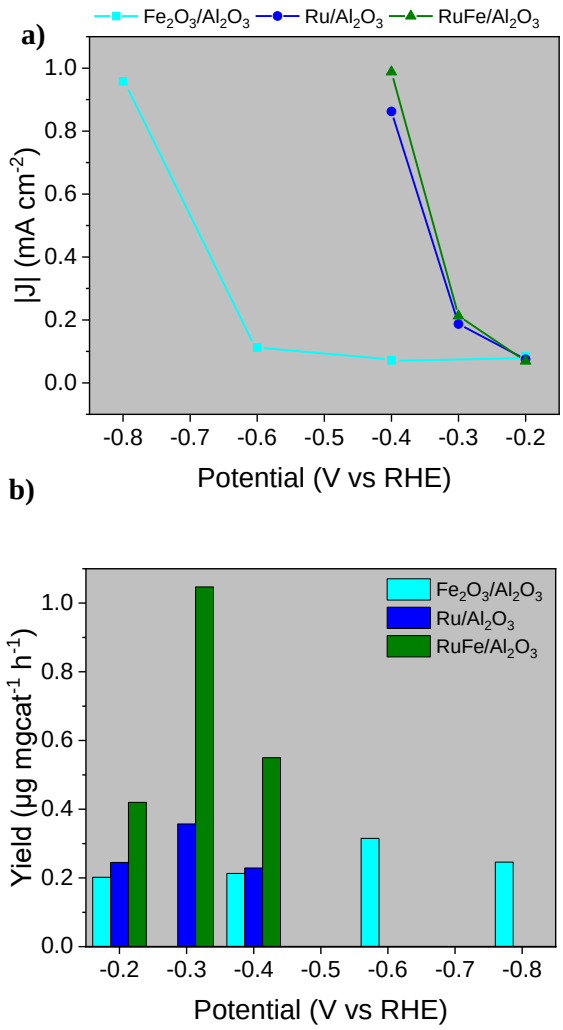

Figure 3.11 *– Different applied potential for different alumina-based materials vs a) absolute value of current density and b) ammonia yield expressed in (μg mg_{cat}^{-1} h^{-1}). Ru (in blue), RuFe (in dark green) Fe_2O_3 (in cyan)*

Summarizing the behaviour of alumina-based catalysts, the best performance (**Figure 3.11b**) was achieved by the ruthenium and iron co-doped catalyst in the order Ru-Fe/Al_2O_3 > Ru/Al_2O_3 > Fe_2O_3/Al_2O_3 >> Al_2O_3. The addition of ruthenium tends to decrease the onset potential of the reaction (**Figure 3.11a**), bringing it to lower potentials. Productivity in Ru-Fe co-doped catalyst is 2.9

times higher than Ruthenium, and 3.3 times higher than Iron (III) oxide supported on alumina.

The reaction potential of iron oxide instead is similar to that of the substrate, catalysing the reaction to higher potentials (**Figure 3.12**). The current is higher at -0.8 V vs RHE because of the hydrogen evolution reaction (HER) catalysed by Fe_2O_3.

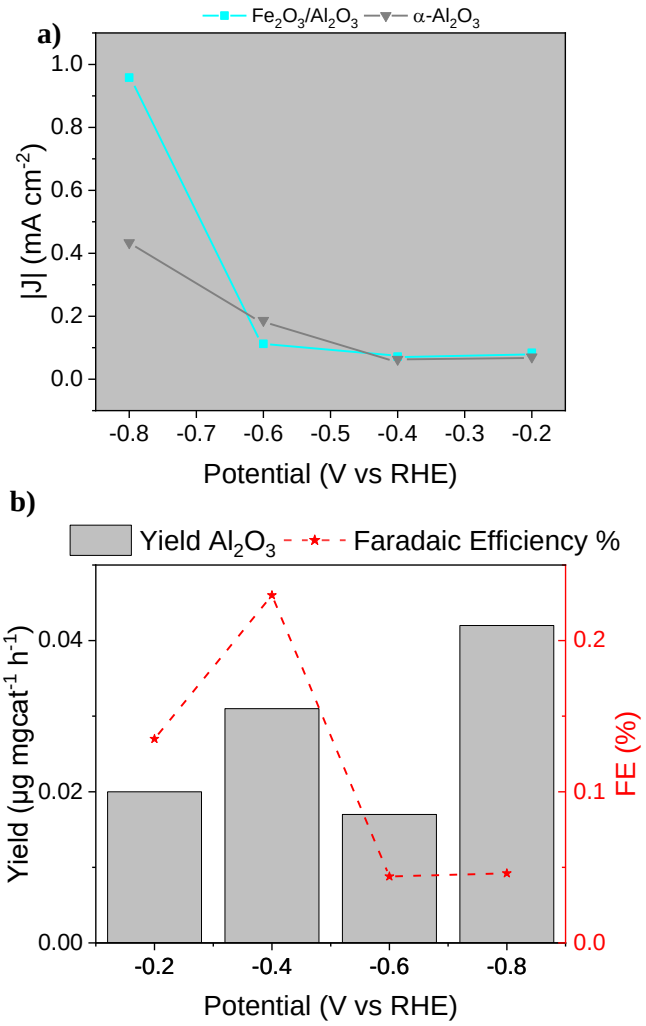

Figure 3.12 *– a) comparison between Fe_2O_3/Al_2O_3 and Al_2O_3 current density and Faradaic efficiency vs applied potential b) Alumina bare on GDL tests at different applied potential.*

3.13.2 | Functionalized Carbon-nanotubes-based catalysts

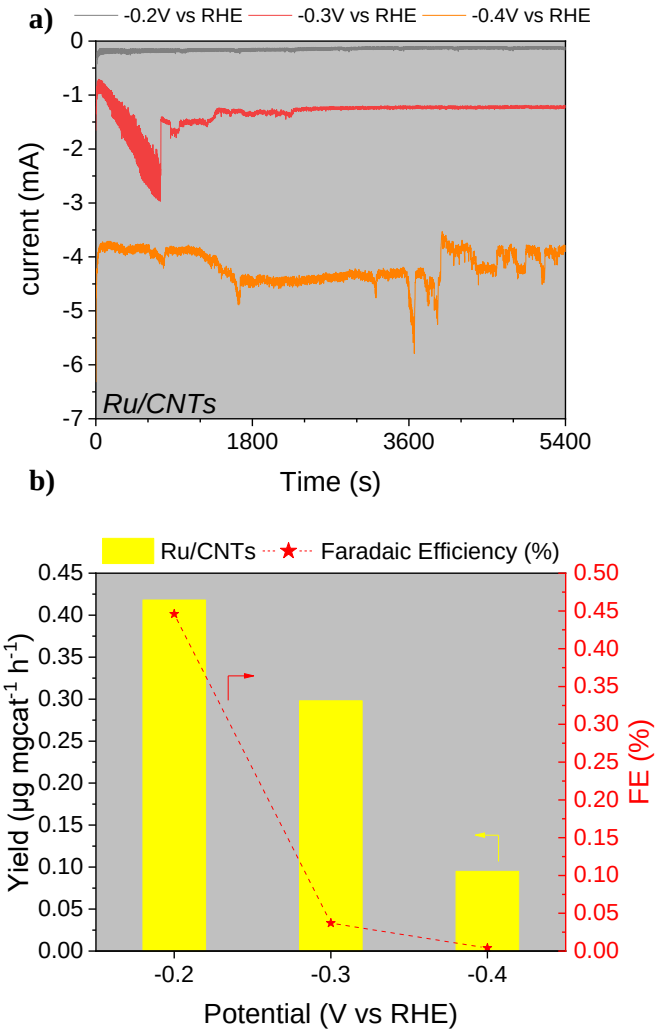

***Figure 3.13** – Different applied potential on Ru/CNTs, a) Chrono-Amperometric detection and b) yield on the left-axis expressed in ($\mu g\ mg_{cat}^{-1}\ h^{-1}$) and Faradaic Efficiency on the right-axis (%)*

Figure 3.13a shows the current trend over time. These currents have a disturbance due to the lability of the MEA, as the CNTs after hot-pressing, remain adhered to the Nafion membrane and partially exfoliated from the substrate. This trend of catalyst delamination in the deposited catalyst has not been observed with alumina-based catalysts. **Figure 3.13b** shows the electrocatalytic behaviour of

Ruthenium catalyst supported on CNTs. Its highest productivity was provided at -0.2 V vs RHE and absolute current density (|J|) of 93 μA cm^{-2}, producing 0.42 μg mg_{cat}^{-1} h^{-1} with a FE of 0.45%. It is also the highest FE achieved by the catalyst.

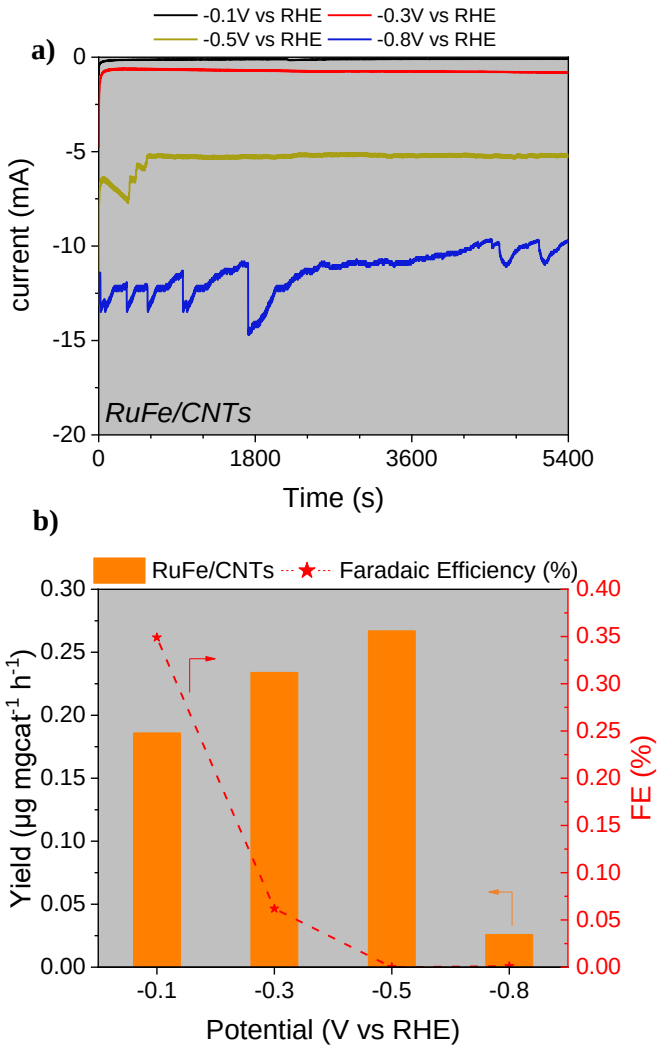

Figure 3.14 *– Different applied potential on RuFe/CNTs, a) Chrono-Amperometric detection and b) yield on the left-axis expressed in (μg* mg_{cat}^{-1} h^{-1}*) and Faradaic Efficiency on the right-axis (%)*

Figure 3.14b shows Ruthenium Iron co-doped on CNTs activity. Its highest productivity occurred at -0.5 V vs RHE and an absolute current density (|J|) of 3.13 mA cm^{-2}, producing 0.27 μg mg_{cat}^{-1} h^{-1} with a FE of 0.01%. The highest FE

achieved by the catalyst is 0.34% reached at -0.1V vs RHE, at an absolute current density of 63 μA cm^{-2} and a productivity of 0.19 μg mg_{cat}^{-1} h^{-1}. Also in this case, the Chrono amperometries were noisy at high potentials. This can be explained by the fact that the production of H_2 as a side reaction, is predominant at high potentials and, being generated at the interface between catalyst and membrane, does not have time to flow to the gas phase and therefore the result is in a damage of the MEA.

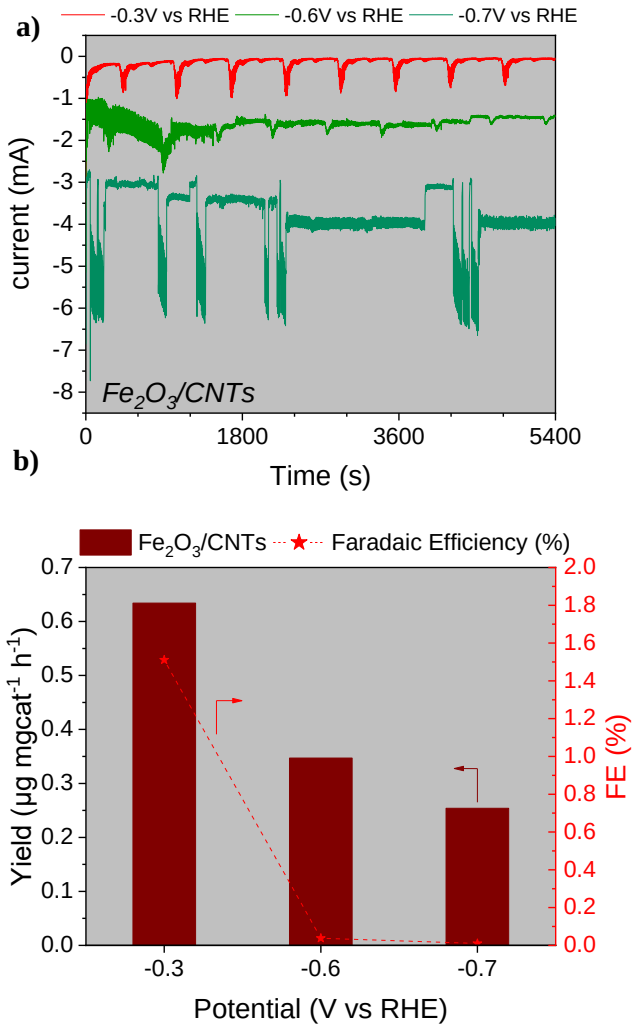

Figure 3.15 *– Different applied potential on Fe_2O_3/CNTs, a) Chrono-Amperometric detection and b) yield on the left-axis expressed in (μg mg_{cat}^{-1} h^{-1}) and Faradaic Efficiency on the right-axis (%)*

Iron(III) oxide on CNT shows its highest productivity at -0.3V vs RHE and an absolute current density (|J|) of 40 μA cm^{-2}, producing 0.63 μg mg_{cat}^{-1} h^{-1} with a FE of 1.5 %, and this is also the highest FE achieved by the catalyst as shown in **Figure 3.15b**. Even in this case, CAs are noisy, also from the first applied potential (**Figure 3.15a)**.

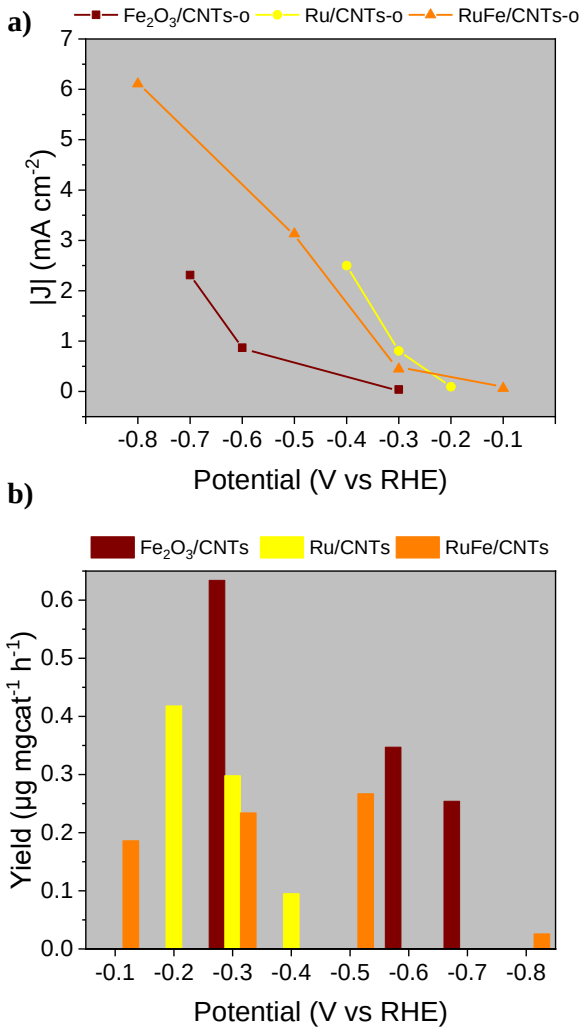

Figure 3.16 *– Different applied potential for different carbon nanotubes-based materials vs a) absolute value of current density and b) ammonia yield expressed in (μg* mg_{cat}^{-1} h^{-1}*). Ru (in yellow), RuFe (in orange)* Fe_2O_3 *(in dark red)*

Among the supported catalysts on CNTs, iron (III) oxide achieved the best performance, in the order Fe_2O_3 > Ru > RuFe (**Figure 3.16b**). Again, the presence of ruthenium lowers the onset potential (**Figure 3.16a**), but there is a change in the productivities, iron oxide produces 1.4 times more than ruthenium, and 2.2 times more than the RuFe co-doped catalyst. Chronoamperometers are noisy due to both the weak Nafion membrane bond and the production of hydrogen at the interface of the catalyst, which can cause membrane detachment.

Alumina-based catalysts show a predominantly best performance (in terms of both ammonia productivity and FE) at -0.3V vs RHE with $RuFe/Al_2O_3$ (1.047 μg mg_{cat}^{-1} h^{-1}, 0.5%, respectively) while functionalized-Carbon-Nanotubes-based catalysts show the best performance at -0.3V vs RHE for Fe_2O_3/CNTs (0.63 μg mg_{cat}^{-1} h^{-1} with a FE of 1.5 %). Productivity in Ru-Fe codoped alumina catalyst is only 1.66 times more than Iron (III) oxide on CNTs.

By preparing the catalyst to form the MEA, a challenge arose as the membrane caused the catalyst to exfoliate alongside carbon nanotubes (CNTs). Following the hot-pressing step, the catalyst exhibited a lack of mechanical stability. On the contrary, for alumina-based catalysts no problems occurred. For this reason, in order to perform EIS, EC 2 was used for CNT and Al_2O_3-based catalysts.

3.14 | Electrochemical Impedance Spectroscopy (EIS)

Electrochemical impedance spectroscopy (EIS) was adopted to investigate more in depth the electrochemical behaviour of *Al_2O_3*- and *CNT-based* samples. The experiments were carried out in the range of 0.1 Hz – 10 kHz using an AUTOLAB PGSTAT204 instrument (by Metrohm) in a custom two-compartment cell (*Electrochemical Cell 2*) filled with 0.1M Na_2SO_4 aqueous solution. The working electrode (WE) has an exposed area of 5.7 cm^2 with catalyst deposited by spray-coating technique. A GDL bare was used as the counter electrode (CE), and an

Ag/AgCl 3.0M KCl as the reference electrode (RE). No electrolyte circulation was used at the moment of the analysis to avoid any noise on the signal. Three potentials were investigated: -0.2V, -0.5V and -0.8V vs. RHE.

3.14.1 | Electrochemical Equivalent Circuits model

The EIS is an analytical technique for studying the electrical properties of an electrochemical system as a function of frequency. EIS is a non-destructive technique and can be used to analyse a wide range of materials and devices, including electrodes, solar cells, batteries, and catalysts, and the phenomena occurring at the electrode interface (**Figure 3.17b**), as well as their kinetics.

The basic principle of EIS is to apply a sinusoidal current signal of small amplitude to the system under test and measure the response, which can be the current, voltage, or another signal of interest. The impedance of the system is defined as the ratio of voltage to current in response to the sinusoidal signal.

EIS data are usually plotted in a Nyquist plot, in which the real part of the impedance (Z') is represented on the X-axis, and the imaginary part (Z'') is represented on the Y-axis. Analysis of EIS data can provide information about the electrical properties of the system, such as resistance, capacitance, and susceptibility.

Electrochemical equivalent circuit models are used to interpret EIS data. These models consist of electrical elements, such as resistors (R), capacitors (C), and inductors (L), which are connected in series or parallel.

The choice of the appropriate equivalent circuit model depends on the electrochemical system under consideration, sometimes defined after the testing to best fit the experimental data.

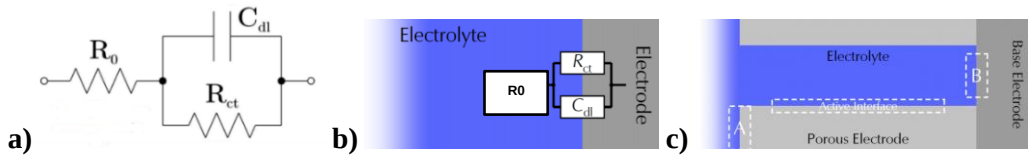

Figure 3.17 *– schematic representation of a) Simplified Randles cell b) Simplified Randles cell at the interface electrolyte-electrode c) region classification of porous electrode* [22]

The simplified Randles cell (**Figure 3.17a**) is a specific instance derived from the Randles cell, a widely recognized equivalent electrical circuit (EEC) used to simulate a semi-infinite diffusion-controlled faradaic reaction occurring at a flat electrode[23]. The Randles cell comprises an electrolyte resistance, denoted as R_0, connected in sequence with the simultaneous pairing of the double-layer capacitance, C_{dl}, and the impedance linked to the faradaic reaction [24].

In this section, the model used is the one depicted in **Figure 3.18**, based on the simplified Randles circuit, which consists of the following elements: the series resistance (Rs), the Electrochemical Equivalent Circuit (EEC) CPE-R for material porosity (**Figure 3.17c**), and the EEC for kinetics. For simplicity , the resistances associated with the phenomenon of porosity and kinetics, will be called R_p and R_k respectively and will be discussed later in Table 3.1.

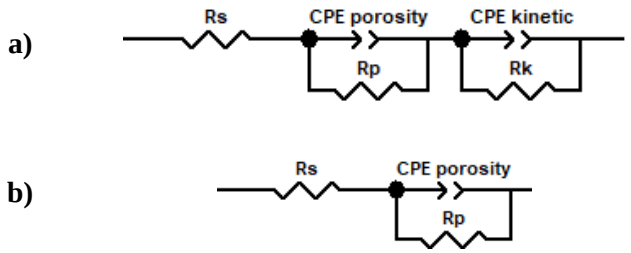

Figure 3.18 *– EECs proposed a) a complete model including an equivalent circuit related to porosity and kinetic part b) a simplified model to be used where porosity is present but difficult to model, thus including only the kinetic part*

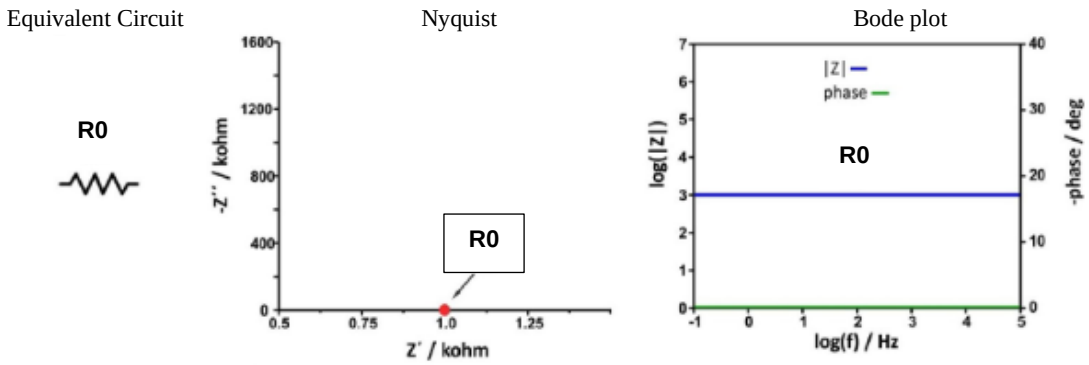

Figure 3.19 *– Equivalent circuit example for a simple resistance [25] with Nyquist and Bode plot*

In electrochemical impedance spectroscopy (EIS), *Rs* denotes the solution resistance and other system parameters such us distance between the electrdode[29,26,27]. R_s is obtained from the intersection with the real axis in the high-frequency limit in the Nyquist plot[26]. (**Figure 3.19**).

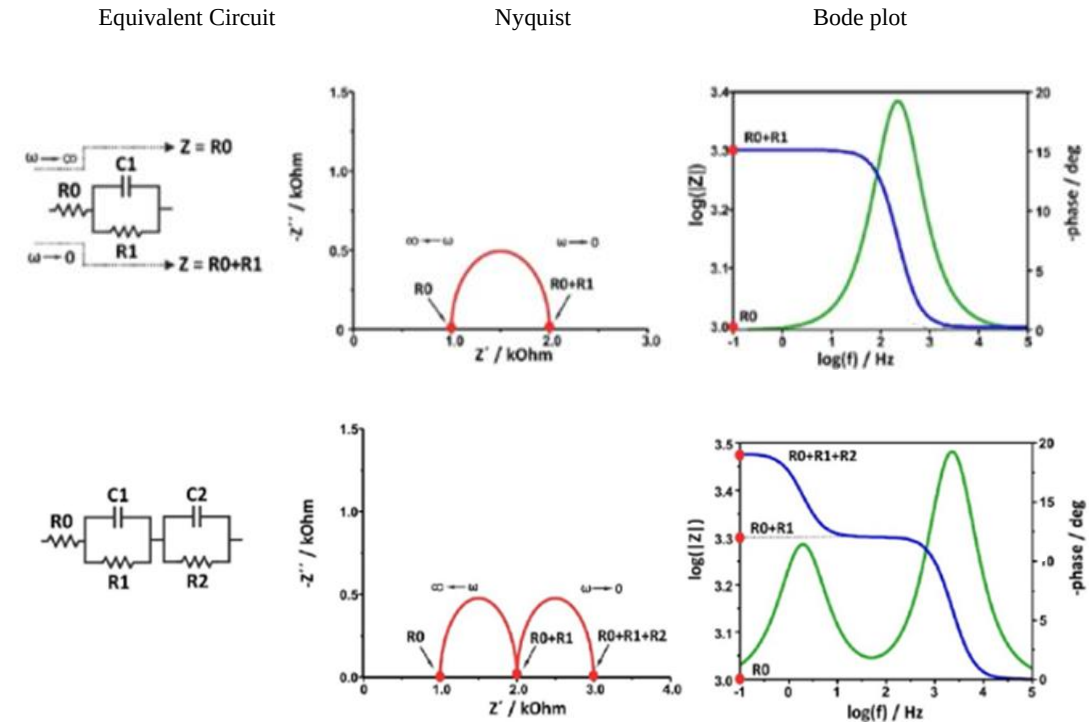

Figure 3.20 *– a) One-constant circuit and b) two-constant circuit [25] with Nyquist and bode plot*

Following the Randles model for phenomena occurring at the interface, each charge or mass transfer phenomenon is associated with a semicircle in the Nyquist. The circuit expressed in **Figure 3.20** could be modelized with equation 3.8. While the bode plot (phase) is useful for explicitly identifying the frequency of the phenomenon, difficult to extrapolate from Nyquist. The module of the bode plot usually is less used.

$$Z(\omega) = \left[R_0 + \frac{R_1}{(\omega R_1 C_2)^2+1}\right] - j\left[\frac{\omega {R_1}^2 C_1}{(\omega R_1 C_1)^2+1}\right] \quad \text{(eq. 3.8)}$$

While, a more complex system, composed by three elements (R_0, C_1R_1 and C_2R_2) could represented from the equation 3.9.

$$Z(\omega) = \left[R_0 + \frac{R_1}{(\omega R_1 C_2)^2+1} + \frac{R_2}{(\omega R_2 C_1)^2+1}\right] - j\left[\frac{\omega {R_1}^2 C_2}{(\omega R_1 C_2)^2+1} + \frac{\omega {R_2}^2 C_1}{(\omega R_2 C_1)^2+1}\right] \quad \text{(eq. 3.9)}$$

CPE stands for *Constant Phase Element*, and represents non-ideal or heterogeneous behaviors in an equivalent circuit model instead. This element is characterized by a mathematical expression (eq. 3.10) that models various nonlinear behaviors such as surface heterogeneity, immobilized ions, porosity, or asymmetries in the electrode/electrolyte interface[25,28].

$$Z_{CPE} = \frac{1}{(i\omega)^{\varphi} T} \quad \text{(eq. 3.10)}$$

Where ω is the angular frequency ($\omega=2\pi\nu$, ν=*frequency*), i is the current, φ is the constant phase angle, T is a constant related to the rotation of the complex plane (α) with respect to purely capacitive behavior, which can be expressed by eq. 3.11

$$\alpha = \frac{\pi}{2}(1 - \varphi) \quad \text{(eq. 3.11)}$$

The equation can represent:

- a pure capacitance for $\varphi = 1$;
- a non-ideal solid electrode for $0.5 < \varphi < 1$;
- a pure resistance for $\varphi = 0$;

It could also represent:

- a Warburg impedance for $\varphi = 0.5$;
- a pure inductance for $\varphi = -1$.

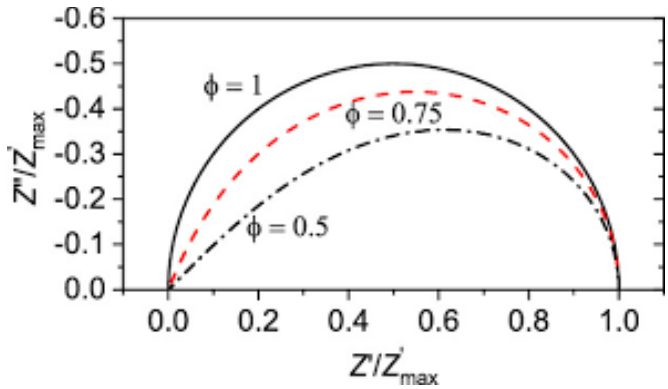

***Figure 3.21** - Behaviour of constant phase element at different φ [28]*

The CPE is used to describe phenomena that cannot be accurately represented by a simple capacitor (C_{DL}). It functions as a *generalized capacitor* adaptable to a wide range of non-ideal situations (**Figure 3.21**). Its incorporation into an equivalent circuit model allows for a more accurate representation of the electrochemical properties of a system, aiding in a better understanding of ongoing processes during electrochemical impedance measurements.

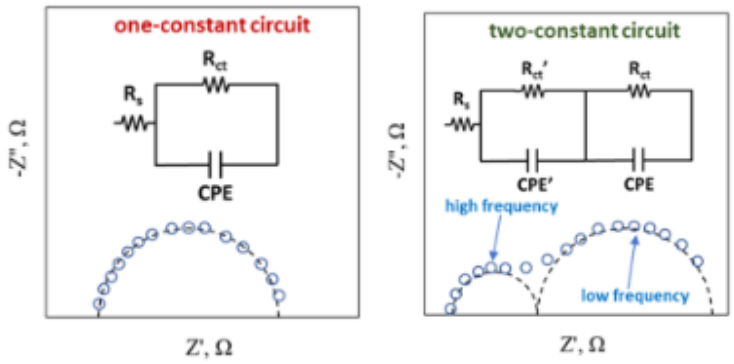

***Figure 3.22** - Real complex systems with a) one-constant circuit and b) two-constant circuit* [29]

Summarizing, as it can be seen from the **figures 3.22a** and **3.22b**, the equivalent circuits express the number of phenomena under investigation. In **figure 3.22a**, it can be seen that in addition to the solution resistance only one phenomenon is investigated with the Randles circuit, while in **figure 3.22b**, it can be seen that the two phenomena occur at different frequencies. Usually, the phenomena at high frequency are related to charge transport, while at low frequency, the phenomena are related to mass transport. Note that, the Nyquist plot starts from high frequencies (left of the plot) to low frequencies (right of the plot). While the bode plot (phase and modulus), has the high frequencies on the right, while the low frequencies on the left.

In this thesis, the terms *kinetics* and *porosity* are related to the phenomena of charge transfer at the interface carbonious substrate/deposited catalyst, and of mass transfer at interface electrode/solution, respectively. Porosity depends on the shape of the pores in the substrate (**Figure 3.23**), and the respective impedance is clearly visible in the Nyquist plot [30].

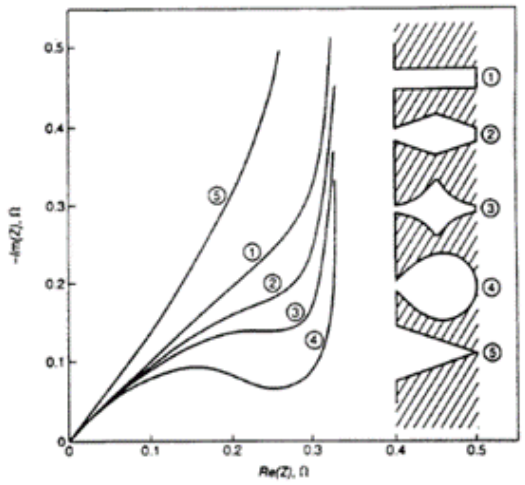

***Figure 3.23** - Impedance curves obtained for ideally polarized porous electrodes of different pore shapes[30]*

3.14.2 | EIS results

Figure 3.24 shows the EISs plots of the alumina-based catalysts. It can be seen in both the Nyquist and Bode plots that the presence of Ru/Al_2O_3 does not lead to any phenomena related to the porosity of the material (while present for both Ru-Fe and Fe_2O_3/Al_2O_3). On the contrary, the kinetic/mass transport phenomena are present at lower frequencies and, as visible in the Bode plots of **Figure 3.24b** and **3.24d**, the presence of iron in the catalyst composition leads to a shift to lower frequencies. This could be attributable to an increase in charges at the electrical double-layer. In **Figure 3.24f**, on the other hand, where the catalyst composition is only Fe/Fe_2O_3, there is a reversal behaviour, where the potential of -0.5 V vs RHE has a higher resistance than the potential at -0.2V vs RHE.

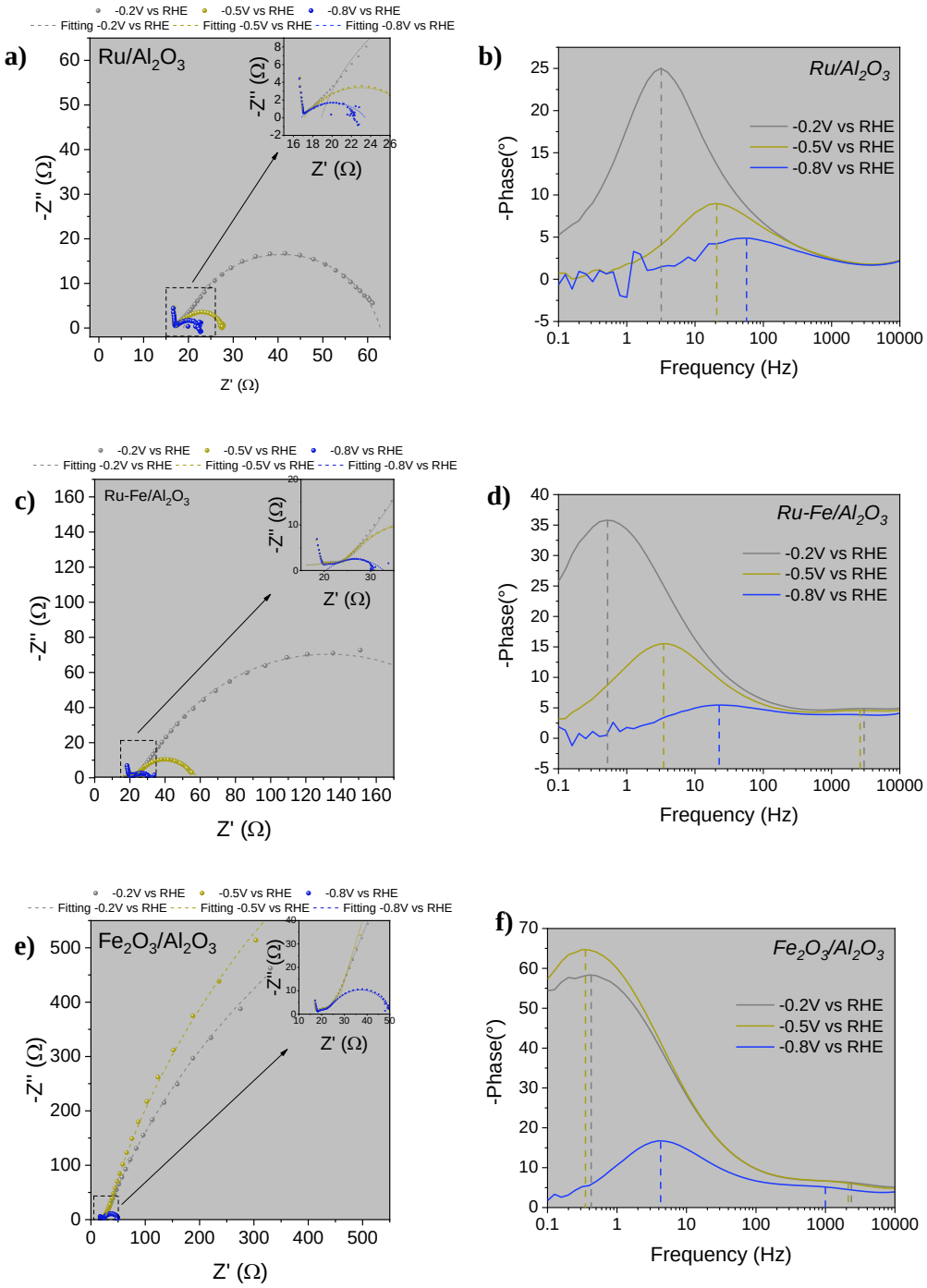

Figure 3.24 *– a, c and e) Nyquist and b, d and f) Bode plot for alumina-based catalysts at different potentials (vs RHE). -0.2V (Light gray), -0.5V (Dark yellow), -0.8V (Blue) vs RHE with no circulation of electrolyte*

Figures 3.25 shows the EIS behaviour of catalysts based on CNTs. Also in this case, the presence of Ruthenium alone does not exhibit the phenomenon at high frequencies, but only those at base frequencies related to mass transport. **Figure 3.25f** at -0.2V vs RHE exhibits a behaviour of semi-infinite diffusion; this means that the redox molecules are diffusing from the bulk to the electrode[33] **(Figure 3.26a**).

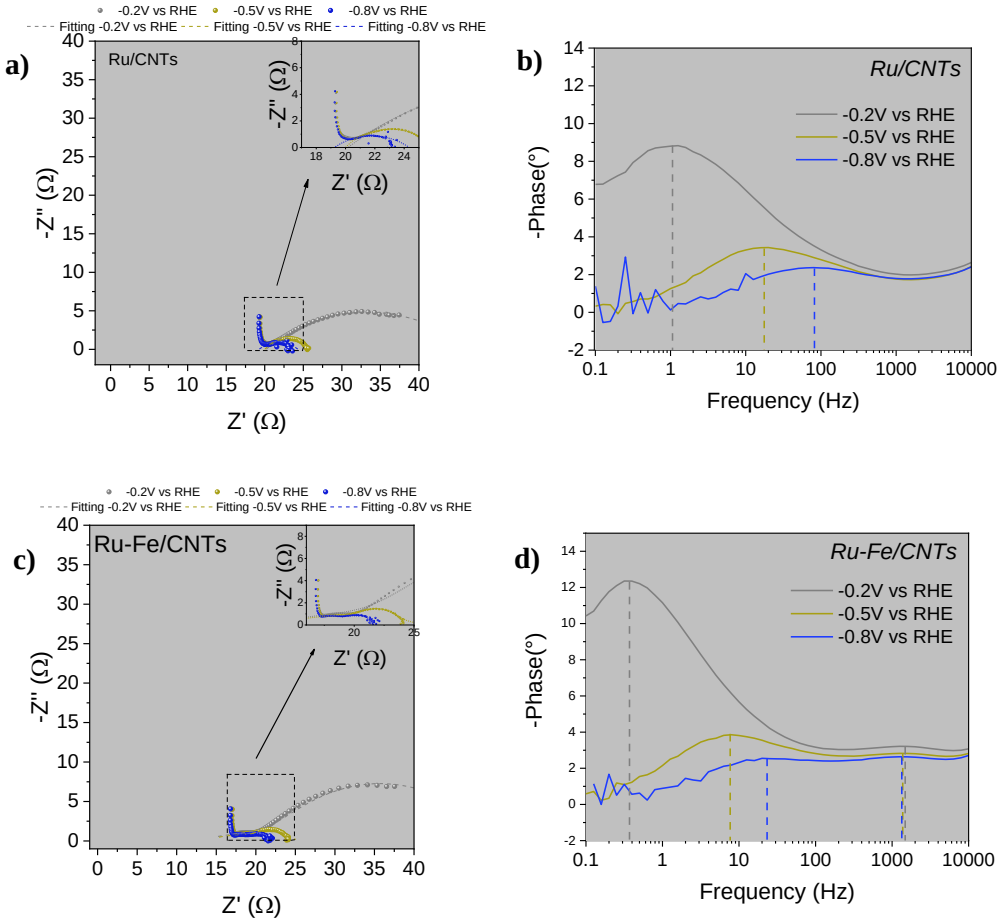

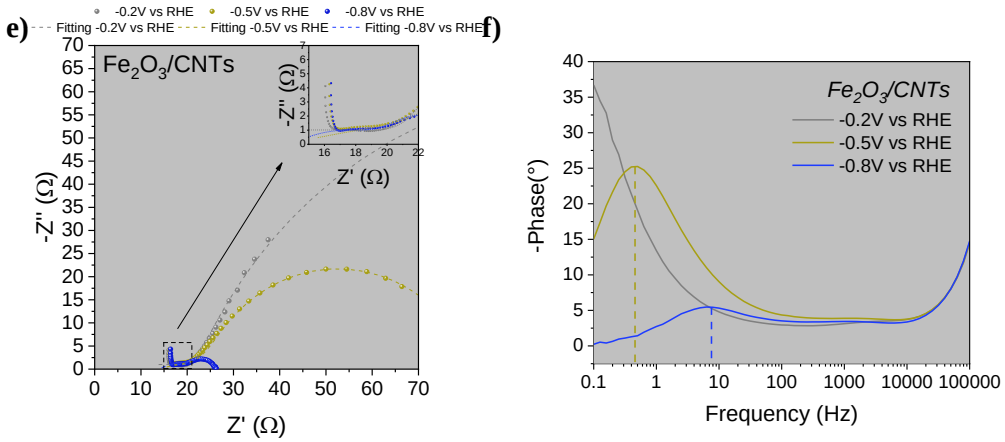

Figure 3.25 *– a, c and e) Nyquist and b, d and f) Bode plot for carbon nanotubes-based catalysts at different potentials (vs RHE). -0.2V (Light gray), -0.5V (Dark yellow), -0.8V (Blue) vs RHE with no circulation of electrolyte*

Furthermore, it can be seen in **Figures 3.24** and **3.25** that most of the Nyquist and Bode plots correspond with the model b of **Figure 3.26.**

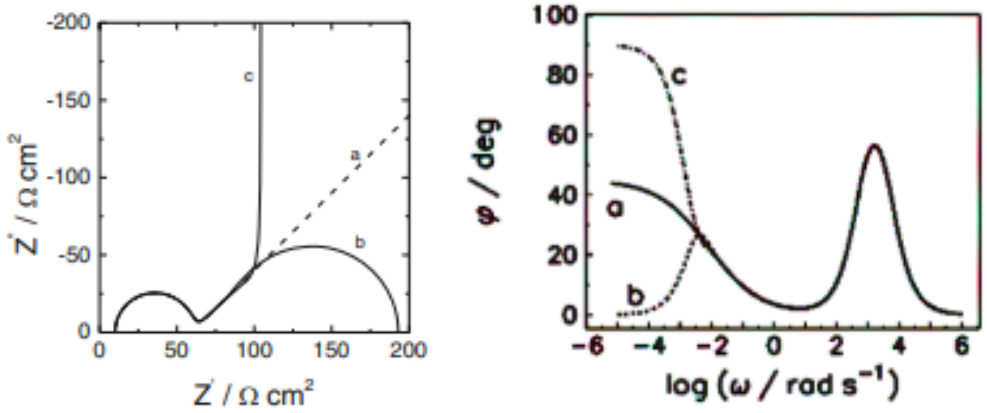

Figure 3.26 *– Nyquist and phase Bode plot for different diffusion in a limited length a) Semi-infinite linear, b) trasmissive, and c) reflective boundary*

The model explains that the phenomenon is a "finite-length diffusion" with transmissive boundary conditions, thus referring to a scenario in which a diffusion process (such as heat or mass transfer) occurs within a finite region but allows

material or energy to pass through the boundary of this region. The only case different from the previous one is the one shown in **Figure 3.25f**, where at -0.2 V vs. RHE, Fe_2O_3/CNTs behaves as a semi-infinite diffusion at lower frequency. This refers to a scenario where a diffusion process occurs within a material or at an interface. The redox molecule diffuses and reacts on the electrode surface from the bulk of the solution[31,32].

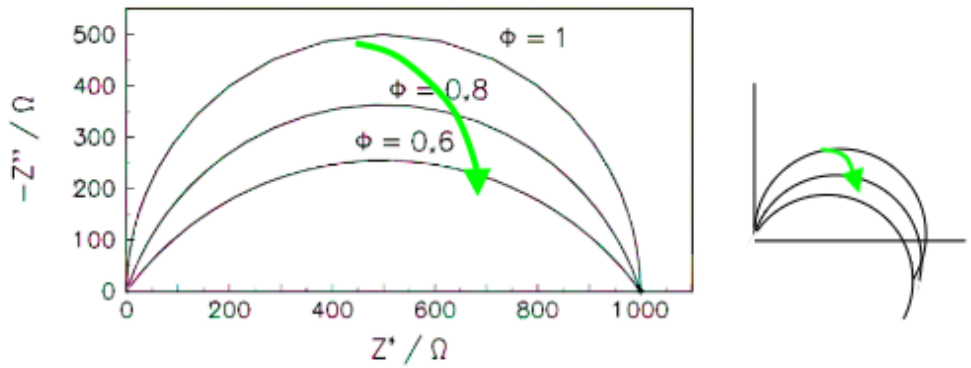

Figure 3.27 *– Behaviour of constant phase element at different φ[28] semplified partial rotation of the dial [31,33]*

Upon analysing the impedance graphs, a notable trend emerges: with an increasing in iron content, there is a corresponding increase in resistance, suggesting a higher overpotential. Additionally, as the potential increases, the Nyquist semicircles depicted in **Figure 3.24a,-c,-e** and **3.25a,-c,-e** undergo partial rotation concerning the dial, a phenomenon attributed to an electronic transfer occurring in parallel with the double-layer capacity (**Figure 3.27**) [28,31,33]. These observations, gleaned from both the graphs and their respective zoomed-in views, point out towards an EIS profile associated with porous electrodes under stationary conditions, prominently influenced by the iron content [28]. Additionally, it is noteworthy to consider the Nyquist plot characteristics of the catalysts doped with ruthenium. In agreement with *Zhang et al.* [34], the shape of the Nyquist plot appears to exhibit a less prominent feature in the porosity-related

aspect. This observation suggests the possibility that the re-positioning of the metal on the support results in pore shapes (as shown in **Figure 3.23**) different from Fe_2O_3 and Ru-Fe. Further exploration of this phenomenon should be conducted using advanced characterization techniques for a more comprehensive understanding.

The data presented in **Table 3.1** indicates that the electrolyte resistance (at low frequencies in the Nyquist plot) exhibits remarkable similarity across all catalysts. It is also clear that the presence of Fe in the structure has a direct effect on the porosity. Indeed, as reported by *Salar-Garcia et al.*[35], they studied the effect of iron oxide content and microstructural porosity changes. However, the reported values might bear influence from errors associated with the challenging task of modelling the equivalent circuit concerning material porosity. For this reason, two equivalent electric circuits (EECs) were used, one for Fe and Ru-Fe catalysts and one for only ruthenium doping. The calculated value of R_s, derived from the root mean square deviation, stands at $14.59 \pm 4.65\ \Omega$. Focusing on the CPE parameters, the CPE part of the porous EEC is very low, it is attributable to a resistive material behaviour ($0 < \text{CPE-P} < 1$, where 0 indicates purely resistive behaviour, and 1 means purely capacitive behaviour).

	Potential (V vs RHE)	**Rs (Ω)**	**CPE-T** (Kinetic)	**CPE-P** (Kinetic)	**Rk** (Kinetic, Ω)	**CPE-T** (Porosity)	**CPE-P** (Porosity)	**Rp** (Porosity, Ω)	**fk_{max} (kinetic, kHz)**	**fp_{max} (porosity, Hz)**
Ru /Al_2O_3	-0.2	18.89	-	-	-	0.00340	0.820	43.95	-	**3.16**
	-0.5	17.13	-	-	-	0.00363	0.677	11.57	-	**19.95**
	-0.8	16.81	-	-	-	0.00564	0.593	6.63	-	**50.12**
RuFe /Al_2O_3	-0.2	7.00	0.01800	0.100	45.15	0.00577	0.761	201.90	**31.62**	**0.5**
	-0.5	7.00	0.01800	0.100	43.89	0.00503	0.861	22.72	**25.12**	**3.98**
	-0.8	20.40	-	-	-	0.00780	0.480	12.41	-	**25.11**
Fe_2O_3 /Al_2O_3	-0.2	15.00	0.00307	0.375	11.17	0.00237	0.775	2000.00	**2.51**	**0.40**
	-0.5	15.00	0.00381	0.354	12.25	0.00201	0.815	3114.00	**1.99**	**0.32**
	-0.8	15.00	0.00381	0.354	12.25	0.00328	0.916	22.78	**1.00**	**3.98**
Ru /CNTs	-0.2	20.17	-	-	-	0.02500	0.447	26.30	-	**1.0**
	-0.5	20.00	-	-	-	0.01000	0.550	6.00	-	**15.85**
	-0.8	19.24	-	-	-	0.01900	0.420	5.10	-	**79.43**
RuFe /CNTs	-0.2	12.40	0.02900	0.149	20.00	0.03500	0.650	22.00	**1.58**	**0.32**
	-0.5	13.52	0.01890	0.200	10.00	0.02300	0.838	2.18	**1.26**	**7.94**
	-0.8	12.71	0.02400	0.167	12.40	0.01995	0.420	5.16	**1.26**	**25.11**

Fe_2O_3 /CNTs	-0.2	4.80	0.01000	0.119	21.62	0.04233	0.778	175.30	**3.98**	-
	-0.5	13.54	0.04133	0.153	38.96	0.01697	0.861	48.62	**3.16**	**0.50**
	-0.8	14.00	0.00500	0.368	6.34	0.02500	0.700	6.25	**1.00**	**7.94**

(-) not possible to model.

***Table 3.1** - Parameters of the equivalent circuit modelling*

Overall, by evaluating how the R_p of the system varies, that is, the sum of the various resistive contributions (Charge transport in solution, polarization and mass transfer, diffusive phenomena), alumina-based materials have a higher R_p than materials based on CNTs. Focusing specifically on the metal aspect, there is a discernible decrease in the R_p following the sequence Fe_2O_3 > Ru-Fe > Ru (**Figure 3.28a,-b**).

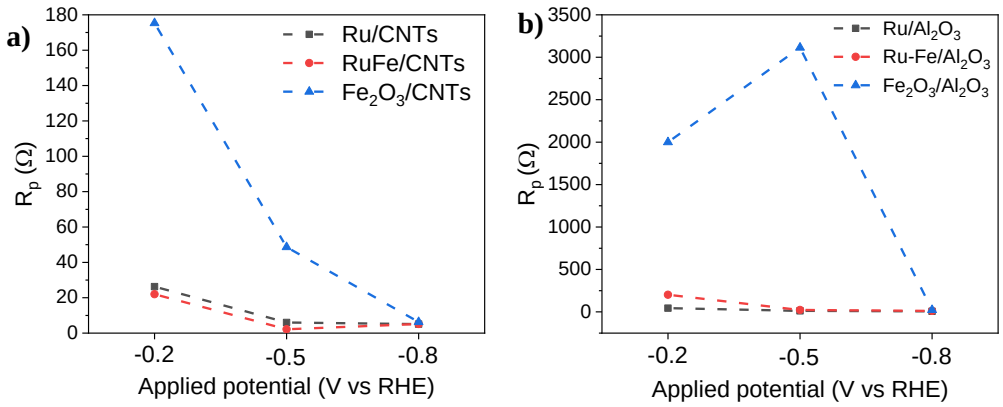

***Figure 3.28** – porosity resistance graphs of a) Alumina-based catalysts and b) CNTs-based catalysts at different applied voltages*

The resistance values of the best-performing alumina-based and CNTs-based catalysts are 201 Ω for Ru-Fe/Al_2O_3 and 178 Ω for Fe_2O_3/CNTs, at -0.3V vs RHE (and they have their maximum yield at -0.3V vs RHE). The resistance value is similar, although it would have been more predictable that the best performance would have been obtained by the catalyst with the lowest resistance. Being an oxide metal therefore generally less conductive than metal alone, its conduction to the electrolyte increases the resistance. This phenomenon is very visible with

Al_2O_3 where both Fe oxide and the combination of Fe and Ru, at low potentials, greatly increase R_p. The effect is mitigated for CNTs that, being conductive, compensate for the increase in mass transfer/charge resistance.

3.15 | Double-layer capacitance (C_{DL}) calculation

Double Layer Capacitance (C_{DL}) was calculated through different Cyclic Voltammetry (CV) at different scan rates (2, 5, 10, 15, 20, 30, 40, 50 mV s^{-1}) in a narrow window (± 35 mV) around the open circuit potential (OCP) as showed in **Figure 3.29**.

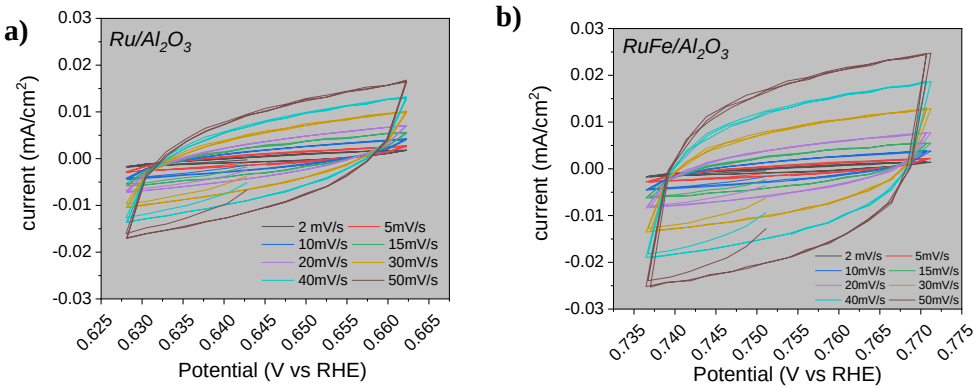

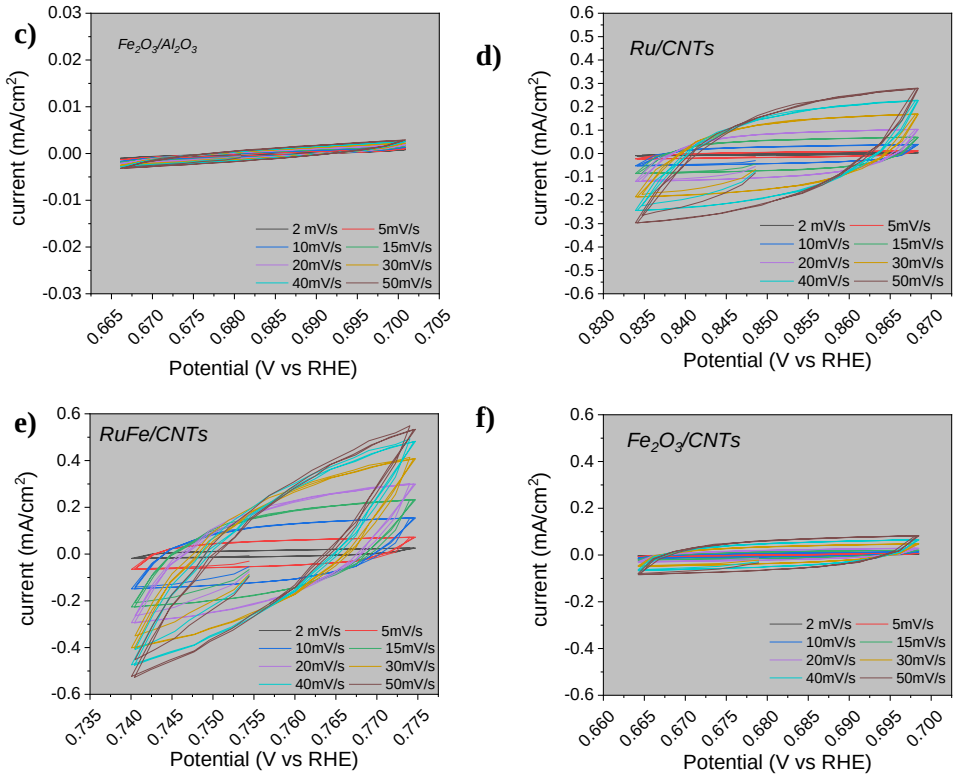

Figure 3.29 – *Cyclic Voltammetry at different scan rates around the OCP for a) Ru/Al_2O_3, b) $RuFe/Al_2O_3$, c) Fe_2O_3/Al_2O_3, d) Ru/CNTs, e) RuFe/CNTs, f) Fe_2O_3/CNTs*

From the CVs at different scan rates shown in **Figure 3.29**, the difference between cathodic current and anodic current density (ΔJ) was calculated. The ΔJ values at different scan-rate were plotted in **Figure 3.30**, and the linear regression was calculated. From this regression, the value of the capacitance of the double layer is extrapolated from the value of the slope expressed in F cm^{-2} (converted in mF cm^{-2}). All the graphs in **Figure 3.30** show approximately a linear profile except for Ru-Fe/CNTs in **Figure 3.30e**. This latter can be attributed to phenomena that do not depend on diffusion.

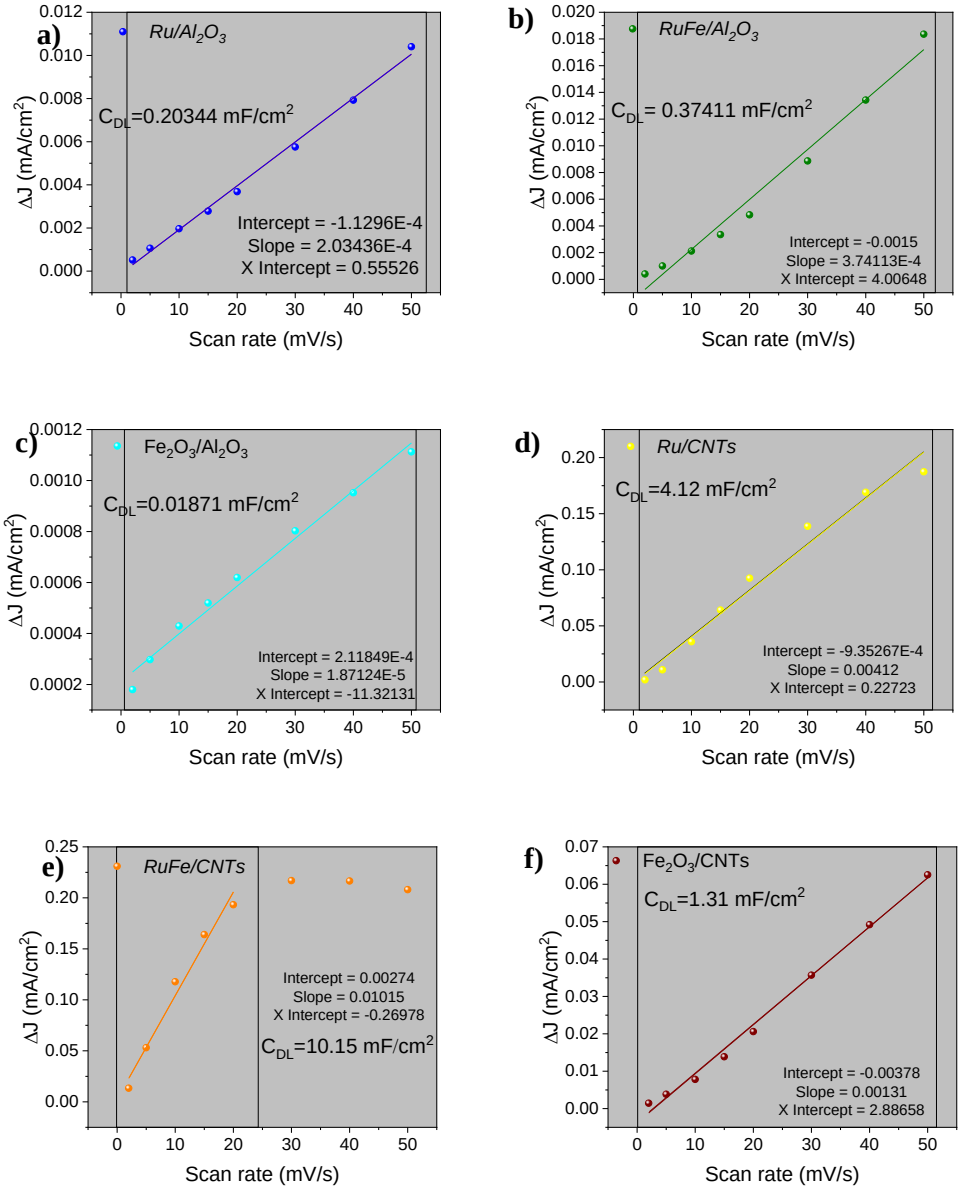

Figure 3.30 *- C_{DL} calculation with linear regression for alumina-based a) Ru b) Ru-Fe c)Fe_2O_3 and functionalized carbon nanotubes d) Ru e)Ru-Fe f)Fe_2O_3 respectively*

Figure 3.31 summarizes all the C_{DL}s calculated for alumina-based and carbon nanotubes-based catalysts in the same graph. Ru-Fe/CNTs exhibit the higher double layer capacitance of 10.15 mF cm^{-2}, in the order Ru-Fe/CNTs > Ru/CNTs > Fe_2O_3/CNTs > Ru-Fe/Al_2O_3 > Ru/Al_2O_3 > Fe_2O_3/Al_2O_3 (respectively 10.15,

4.12, 1.31, 0.37, 0.20, 0.02 mF cm^{-2}). Ru-Fe shows the higher C_{DL}, in every support, in the order Ru-Fe > Ru > Fe_2O_3.

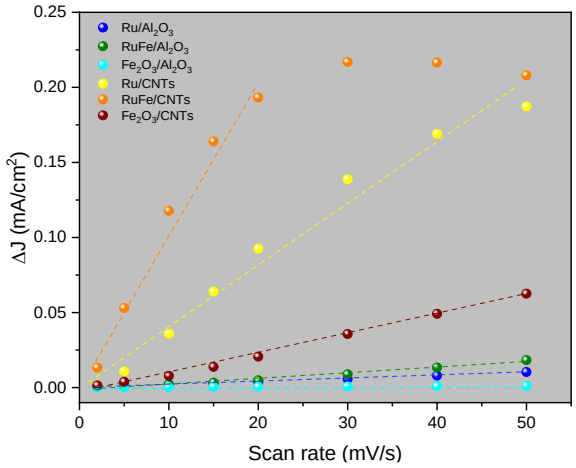

***Figure 3.31** – Comparison between different catalyst alumina and CNTs based*

As *Song et al.*[36] suggest, a higher capacitance value of the double layer (C_{DL}), is synonymous of a majority of active sites/general activity of the catalyst. On the other hand, as *Ananthraj et al.*[37] retort, the electrocatalytic activity cannot only be justified by the C_{DL} value but must also take into account the parallel resistance (in our case R_p).

Table 3.2 summarises data for the different substrates (Al_2O_3 and CNTs) decorated with different metals (Fe_2O_3, Ru-Fe and Ru). The properties such as C_{DL}, C_p, AESA, and ECSA have been calculated, as announced in section 3.9.3.

Sample	C_{DL} (mF/cm^2)	C_p (F/g)	AESA (m^2/g)	ECSA (cm^2)
Ru/Al_2O_3	0.20344	0.395	1941.6	0.8252
$Ru\text{-}Fe/Al_2O_3$	0.37411	0.536	1432.7	0.6089
Fe_2O_3/Al_2O_3	0.01871	0.081	4329.2	1.840
Ru/CNTs	4.12	13.5	3276.7	1.393
Ru-Fe/CNTs	10.15	18.2	1793.1	0.7621
Fe_2O_3/CNTs	1.31	4.96	3786.2	1.609

***Table 3.2** – summary of C_{DL}, C_p, EASA, and ECSA calculation*

Table 3.2 shows that Fe_2O_3/Al_2O_3 and Fe_2O_3/CNTs have the lowest C_{DL} (0.02 and 1.31 mF cm^{-2}, respectively) while Ru-Fe/Al_2O_3 and Ru-Fe CNTs the highest (0.37 and 10.15 mF cm^{-2} respectively). This means that the Ru-Fe hybrid catalyst has a greater tendency to accumulate charges at the electrode-solution interface than the other catalysts with the same support.

This trend can also be observed in specific capacitance (C_p), which follows the same trend of C_{DL}; thus it is assumed that catalysts on CNTs tend to accumulate charges on the surface better than Al_2O_3. The C_{DL} and C_p values obtained here are in line with the results available in the literature [38].

In contrast, it seems that according to the calculated data of AESA and ECSA, they tend to favor Fe_2O_3/Al_2O_3 and Fe_2O_3/CNT as the active and electrochemically active area. The AESA values follows the trend Fe_2O_3/Al_2O_3 > Fe_2O_3/CNTs> Ru/CNTs > Ru/Al_2O_3 > Ru-Fe/Al_2O_3 > Ru-Fe/CNTs (4329.2, 3786.2, 3276.7, 1941.6, 1793.1, and 1432.7 m^2/g respectively) while the trend of ECSA becomes Fe_2O_3/Al_2O_3 > Fe_2O_3/CNTs > Ru/CNTs > Ru/Al_2O_3 > Ru-Fe/CNTs > Ru-Fe/Al_2O_3 (1.840, 1.609, 1393, 0.825, 0.762, 0.609 cm^2 respectively).

From the other hands, from BET surface characterization, it is possible to see the trend Ru/CNTs > Ru-Fe/CNTs > Fe_2O_3CNTs >> Ru-Fe/Alu > Fe_2O_3/Alu > Ru/Alu (105.7, 63.6, 61.8, 17.59, 8.9, and 1.8 m^2 g^{-1}, respectively). It can be seen that Ru-Fe/Al_2O_3 has the largest surface area (and C_{DL}) compared with the other alumina-based catalysts. However, Fe_2O_3/CNTs compared to the Ru-Fe/CNTs hybrid possesses comparable surface area. Ru/CNTs shows the largest surface area per gram of catalyst among all the electrodes.

The surface area of Ru-Fe and Ru/Al_2O_3 in combination with the paucity of pores could explain their activity related to the fact that doping occurred mainly on the surface. The catalyst with Fe in the structure seems to benefit from this co-doping. *Liu et al.* [39] observed a similar behaviour with Fe-Ru bimetallic catalyst prepared

by atomically dispersing the metals on *Metal Organic Framework* (MOF) matrix by wetness incipient impregnation. The bi-metallic compared to the single metals gave the best performance. Also comparing the adsorption/desorption energies by DFT calculations, the presence of atomically dispersed Ru together with Fe lowers the N_2-Fe path of reaction. In addition, this atomic dispersion of Ru and Fe could confirm the absence of both metals at XRD analysis (both Ru-Fe on Al_2O_3 and CNTs).

Fe_2O_3/CNTs exhibited the largest calculated AESA (3786.2 m^2 g^{-1}) of the doped CNTs catalysts slightly higher than Ru/CNTs (3276.7 m^2 g^{-1}). This value could be related to the EDX analysis, where the higher activity of this catalyst may lie in the fact that being more porous, it allows N_2 coming from the gas phase to reside longer within the fibrous structure.

A further aspect to consider is the effect of the decontamination test on the structure of the catalyst. As announced by *Chen et al.*[40], the application of a low potential can change the structure of the active site by forming the active species γ-FeOOH (Lepidocrocite) from γ-Fe_2O_3 phase found in XRD characterization (see section 2.5.2)[41]. The active γ-FeOOH is able to promote the reaction in agreement also with the example found in nature with Nitrogenase FeMo-cofactor[42]. Fe_2O_3/CNTs performed 1.5 times better than Ru/CNTs. Ruthenium, having a stronger nitrogen binding strength than Iron, shifts the onset potential toward lower potentials. These defect lattice sites may be possibly enhanced from the strains induced by the strong interaction with CNTs defects, which are absent on alumina.

Catalyst composition	**FE** (%)	**NH_3 Formation rate** ($\mu g\ mg_{cat}^{-1}\ h^{-1}$)	**Potential** (V) **and electrolyte**	**Detection method**	**Ref.**
Ru-Fe/Al_2O_3	0.5	1.05	-0.3 vs RHE 0.1M Na_2SO_4	Salicylate IC	This work
Fe_2O_3/CNTs	1.5	0.63	-0.2 vs RHE 0.1M Na_2SO_4		

α-Fe_2O_3 oxigen enriched /CNTs	6.0	0.459 $\mu g\ h^{-1}\ cm^{-2}$	-0.9 vs Ag/AgCl 0.1M KOH	Nessler's reagent	[3]
Cu/Pd nanoclusters/ GOx	0.6	2.80	-0.2 vs RHE 0.1M KOH	Salicylate	[4]
Ultrathin Rh nanosheet	0.22	23.88	-0.2 vs RHE 0.1M KOH	Indophenol	[43]
Au nanoparticles anchored on CeO_x-GRO	10.10	8.3	-0.2 vs RHE 0.1M HCl	Salicylate	[44]
Mo_2N nanorods	4.5	78.4	-0.3 vs RHE 0.1M HCl	Salicylate	[45]
Nb_2O_5 nanofiber	9.26	43.6	-0.55 vs RHE 0.1M HCl	Salicylate	[46]
Fe_2O_3/CNTs	0.16	2.2 mg $h^{-1}\ m^{-2}$	-2.0 vs Ag/AgCl 0.5M KOH	Salicylate	[2]
FeRu-CNS	29.3	43.9	-0.2V vs RHE 0.1M Na_2SO_4	Indophenol	[39]
Mn_3O_4 nanocubes	3.0	11.6	-0.8 vs RHE 0.1M Na_2SO_4	Salicylate	[47]

Table 3.3 *– comparative table between this work and literature results*

By comparing the data obtained in this thesis with the various works in the literature (**Table 3.3**), it can be seen that the landscape of electrocatalytic ammonia productions is very variegated. Many parameters must be taken into account, such as the geometric area of the electrode, catalyst loading, electrolyte and configuration (Section 3.9), cell size and so on. Consequently, FE and yield calculations are strongly influenced by these parameters. In addition, the decontamination factor preceding the tests helps to eliminate sources of contamination as seen in section 3.12.

The following **summary table 3.4**, shows the catalytic performance obtained by doping CNTs and Al_2O_3 supports with Fe, Ru and cooping and different advanced characterization parameters.

Catalyst	Teorical metal load (wt.%)	EDX Load (at.%)	Maximum productivity ($\mu g\ mg_{cat}^{-1}\ h^{-1}$)	FE (%)	Applied potential (V vs RHE)	Current density ($mA\ cm^{-2}$)	AESA (cm^2/g)	ECSA (cm^2)
GDL	0	0	0.04	0.09	-0.5	-	-	-
Al_2O_3	0	0	0.04	0.05	-0.8	-0.433	-	-
Fe_2O_3 / Al_2O_3	5 (3.5†)	5.75±1.45*	0.31	0.21	-0.6	-0.112	4329.2	1.840
Ru-Fe / Al_2O_3	Ru 2.5 Fe 2.5†	Ru 1.2±0.1 Fe 2.6±0.3*	1.05	0.5	-0.3	-0.294	1432.7	0.6089
Ru / Al_2O_3	5	2.55±0.15	0.36	0.23	-0.3	-0.187	1941.6	0.8252
CNTs	0	0	-	-	-	-	-	-
Fe_2O_3 / CNTs	30 (21†)	24.8±4.4*	0.63	1.5	-0.3	-0.040	3786.2	1.609
Ru-Fe / CNTs	Ru 2.5 Fe 2.5†	Ru 8.3±2.1 Fe 5.2±1.9*	0.27	0.01	-0.5	-3.13	1793.1	0.7621
Ru / CNTs	5	32.1±3.7	0.42	0.45	-0.2	-0.093	3276.7	1.393

(*) related to at.% of Fe
(†) related to wt.% of Fe calculated
(-) not possible to calculate

Table 3.4 *– Summary table of Electrochemical tests*

3.16 | Electrochemical cell comparison performance

In this section, electrochemical tests performed on reduced graphene oxide (rGO), manganese oxide on rGO, and iron-manganese oxide on rGO catalysts (rGO, rGO-Mn_xO_y, and rGO-Mn_xO_y-Fe) will be discussed. Tests on these catalysts were made in collaboration with the University of Trieste with the aim to find the best reactor conditions between gas-phase approach (EC1 – section 3.9.1) and gas-liquid phase approach (EC 2 – Section 3.9.2) beyond the properties of the electrocatalysts themselves. The used protocol is similar to the one discussed previously. Reactions were carried out on rGO-Mn_xO_y-Fe, rGO-Mn_xO_y and rGO in both EC1 and EC2. Refer to section 3.9 for complete experimental conditions.

3.16.1 | Working potential (EC1-EC2)

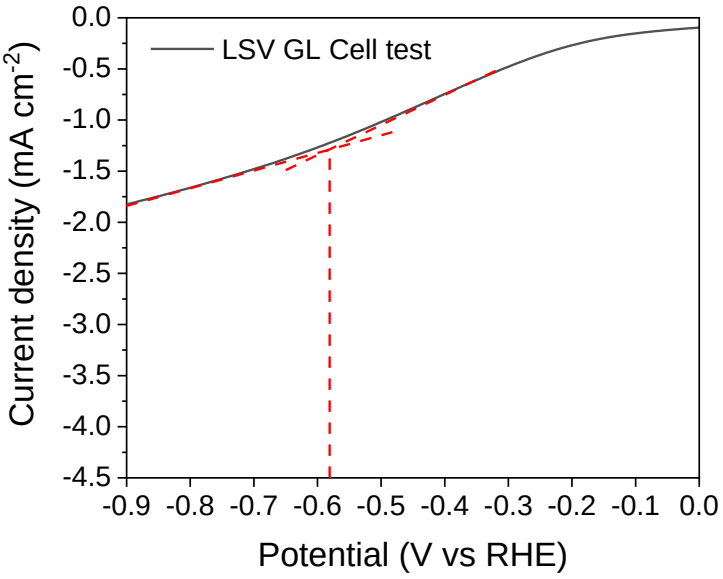

Figure 3.32 *– Linear Sweep Voltammetry for rGO-Mn_xO_y-Fe*

The selection of working potentials, in this case, was based on the use of linear sweep voltammetry (LSV), carried out in the gas phase (EC1) after preparing the MEA (section 3.7) and placing it in the cell. The oscillation of the peristaltic pump generated noise in the signal, thus the pump was turned off during the LSV. From

the black lines in **Figure 3.32**, the onset potential around -0.6V vs RHE is clearly seen.

3.16.2 | Decontamination and UV-Detection

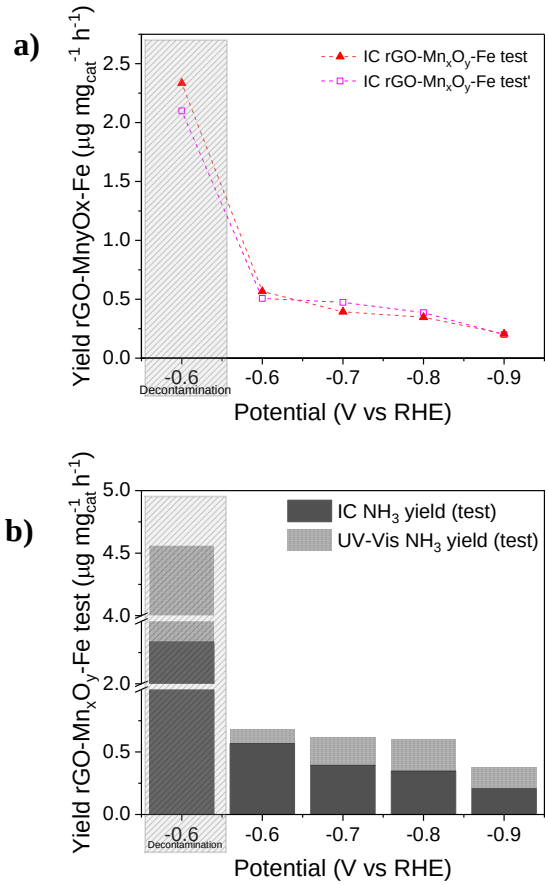

Figure 3.33 *– Yield comparison between applied potentials and decontamination test for rGO-Mn_xO_y-Fe in EC1 a) only IC test and test' b) IC+UV-detected ammonia test*

The decontamination test was performed at the lowest applied potential for 30 minutes (-0.6 V vs RHE). In **Figure 3.33**, the importance of the decontamination test in reporting reliable results relating to the actual ammonia production is evident. The decontamination results will not be reported for the other tests. Moreover, the ammonia detected from Salicylate method (passed from the

cathode to the anode by crossover, **Figure 3.33b**) is omitted for graphical simplicity but considered for efficiencies.

3.16.3 | EC1 tests

Different chronoamperometries (CA) were carried out, and different potentials (from -0.6 to -0.9 V vs. RHE) were investigated. The current was recorded for a total of 1.5h at each potential, and at the end of the analysis the products were analysed by the methods described in section 3.11.1 and 3.11.2. From **Figure 3.34a** and **3.34b** showing tests with the rGO-Mn_xO_y-Fe, it can be seen that the current density profiles are constant at low potentials, and that the currents at low potentials are similar between the first and second tests carried out to verify the reproducibility (test and test', respectively).

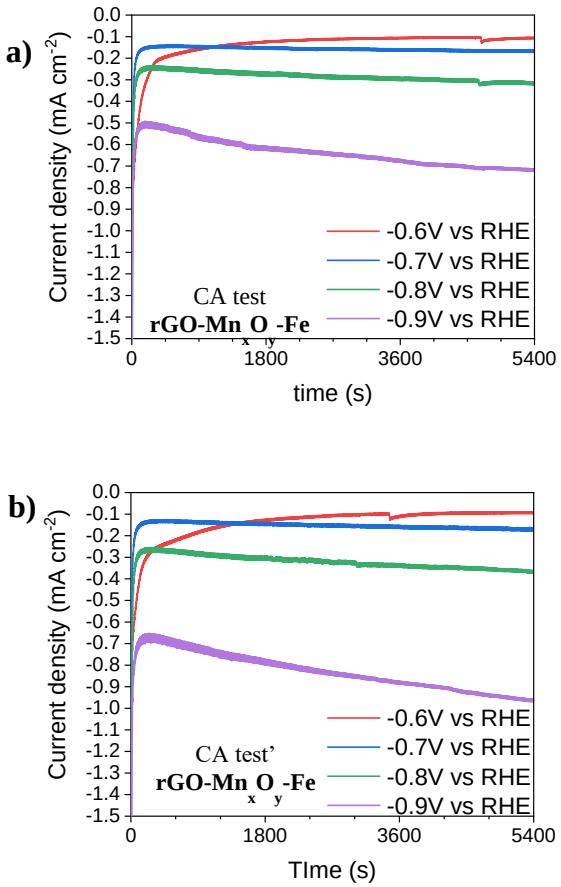

Figure 3.34 *– CAs for rGO-Mn_xO_y-Fe for a) first test (test) and b) second test (test')*

In **Figure 3.35**, productivity (in $\mu g_{NH3}\ mg_{cat}^{-1}\ h^{-1}$) on the left Y-axis and Faradaic efficiency (FE%) on the right Y-axis are depicted. The maximum error bars between test and test' are also shown. The rGO-Mn_xO_y-Fe catalyst shows the highest productivity at -0.6 V vs. RHE ($0.537 \pm 0.030\ \mu g\ mg_{cat}^{-1}\ h^{-1}$) with a FE of $0.45 \pm 0.04\%$. The resulting current density is relative to the average between the two tests ($136.6 \pm 6.1\ \mu A\ cm^{-2}$).

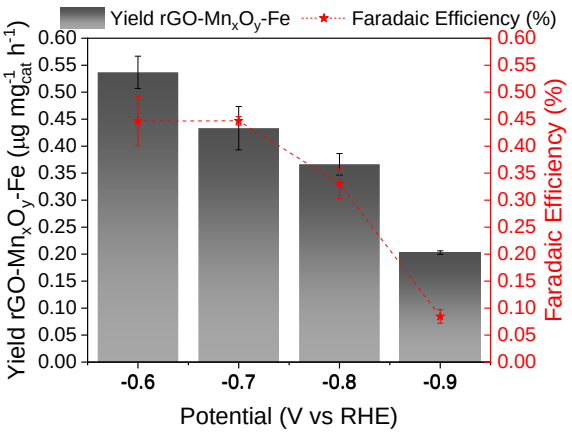

Figure 3.35 *– Yield (left axis) and Faradaic efficiency (right axis) for rGO-Mn_xO_y-Fe*

Instead, **Figure 3.36a** and **3.36b** show the current density and yield of rGO-Mn_xO_y (no Fe), while **Figure 3.36c** and **3.36d**, the current density and productivity trends of the bare rGO, respectively. It can be seen that rGO-Mn_xO_y shows its maximum productivity ($0.467\ \mu g_{NH3}\ mg_{cat}^{-1}\ h^{-1}$) at -0.7 V vs. RHE and an FE of 1.1%, at a recorded current value of 61.4 $\mu A\ cm^{-2}$. While the best performance for the rGO carbon support was recorded at -0.6 V vs. RHE ($0.307\ \mu g_{NH3}\ mg_{cat}^{-1}\ h^{-1}$) and an efficiency of 0.2% at a current density of 128.3 $\mu A\ cm^{-2}$. The comparison of the three catalysts shows that iron shows the highest performance at each applied potential. At -0.6V vs. RHE, the catalyst with Fe provided a yield 1.32 times higher than Mn_xO_y and 1.74 times higher than rGO.

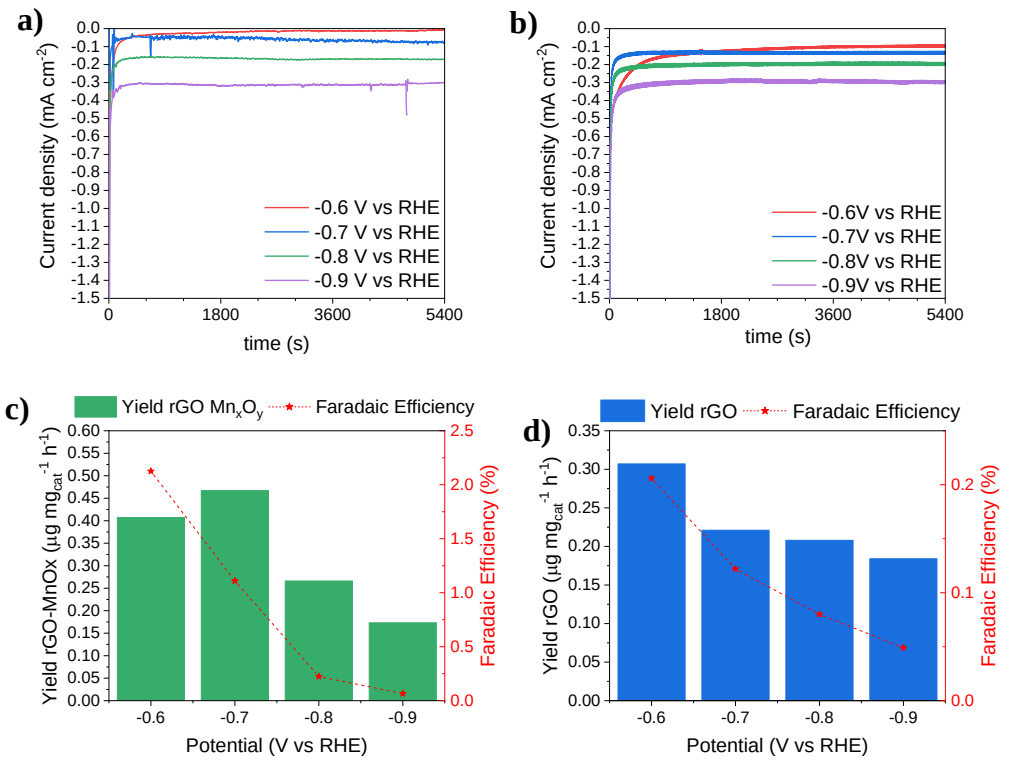

Figure 3.36 *– Chronoamperometries for a) rGO-Mn_xO_y and b) rGO and yield (on the left Y-axis) and Faradaic efficiency (on right Y-axis) for c) rGO-Mn_xO_y and d) rGO*

Finally, reporting the current densities versus potentials (**Figure 3.37a**) shows that the catalyst with iron has a higher current density than rGO-Mn_xO_y and rGO. Looking at the trend of EC1 (see **Figure 3.37b**), cell voltages (working-counter) are about the same at -0.6, -0.7 and -0.8V vs RHE, while it deviates at -0.9 V vs RHE for the rGO-Mn_xO_y-Fe. This is an indication that the catalyst at high potentials favours more the HER, due to the higher current.

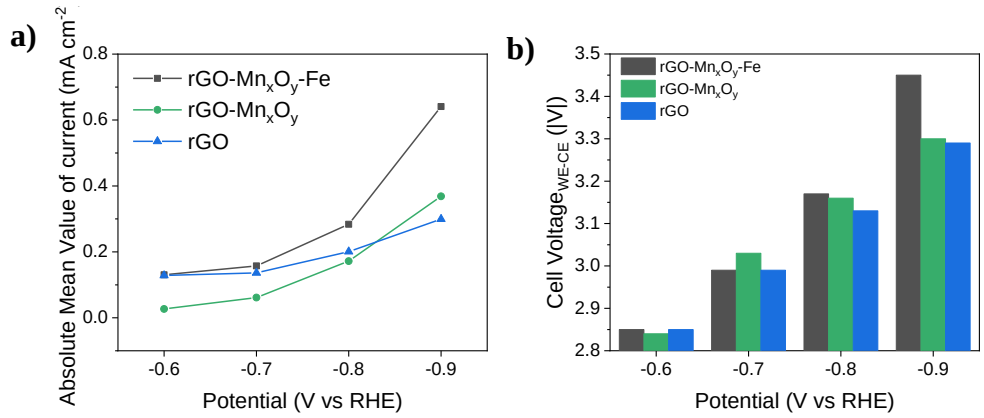

Figure 3.37 *– a) current density trend and b) Cell Voltage at different potential*

3.16.4 | EC 2 tests

To have a direct comparison with the EC1 configuration, tests were carried out with the same catalysts in the EC2 configuration. After decontamination (-0.6 V vs RHE for 1 h), 4 h of testing (at -0.6 V vs RHE) was performed (**Figure 3.38**). The liquid in the absorber (in the gas-phase line) was analysed at the end of each hour, while the liquids in anodic and cathodic compartments were analysed at the end of 4 h by the salicylate method. At the end of the fourth hour, the GDL broke down and the test was stopped. The current density during the test fluctuated around 50 μA cm^{-2} (**Figure 3.38a**), while the total ammonia production (IC yield + cathode yield + anode yield) remained constant (**Figure 3.38b**).

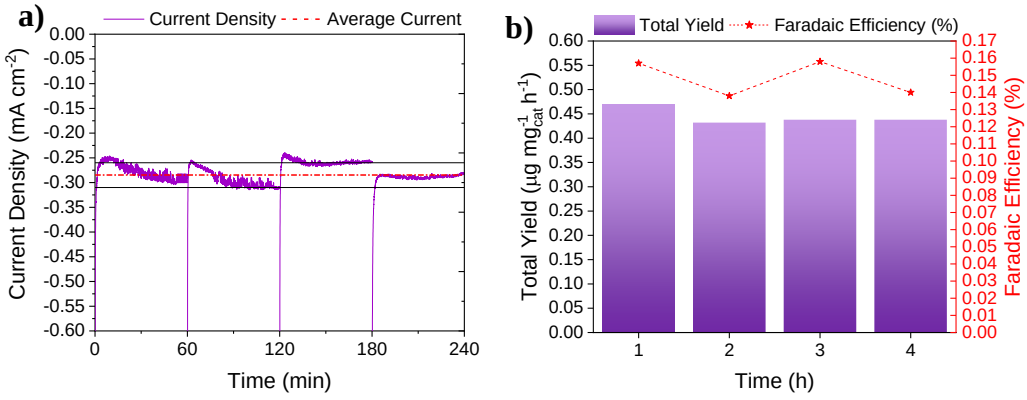

Figure 3.38 *– rGO-Mn_xO_y-Fe a) current density and b) total yield of ammonia under 4h test in EC2*

The same trend occurred for rGO-Mn_xO_y during the -0.6 V vs RHE test of 4 h, as showed in **Figure 3.39a** and **3.39b**. The difference from the corresponding iron doped catalyst, is in a higher FE due to the lower current.

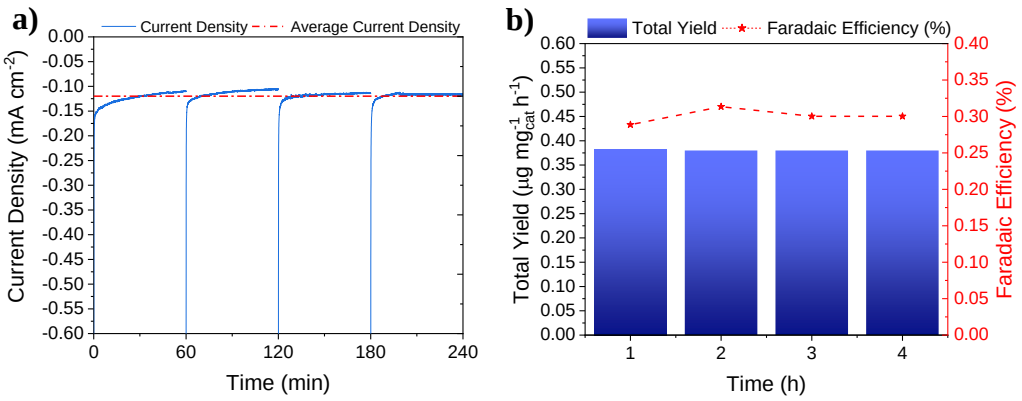

***Figure 3.39** - rGO-Mn_xO_y a) current density and b) total yield of ammonia for 4h test in EC2*

Figure 3.40a and **3.40b** show the total cumulative yields detected fin absorber (by IC), cathode and anode (by salicylate method). As shown in **Figure 3.40a**, ammonia is distributed about 20% in the gas phase, 46% in the cathode electrolyte and 33% in the anode electrolyte, for a total yield of 1.78 µg mg_{cat}^{-1}. While in **Figure 3.40b** the distribution follows the pattern absorber 17%, cathode 58% and anode 24%, with a cumulative total of 1.52 µg mg_{cat}^{-1}. **Figure 3.40c**, on the other hand, shows a direct comparison between Mn_xO_y and Mn_xO_y-Fe. It can be seen that the productivity of the Fe-doped catalyst is 1.17 times higher the electrode without Fe.

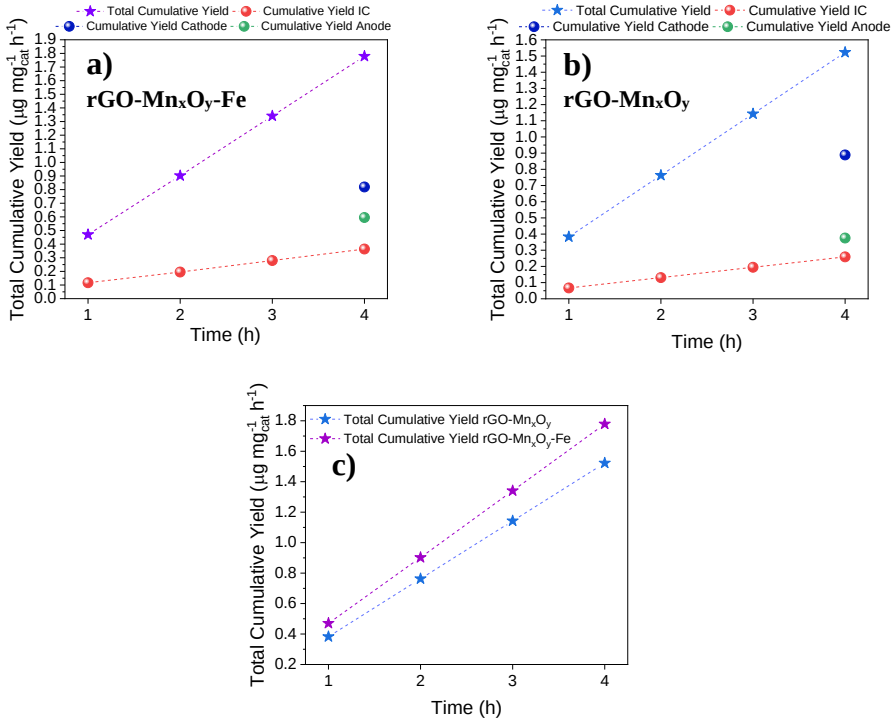

Figure 3.40 *– Total cumulative yield of ammonia for a) rGO-Mn_xO_y-Fe, b) rGO-Mn_xO_y , and c) comparative yield of both*

3.16.5 | Cell comparison

In **table 3.5** and in **table 3.6**, a direct comparison between the two configurations EC 1 and EC 2 for Mn_xO_y-Fe and Mn_xO_y is given, respectively. The same working potential was applied for all the reported tests. It can be seen that in the case in both cases the efficiency and yield values are higher in the gas-phase approach configuration (EC 1).

Cell parameters (rGO-Mn_xO_y-Fe)	**EC1**	**EC2**
Working Potential (V_{WE-RE} vs RHE)	-0.6	-0.6
Cell Potential ($\|V\|_{WE-CE}$)	2.8	2.6
Average current density ($\mu A\ cm^{-2}$)	-136.6 ± -6.1**	-284.7*
Counter Electrode	Pt	GDL 39BB
Area Catalyst (cm^2)	1.7	5.7
Faradaic Efficiency (%)	0.45 ± 0.04**	0.15 ± 0.01*
Yield ($\mu g\ mg_{cat}^{-1}\ h^{-1}$)	0.537 ± 0.030**	0.451 ± 0.019*

(*) Normalized values for the 4 h of testing
(**) Average values between the two tests performed (test and test' respectively)

Table 3.5 *– Cell parameters comparison between EC1 and EC2 for rGO- Mn_xO_y-Fe*

Cell parameters (rGO-Mn_xO_y)	**EC1**	**EC2**
Working Potential (V_{WE-RE})	-0.6	-0.6
Cell Potential ($\|V\|_{WE-CE}$)	2.8V	2.8V
Average current density ($\mu A\ cm^{-2}$)	-26.9	-119.9*
Counter Electrode	Pt	GDL 39BB
Area Catalyst (cm^2)	1.7	5.7
Faradaic Efficiency (%)	2.12	0.30 ± 0.01*
Yield ($\mu g\ mg_{cat}^{-1}\ h^{-1}$)	0.407	0.385 ± 0.019*

(*) – Normalized values for the 4 h of testing

Table 3.6 *- Cell parameters comparison between EC 1 and EC 2 for rGO- Mn_xO_y-Fe*

Upon direct comparison between the two configurations, EC 1 (gas-phase) demonstrates superior performance compared to EC 2 (liquid-phase), as shown in **Table 3.5** and **3.6**. The presence of the cathodic electrolyte in EC 2 promotes the competitive reaction of hydrogen (HER). Additionally, the inclusion of the MEA facilitates nitrogen from the gas phase to permeate through the GDL, react on the surface with the protons coming from the membrane, and subsequently undergo desorption of the produced ammonia (as outlined in the mechanism described in section 1.5.2.1).

3.16.6 | Electrochemical Impedance Spectroscopy (EIS) and Equivalent Electrochemical Circuits (EEC)

Electrochemical impedance spectroscopy (EIS) was adopted to investigate more in depth the electrochemical behaviour of rGO-Mn_xO_y and rGO-Mn_xO_y-Fe samples. The experiments were carried out in the range of 0.1 Hz – 100 kHz using an AUTOLAB PGSTAT204 instrument (by Metrohm) in a custom two-compartment cell (*Electrochemical Cell 1*) filled with 0.1M Na_2SO_4 aqueous solution. The working electrode (WE) has an exposed area of 1.7 cm^2 with catalyst deposited by spray-coating technique. A platinum wire was used as the counter electrode (CE), and an Ag/AgCl 3.0M KCl as the reference electrode (RE). No electrolyte circulation was used at the moment of the analysis to avoid any noise on the signal. Four potentials were investigated: -0.6, -0.7, -0.8 and -0.9 V vs RHE.

In **Figure 3.41a**, an illustrative Nyquist plot is presented, obtained at -0.6 V versus RHE, wherein distinct regions of interest are delineated through the use of varied colour highlights. In **Figure 3.41b** instead we have the Equivalent Electrochemical Circuit (EEC) with the respective parts indicated.

The R_s (shown in red – **Figure 3.41a, -b**), as already previously mentioned, is the series resistance, while the highlighted in orange is the inductive loop. The inductive loop can be attributed to atomic-scale surface inhomogeneities such as grain boundaries, crystal faces on a polycrystalline electrode, or other variations in surface properties. It is probably an instrumental artifact due either to cabling in the cell or to the cell design itself, or badly shielded cable[31,48,49,50]. In green and purple there are the kinetic and porosity factors, respectively. Finally, in light blue the diffusive phenomenon due to the resistance to mass transfer due to the presence of the nafion membrane in the Membrane Electrode Assembly (MEA).

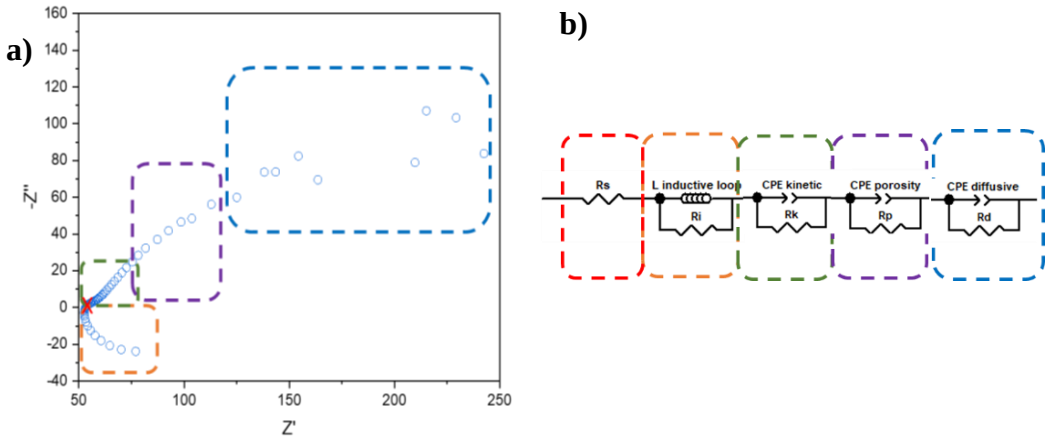

Figure 3.41 *– Example of a) Nyquist plot and b) Equivalent Electrochemical Circuit (EEC) for -0.6 V vs RHE rGO-Mn_xO_y-Fe*

Figure 3.42 shows the Nyquist plot of the same catalyst (rGO-Mn_xO_y-Fe) but at the open circuit voltage (OCP). Shows the same profiles as the previous one, but with the differentiation for the diffusive phenomenon. Comparing the diffusive phenomenon of **Figure 3.41a** at potential -0.6 V with that of **Figure 3.42a** recorded at the OCP, we see a difference of a semicircle in the former case, while in the latter a straight 45° line.

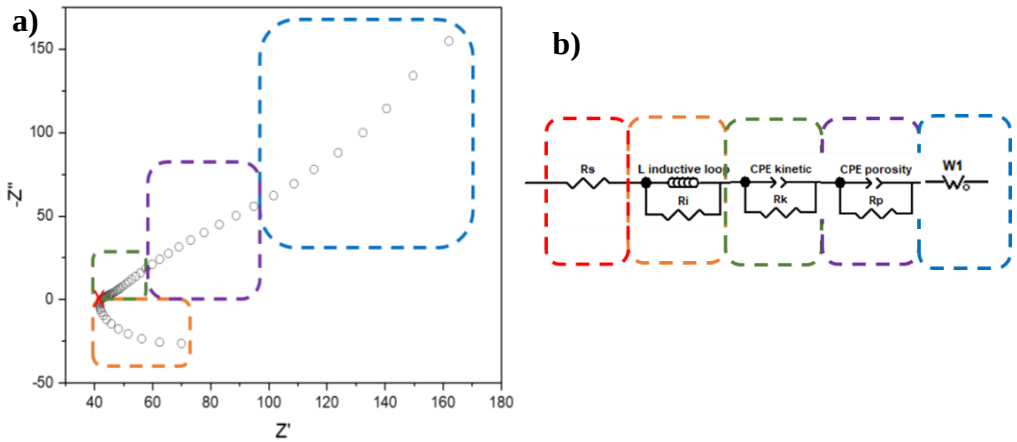

Figure 3.42 *– Example of a) Nyquist plot and b) Equivalent Electrochemical Circuit (EEC) for OCP rGO-Mn_xO_y-Fe*

The Warburg phenomenon (indicated as W1 in **Figure 3.42b**) is associated with the electrode's response at very low potentials or under low-current conditions, where the transport of reagents to the electrode surface becomes limiting. This occurs when the electrode reaction involves chemical species that need to diffuse through the solution volume to reach the electrode. The Warburg coefficient is a measure of the diffusion capacity of chemical species through the electrolyte toward the electrode. The Law of Warburg describes the dependence of electrochemical current on time or frequency, displaying a linear relationship between the current and the square root of the electrode's rotation speed or the square root of the frequency.

Every applied potential has the same behaviour of transmissive finite-length diffusion (represented by red dots in **Figure 3.43** in the case of -0.6 V) as the active species are exchanged between surface and solution (discharge on the electrode). Moreover, EIS at OCP has the same behaviour of reflective finite-length diffusion (black dots in **Figure 3.43**). The charged species are diffusing (Warburg-zone) but after the saturation of active sites, no more sites are available for electron transfer (capacitive saturation) i.e. due to lacks of redox molecules [31,51].

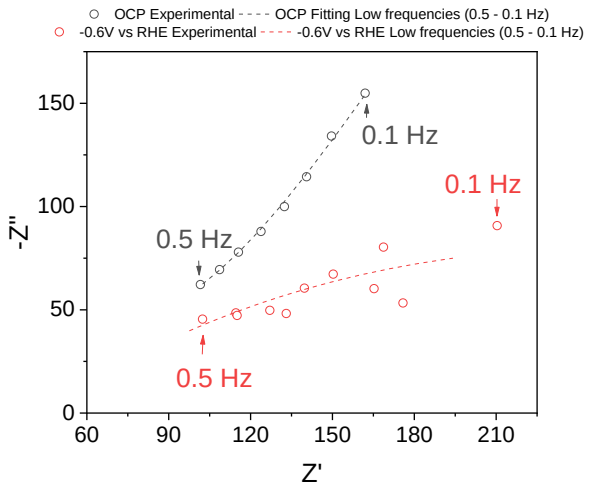

Figure 3.43 *- Nyquist rGO-Mn_xO_y-Fe OCP vs -0.6V vs RHE comparison (low frequencies)*

As previously mentioned, the inductive loop, coming from an electronic/electrical disturbance was not considered for fitting purposes. Thus, the high frequencies relative to the inductive loop, were cut off (from 100 to 2.5 kHz). The parameters of the remaining equivalent circuits are shown in **Table 3.6**, and **3.7**, where rGO-Mn_xO_y-Fe, and rGO-Mn_xO_y are discussed, respectively.

In **Figure 3.44a** and **3.44b**, the Nyquist and Bode plot for rGO-Mn_xO_y-Fe are shown, respectively. From 2.5 kHz up to 0.5 Hz the porosity and kinetic factors (i.e. polarization and charge transfer at the interphase) are present. At lower frequencies (from 0.5 to 0.1 Hz) it can be seen as anticipated in **Figure 3.43**, how the diffusive phenomenon is different between OCP and applied potentials.

As anticipated in the explanation of the electronic component Warburg, when the voltage is as low as at OCP, the Warburg effect occurs. This is also confirmed by the presence in the 45° Bode plot at low frequency (black line in **Figure 3.44b**). In this case, where the phenomena are multiple, it is hard to extrapolate the maximum frequencies from the Bode plot, and the Nyquist is also difficult to interpret and visualize.

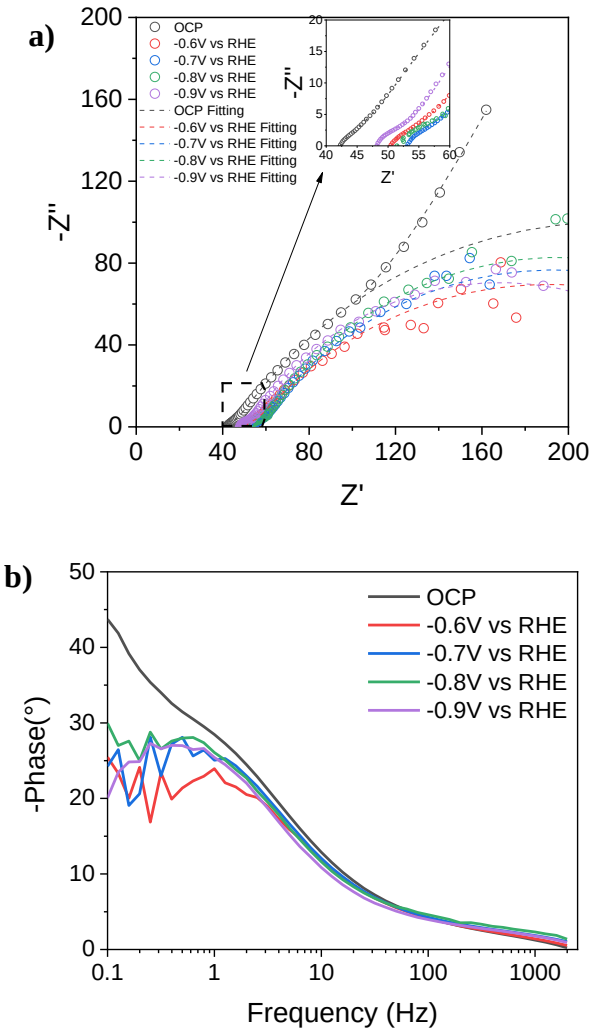

Figure 3.44 *– Nyquist and Bode plot for rGO-Mn_xO_y-Fe*

In **table 3.7**, the parameters of the EEC of the modelled electronic components are shown. It can be seen that the tail of the EIS at low frequencies is disturbed, due to ionic/mass transport phenomena through the membrane. Therefore, it is not possible to find a correlation with those resistances (R_d). The resistance related to the mass transfer (R_p) increases when the potential goes from -0.6 to -0.8V vs RHE. While looking at the resistance related to charge transfer between GDL/ deposited catalyst (R_k), the phenomenon has a small resistance, so it is overall difficult to model. Thus, distinguishing the contribution of porosity and kinetic is

difficult. Also the R_d is disturbed and the trend in **Table 3.7** does not follow a linear pattern.

Potential (V vs RHE)	R_s (Ω)	CPE-T (kinetic)	CPE-P (kinetic)	R_k (kinetic, Ω)	CPE-T (porosity)	CPE-P (porosity)	R_p (porosity, Ω)	*CPE-T (Diffusive)*	*CPE-P (Diffusive)*	*Rd (Diffusive, Ω)*	*W0-R*	*W0-T*	*W0-P*
OCP	42.25	0.00500	0.600	4.00	0.00500	0.662	390.00	-	-	-	258.4	3.021	0.35711
-0.6	50.45	0.00150	0.650	4.00	0.003446	0.696	153.00	0.00486	0.476	405.40	-	-	-
-0.7	53.10	0.00047	0.800	4.00	0.00341	0.679	254.00	0.00366	0.713	292.20	-	-	-
-0.8	51.50	0.00077	0.690	7.50	0.00418	0.641	362.70	0.00480	0.473	803.00	-	-	-
-0.9	48.23	0.00140	0.700	5.00	0.00448	0.670	244.80	0.00467	0.637	272.90	-	-	-

(-) not possible to model

Table 3.7 *– Electrochemical circuit value for rGO- Mn_xO_y-Fe*

On the other hand, analysing the EEC for rGO-Mn_xO_y, the R_k values are lower than those with Fe while the R_p values are almost similar. Also in this case, the EIS spectrum reported in **Figure 3.45** shows the same behaviour as shown in **Figure 3.44**. The Nyquist profile at -0.6 and -0.7 V vs RHE shows a disturbed tail in the EIS, difficult to model. The OCP also in this case shows the Warburg effect.

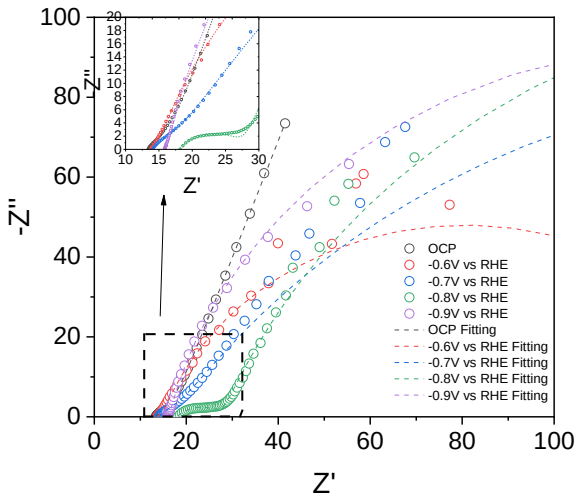

Figure 3.45 *– Electrochemical circuit value for rGO-Mn_xO_y*

Potential (V vs RHE)	Rs (Ω)	CPE-T (kinetic)	CPE-P (kinetic)	Rk (kinetic, Ω)	CPE-T (porosity)	CPE-P (porosity)	Rp (porosity, Ω)	*CPE-T (Diffusive)*	*CPE-P (Diffusive)*	*Rd (Diffusive, Ω)*	*W0-R*	*W0-T*	*W0-P*
OCP	13.36	0.01500	0.647	12.57	-	-	-	-	-	-	12.96	0.16784	0.39677
-0.6	13.70	0.01000	0.800	1.00	0.01300	0.800	132.00	-	-	-	-	-	-
-0.7	14.10	0.01021	0.630	3.40	0.01600	0.650	250.00	-	-	-	-	-	-
-0.8	18.00	0.00090	0.550	10.00	0.01600	0.780	300.00	0.01684	0.782	427.10	-	-	-
-0.9	15.86	0.01500	0.910	0.40	0.01800	0.864	230.00	0.01810	0.893	187.60	-	-	-

(-) not possible to model

Table 3.8 *– Electrochemical circuit value for rGO-Mn_xO_y*

Differences of the series resistances are evident in **Table 3.7** and **Table 3.8**, for the two catalysts resulting in a R_s of 49.11 ± 3.09 and 15.00 ± 1.54 Ω for rGO-Mn_xO_y-Fe and rGO-Mn_xO_y, respectively. We believe that this difference is due to the presence of MEA, which depending on the preparation and mode of hot pressing, varying the catalyst/membrane/solution interface. However, it is difficult to correlate exactly the individual phenomena occurring in complex and dynamic systems such as these.

3.16.7 | Double layer capacitance

Figure 3.47 shows the different CVs at different scan speeds for different materials deposited on GDL. From these CVs, the C_{dl} and C_p were calculated as shown in **section 3.9.1**.

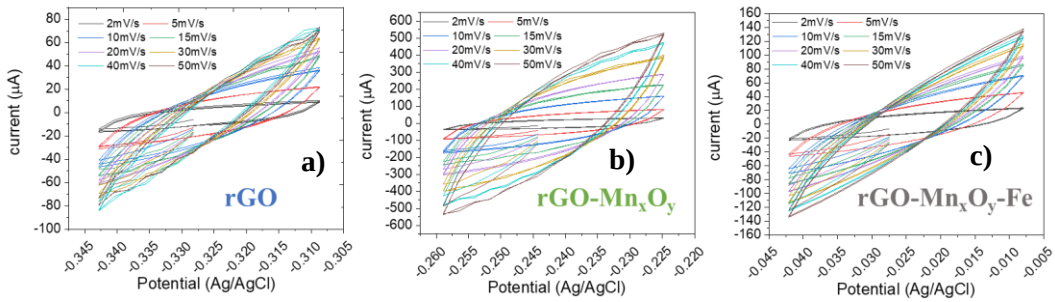

Figure 3.47 *– Different CVs scan-rate for a) rGO b) rGO-Mn_xO_y , and c) rGO-Mn_xO_y-Fe*

From **Figure 3.48**, it can be seen that two trends exist at two different ranges of scan rate, probably depending on diffusion phenomena.

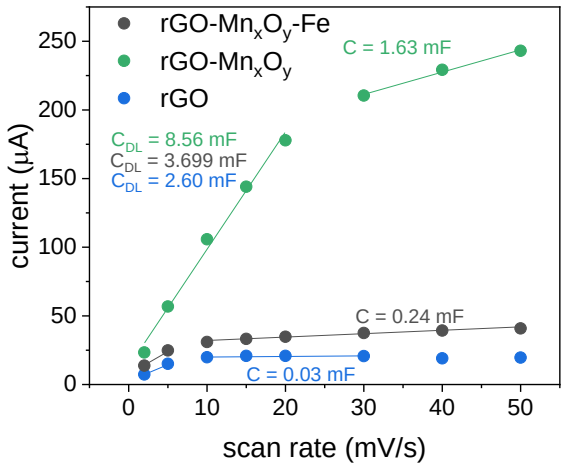

Figure 3.48 *– Double layer capacitance calculation for different catalysts under exam.*

Table 3.9, shows the calculated values of double-layer capacitance, specific capacitance, AESA and ECSA calculated by the methods described in **section 3.9.1**. It can be seen that rGO-Mn_xO_y has a higher double-layer capacitance (C_{dl}) value than both rGO-Mn_xO_y-Fe and rGO (8.6, 3.7, and 2.6 mF/cm^2, respectively). The specific capacitance (C_p) value also follows the trend rGO-Mn_xO_y > rGO-Mn_xO_y-Fe > rGO (12.98, 6.305, and 0.593 F g^{-1}, respectively). The value for rGO-MnxOy and rGO are similar to the data reported from *Huang et al.*[52] and also in according with carbonious value of C_{DL} found in literature[38].

Sample	C_{dl} (mF cm^{-2})	C_p (F g^{-1})	AESA (m^2 g^{-1})	ECSA (cm^2)
rGO	2.6	0.593	0.0319	0.1067
rGO-Mn_xO_y	8.6	12.98	0.2274	0.7597
rGO-Mn_xO_y-Fe	3.7	6.305	0.2898	0.9689

Table 3.9 *– C_{dl}, C_p, AESA, and ECSA calculated for the different catalysts under exam*

This means that the catalyst not doped with Fe has a greater tendency to accumulate charges on the surface of the electric double layer and on the surface

of the catalyst due to the presence of the manganese oxides. Doping with iron acts as a catalytic spot at the electrode/membrane interface.

3.17 | Conclusions

In this chapter, a wide range of potentials (from -0.1 to -0.8 V vs RHE) was investigated, by evaluating the behaviour of Nitrogen Reduction Reaction (NRR), in relation to the competitive Hydrogen Evolution Reaction (HER). Notably, the investigation revealed the prevalence of NRR at potentials approximately within the range from -0.2 to -0.4 V vs RHE, exhibiting enhanced Faradaic efficiency (FE) and productivity. Conversely, the dominance of hydrogen evolution reaction emerged notably at applied potentials exceeding -0.5 V vs RHE.

In the case of catalysts based on carbon nanotubes (CNTs), they show similar activity, such as Fe_2O_3 in comparison to Ru and Ru-Fe co-doped variants. While alumina-based catalysts showcased distinctive trends. Specifically, doping with Ru provides higher catalytic performance compared to Fe_2O_3, while the substitution of Fe with Ru in a co-doped configuration yielded the highest observed catalytic performance of 1.047 $\mu g\ mg_{cat}^{-1}\ h^{-1}$.

It is evident in this case that, partially replacing an expensive metal such as ruthenium with a less expensive one (Iron) brings benefits, although many aspects of NRR need to be studied to make significant progress in this field (summary **Table 3.4**).

Moreover, a direct comparison between two cell setups (EC1 and EC2), shows that the gas phase (EC1) promotes ammonia formation due to the presence of the Membrane Electrode Assembly which limits the HER. In contrast MEA is more fragile in terms of mechanical stability.

3.18 | References

[1] Yu, L., Pan, X., Cao, X., Hu, P., & Bao, X. (2011). Oxygen reduction reaction mechanism on nitrogen-doped graphene: A density functional theory study. *Journal of Catalysis, 282*(1), 183–190.

[2] Chen, S., Perathoner, S., Ampelli, C., Mebrahtu, C., Su, D., & Centi, G. (2017). Electrocatalytic synthesis of ammonia at room temperature and atmospheric pressure from water and nitrogen on a carbon-nanotube-based electrocatalyst. *Angewandte Chemie International Edition, 56*(10), 2699–2703.

[3] Cui, X., Tang, C., Liu, X., Wang, C., Ma, W., & Zhang, Q. (2018). Highly selective electrochemical reduction of dinitrogen to ammonia at ambient temperature and pressure over iron oxide catalysts. *Chemistry – A European Journal, 24*(69), 18494–18501.

[4] Shi, M., Bao, D., Li, S., Wulan, B., Yan, J., & Jiang, Q. (2018). Anchoring PDCU amorphous Nanocluster on graphene for electrochemical reduction of N_2 to NH_3 under ambient conditions in aqueous solution. *Advanced Energy Materials, 8*(21).

[5] Geng, Z., Liu, Y., Kong, X., Li, P., Li, K., Liu, Z., Du, J., Shu, M., Si, R., & Zeng, J. (2018). Achieving a record-high yield rate of 120.9 μg mg_{cat}^{-1} h^{-1} for N_2 electrochemical reduction over Ru single-atom catalysts. *Advanced Materials, 30*(40).

[6] Agour, A. M., Elkersh, E., Khedr, G. E., El-Aqapa, H. G., & Allam, N. K. (2023). Fe-single-atom catalysts on nitrogen-doped carbon nanosheets for electrochemical conversion of nitrogen to ammonia. *ACS Applied Nano Materials, 6*(17), 15980–15989.

[7] Wei, Y., Yu, Y., Chen, J., Wei, M., Huang, Y., Zhou, X., & Liu, W. (2023). Fabrication of high surface area Fe/Fe_3O_4 with enhanced performance for electrocatalytic nitrogen reduction reaction. *Chemistry – A European Journal, 29*(71).

[8] He, Z., Cui, X., Lei, G., Liu, Z., Yang, X., Liu, Y., Wan, J., & Ma, F. (2023). Coral-like Fe-doped MoO_2/C heterostructures with rich oxygen vacancies for efficient electrocatalytic N_2 reduction. *Dalton Transactions, 52*(9), 2887–2897.

[9] Sun, W., Sahin, N. E., Sun, D., Wu, X., Munoz, C., Thakare, J., Aulich, T., Zhang, J., Hou, X., Oncel, N., Pierce, D., & Zhao, J. X. (2022). One-pot synthesis of ruthenium-based nanocatalyst using reduced graphene oxide as matrix for electrochemical synthesis of ammonia. *ACS Applied Materials & Interfaces*, *15*(1), 1115–1128.

[10] Weidner, E., Dubadi, R., Samojeden, B., Piasecki, A., Jesionowski, T., Jaroniec, M., & Ciesielczyk, F. (2022). Mechanochemical synthesis of alumina-based catalysts enriched with vanadia and Lanthana for selective catalytic reduction of nitrogen oxides. *Scientific Reports*, *12*(1).

[11] Jiang, G., Peng, M., Hu, L., Ouyang, J., Lv, X., Yang, Z., Liang, X., Liu, Y., & Liu, H. (2022). Electron-deficient $Cu^{\delta+}$ stabilized by interfacial Cu–O-Al bonding for accelerating electrocatalytic nitrate conversion. *Chemical Engineering Journal*, *435*, 134853.

[12] Bae, W. B., Kim, D. Y., Byun, S. W., Lee, S. J., Kuk, S. K., Kwon, H. J., Lee, H. C., Hazlett, M. J., Liu, C., Kim, Y. J., Kim, M., & Kang, S. B. (2023). Direct no decomposition over Rh-supported catalysts for exhaust emission control. *Chemical Engineering Journal*, *475*, 146005.

[13] Khatri, P., & Bhatia, D. (2023). Influence of catalyst composition on NO_x storage and reduction characteristics of Ag catalyst supported on MgO-doped alumina. *Chemical Engineering Research and Design*, *197*, 476–495.

[14] Lin, B., Heng, L., Fang, B., Yin, H., Ni, J., Wang, X., Lin, J., & Jiang, L. (2019). Ammonia synthesis activity of alumina-supported ruthenium catalyst enhanced by alumina phase transformation. *ACS Catalysis*, *9*(3), 1635–1644.

[15] Tavella, F., Giusi, D., & Ampelli, C. (2022). Nitrogen reduction reaction to ammonia at ambient conditions: A short review analysis of the critical factors limiting electrocatalytic performance. *Current Opinion in Green and Sustainable Chemistry*, *35*, 100604.

[16] Xiong, G., He, P., Lyu, Z., Chen, T., Huang, B., Chen, L., & Fisher, T. S. (2018). Bioinspired leaves-on-branchlet hybrid carbon nanostructure for supercapacitors. *Nature Communications*, *9*(1).

[17] *DL supplementary information - The Royal Society of Chemistry*. www.rcs.org. (2019). https://www.rsc.org/suppdata/c9/dt/c9dt00520j/c9dt00520j1.pdf

[18] Giner-Sanz, J. J., Leverick, G. M., Pérez-Herranz, V., & Shao-Horn, Y. (2020). Salicylate method for ammonia quantification in nitrogen electroreduction experiments: The Correction of Iron III interference. *Journal of The Electrochemical Society, 167*(13), 134519.

[19] Greenlee, L. F., Renner, J. N., & Foster, S. L. (2018). The use of controls for consistent and accurate measurements of electrocatalytic ammonia synthesis from dinitrogen. *ACS Catalysis*, *8*(9), 7820–7827.

[20] Zhang, X., Serincan, M. F., Pasaogullari, U., & Molter, T. (2009). Contamination of membrane-electrode assemblies by ammonia in polymer electrolyte fuel cells. *ECS Transactions*, *25*(1), 1565–1574.

[21] Licht, S., Cui, B., Wang, B., Li, F.-F., Lau, J., & Liu, S. (2020). Retraction. *Science*, *369*(6505).

[22] *Use of transmission lines for electrochemical impedance spectroscopy*. Gamry Instruments | Market Leader in the Support of Electrochemical Research. (n.d.). https://www.gamry.com/application-notes/EIS/use-of-transmission-lines-for-eis/

[23] Barsoukov, E., & Macdonald, J. R. (2005). *Impedance spectroscopy theory, experiment, and applications*. Wiley-Interscience.

[24] Giner-Sanz, J. J., Ortega, E. M., García-Gabaldón, M., & Pérez-Herranz, V. (2018). Theoretical determination of the stabilization time in galvanostatic EIS measurements: The Simplified Randles Cell. *Journal of The Electrochemical Society*, *165*(13).

[25] Lazanas, A. Ch., & Prodromidis, M. I. (2023). Electrochemical impedance spectroscopy─a tutorial. *ACS Measurement Science Au*, *3*(3), 162–193.

[26] Ariyoshi, K., Siroma, Z., Mineshige, A., Takeno, M., Fukutsuka, T., Abe, T., & Uchida, S. (2022). Electrochemical impedance spectroscopy part 1: Fundamentals. *Electrochemistry*, *90*(10), 102007–102007.

[27] Magar, H. S., Hassan, R. Y., & Mulchandani, A. (2021). Electrochemical impedance spectroscopy (EIS): Principles, construction, and Biosensing Applications. *Sensors*, *21*(19), 6578.

[28] Lasia, A. (2022). The origin of the constant phase element. *The Journal of Physical Chemistry Letters, 13*(2), 580–589.

[29] Giusi, D., Miceli, M., Genovese, C., Centi, G., Perathoner, S., & Ampelli, C. (2022). In situ electrochemical characterization of Cu_xO-based gas-diffusion electrodes (GDEs) for CO_2 electrocatalytic reduction in presence and absence of liquid electrolyte and relationship with C_{2+} Products Formation. *Applied Catalysis B: Environmental, 318,* 121845.

[30] Keiser, H., Beccu, K. D., & Gutjahr, M. A. (1976). Abschätzung der Porenstruktur Poröser Elektroden aus Impedanzmessungen. *Electrochimica Acta, 21*(8), 539–543.

[31] Lasia, A. (2020). Dispersion of Impedances at Solid Electrodes. In *Electrochemical impedance spectroscopy and its applications*. essay, Springer.

[32] Diard, J.-P., Le Gorrec, B., & Montella, C. (2020, July 7). *(PDF) Handbook of Electrochemical Impedance Spectroscopy. DIFFUSION IMPEDANCES - researchgate*. Researchgate. https://www.researchgate.net/publication/342833389_Handbook_of_Electrochemical_Impedance_Spectroscopy_DIFFUSION_IMPEDANCES

[33] Mussini, P. R. (n.d.). *Chimica Elettroanalitica Avanzata, Modulo A*. sites.unimi. https://sites.unimi.it/ECEA/0910Impedenza.pdf

[34] Zhang, X., He, Y., Zhu, B., Wan, X., Hua, S., & Tang, H. (2023). A bottom-up method to construct Ru-doped FeP nanosheets on foam iron with ultra-high activity for hydrogen evolution reaction. *International Journal of Hydrogen Energy, 48*(12), 4686–4693.

[35] Salar-García, M. J., Walter, X. A., Gurauskis, J., de Ramón Fernández, A., & Ieropoulos, I. (2021). Effect of iron oxide content and microstructural porosity on the performance of ceramic membranes as microbial fuel cell separators. Electrochimica Acta, 367, 137385.

[36] Song, Y., Tian, T., Li, C., Zeng, X., Zhang, S., Chen, L., Yang, Z., Ji, Q., Zhao, X., & Chen, F. (2023). Controlled fabrication of Fe_3N@NG composites as superior oxygen evolution reaction electrocatalysts. *Carbon Resources Conversion*, 100207.

[37] Anantharaj, S., Sugime, H., & Noda, S. (2021). Why shouldn't double-layer capacitance (CDL) be always trusted to justify Faradaic electrocatalytic activity differences? *Journal of Electroanalytical Chemistry, 903*, 115842.

[38] Kurzweil, P. (2009). Capacitors | electrochemical double-layer capacitors: Carbon materials. *Encyclopedia of Electrochemical Power Sources*, 634–648.

[39] Liu, M., Zhang, S., Chen, M., Zhou, S., & Wu, L. (2023). An isolated bimetallic Fe–Ru single-atom catalyst for efficient electrochemical nitrogen reduction. *Journal of Materials Chemistry A, 11*(27), 14900–14910.

[40] Chen, S., Perathoner, S., Ampelli, C., Wei, H., Abate, S., Zhang, B., & Centi, G. (2020). Enhanced performance in the direct electrocatalytic synthesis of ammonia from N_2 and H_2O by an in-situ electrochemical activation of CNT-supported iron oxide nanoparticles. *Journal of Energy Chemistry, 49*, 22–32.

[41] Sahoo, S. K., Agarwal, K., Singh, A. K., Polke, B. G., & Raha, K. C. , Characterization of γ- and α-Fe_2O_3 nanopowders synthesized by emulsion precipitation-calcination route and rheological behaviour of α-Fe_2O_3. *International Journal of Engineering, Science and Technology* (2011), *2*(8).

[42] Einsle, O. (2014). Nitrogenase FeMo cofactor: An atomic structure in three simple steps. *JBIC Journal of Biological Inorganic Chemistry, 19*(6), 737–745.

[43] Liu, H.-M., Han, S.-H., Zhao, Y., Zhu, Y.-Y., Tian, X.-L., Zeng, J.-H., Jiang, J.-X., Xia, B. Y., & Chen, Y. (2018). Surfactant-free atomically ultrathin rhodium nanosheet nanoassemblies for efficient nitrogen electroreduction. *Journal of Materials Chemistry A, 6*(7), 3211–3217.

[44] Li, S., Bao, D., Shi, M., Wulan, B., Yan, J., & Jiang, Q. (2017). Amorphizing of au nanoparticles by CeO_x–rGO hybrid support towards highly efficient electrocatalyst for N_2 reduction under ambient conditions. *Advanced Materials, 29*(33).

[45] Ren, X., Cui, G., Chen, L., Xie, F., Wei, Q., Tian, Z., & Sun, X. (2018). Electrochemical N2fixation to NH3 under ambient conditions: Mo_2N nanorod as a highly efficient and selective catalyst. *Chemical Communications, 54*(61), 8474–8477.

[46] Han, J., Liu, Z., Ma, Y., Cui, G., Xie, F., Wang, F., Wu, Y., Gao, S., Xu, Y., & Sun, X. (2018). Ambient N_2 fixation to NH_3 at ambient conditions: Using NB2O5 nanofiber as a high-performance electrocatalyst. *Nano Energy*, *52*, 264–270.

[47] Wu, X., Xia, L., Wang, Y., Lu, W., Liu, Q., Shi, X., & Sun, X. (2018). Mn3O4 nanocube: An efficient electrocatalyst toward artificial N_2 fixation to NH_3. *Small*, *14*(48).

[48] Martin, M. H., & Lasia, A. (2011). Influence of experimental factors on the constant phase element behavior of Pt electrodes. *Electrochimica Acta*, *56*(23), 8058–8068.

[49] Pajkossy, T. (1994). Impedance of rough capacitive electrodes. *Journal of Electroanalytical Chemistry*, *364*(1–2), 111–125.

[50] Kerner, Z., & Pajkossy, T. (1998). Impedance of rough capacitive electrodes: The role of surface disorder. *Journal of Electroanalytical Chemistry*, *448*(1), 139–142.

[51] Birry, L., & Lasia, A. (2006). Effect of crystal violet on the kinetics of H sorption into PD. *Electrochimica Acta*, *51*(16), 3356–3364.

[52] Huang, H., Gong, F., Wang, Y., Wang, H., Wu, X., Lu, W., Zhao, R., Chen, H., Shi, X., Asiri, A. M., Li, T., Liu, Q., & Sun, X. (2019). Mn_3O_4 nanoparticles@reduced graphene oxide composite: An efficient electrocatalyst for artificial N_2 fixation to NH_3 at ambient conditions. *Nano Research*, *12*(5), 1093–1098.

4. | Plasma-assisted catalysis

4.1. | Preface

Plasma processes have a variety of applications and can be artificially created by passing a high-voltage electric current through a gas. Among the most popular uses are surface cleaning[1], material slicing[1], coating[1], ozone production and reactive oxygen species[2], cleaning air from Volatile Organic Compounds (VOCs) pollutants[3], and potential use in the field of medicine[1]. Other processes that have been investigated but are not yet commercially available, as they are still in the developmental phase, include the generation of NO_x from air (N_2 approximately 80% and O_2 approximately 20%) and the conversion of N_2 and H_2 into NH_3 using plasma reactors. Numerous studies have been published in the scientific literature to enhance the energy efficiency of the system (through catalyst research) and to improve reactor design, aiming to gain a deeper understanding of the mechanism and fully comprehend the synergistic effect between plasma and catalysis. This chapter will present experiments on nitrogen fixation in a non-thermal plasma way. The study was conducted at Technical University of Eindhoven (TU/e) under the supervision of Prof. Fausto Gallucci and Dr. Sirui Li.

4.2. | State-of-the-art

Ammonia, a chemical abundantly produced on a large scale, requires molecular nitrogen and hydrogen as feed gases. The possibility of producing ammonia has also been seen by providing molecular nitrogen and water in a vapor state instead of H_2. However, the use of an oxygenated compound (H_2O) in a plasma environment, generates a mixture of products [4,5,6] (NO, NO_2^-, NO_3^-, NH_4^+, N_2O_4) independently from the plasma reactor used, due to the lower selectivity and high energy transmitted of plasma. *Xie et al.*[7] investigated ammonia production from

N_2 and water in gas phase, in a Dielectric Barrier Discharge (DBD) reactor, catalysed by Ru/Al_2O_3, reporting the best performances for N_2 + water (0.14%v/v), $N_2 + H_2$ (40%v/v), and N_2 + water (0.14%v/v) + H_2 (40%v/v) with an ammonia production of 18, 640 and 680 mg_{NH3} kW^{-1} h^{-1}, respectively. A new recent technology, which will be discussed in the technical-economical part (Chapter 5), is a reactor "all-in-one" reported by *Sharma et al.*[8], where a part of the reactor, a solid oxide electrolyser (SOE, $BaCe_{0.2}Zr_{0.7}Y_{0.1}O_{3-\delta}$ ceramic material) separates H_2 from vapour H_2O, and a Radio Frequency plasma is generated under Nitrogen feed gas. The best performance in terms of produced ammonia is 14.5 nmol s^{-1} cm^{-2} with a 66% Faradaic efficiency at 6.36 mA cm^{-2}. *Gomez-Ramirez et al.*[9] used a planar DBD packed with ferroelectric material with two different discharge gap tests of 3 and 10 mm. Feeding N_2 and H_2, they obtained an ammonia production of 0.45 and 0.55 g_{NH3} kW^{-1} h^{-1} (and a conversion of 2.7 and 1.8%), respectively. This type of reactor[10] (planar DBD or coaxial) offers great flexibility, *Peng et al.*[11] reported an ammonia production of 45 ppm and an energy efficiency of 1.7 g kW^{-1} h^{-1} over a Ruthenium-based mesoporous material (*Mobil Composition of Matter-41* - MCM-41), Ru/Si-MCM-41 catalyst, with a very high Specific Energy Input (SEI) of 124 kJ L^{-1}. *Zhu et al.*[12] carried out experiments on different types of commercial γ-Al_2O_3 (acidic, neutral, and alkaline) in a DBD reactor, without metal doping, with the highest concentration produced with the alkaline γ-Al_2O_3 (1565.5 ppm, SEI of 14.55 kJ L^{-1} and an energy consumption of 6.58 g kW^{-1} h^{-1}). In literature, the effect of promoters was also investigated, as explained by *Kim et al.*[13] that measured the ammonia produced with different promoters in the Ruthenium – γ-Al_2O_3 structure, and obtained the best performance in the ratio N_2:H_2 of 4:1 , operating in a DBD reactor temperature under 250°C. The role of metal promoters in the improvement yield was in the order of Mg > K > Cs > no promoter. It is also important to understand the effect of the support in ammonia synthesis. Carbon nanotubes (CNTs) can support metals, and provide high surface area and pore dimension, as

described by *Peng et al.*[14]. Ruthenium catalysts coupled with CNTs or MCM-41 supports were tested in a non-thermal, low-temperature, atmospheric-pressure plasma in the presence of metallic cesium or magnesium (II) oxide, as promoters. At a voltage of 6 kV, a frequency of 10 kHz, and a feed gas ratio of 3:1 (N_2:H_2), the catalyst with CNTs achieved the best results, with 2.3 $g_{NH3}\,kW^{-1}\,h^{-1}$ resulting from all optimizations.

4.3. | Aim of chapter

Using appropriate metals (Fe, Ru, or a mix of both) selected from the vertex of the volcano plot (**section 1.5.2**) and deposited onto two chemically and physically different media (Alumina and CNTs), will be compared in this chapter. The synthesis of these catalysts has already been described in chapter 2. For this study, they were packed in a coaxial DBD reactor, having a discharge gap of 2 mm and then tested in combined plasma-catalysis process for the production of ammonia. The most important operational parameters such as feed gas ratio (N_2:H_2, from 3:1 to 1:3) and flow rate (from 120 to 360 mL min^{-1}) were investigated while maintaining a constant power and AC frequency. A plasma discharge study and its interaction with surrounding materials was also conducted with a high-speed camera.

4.4. | Dielectric Barrier Discharge (DBD) reactor

The simplest DBD reactor is characterized by two parallel electrodes (high voltage and ground electrode) with an insulating material in the plasma discharge path. Typically, ceramics and quartz are used as reactors, with a discharge path of 0.1-10 mm and because of the capacitive behaviour of the discharge a high voltage (1-100 kV) is required (alternating with frequency 1-40 kHz, occasionally with nanosecond pulses current)[10]. The discharge in the reactor is self-sustained and occurs at ambient pressure; the temperature is also relatively mild between room temperature and 200°C. Reactor configuration can be either planar (**Figure 4.1a**,

4.1b, and **4.1c** in different configurations) or coaxial (**Figure 4.1d**), and could be packed with catalyst pellets or powder.

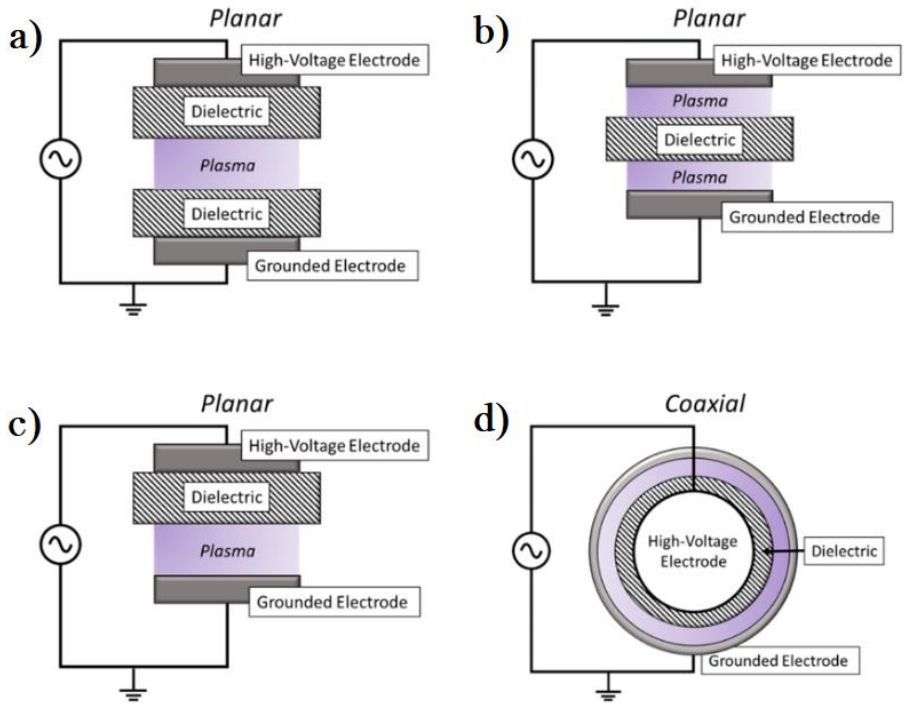

Figure 4.1 *– Schematic representation of different configurations of planar DBD a) "two-sided" b) and c) "one-sided" and d) coaxial DBD, Reproduced with permission of* [15]

4.5. | Plasma experiment set-up

The plasma generation plant consists of a generator (Siglent SDG 1025 – **Figure 4.2-1**), an amplifier (Behringer EP 4000 - **Figure 4.2-2**), and a transformer (Xenionik HV – **Figure 4.2-3**). Voltage waveforms were measured with an oscilloscope (Picoscope 3000 – **Figure 4.2-4**). The measured voltage was used and processed together with the capacitor to generate the Lissajous figure and then to calculate the plasma power. The voltage was measured by a Tektronik P6015A HV probe with a ratio of 1000:1 (**Figure 4.2-5**). The low voltage was measured through a 10:1 probe, and a 100 nF capacitor was connected (**Figure 4.2-6**) between the electrode around the reactor (aluminum foil – **Figure 4.2-7**) and the

High-Voltage electrode (**Figure 4.2-8**). A Fourier transform IR (Shimadzu IRTracer-100 - **Figure 4.2-9**) was used for the ammonia detection. Mass flow controllers (Bronkhorst - **Figure 4.2-10**) were used to set the flow rate of N_2 and H_2 feed gases entering the reactor.

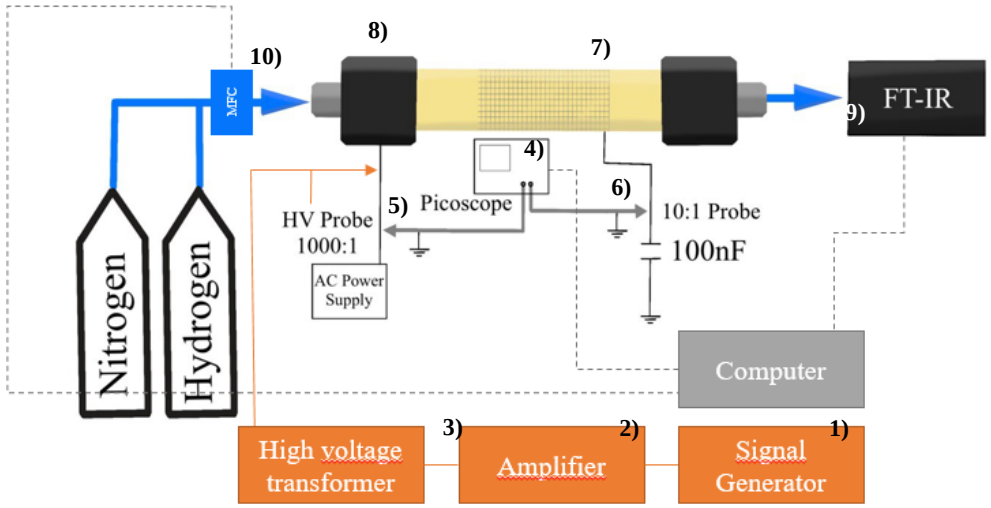

***Figure 4.2** - Schematic diagram of the experimental setup: 1) Signal Generator, 2) Amplifier, 3) High Voltage (HV) Transformer, 4) Oscilloscope, 5) HV probe, 6) Low voltage (LV) probe, 7) Ground electrode (aluminium foil), 8) HV electrode Voltage, 9) Fourier-Transform IR, 10) Mass Flow Controller*

4.6. | Reactor

The DBD reactor used in this work is composed of an alumina tube which works as a dielectric barrier. The external and the inner diameters of the shell are 15 mm and 10 mm (**Figure 4.3a-2**), respectively. The ground electrode was made of an aluminium foil tightly placed (Figure **4.3a-3**) in the external part of the alumina tube with a length of 20 mm (Figure **4.3a-2**).

A stainless-steel rod was used as the high-voltage (HV) electrode (**Figure 4.3b-5**), connected with the HV probe through a connector (**Figure 4.3a-4**). The HV electrode was held in position with two ceramic rings (**Figure 4.3b-6**) that confine the active zone and minimize the edge effects (**Figure 4.3b-7**). The HV electrode has a diameter of 6 mm (**Figure 4.3b-5**) and the discharge gap is 2 mm. Each side

of the reactor was connected to the pipeline through two Swagelok Ultra-Torr sealing pieces (**Figure 4.3a-1** and **4.3a-4**).

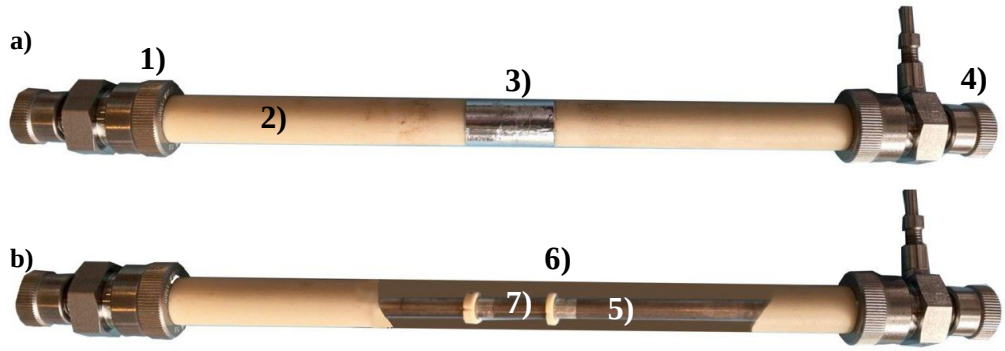

Figure 4.3 *– DBD reactor a) external view: 1) Ultra-Torr piece, inlet gases, 2) alumina tube reactor, 3) aluminium foil (ground electrode), 4) Ultra-Torr piece, outlet gases with High Voltage (HV) probe connector; b) internal view: 5) HV electrode, 6) ceramic rings, 7) catalyst compartment*

4.7. | Methodology

Once the plasma reactor was loaded with an appropriate amount of catalyst (summary **Table 1** in section 4.11), dependent on its density to ensure complete coverage of the plasma area, the reactor was positioned horizontally. Before starting the reaction, a leak test was conducted for around 15 minutes to monitor any pressure loss. The power was set to a fixed value, with an alternating current frequency of 20 kHz, and a flow rate of 120 mL min^{-1}. The ratio of nitrogen to hydrogen was then adjusted from 3:1 (nitrogen-rich) to 1:3 (stoichiometric for the Haber-Bosch process). Prior to activating the plasma, the mixture was allowed to flow in the reactor at the chosen rate for 5 minutes, ensuring a uniform distribution of reagent gas inflow within the chamber. The plasma exposure lasted a total of 30 minutes, with the reactor being cleaned using an only-nitrogen flow of 500 mL min^{-1} between each test. Subsequently, to investigate the optimal flow, the ratio providing the best results was maintained while the flow rate was varied to 160, 200, 300, and 360 mL min^{-1}. FT-IR was used to analyse ammonia from gas outlet.

4.8. | Stability tests

In literature, many works have investigated Al_2O_3-based catalysts (e.g. *Li et al.*[16]), and the behaviour of Al_2O_3 as the support is clear but less evident is how carbon nanotubes (CNTs) behave[17]. To study the behaviour of bare CNTs under plasma conditions, tests were carried out for 7 hours, for a total of 30 minutes of plasma exposure, with short periods of non-exposure (10 min), due to electronic limitations (overheating of components) to avoid harmful action on instrumentation.

a)

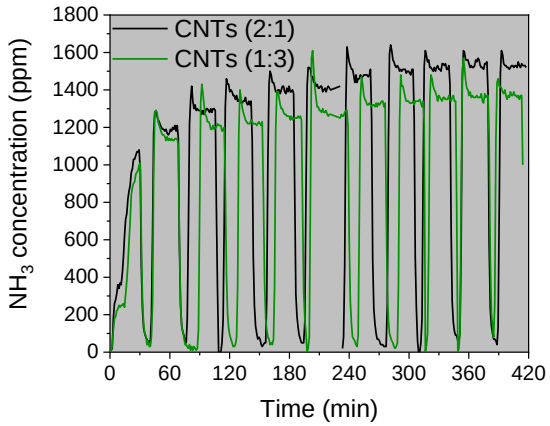

b)

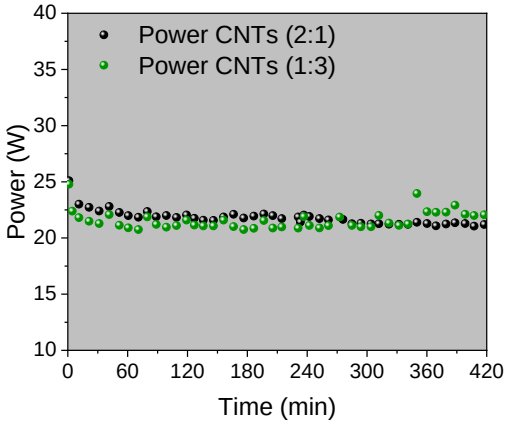

***Figure 4.4** – a) Stability test and b) power input level of functionalized CNTs at different feed-gas ratio N_2:H_2 (2:1 - green line) and (1:3 - black line)*

NH_3 production and power input were monitored. Bare functionalized CNTs needed a time of plasma exposure (**Figure 4.4a**) to reach a stable production, with a stable power input level (in this case 21.5±0.5 W, **Figure 4.4b**). Two

experiments were compared: two long tests at two different feed gas ratio N_2:H_2 of 2:1 and 1:3 respectively. The frequency was maintained at 20 kHz and the total flow rate was of 120 mL min^{-1}.

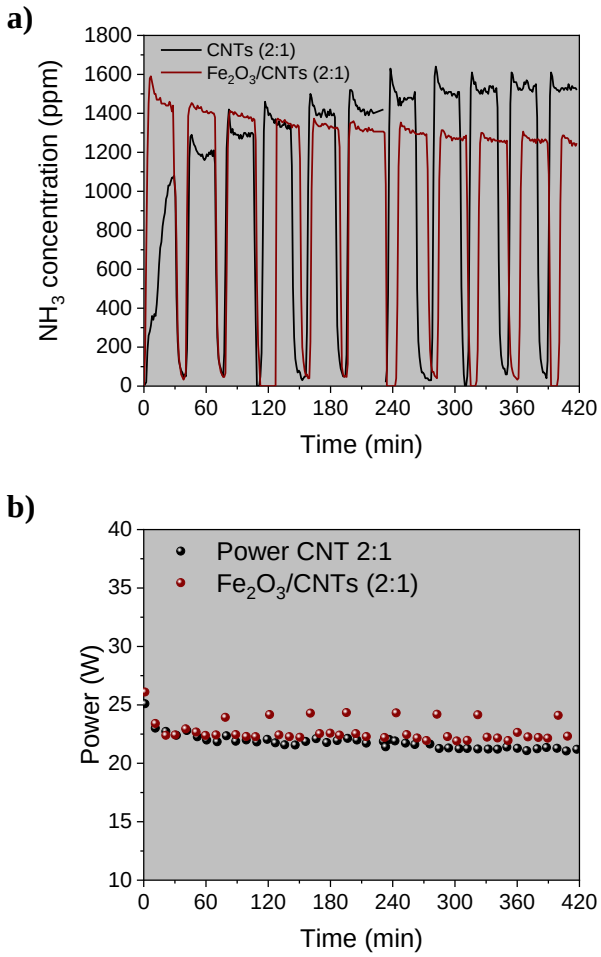

***Figure 4.5** – a) Stability test and b) power input level of functionalized CNTs (black line) and Fe_2O_3/CNTs (dark red line) at the same feed-gas ratio N_2:H_2 (2:1)*

A long test (7 h) with Fe_2O_3/CNTs catalyst was also performed. It is possible to notice (**Figure 4.5a**) that the catalyst did not need a "pre-activation", and the NH_3 production decreased during the time. Both tests were conducted with a stable power input level (in this case 21.7 ± 0.6 W, **Figure 4.5b**), a feed gas ratio of 2:1,

and the frequency was maintained at 20 kHz with a total flow rate of 120 mL min^{-1}.

4.9. | Synthesis of NH_3 via Non-Thermal Plasma method in DBD reactor

4.9.1. | Investigation of operational parameters: Optimal N_2:H_2 ratio

In these experiments, the feed gas N_2:H_2 ratio was varied from 3:1 to 1:3, the flow-rate was kept at 120 mL min^{-1}, and the energy power input was maintained at 26.7 ± 0.3 W. Blank DBD reactor and packed reactor were tested as shown in **Figure 4.6**. The blank reactor (purple circle) has his maximum at 1:2 (N_2:H_2) feed gas ratio with an energy consumption (EC) of 115.7 MJ mol^{-1} and production of 2870 ppm (13.94 μmol min^{-1}).

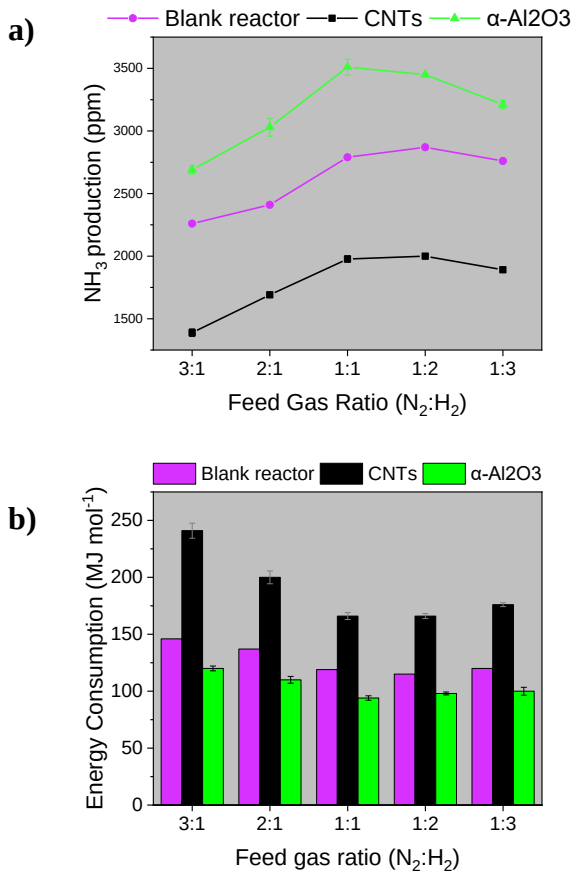

Figure 4.6 *– a) Ammonia production and b) energy consumption for blank reactor (purple), CNTs-o (black), and α-alumina (green)*

The maximum production for the functionalized CNTs is at 1:2 N_2:H_2 content (2000 ppm, that corresponds to a production of 9.62 μmol min^{-1}) with an energy consumption of 166.0 MJ mol^{-1}; instead for the alumina the best ratio is 1:1 with a production of 3510 ppm (17.05 μmol min^{-1}) and an EC of 94.7 MJ mol^{-1}. The metal-doped CNTs and Alumina supports, prepared as described in chapter 2, were thus tested in the DBD reactor.

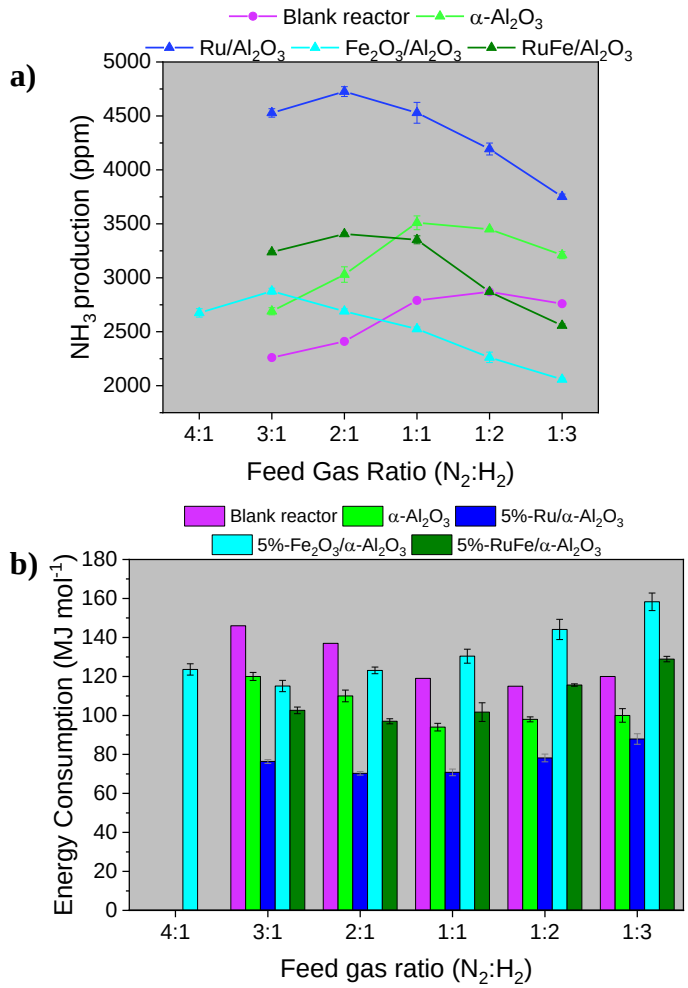

Figure 4.7 *– a) Ammonia production and b) energy consumption for α-alumina-based catalysts: blank reactor (purple), α-alumina (green), Fe_2O_3/Al_2O_3 (cyan), Ru/Al_2O_3 (blue) and $RuFe/Al_2O_3$ (dark green).*

The catalysts on alumina are generally more efficient than catalysts on CNTs (**Figure 4.7-a** and **4.8-a**). The best results were reached by Ru/Al_2O_3 catalyst, at 2:1 ratio N_2:H_2 with an ammonia production of 4725.7 ppm (22.7 μmol min^{-1}) with an EC of 70.1 MJ mol^{-1}. The catalyst Fe_2O_3/Al_2O_3 shifts the maximum performance at a higher N_2:H_2 ratio (3:1), with an ammonia production of 2876 ppm (13.9 μmol min^{-1}) and a corresponding EC of 115.1 MJ mol^{-1}. Replacing partially the Ru with Fe forming a hybrid catalyst with half percentage in weight of the two metals ($RuFe/Al_2O_3$, **Section 2.3.4**), allowed obtaining a higher performance compared to Fe_2O_3/Al_2O_3 catalyst (no Ru), with a maximum at 2:1 N_2:H_2 ratio, providing an ammonia production of 3406.7 ppm (16.5 μmol min^{-1}) and an EC of 97.0 MJ mol^{-1}. Results also showed that switching from Ru to Fe_2O_3 in Al_2O_3, the optimal feed gas ratio was shifted to higher nitrogen content (from 2:1 to 3:1) but with a less productivity. Substitution with iron, a non-critical raw material, is a promising route to avoid the use of noble metals.

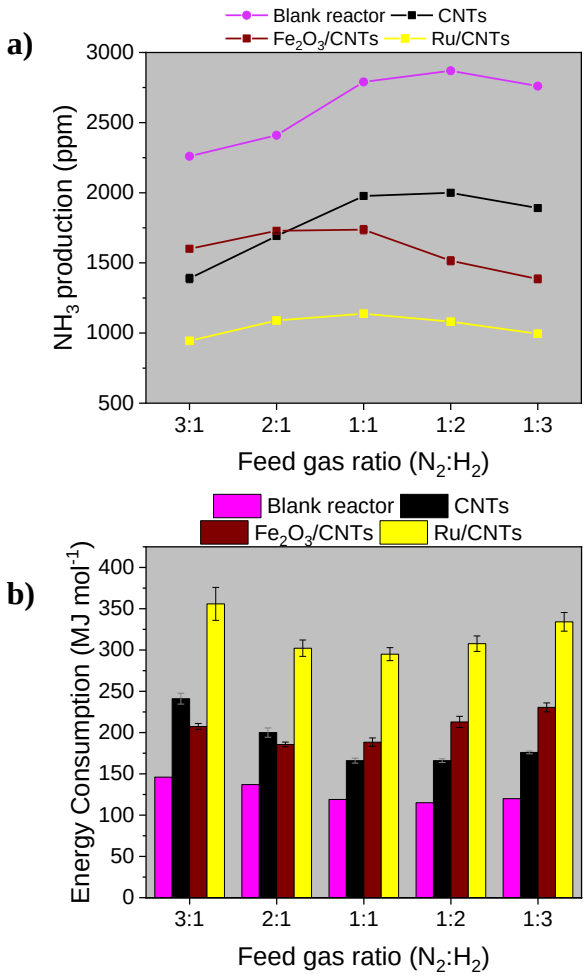

Figure 4.8 *– a) Ammonia production and b) energy consumption for CNTs-based catalysts: blank reactor (purple), CNTs (black), Fe_2O_3/CNTs (dark red), and Ru/CNTs (yellow).*

In general, it is easy to observe that the metal-doped catalysts shift the maximum of productivity (expressed in μmol min^{-1}) toward higher N_2:H_2 feed gas ratio with respect to the bare supports.

CNTs, Fe_2O_3/CNTs, and Ru/CNTs show their best ammonia production at 1:2, 2:1, and 1:1, respectively (**Figure 4.8**). At the best feed gas ratio, Fe_2O_3/CNTs allowed to obtain 1729 ppm (8.31 μmol min^{-1}) corresponding to an energy consumption of 185.6 MJ mol^{-1} and Ru/CNTs that shows the best productivity of 1138 ppm (5.49 μmol min^{-1}) with an EC of 295.0 MJ mol^{-1}, relatively lower with respect to pure CNTs (2000 ppm, 9.62 μmol min^{-1}).

4.9.2 | Investigation of operational parameters: Optimal flowrate

Significant differences between the graphs of the two supports (CNTs and alumina) are shown in **Figure 4.9**. As a result of dilution of the flow per unit of time, CNTs show a classical decreasing productivity trend (at a fixed N_2:H_2, 1:2 feed gas ratio). However, the cumulative ammonia production (calculated as the total micromoles produced) was higher at 160 mL min^{-1} (**Figure 4.9b**), with an energy consumption of 166.9 MJ mol^{-1} (**Figure 4.9a**). On the other hand, alumina (at a fixed feed gas ratio N_2:H_2 of 1:1) has its cumulative maximum at 360 mL min^{-1} (**Figure 4.9d**) with 65 MJ mol^{-1} (**Figure 4.9c**) as the energy consumption. According to **section 4.8**, the bare functionalized CNTs was pretreated under nitrogen for 30 minutes as an activation step. The activation step was applied only for the bare CNTs. Metals supported on CNTs did not require activation as described in **section 4.8**.

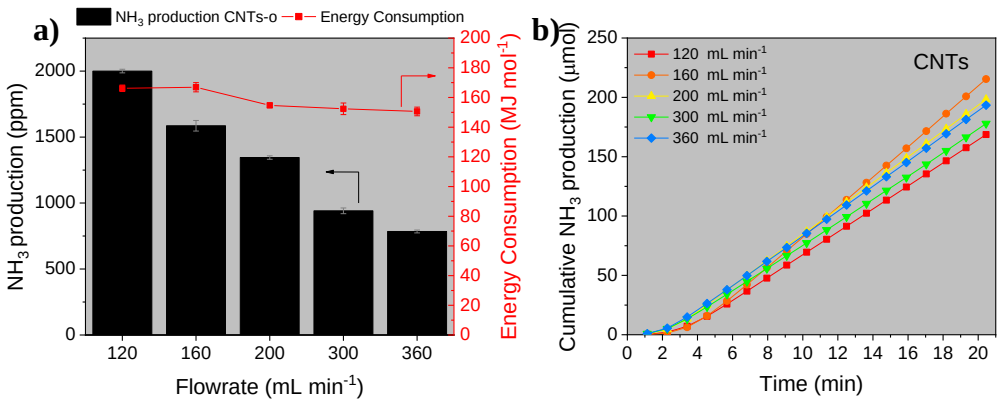

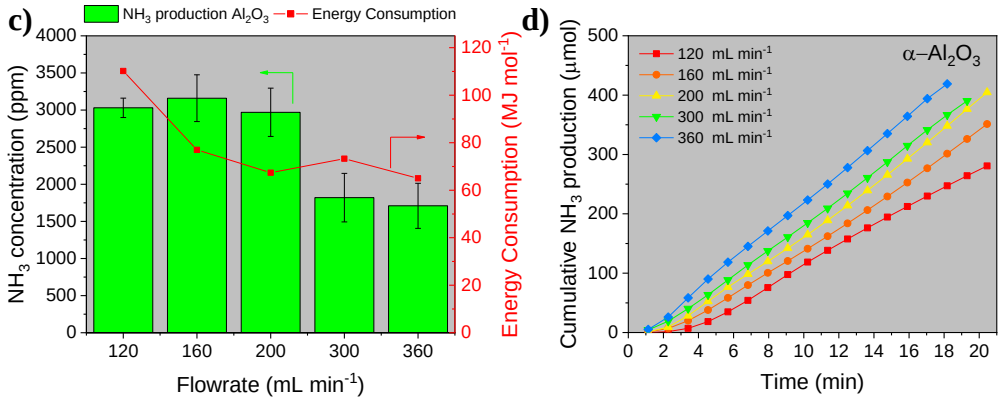

***Figure 4.9** - Different ammonia production for a) CNTs and c) Al_2O_3. Cumulative NH_3 production at different flowrate for b) CNTs and d) Al_2O_3*

Referring to the *metal-doped catalysts alumina-based* (**Figure 4.10**), Fe_2O_3/Al_2O_3 and Ru/Al_2O_3 show better performance at 360 mL min^{-1} (**Figure 4.10b** and **4.10f**), with a cumulative NH_3 production of 321.4 µmol in 20 min (16.1 µmol min^{-1}) and 551.3 µmol in 20 min (27.6 µmol min^{-1}), respectively. Differently, $RuFe/Al_2O_3$ (**Figures 4.10d**) shows the best performance at 300 mL min^{-1}, with a cumulative NH_3 production of 364.5 µmol in 20 min (18.2 µmol min^{-1}). However, Ru/Al_2O_3 (Figure 4.10f) shows similar production at 300 and 360 mL min^{-1} (547.2 and 551.3 µmol, respectively, in 20 min), and the same occurs for $RuFe/Al_2O_3$ (**Figures 4.10d**), showing a similar behaviour at 300 and 360 mL min^{-1} (364.5 and 358.9 µmol in 20 min). According to these small variations, ammonia production becomes flow independent at higher flowrates.

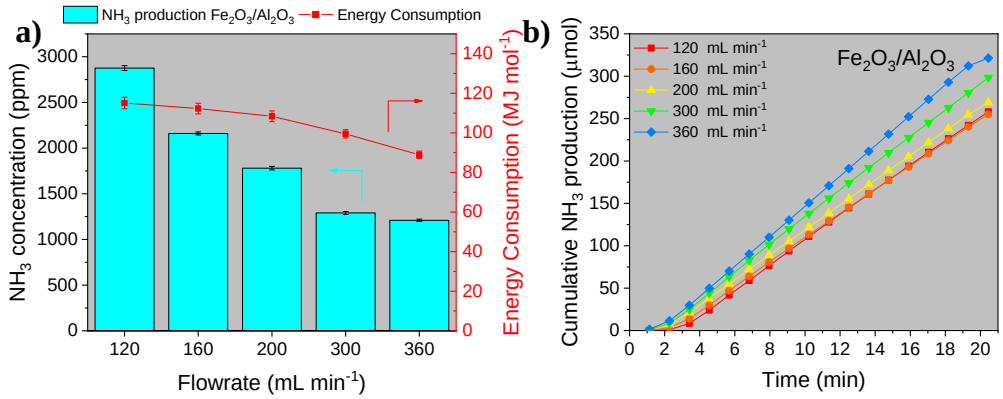

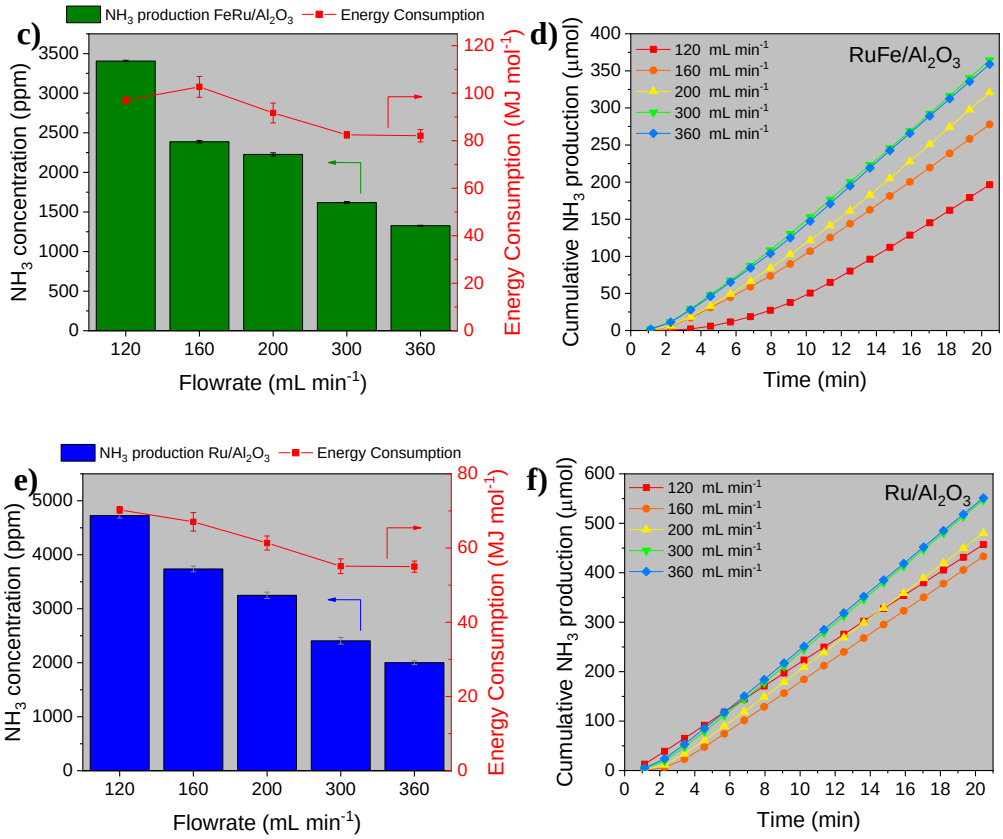

Figure 4.10 *- Illustrates various α-alumina-based catalysts for ammonia production, showcasing the cumulative NH_3 production at different flow rates. Panels (a), (c), and (e) represent ammonia production for Fe_2O_3, Ru-Fe, and Ru/Al_2O_3, respectively. Additionally, panels (b), (d), and (f) depict the cumulative NH_3 production at different flow rates specifically for Fe_2O_3, Ru-Fe, and Ru/Al_2O_3*

The results for the catalysts based on CNTs (Fe_2O_3/CNTs and Ru/CNTs) demonstrated a maximum at 360 mL min^{-1}, and productivity of 173.4 µmol in 20 minutes (8.7 µmol min^{-1}) and 124.4 µmol in 20 minutes (6.2 µmol min^{-1}), respectively (**Figure 4.11b** and **4.11d**).

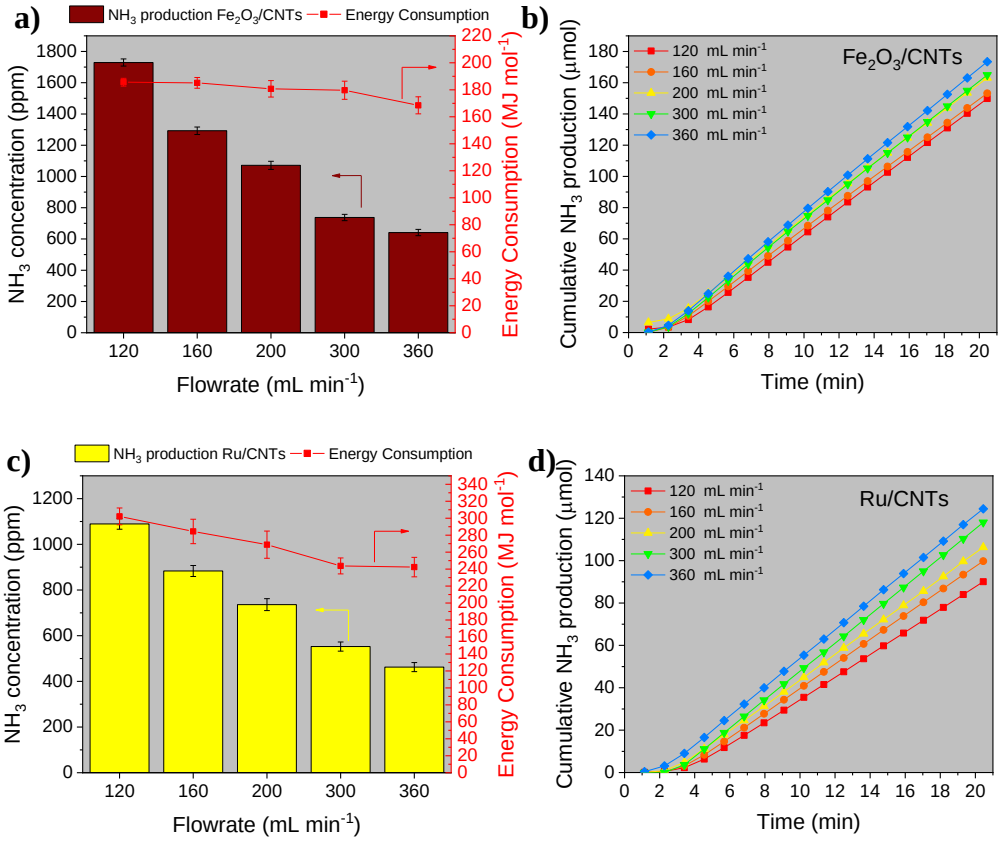

Figure 4.10 *- Illustrates various CNTs-based catalysts for ammonia production, showcasing the cumulative NH_3 production at different flow rates. Panels (a), and (c) represent ammonia production for Fe_2O_3, and Ru/CNTs, respectively. Additionally, panels (b), and (d) depict the cumulative NH_3 production at different flow rates specifically for Fe_2O_3, and Ru/CNTs*

The decreasing production of ammonia (bar charts) is due to the different residence time in the reactor (higher flowrate mean less residence time and dilution of ammonia detected in the volumetric percentage of product arrived at IR detector, expressed in ppm), while the increasing of ammonia in cumulative production (dot-line charts) takes into account the flowrate (mL min^{-1}) and the amount of reagent supplied. Thus, the calculations express better the moles produced from volumetric results for every different feed gas flowrate (calculation in **Supplementary information – section C**).

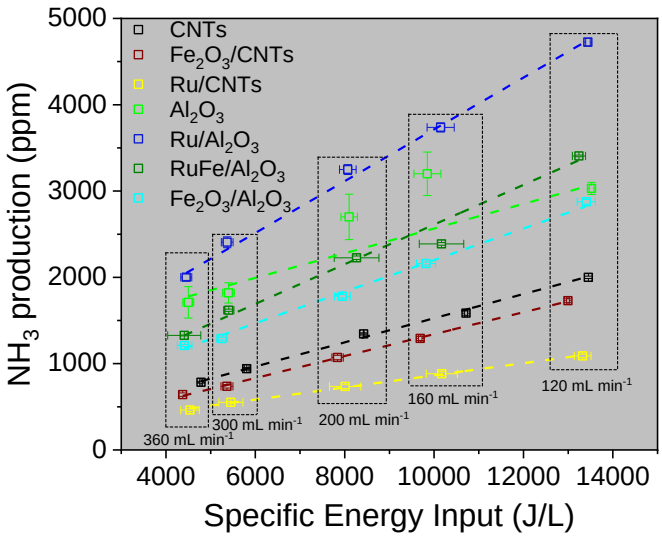

***Figure 4.12** - Effect of SEI on NH_3 concentration of different Al_2O_3 and CNTs-based catalysts at different flowrates (from 120 to 360 mL min^{-1} at fixed N_2:H_2 ratio*

As showed in **Figure 4.12**, the NH_3 concentration (ppm) against Specific Energy Input (SEI) trend, it is possible to observe that for all SEI, Ru/Al_2O_3 is the most efficient, at every flowrate. $RuFe/Al_2O_3$ have an average performance between Ru/Al_2O_3 and bare α-Al_2O_3 at 120 mL min^{-1}, but at higher flowrate the trend changes in the order Ru/Al_2O_3> bare α-Al_2O_3 > $RuFe/Al_2O_3$. The performance of Fe_2O_3/Al_2O_3 catalyst is lower thsn every α-alumina supported catalysts; this could be attributed to a localized NH_3 decomposition by Fe-species[18]. In the lower side of graph, CNTs-based catalysts follow the reactivity order CNTs > Fe_2O_3/CNTs > Ru/CNTs. A hypothesis is that CNTs active site[**Errore. Il segnalibro non è definito.** may m ake the CNTs less inert[14]. The position of Fe_2O_3/CNTs on the graph of **Figure 4.12** suggests that the decomposition mentioned above may occur leading to a lower production of NH_3. The lowest production of Ru/CNTs could be attributable to the lower load in metal of Ru and also with the loading inside the reactor (**Section 4.11 - Table 4.1**).

4.10. | Plasma discharge behavior

The analysis of the Lissajous figures allows to describe the discharge behaviour of the packed catalysts reactor. When the discharge gap is packed with a catalyst, the Lissajous figure changes from a parallelogram shape (**Figure 4.13a**), which is typical for nonpacked DBD plasma reactors, to an oval shape (almond shape). This can be attributed to the occurrence of a combination of filamentary discharges accompanied with surface discharges, which are formed across the packed bed, rather than only filamentary discharges, which are typically formed when no packing is utilized [19,20,21]. In particular, the α-alumina-packed reactor (**Figure 4.13c**) looks more similar in amplitude and discharges number (i.e. filamentary discharges on the curve) to blank reactor (**Figure 4.13a**). Furthermore, to maintain a constant power input level (27 W) in Lissajous figures, the *peak-to-peak* voltage changes [22].

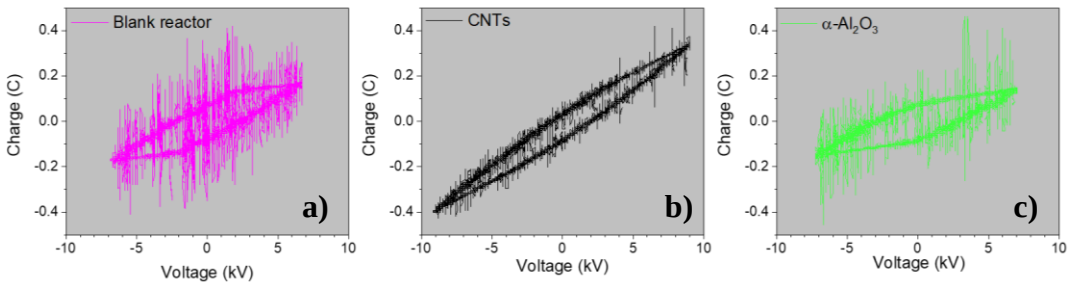

***Figure 4.13** - Lissajous figures for a) blank reactor b) CNTs c) a-alumina packed reactor with a power input of 27.0±0.1 W, 20 kHz, best feed gas ratio (see experimental part)*

Moving the attention onto our CNTs and α-alumina-based catalysts, the metal-doping changes the behaviour of plasma that surrounds the materials.

In **Figure 4.14a** and **-b**, the shape is similar to the starting material, with some differences in filamentary discharge attributable to the presence of Fe_2O_3 and Ru. While for the Alumina-based catalysts (**Figures 4.14c**, **-d** and **-e**) show how Fe_2O_3 closely resembles the starting material, the addition of Ru increases the number of surface discharges. For this reason, the Ru/Al_2O_3 might suggest higher catalytic

activity under plasma conditions. The Lissajous figure of *hybrid iron-ruthenium co-doped catalyst* shows an average attitude (**Figure 4.14d**).

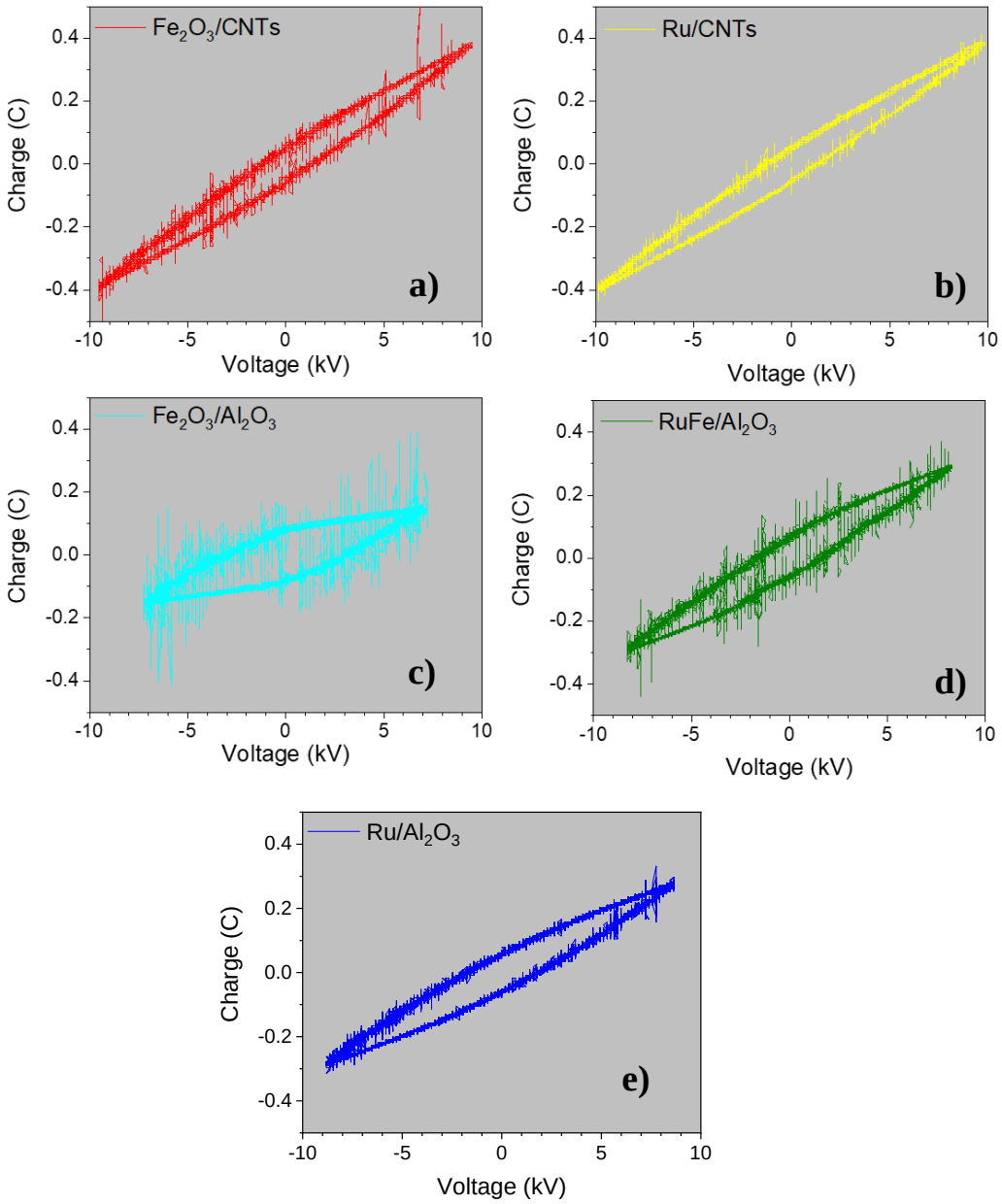

Figure 4.14 - *Lissajous figures for a) Fe_2O_3/CNTs b) Ru/CNTs c) Fe_2O_3/Al_2O_3 d) RuFe/Al_2O_3 e) Ru/Al_2O_3 packed reactor with a power input of 26.4±0.6 W, 20 kHz, best feed gas ratio (see experimental part)*

4.11. | Conclusions

In this chapter, the field of plasma catalysis was explored by investigating the operating parameters, such as the ratio of nitrogen to hydrogen as feed gas and the reactant gas flowrate at fixed ratio, for both CNTs- and alumina-based catalysts.

The main conclusion is that the dielectric created by alumina performed better under plasma conditions than functionalized carbon nanotubes. Furthermore, the metal used to increase the performance of the substrate plays a key role in the case of alumina, where the performance follows the order Ru > RuFe > Fe_2O_3/Al_2O_3 >> Fe_2O_3 > Ru/CNTs.

The difference in productivity between the two media may also be influenced by mesopore size and surface area, in addition to the fact that CNTs conduct more than alumina. Furthermore, the metal distribution on the surface and the plasma path in a packed reactor, which is commonly known as a surface streamer[23,24], may contribute to the difference in productivity. There is a strong correlation between surface propagation and catalytic performance.

CNTs, being more conductive, have shown an opposite trend with respect to alumina catalysts, where metal-doped catalysts have lower productivity than the support alone. Moreover, the smaller the surface area, the more metal will be on the surface that will undergo surface discharge. While the surface area increases (e.g. CNTs), the metal may be inside the support and not be affected by surface discharge.

Modifying the flowrate, on the other hand, resulted in a decline in ammonia productivity in parts per million (in agreement with Supporting info – C, equation 3), and a subsequent decrease in SEI, as illustrated in **Figure 4.12**, which demonstrates a linear relationship between SEI and NH_3 production. The overall calculation, which considers not only the parts per million (volumetric) of

ammonia produced but also the flow of reactant gas, reveals that as the flowrate increases, the overall ammonia production rate also increases, except for CNTs, which exhibited the highest overall value at 160 mL min^{-1}.

Stability tests have also shown that CNTs alone require plasma treatment to activate, to achieve a stability production. While CNTs doped with metals do not require a period of activation.

Catalysts	Catalyst in the reactor (g)	Teorical metal load (%wt.)	EDX Load (%wt.)	Best ratio (N_2:H_2)	Maximum productivity 120 mL min^{-1}	Best Flowrate (mL min^{-1})	Maximum productivity (µmol min^{-1})	Cumulative (µmol)
Blank	0	0	0	1:2	13.94	-	-	-
Al_2O_3	1.350	0	0	1:1	17.05	360	23.2	419.0
Fe_2O_3 /Al_2O_3	0.770	5(3.5†)	5.75±1.45*	3:1	13.9	360	16.1	321.4
Ru-Fe /Al_2O_3	1.149	Ru 2.5 Fe 2.5	Ru 1.2±0.1 Fe 2.6±0.3*	2:1	16.5	300	18.2	364.5
Ru /Al_2O_3	1.696	5	2.55±0.15	2:1	22.7	360	27.6	551.3
CNTs	0.180	0	0	1:2	9.62	160	10.8	215.4
Fe_2O_3 /CNTs	0.364	30 (21†)	24.8±4.4*	2:1	8.31	360	8.67	173.4
Ru-Fe /CNTs	-	Ru 2.5 Fe 2.5†	Ru 8.3±2.1 Fe 5.2±1.9*	-	-	-	-	-
Ru /CNTs	0.100	5	32.1±3.7	1:1	5.49	360	6.22	124.4

(*) related to at.% of Fe
(†) related to wt.% of Fe calculated
(-) data not available

Table 4.1 *– Summary table of plasma experiment*

4.12. | Supporting information

A - Only nitrogen plasma tests: Blank and CNTs packed reactor
B - Different power input on Fe_2O_3/CNTs-o
C - Calculation formulas
D - High-speed camera images
E - IR Camera images
F - Different power input – Blank reactor
G – BET before and after Plasma experiment

A- Only nitrogen plasma tests: Blank and CNTs packed reactor

Tests were conducted exclusively with nitrogen plasma in both the empty reactor and the reactor with carbon nanotubes (CNTs) to elucidate the unique influence of N_2 under plasma conditions. This investigation aims to provide an understanding of the background scale behaviour of the tests (16.5±11.9 ppm).

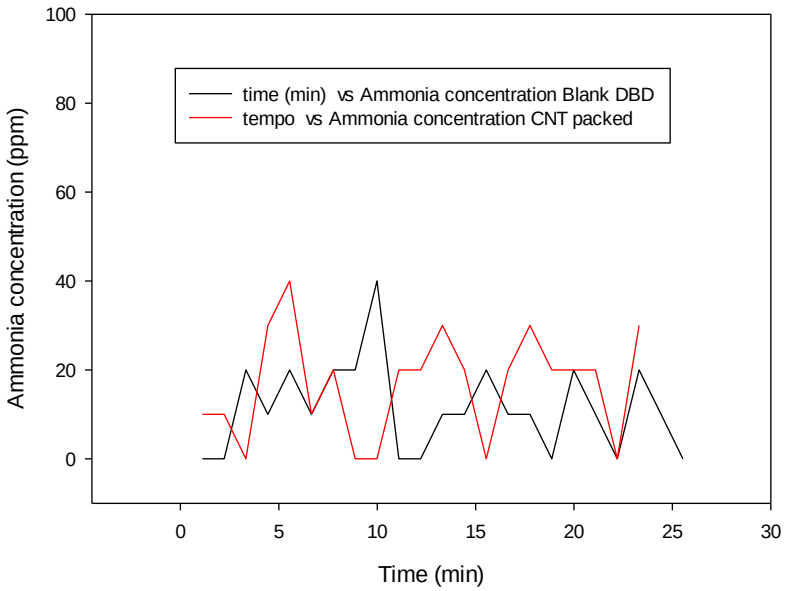

Figure S4.1 *- Blank DBD vs CNT Packed DBD Only N_2, 20 kHz , total flowrate 120 mL/min.*

B- Different power input on Fe_2O_3/CNTs

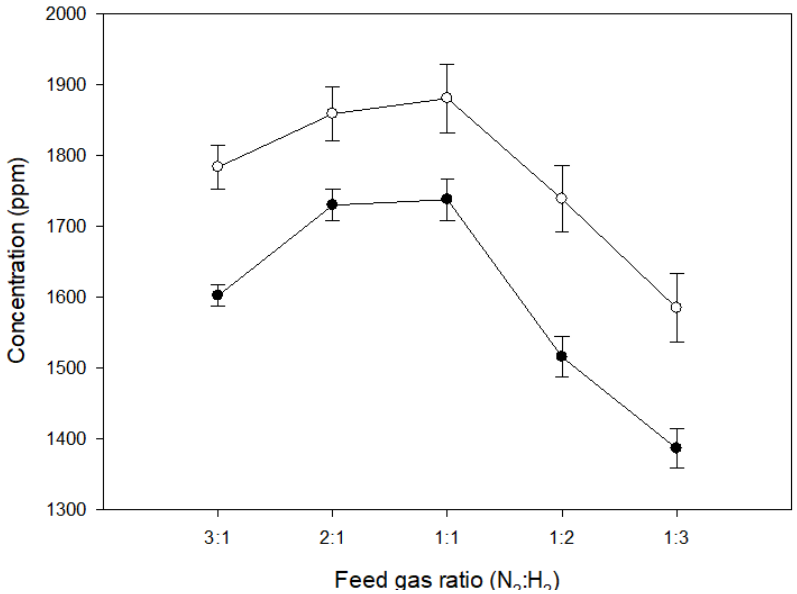

Figure S4.2 *– Different power input levels for packed DBD reactor with Iron (III) oxide on functionalized CNTs at different N_2:H_2, 20 kHz, total flowrate 120 mL min^{-1}, black dot (26.3 ± 0.4W) and white dot (43.5± 0.2W).*

C- Calculation formulas

$$\text{Specific Energy Input} = \text{SEI}\left(\frac{\text{J}}{\text{L}}\right) = \frac{\text{Power input (W)} * 60\ (\text{s min}^{-1})}{\text{Flowrate (L min}^{-1})} \qquad \text{(eq. S1)}$$

$$\text{Energy Consumption}\left(\frac{\text{J}}{\text{mol}}\right) = \frac{\text{Energy (J)}}{\text{Produced NH}_3\ \text{(mol)}} = \frac{\text{Power input (W)} * 60\ (\text{s min}^{-1})}{\text{NH}_3\ \text{concentration} * \text{Outlet flowrate (L min}^{-1})} \qquad \text{(eq. S2)}$$

$$\text{Productivity}\left(\frac{\text{mol}}{min}\right) = \frac{NH_3\ production\ (ppm)/10^6 * \text{Flowrate (L min}^{-1})}{24.7\ (\text{L mol}^{-1})} \qquad \text{(eq. S3)}$$

(eq. S4)

Cumulative (mol)

$$= \sum_{x=0}^{n} \left((time_{x+1} - time_x) * prod_x \right) + \left(\left((time_{x+1} - time_x) * (prod_{x+1} - prod_x) \right) / 2 \right)$$

D- High-speed camera images

A high-speed camera (SpeedSense Dantec Dynamics) was used for monitoring the plasma path and plasma behaviour, with an AF Micro-Nikkor 200mm f/4D IF-ED as optical lens. A quartz tube was used for this experiment, with a window of 0.28 cm^2 on the ground (stainless steel).

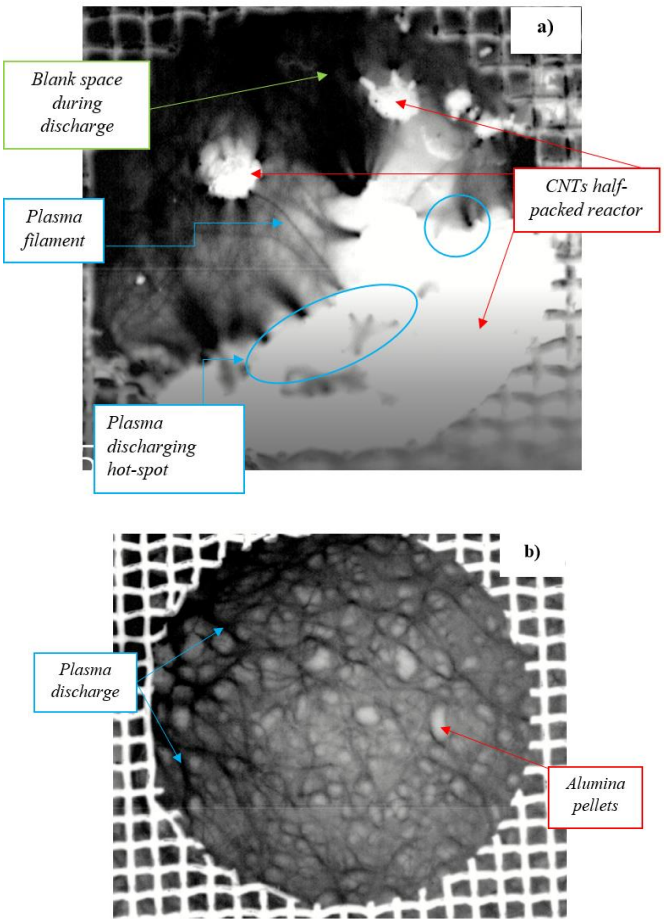

***Figure S4.3** – a) Functionalized Carbon-Nanotubes b) alumina discharging view, recorded with a High-Speed Camera, through a 1 cm diameter window on a quartz tube as reactor, and a stainless-steel mash as ground electrode.*

High speed camera images show how plasma is generated and propagated into our material. For CNTs-o (**Figure S4.3a**), it is appreciable that plasma discharge takes place from specific hot spot, where the discharge path for plasma is through CNTs, dissipating energy as heat, and for this reason at the same power energy input than alumina based, we have less plasma discharge. The alumina bare pellets (**Figure S4.3b**) did not conduct the plasma and the discharge happened in the void space and on the surface. For this reason, alumina values are higher than CNTs-based.

E- IR Camera images

A FLIR One Pro infrared thermal imaging camera was used to measure the temperature of the reactor wall. From IR Camera images at the same time of test, CNTs look warmer with respect to alumina in the same packed quartz tube.

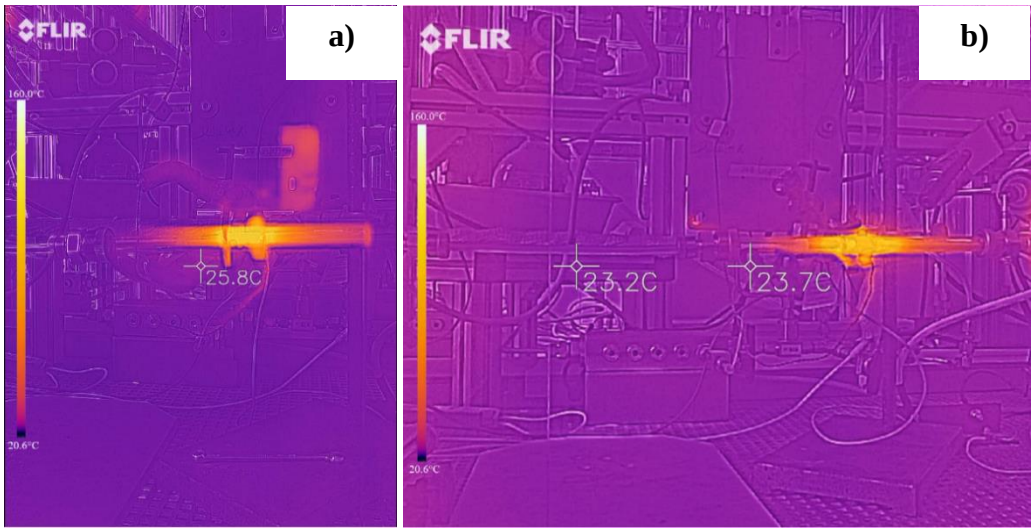

Figure S4.4 *– Infrared camera image of plasma treatment of a) CNTs-o packed reactor b) α-alumina packed reactor*

F – Different power input – Blank reactor

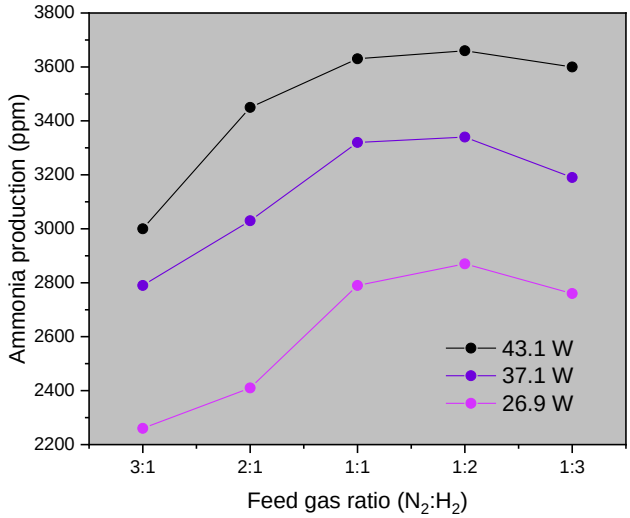

Figure S4.5 *- Different power input for blank reactor (black) 43.1W, (violet) 37.1 W, (purple) 26.9W, 20kHz, 120mL min^{-1}*

Blank reactor power input (W)	***Ammonia Production (ppm)***	***Productivity (μmol min^{-1})***	***Energy Consumption (MJ mol^{-1})***	***Specific Energy Input (J L^{-1})***
26.9	2870	13.9	115.7	13450
37.1	3340	16.2	137.2	18550
43.1	3660	17.8	145.4	21550

Table S4.1 *– Productivity, EC and SEI for different power inputs for blank reactor*

G – BET before and after Plasma experiment

Catalysts	***Al_2O_3***	***Fe_2O_3 /Al_2O_3***	***FeRu /Al_2O_3***	***Ru /Al_2O_3***	***CNTs***	***Fe_2O_3 /CNTs***	***Ru-Fe /CNTs***	***Ru /CNTs***
BET$^{(F)}$ (m^2/g)	0.21	8.9	17.6	1.84	54.75	61.82	63.6	105.7
BET$^{(AP)}$ (m^2/g)	0.19	-	-	1.32	44.3	59.6	-	85.2

(F) BET performed on fresh catalysts;
(AP) BET performed after plasma experiment;
(-) Data not available;

Table S4.2 *– BET surface area before and after plasma;*

4.13. | References

[1] Kong, M. G., Kroesen, G. G., Morfill, G. E., Nosenko, T., Shimizu, T., Dijk, V. J. J., & Zimmermann, J. L. (2009). Plasma medicine: an introductory review. New Journal of Physics, 11(11), 115012.

[2] Huang, M., Hasan, M. K., Rathore, K., Baky, M. a. H., Lassalle, J., Kraus, J., Burnette, M., Campbell, C., Wang, K., Jemison, H., Pillai, S. D., Pharr, M., & Staack, D. (2022). Plasma generated ozone and reactive oxygen species for point of use PPE decontamination system. PLOS ONE, 17(2), e0262818.

[3] Qu, M., Cheng, Z., Sun, Z., Chen, D., Yu, J., & Chen, J. (2021). Non-thermal plasma coupled with catalysis for VOCs abatement: A review. Process Safety and Environmental Protection, 153, 139–158.

[4] Peng, P., Chen, P., Addy, M., Cheng, Y., Zhang, Y., Anderson, E., Zhou, N., Schiappacasse, C., Hatzenbeller, R., Li, F., Liu, S., Chen, D., Liu, J., Liu, Y., & Ruan, R. (2018). In situ plasma-assisted atmospheric nitrogen fixation using water and spray-type jet plasma. Chemical Communications, 54(23), 2886–2889.

[5] Park, D. P., Davis, K., Gilani, S., Alonzo, C., Dobrynin, D., Friedman, G. D., Fridman, A., Rabinovich, A., & Fridman, G. (2013). Reactive nitrogen species produced in water by non-equilibrium plasma increase plant growth rate and nutritional yield. Current Applied Physics, 13, S19–S29.

[6] Pavlovich, M. J., Ono, T., Galleher, C., Curtis, B., Clark, D. S., Machala, Z., & Graves, D. B. (2014). Air spark-like plasma source for antimicrobial NO_x generation. Journal of Physics D, 47(50), 505202.

[7] Xie, D., Yu, S., Zhu, T., Fan, X., Hong, X., & Yang, W. (2016). Ammonia synthesis and by-product formation from H_2O, H_2 and N_2 by dielectric barrier discharge combined with an Ru/Al_2O_3 catalyst. RSC Advances, 6(107), 105338–105346.

[8] Sharma, R. K., Patel, H., Mushtaq, U., Kyriakou, V., Zafeiropoulos, G., Peeters, F., Welzel, S., Van De Sanden, M., & Tsampas, M. N. (2020). Plasma Activated Electrochemical Ammonia Synthesis from Nitrogen and Water. ACS Energy Letters, 6(2), 313–319.

[9] Gómez-Ramírez, A., Cotrino, J., Lambert, R. M., & González-Elipe, A. R. (2015). Efficient synthesis of ammonia from N2and H2alone in a ferroelectric

packed-bed DBD reactor. Plasma Sources Science and Technology, 24(6), 065011.

[10] Brandenburg, R. (2017). Dielectric barrier discharges: progress on plasma sources and on the understanding of regimes and single filaments. Plasma Sources Science and Technology, 26(5), 053001.

[11] Peng, P., Cheng, Y., Hatzenbeller, R., Addy, M., Zhou, N., Schiappacasse, C., Chen, D., Zhang, Y., Anderson, E., Liu, Y., Chen, P., & Ruan, R. (2017). Ru-based multifunctional mesoporous catalyst for low-pressure and non-thermal plasma synthesis of ammonia. International Journal of Hydrogen Energy, 42(30), 19056–19066.

[12] Zhu, X., Hu, X., Wu, X., Cai, Y., Zhang, H., & Tu, X. (2020). Ammonia synthesis over γ-Al_2O_3 pellets in a packed-bed dielectric barrier discharge reactor. Journal of Physics D, 53(16), 164002.

[13] Kim, H., Teramoto, Y., Ogata, A., Takagi, H., & Nanba, T. (2016). Atmospheric-pressure nonthermal plasma synthesis of ammonia over ruthenium catalysts. Plasma Processes and Polymers, 14(6).

[14] Peng, P., Li, Y., Cheng, Y., Deng, S., Chen, P., & Ruan, R. (2016). Atmospheric pressure ammonia synthesis using non-thermal plasma assisted catalysis. Plasma Chemistry and Plasma Processing, 36(5), 1201–1210.

[15] Koga-Ito, C. Y., Kostov, K. G., Miranda, F. S., Milhan, N. V. M., Azevedo Neto, N. F., Nascimento, F., & Pessoa, R. S. (2023). Cold atmospheric plasma as a therapeutic tool in medicine and Dentistry. Plasma Chemistry and Plasma Processing.

[16] Li, S., van Raak, T., & Gallucci, F., Investigating the operation parameters for ammonia synthesis in dielectric barrier discharge reactors. *Journal of Physics D: Applied Physics* (2019), *53*(1), 014008.

[17] Hong, J., Aramesh, M., Shimoni, O., Seo, D. H., Yick, S., Greig, A., Charles, C., Prawer, S., & Murphy, A. B., Plasma catalytic synthesis of ammonia using functionalized-carbon coatings in an atmospheric-pressure non-equilibrium discharge. *Plasma Chemistry and Plasma Processing* (2016), *36*(4), 917–940.

[18] Lu, A.-H., Nitz, J.-J., Comotti, M., Weidenthaler, C., Schlichte, K., Lehmann, C. W., Terasaki, O., & Schüth, F., Spatially and size selective synthesis of Fe-based nanoparticles on ordered mesoporous supports as highly active and stable

catalysts for ammonia decomposition. *Journal of the American Chemical Society* (2010), *132*(40), 14152–14162.

[19] Butterworth, T., Elder, R., & Allen, R. (2016). Effects of particle size on CO_2 reduction and discharge characteristics in a packed bed plasma reactor. *Chemical Engineering Journal*, 293, 55–67.

[20] Tu, X., Gallon, H. J., Twigg, M. V., Gorry, P. A., & Whitehead, J. C. (2011). Dry reforming of methane over a Ni/Al_2O_3 catalyst in a coaxial dielectric barrier discharge reactor. *Journal of Physics D: Applied Physics, 44*, 274007.

[21] Peeters, F. J. J., & van de Sanden, M. C. M. (2015). The influence of partial surface discharging on the electrical characterization of DBDs. *Plasma Sources Science and Technology, 24*, 015016.

[22] Taheraslani, M., & Gardeniers, H. (2020). Coupling of CH_4 to C_2 hydrocarbons in a packed bed DBD plasma reactor: The effect of dielectric constant and porosity of the packing. *Energies*, *13*(2), 468.

[23] Kim, H.-H., & Ogata, A. (2011). Nonthermal plasma activates catalyst: From current understanding and future prospects. *The European Physical Journal Applied Physics*, *55*(1), 13806.

[24] Kim, Hyun-Ha, Kim, J.-H., & Ogata, A. (2009). Microscopic observation of discharge plasma on the surface of zeolites supported metal nanoparticles. *Journal of Physics D: Applied Physics*, *42*(13), 135210.

5. | Conventional and non-conventional techniques for ammonia synthesis: A technical economical evaluation

5.1 | Preface

This chapter aims to provide a comprehensive and objective view of technologies for ammonia production, comparing the advantages and disadvantages of different technologies, and the challenges that each methodology brings. The pursuit of sustainable and innovative solutions is crucial to shape a future where chemical industry can ensure efficient, eco-friendly ammonia production that meets evolving global needs [1].

5.2 | State-of-the-art

In the current industrial landscape, the production of ammonia plays a crucial role in supplying fertilizers, explosive components, pharmaceuticals, and countless other sectors. The Haber-Bosch ammonia synthesis method has served as a cornerstone for over a century, ensuring a reliable approach to mass production. However, the evolution of environmental needs, resource optimization, and the pursuit of more efficient processes have prompted the industry to consider unconventional alternatives [2]. A thorough preliminary analysis of the processes will reveal benefits and drawbacks.

Exploring emerging technologies will involve investigating methodologies based on electrocatalysis, plasma catalysis, or a combination thereof, as well as an electrification process such as magnetic induction heating. The use of these methodologies holds promises of greater sustainability, potential for decentralization, reduced greenhouse gas emissions, and the ability to harness

renewable energy sources. However, their implementation on an industrial scale requires a detailed analysis of technical, economic, and environmental aspects, employing various scenarios in which the technology can be valorised.

Macro areas can be defined for the various technologies: thermal and pressure-based technology (Traditional Haber-Bosh -HB- as reference, Green HB, Magnetic induction heating); electrocatalysis-based processes (EC in aqueous, organic and ionic liquids); plasma-based processes: thermal plasma (TP), Thermal Plasma – Solid Oxide Electrochemical Cell (TP-SOEC), and non-thermal plasma (NTP); and a hybrid plasma-electrocatalytic process (HPE), found in the literature.

The TP-SOEC in-house building reactor is based on a commercial half-anode supported cell (Ni-BCZY/BCZY, BCZY is $BaCe_{0.2}Zr_{0.7}Y_{0.1}O_{3-\delta}$ ceramic material) and micrometric thickness Pt porous cathode. The porous material favours the diffusion of the reactant gases and increases the surface area. This reactor matches a technology to produce H_2 from H_2O in vapor form (Solid Oxide Electrolysis) in situ and passes in the other part (thermal plasma side) where the nitrogen fixation takes part. Plasma is made with a Radio Frequency power supply on N_2 flow (acting both as the reagent gas and plasma gas). To allow the SOEC reactor to work, a heating mantle surrounds the reactor tube. As output species plasma side (N_2 side) there is ammonia, N_2, and H_2. The output species on the SOEC side are He, H_2O, and O_2.

The hybrid plasma electrocatalysis technique will also be discussed, as this technique matches the plasma conversion of air and water in Nitric or Nitrous oxides, sequentially electro-converted on the surface of the electrode (cathode) into ammonia. This process employs the activation of triple bond nitrogen into NO_x as intermediates of reaction, which is more easily converted into ammonia. Air flows in the plasma jet reactor (plasma bubbler) as the feed gas, plasma generates Nitric and Nitrous Oxide in solution (Acid Solution 1mM H_2SO_4) and

species reduced into ammonia from the cathode (Copper Nanowires). Ammonium in solution has to be separated or used as Ammonium nitrate.

Figure 5.1 shows the trend of publications related to the various technologies. It is possible to see an increasing trend over the last 10 years, which is synonymous of active efforts in these environmental impact issues. Electrocatalysis in an aqueous environment has the highest number of publications per year, but also novel technologies, such as NTP, have attracted a lot of interest over the past 5 years in the catalytic field for nitrogen fixation.

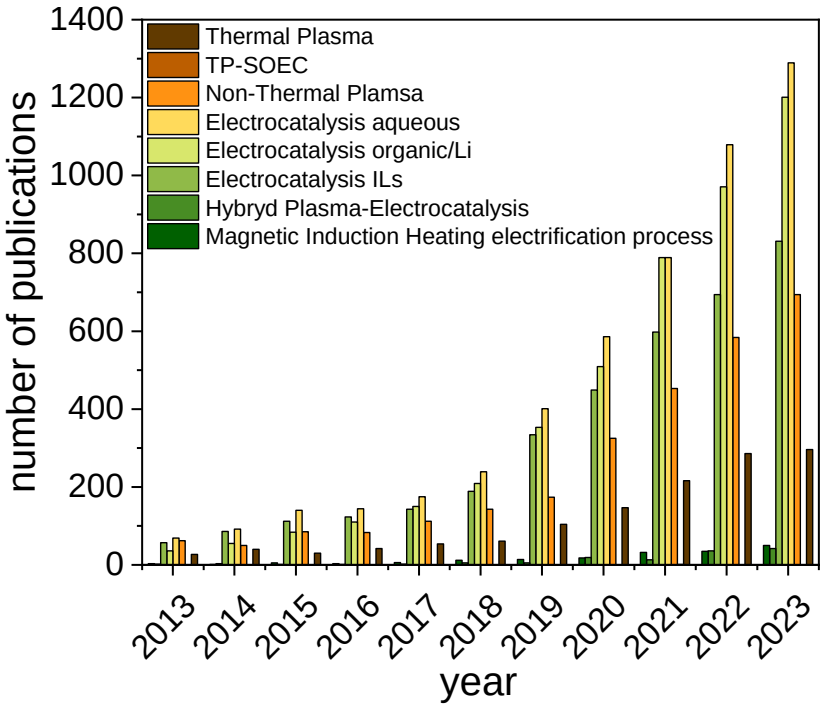

Figure 5.1 *– Trend publications in the period 2013-2023 for different technologies*

5.3 | Aim of chapter

In agreement with *Programma Operativo Nazionale (PON), Innovative Doctorates with Industrial Characterization (DOT20JCJJA) cycle 36th*, the

technical and economic evaluation for the processes on ammonia was carried out at Casale SA (Lugano – Switzerland) during a six-months period, under the supervision of Dr. Pierdomenico Biasi and Dr. Alberto Garbujo. Most of the technologies have already been mentioned in the introductory **Chapter 1**. The aim of this chapter is to evaluate the techno-economical aspects of the various technologies (including new and emergent technologies) for the process of ammonia production. In addition, clarifications on TP-SOEC, described by *Sharma et al.*[3], and Hybrid Plasma-Electrocatalysis reported by *Sun et al.*[4], will be discussed. These technologies combine several techniques, such as Thermal Plasma – Solid Oxides Electrolysis Cell, which in an all-in-one instrument produces both H_2 (SOEC part) and later NH_3 by thermal plasma.

5.4 | Techno-Economical part

This section comprises three components: a description of various technologies, accompanying diagrams, and a compilation of Capital Expenditure (CapEx) and Operating Expenditure (OpEx) data for the aforementioned technologies. It culminates in a summary table highlighting the primary advantages and disadvantages of each technology.

5.4.1 | Traditional HB analysis

As described in section 1.3, the traditional HB process operating at high pressure and temperature, starts from fossil fuels, followed by Steam Methane Reforming (SMR) and Water Gas Shift (WGS), to obtain heat for the startup, and grey H_2 as feed gas for ammonia. The other feed gas (N_2) comes from the air (**Figure 5.2**).

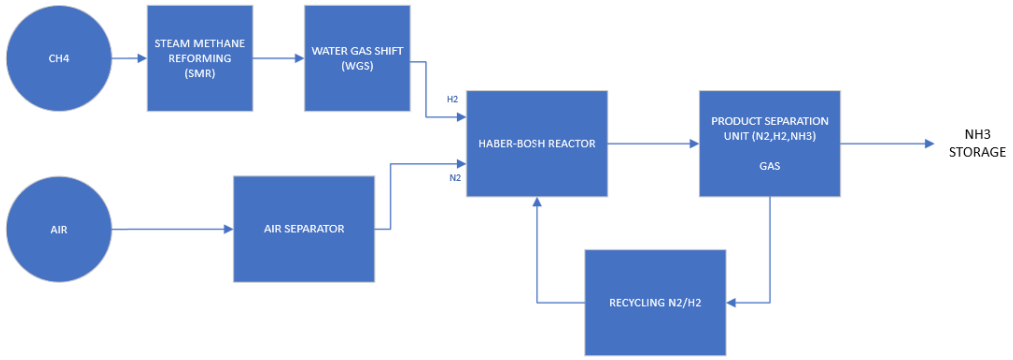

Figure 5.2 *- Schematic process diagram for traditional Haber-Bosh*

5.4.2 | Green HB analysis

As described in section 1.4, Green HB process operating at high pressure and temperature, starts from H_2O through an electrolyzer to obtain H_2 (green if the electrolyzer is supplied by renewable energy sources) as feed gas for ammonia, while the other feed gas (N_2) from the air (**Figure 5.3**).

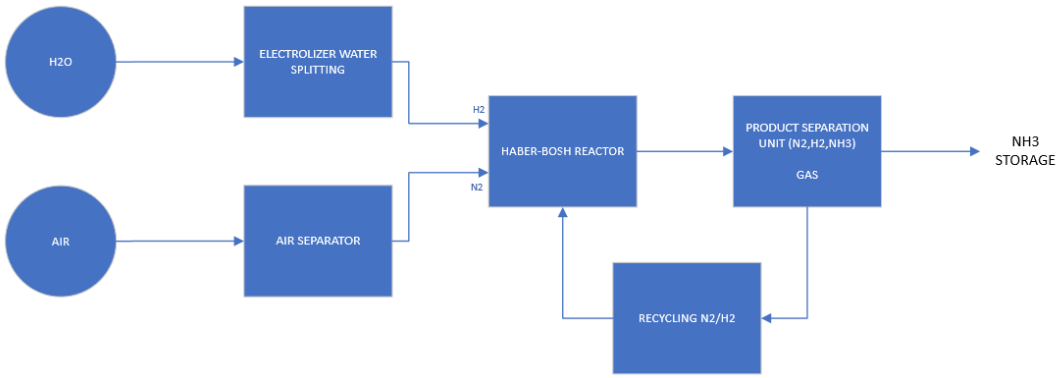

Figure 5.3 *- Schematic process diagram for green Haber-Bosh*

5.4.2.1 | Green HB CapEx

Ofori-Bah et al. [5] include capital and operating costs in their analysis. The technical economic calculation was based on the boundary condition determining how much ammonia would be required to produce fertilizers for an area of 1.4

million hectares supported by wind renewable energy. For the green Haber Bosh, in which the hydrogen supplier is an electrolyzer, the calculation also takes into account the Solid oxide electrolyzer. Furthermore, SOE results a competitive option in the conversion Power-to-ammonia as described by *Zhang et al.*[6].

Total capital cost: 781.72-929.88 mln$ (SOEC)

5.4.2.2 | Green HB OpEx

Operative expenditures 6.5 – 8.1MWh/t, 3.149 – 3.746 k$/t

5.4.3 | Magnetic Induction Heating analysis

As described in section 1.5.1, Magnetic Induction Heating through coils is a technology that use the hysteresis losses for heating of magnetic material, which is surrounded by High-frequency current (**Figure 5.4**). All available information has been taken from *Ponikvar et al.* **[7]** and from patent descripted in *ref.* **[22]**.

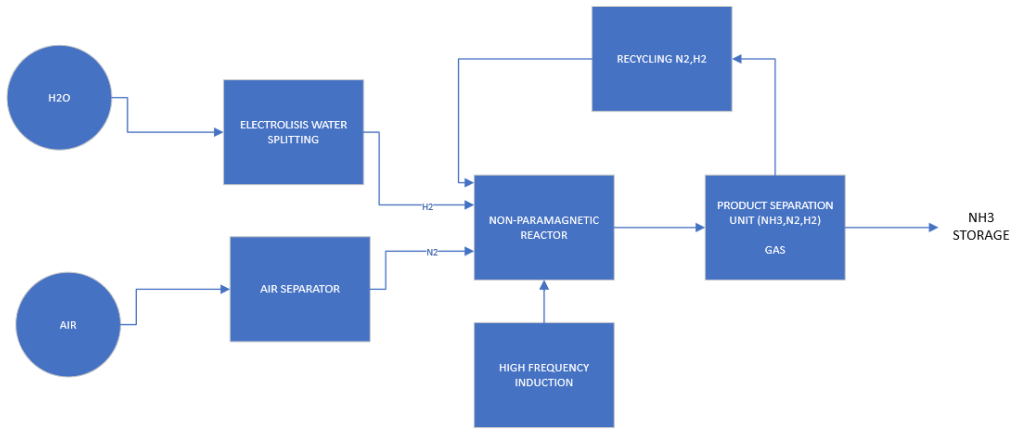

Figure 5.4 *- Schematic process diagram for magnetic induction heating applied on green Haber-Bosh*

Capital Expenditure (CapEx) for Magnetic Induction Heating involves the acquisition of essential components such as induction coils, power supplies, and non-paramagnetic reactors.

On the other hand, Operational Expenditure (OpEx) primarily encompasses the cost of electricity required to power the magnetic induction heating system.

There is a scarcity of literature on the subject of magnetic induction heating catalysis at present. As mentioned in section 1.5.1, one advantage of this technique is its ability to provide localized heating and achieve rapid operating temperatures. It can be applied to existing HB plants in conjunction with a renewable energy source. However, there are drawbacks to consider. The necessity of a reactor that can withstand magnetic stress or the use of coils within the reactor is one such limitation. Additionally, the intermittent nature of renewable energy must be taken into account. The required modifications to the pre-existing plant will incur additional capital costs.

5.4.4 | Electrochemical technologies

The Nitrogen Reduction Reaction (NRR) by electrocatalysis has been already described in section 1.5.2. Electrochemical technologies do not require the use of SOEC, as the proton source is already available in solution. Therefore, only the supply of nitrogen needs to be evaluated (air or compressed N_2). These technologies are very intriguing for bringing Haber-Bosch conditions into milder settings. That is why research has also extensively ventured in this direction, as described by *Fernandez et al.*[8], who conducted a technical-economic evaluation between Haber-Bosh and electrochemical ammonia production.

5.4.4.1 | EC in aqueous environment analysis

Electrocatalysis in aqueous environment consists of two reactions, in cathodic and anodic chambers separated from an ion exchange membrane. Ammonia is produced in the cathodic part, and proton sources are supplied by H_2O contained

in both reservoirs, applying a difference of potential, electron moving from the anode to cathode and protons closing the electrical circuit. The salt dissolved in H_2O supplies the charge and maintains the current. Oxygen is developed at the anode by water dissociation as the counter-reaction (**Figure 5.5**).

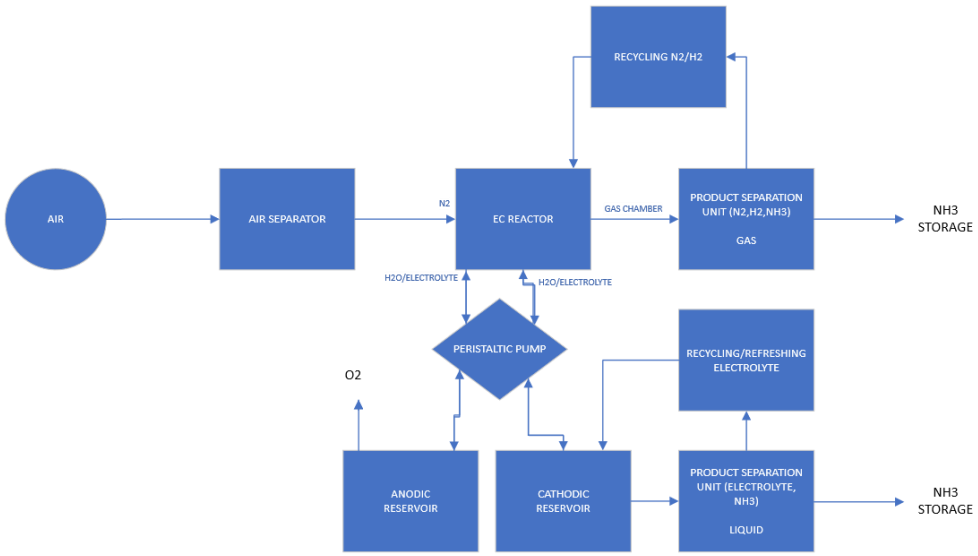

***Figure 5.5** - Schematic process diagram for Electrocatalytic process in aqueous environment*

5.4.4.2 | EC in organic environment analysis

Electrocatalysis in Organic solvent with Li-cycle takes feed gas H_2 and N_2 from electrolysis and air separation respectively. Tetrahydrofuran (THF) inside the reactor is the solvent and ethanol (EtOH) is the proton source. A pressure gradient is used for avoiding flooding in the gas compartment N_2 or H_2 (**Figure 5.6**), Lithium is used for breaking the N_2 triple bond.

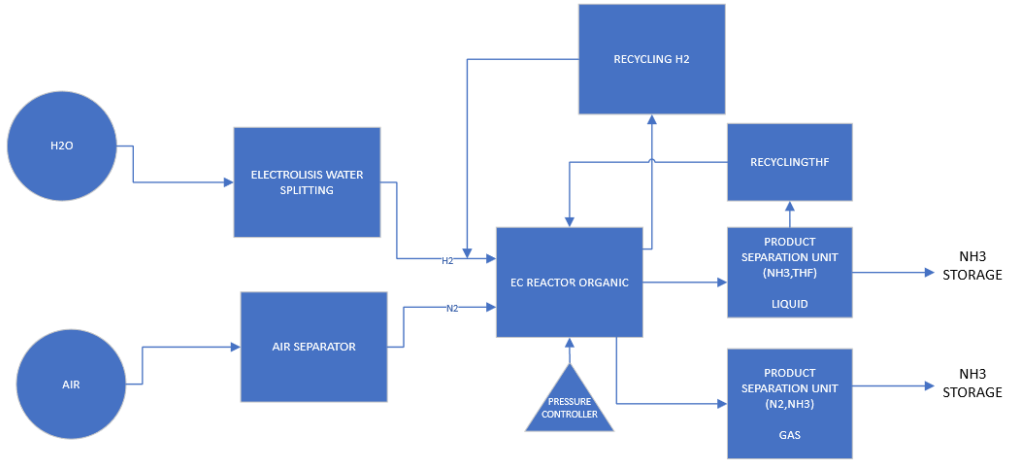

Figure 5.6 *- Schematic process diagram for Electrocatalytic process in organic environment with Lithium cycle*

5.4.4.3 | EC with ILs description

As described in section 1.5.2.4, Electrocatalysis mediated by Ionic Liquids (ILs) is a technique where N_2 and H_2 were flowed into a batch reactor containing the ILs, a catalyst (cathode) a reference, and a counter electrode (anode). Gaseous products are separated (H_2 and N_2), and NH_3 into IL needs to be separated and IL recycled (**Figure 5.7**).

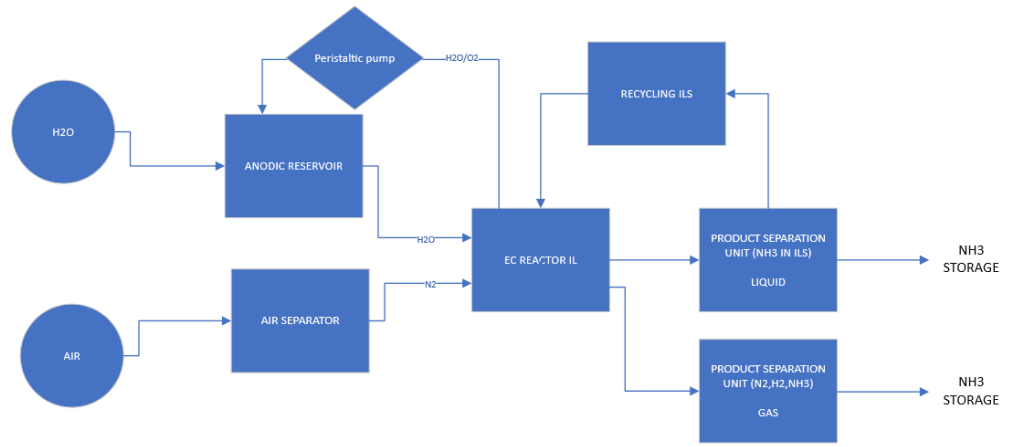

Figure 5.7 *- Schematic process diagram for Electrocatalytic process in Ionic Liquids environment*

5.4.4.4 | CapEx for electrochemical technologies

The main contributors to the capital expenditure are the following:

- Electrodes: The purchase of specific electrodes for electrochemical tests, such as platinum or graphite, with gas-diffusion layers that support the catalysts.
- Membranes: Enable protonic or anionic exchange between the cathodic and anodic compartments.
- Dedicated electrochemical cell: The electrochemical cell is the equipment that houses the electrodes and the testing solution (purchase or construction of electrochemical cells).
- Potentiostat/Galvanostat: These instruments are used to control/monitor the potential or current during an electrochemical test. The purchase of a potentiostat or galvanostat represents an investment in laboratory equipment.
- Analysis tools: Other analysis tools, such as spectrometers or imaging instruments, may be necessary to acquire data during electrochemical tests. The purchase of these instruments is a capital expense.
- Peristaltic pumps: Under flow conditions, it is necessary to recirculate the electrolyte to avoid electrode polarization.
- Flow mass controller: Necessary to control the flow rate of Feed Gas reagents (N_2 and/or H_2).

5.4.4.5 | OpEx for electrochemical technologies

- Catalytic Precursors: It is necessary to take into consideration the cost of materials for preparing the catalysts (this cost varies from catalyst to catalyst).
- Solvent Cost
- Electricity Cost

5.4.4.6 | Electrochemical technology notes

Furthermore, focusing on individual needs, the **EC in an aqueous environment** requires a Water Purification System: The water used in electrochemical tests

must be of high purity. Installing water purification systems, such as reverse osmosis systems, is an equipment investment (CapEx).

In **EC in organic environment** (Lithium cycle), a specific testing chambers or environments need to be created to test lithium-related technologies. The design and construction of these structures can be regarded as capital expenditures (Capex). Safety and environmental control measures or specific environmental control are required to ensure secure and reliable testing conditions, the associated costs can be considered capital expenditures (CapEx).

Ionic Liquids (ILs) need a Ionic liquid purification and management system, if the ionic liquid must be prepared or handled in a particular manner, the purification system or management system may need to be customized (CapEx). In **Table 3.1**, all the main costs for electrochemical technologies discussed are reported.

	EC-Aquous	**EC-Li cycle**	**EC-ILs**
CapEx	Platinum Wire (4.06€/cm) [1] Water purification system (4'271€/pz) [4] Membranes (0.14-0.20€/cm^2)[2] Electrochemical cell (20-100€/m^2) Potentiostat/Galvanostat (10-50'000€/pz) [5] Peristaltic Pump (500-2'000€/pz – 100€/channel – 15-20€/W) [3]	Platinum Wire (4.06€/cm) [1] Membranes (0.14-0.20€/cm^2)[2] Stainless-Steel electrochemical cell (50-200€/m^2) Potentiostat/Galvanostat (10-50'000€/pz) [5] Micropressure controller Peristaltic Pump (500-2'000€/pz – 100€/channel – 15-20€/W) [3]	ILs purification system Peristaltic Pump (500-2'000€/pz – 100€/channel – 15-20€/W) [3]
OpEx	Gas Diffusion Layer o Metal surface [1-2] (0.12€/cm^2 – 7€/cm^2) Ultrapure water (2.67€/L) [1]	Stainless-steel mesh (0.02€/cm^2)[2] Tetrahydrofuran (142€/L) [1] Lithium perchlorate (3.35€/g) [1]	ILs (12€/g) [1] Electricity

	Sodium Sulphate (24.00€/kg)[1]	Electricity
	Electricity	

1 - Merck (price related to area or weight, are calculated on the maximum amount of chemical available in the store for piece for single purchase)
2 -fuelcell store (price related to area calculated on the maximum area available in the store 40x40cm for single purchase)
3-drifton (https://www.drifton.eu/shop/9-flow-rate-tube-pumps/2402-labn1-peristaltic-flow-rate-pump/) peristaltic pump price could variate based on the channels number, for this kind of pumps the power is the same, 50W, range 0-0.6L min^{-1}
4 - https://profilab24.com/en/laboratory/water-stills-treatment/elga-water-purification-system-purelab-quest
5 – www.metrohm.com

Table 3.1 *– CapEx and OpEx for electrochemical technologies.*

5.4.5 | Plasma Technologies

5.4.5.1 | Thermal Plasma reactor analysis

Thermal plasma reactor is an empty reactor of different dimension, where in the head a plasma jet generates an Ar plasma. N_2 and H_2 as reagents are injected in the line of non-ionized Ar. The produced ammonia, Ar, N_2 and H_2 are pumped continuously outside of the reactor. Plasma arc-torch works in a sub-atmospheric pressure of 40 kPa, and high temperatures (800 < T < 3000°C).

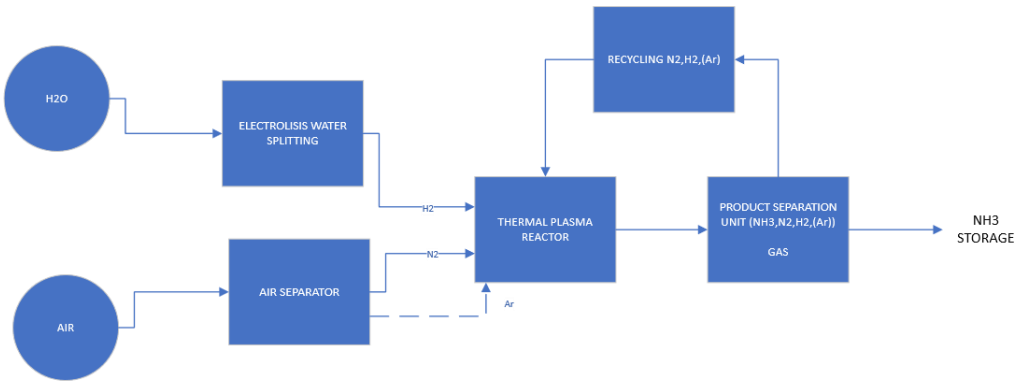

Figure 5.7 *- Schematic process diagram for Plasma-Catalytic process for Thermal-Plasma*

5.4.5.2 | TP-SOEC analysis

TP-SOEC match a technology to produce H_2 from H_2O (Solid Oxide Electrolysis) with Thermal plasma, where the plasma is made with RF (Radio Frequency) power supply on N_2 flow (reagent gas and plasma gas)[3].

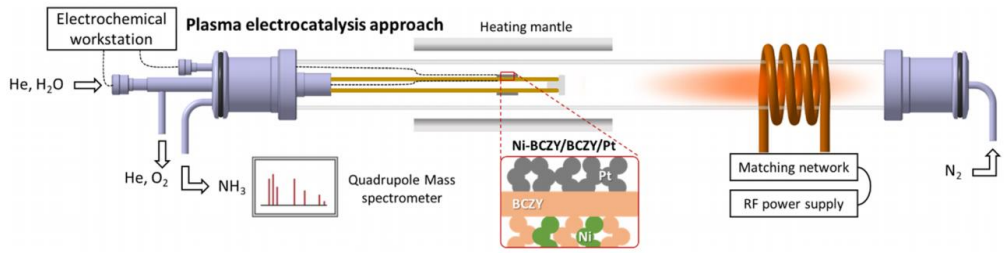

***Figure 5.8** - Schematic process diagram for Plasma-Catalytic process for Thermal-Plasma Solid Oxide Electrolysis.*

5.4.5.3 | Non-Thermal Plasma analysis

Non-thermal plasma reactor works with a H_2:N_2 ratio that flows into the alumina tubular reactor, packed with catalyst. Applying a tension higher than breakdown voltage, plasma is generated and the reaction starts.

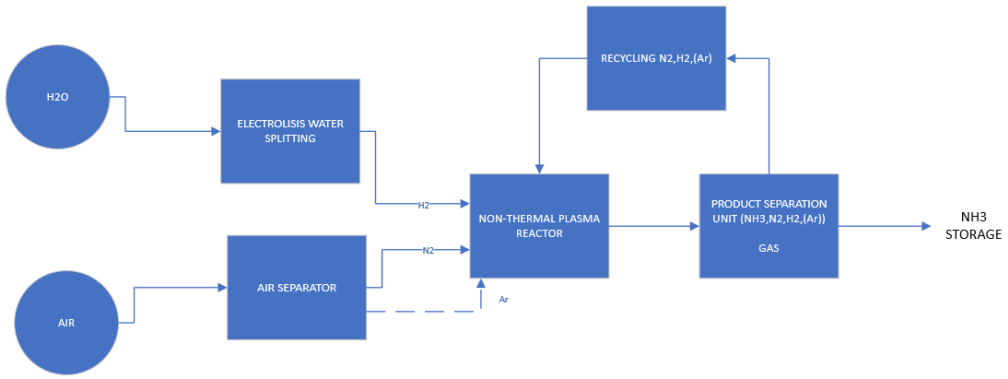

***Figure 5.9** - Schematic process diagram for Plasma-Catalytic process for Non-Thermal Plasma process.*

5.4.5.4 | Hybrid-Plasma electrocatalysis analysis

Hybrid plasma-electrocatalytic reactor[4] works with air (as feed gas). Flowing in the plasma jet reactor (plasma bubbler), plasma generates Nitric and Nitrous Oxide in solution (Acid Solution 1mM H_2SO_4) and intermediate species are reduced into ammonia from the cathode (Copper Nanowires). Ammonium in solution has to be separated.

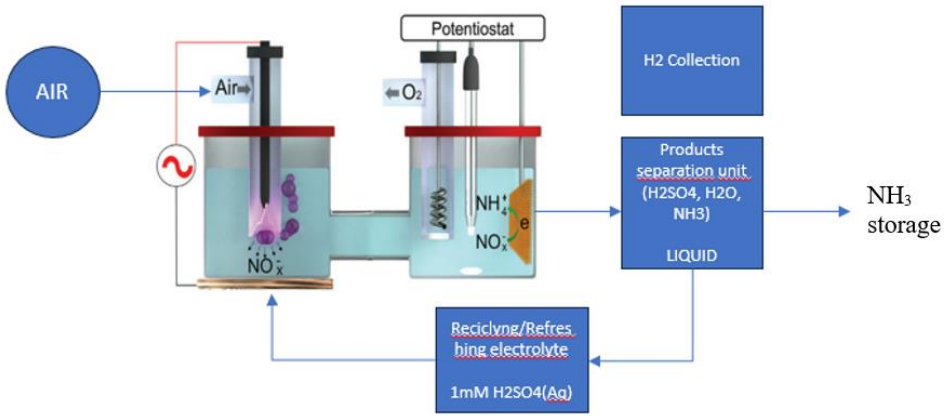

***Figure 5.10** - Schematic process diagram for Plasma-Catalytic process hybrid plasma-electrocatalysis process.*

5.4.5.5 | CapEx for plasma technologies

Plasma-based methods have almost the same capex

- Plasma Torch or Arc System: The acquisition of the primary plasma torch or arc system, which generates and sustains the thermal plasma, is a significant CapEx component. This includes the purchase of the plasma torch itself and any associated power supply equipment.
- Gas Supply Systems: Gas supply and control systems are essential for delivering the working gas (usually a gas such as argon or nitrogen) to the plasma torch. This includes gas storage tanks, flow controllers, and related infrastructure.

- Facility Construction: If a specific facility or lab setup is needed to house the plasma system, the construction and outfitting of the facility will be part of the CapEx.
- Safety Measures: Safety measures such as ventilation systems, fire suppression systems, and safety equipment may be required to ensure safe operation. The costs of these safety measures can be considered part of the CapEx.
- Instrumentation and Control Systems: The purchase of specialized instrumentation, control systems, and data acquisition equipment for monitoring and controlling the plasma process.
- Flow mass controller: Necessary to control the flow rate of Feed Gas reagents (Air, N_2 and/or H_2).

5.4.5.6 | OpEx for plasma technologies

Operational Expenditure (OpEx) for plasma technologies mainly includes expenses related to electricity for plasma generation and reagents for the synthesis of catalysts.

5.4.5.7 | Plasma technologies notes

In order to achieve plasma-electrocatalization, it is imperative to consider both the CapEx and OpEx associated with plasma and electrocatalysis. In **table 3.2**, plasma technologies costs are summarized.

	Thermal Plasma	**TP-SOEC**	**Non-Thermal Plasma**	**Hybrid Plasma-Electrocatalysis**
CapEx	Cascade arc [2-3] Reactor [2-3]	RF plasma sources SOEC coupled reactor (custom) Oscilloscope (~15-5€/MHz – 900€/pz)	Generator, Amplifier, Transformer (~30’000€/pz max 500W) 60€/W Oscilloscope (~15-5€/MHz – 900€/pz)	Plasma-Bubbler (~1000€/pz) Reactor (custom H-Type cell, ~9€/mL – 600€/pz) Potentiostat/Galvanostat (10 -50’000€/pz)

			Alumina tube ($69€/dm^3$) Stainless steel electrode	Platinum electrode ($75€/cm^2$) Reference Electrode
OpEx	H_2 source 1'440-3'605 €/t[1] Electricity	Electricity	H_2 source 1'440-3'605 €/t[1]	Copper electrode ($0.19€/cm^2$)

1 - Cost of electrolysis-based, renewable hydrogen ranges
2-https://www.tue.nl/en/our-university/about-the-university/support-services/equipment-and-prototype-center/products/plasma-deposition/plexis
3-https://www.tue.nl/en/our-university/about-the-university/support-services/equipment-and-prototype-center/products/plasma-deposition/depo-2-experiment

Table 3.2 *– CapEx and OpEx for plasma technologies.*

5.5 | Summary Table of Benefits and Drawbacks

The **table 3.3** summarizes the principal benefits and drawbacks of technologies taken in exam:

		Benefits	Drawbacks
Thermal-Pressure processes	**Haber Bosh (HB)**	• Production of NH_3 on a large scale; • Current industrial-level process for the production of fertilizers, explosives, • TRL: Commercial • Optimized Process; • Lowest LCOA (Levelized Cost of Ammonia) •	• High energy consumption (high P and T); • Considerable amount of CO_2 emitted as a byproduct; • Complex pure hydrogen generation system; • Expensive;
	g-HB	• Production of NH_3 on a large scale; • Reduction of CO_2 emissions due to electrification (from renewable sources); • Current industrial-level process for the production of fertilizers, explosives; • TRL: Commercial	• High energy consumption (high P and T); • Technical complexity limited by electric motor technology (batteries/accumulators); • Intermittency of renewable sources not always available;

	Magnetic Induction Heating	• Ready heat up due to hysteresis losses; • Deliver heat locally; • Selective heating;	• Catalytic magnetic hyperthermia TRL 1-3 (some biomedical TRL 8-9); • Heating limitations with the depth of the ferromagnetic material; • Difficulty in maintaining stable the reaction conditions; • Loss of activity in the material due to the conditions;
Electrocatalytic-based processes	**Aqueous environment**	• Small-scale and decentralized NH_3 production; • Less energy-intensive than a traditional HB process, ambient P and T; • Safe solvent; • O_2 (Oxygen Evolution Reaction, OER) as a product of the anodic reaction that can be used in other applications; • Easy management of products and disposal;	• Hydrogen Evolution Reaction (HER) as a competitive reaction at the cathode to the desired Nitrogen Reduction Reaction (NRR); • Corrosive effects of water; • Pure water is non-conductive and thus requires a salt; • Low solubility of N_2 in H_2O; • TRL Electrocatalysis 2-4;
	Organic	• Limiting the protons availability; • Efficiencies improvement; • Wide availability of organic solvents;	• The use of organic solvents needs to be managed for safety, as well as the products and byproducts; • The implementation of the Lithium cycle requires operating in a Glove Box; • In some cases where the EtOH/EtO- shuttle system is also present, the limit affects the test time; • The catalyst support needs to be changed because the Gas Diffusion Layers (GDL) are hydrophobic. This involves replacing steel meshes and/or applying a pressure gradient to prevent leaks; • TRL Electrocatalysis 2-4;
	Ionic Liquids	• High/Good solubility of N_2 compared to traditional solvents; • High efficiencies; • Thermal stability;	• High ILs costs; • Toxicity; • Complex recycling or reuse in separation/purification processes; • TRL Electrocatalysis 2-4;

		• Possibility to reuse / Recycling;	
Plamsa-catalysis based processes	**Thermal Plasma (TP)**	• Accessible to small-scale, on-site production;	• Usually high temperature needed; • Conversion and efficiency need to be improved; • Available only at small scale; • Cost of Plasma apparatus; • No control on side reaction; • TRL TP: 2-4;
	TP-SOEC	• SOEC lower energy input (250 kJ/mol H_2) than PEM (280); • Nitrogen and Hydrogen feed in a single unit; • High SOEC efficiency; • Synergy with plasma;	• High temperature needed for SOEC; • Cost of SOEC; • Cost of Plasma apparatus; • Critical material; • TRL SOEC 5-6; • TRL Plasma: 2-4; • No control on side reaction made by plasma;
	Non-Thermal Plasma	• Lower temperature compared to traditional plasma (T.R. – 160°C); • Energy saving; • Selectivity; • Fast Reaction; • Scalability/Modularity of the plant; • Dielectric Barrier Discharge offers a good match between plasma and catalysis;	• System complexity; • High initial equipment costs; • Lack of control over undesired reaction (radical intermediates); • Spatial and temporal non-uniformity of discharge conditions; • TRL Plasma 2-4;
Hybrid Plasma Electrocatalysis		• Reaction intermediates (NO_x) as activated nitrogen molecules; • Safe environment; • Aqueous Environment; • Moldable;	• Lab scale • Copper deactivation • 1cm^2 tests • TRL : 2-3

Table 3.3 *– Summary of benefits and drawbacks of the technology of producing ammonia*

5.6 | Boundaries conditions

Boundary conditions are necessary to fix some variables for the purpose of calculation and are stated below. The comparison will have on the basis of the electrical demand (in kWh) of the individual reactor.

5.6.1 | Starting point

The starting point for all technologies is H_2O and air input, except for the traditional Haber-Bosch process, which uses CH_4 and air, included solely as a reference. The energy efficiency of the SOEC will be taken into account where necessary and included into the calculations. Other costs will be neglected at the moment.

5.6.2 | Hydrogen generation system

As a boundary condition, SOEC technology will be used as the hydrogen production technology for various processes (where needed). SOEC technology as reported by *Rouwenhorst et al.* [9] has an installed capital cost of 935-1865 k€ t_{NH3}/d referred to 2020 with a maximum capacity of 0.2 MW working in the range of 0.3-2.0 A cm^{-2} with a maximum stack lifetime of 30’000h and an energy consumption of 24-27 GJ/t_{NH3}.

5.6.3 | Renewable energy

The choice of which renewable energy to use depends on the previously outlined scenarios (refer to Proposed Scenarios). For **Scenario 1**, only solar energy is considered, while **Scenarios 2** and **3** involve a combination of solar and wind energy[10].

5.6.4 | Electrical input

Table 3.4 reports the electrical input in Wh required for each technology. Assumption made:

- Size plant: 1 ton/d;

- For daily production 10h is assumed;
- For electrochemical technologies, H_2 is generated from H_2O and therefore included in the electrical efficiency calculation;
- Single electrochemical cell voltage is assumed 2 V;
- For plasma reactors and for EC-organic, SOEC, H_2 efficiency is set at 80%;
- SOEC efficiency for TP-SOEC is included into the reported efficiency (i.e. 10%)

Technology	Electrical efficiency %	Total electrical input reactor
EC aq.	29	32.6 MWh
EC org./Li	40	29.6 MWh
EC ILs	60	15.8 MWh
TP	33	0.083 – 0.31 MWh
TP-SOEC	10	98.8 GWh
NTP	20	26.9 MWh
HPE	55-85	29.8 – 46.0 MWh

Table 3.4 *– Electric consumption for each technology calculated on the assumption of 1 ton of ammonia per day*

5.6.5 | Catalyst lifetime

The lifespan of Electrocatalysis, Plasma Catalysis catalysts and ionic exchange membrane has been assumed to be around 1000 operational hours, as reported from *Zhang et al.*[11].

5.7 | Scenarios Introduction

In this part, values (from 1 to 7, where 1 indicates the worst value and 7 the best) have been arbitrarily assigned to certain parameters related to the state of the art of the respective technology under consideration (parameters on plant size/robustness: RLT, Specific NH_3 production, estimated lifetime catalyst, estimated lifetime plant, plant size, efficiency) and operational parameters (such as operating temperatures and pressures, startup/shutdown speed, adaptability

with renewables, safety levels, scalability). Radar charts (**Figure 5.11a, b**) are used to get at a glance the strengths and weaknesses of the relevant technologies.

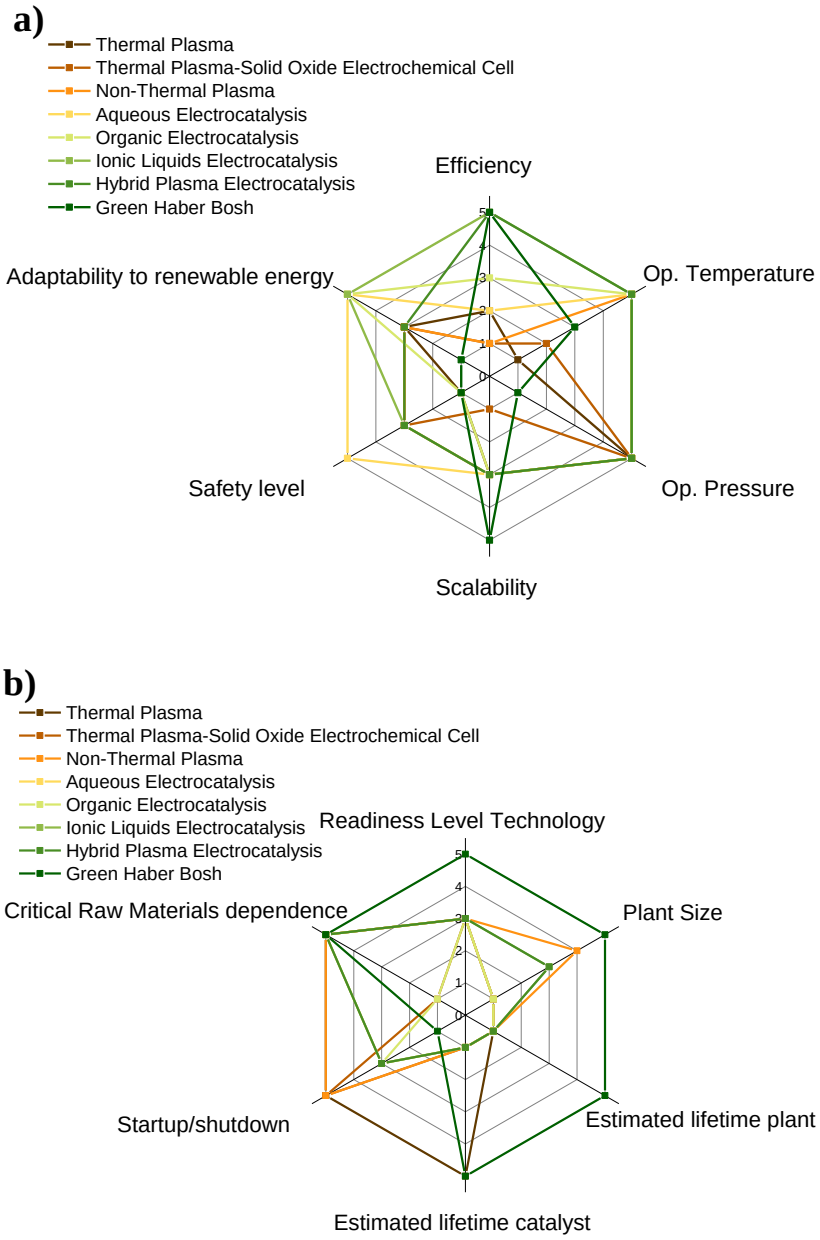

Figure 5.11 *– radar diagrams of a) operational parameters and b) plant parameters for each technology*

It is well established that an abundantly established technology, such as the HB process, has many strengths, as the largest plants can produce up to 6000 MTD [12], but it requires a pure hydrogen production system for synthesis to avoid oxygenated (H_2O, O_2) or sulfur compounds that would poison the catalyst. It is difficult to start or shut down the plant without disrupting production, and due to catalyst activation, the operation can take days or even weeks. In addition, because renewable energies are intermittent, they cannot be used continuously.

If the cost of gas were to increase, perhaps in reference to policies to reduce CO_2 emissions, this could make emerging technologies competitive. Among these technologies such as electrocatalysis, it can be fed with water and electrolyte to support the passage of electrons, with a much faster turn-on and turn-off time, In the case of EC in an aqueous environment, it provides a high degree of safety due to the aqueous environment, at the expense of productivity which is generally low 0.1-29%, compared to the organic environment or ionic liquids which are able to provide higher percentages of efficiency to the detriment of the safety and duration of the reference tests and the relative safety of the presence of organic solvents and metallic lithium.

Additionally, electrocatalysis has the potential for scalability due to the possibility of stacking catalysts to reach a higher surface area, as demonstrated by *Takeda et al.* [13] in which a surface area of 1 m^2 was achieved in an aqueous environment.

In addition to plasma technology, which enables the instantaneous production of ammonia through the supply of pure H_2 and N_2, the presence of impurities such as H_2O in the vapor phase could potentially result in the formation of nitrogen oxides. However, if the impurity level in the vapor phase is approximately 0.14% by weight, the production process consistently focuses on the generation of ammonia[14]. Furthermore, the temperature and pressure conditions required for EC aq. and NTP are comparatively milder. The ease of startup and shutdown aligns perfectly with the intermittent nature of renewable energy sources. TP-

SOEC, which combines thermal plasma and an electrolyzer to provide H_2 within the reactor, offers a compact solution for ammonia production with similar advantages in terms of startup time as NTP. However, it does require higher temperatures for both SOEC and TP operation. Additionally, the use of critical materials in electrode construction poses a drawback for a device with a lifespan of 1-5 years, relative to SOEC technology.

Electrocatalytic technologies and plasma can exhibit a remarkable synergy, enabling the activation of nitrogen into NO_x^- in an acidic solution through the use of a plasma jet. Additionally, this highly adaptable approach could facilitate enhanced electrocatalytic plasma generation, resulting in elevated conversion efficiencies and rendering it an outstanding complement to renewable energies. However, it is important to note that the start-up time is impacted by the conversion of nitrate to ammonium using a copper catalyst, which may take longer for electrocatalytic processes compared to plasma catalytic processes. Despite the immediate production higher energy consumption associated with plasma catalytic processes.

5.8 | Proposed scenarios

The study aims to suggest alternative scenarios that can improve emerging techniques for ammonia production. Four distinct scenarios are outlined as follows:

- **Scenario 0** represents the current state, referencing the traditional HB and green HB process.
- **Scenario 1** envisions a decentralized stand-alone device powered solely by photovoltaics, allowing continuous movement.
- **Scenario 2** entails a medium-sized, decentralized facility capable of utilizing various renewable sources.

- **Scenario 3** implementing magnetic induction heating for pre-existing HB plants (electrification).

One critical consideration within **Scenarios 1, 2,** and **3** revolves around the necessity for the cost of electricity to achieve greater competitiveness compared to the cost of gas.

5.8.1 | Scenario 0: Ammonia produced by traditional and green Haber-Bosh

This is the current scenario, where demand for ammonia is high and high production volumes are needed, in a localized production context.

Ammonia is produced at high temperatures and high pressure (400-600°C and 150-350 bar) in the catalytic HB process fed with an H_2/N_2 mixture produced by SMR and WGS in the first case (the reference). The second case is the production of ammonia using an electrolyzer (as mentioned before, in this scenario and the following one SOEC will be taken into account), which is used for producing Hydrogen, while Nitrogen is supplied by condensation of air (this technique of extraction on nitrogen will be taken into account for this scenario and the followings ones). If fossil fuel prices are low and we require large-scale production, this scenario is to be considered with the most favourable conditions.

The traditional Haber-Bosch approach consumes around 33 GJ/t practically, while theoretically, it is estimated at 26 GJ/t [9]. Plant lifespan ranges from 20 to 25 years, and the catalyst typically lasts 10 to 15 years, achieving an efficiency of 62% to 70%[**Errore. Il segnalibro non è definito.**]. On the other hand, the greener version of Haber-Bosch currently consumes 46-50 GJ/t [9], theoretically estimated at 30-35 GJ/t. According to the *European Association for Storage Energy*[15], its efficiency stands at approximately 50-55%, operating around 8500 hours per year, and an energy density of 5.2 MWh/t.

5.8.2 | Scenario 1: Ammonia produced by decentralized *stand-alone* device

In this scenario, a portable ammonia production device could be utilized: in agriculture for on-site fertilizer creation, in the food industry as a cleaning agent, in chemical synthesis, in decentralized scientific research through mobile laboratories, as a source of green hydrogen for fuel cell vehicles, and as a resource in emergency situations or to start ammonia production in remote areas where the cost of transporting raw materials would greatly increase costs. The flexibility of this device provides an adaptable and practical approach to meet diverse needs across multiple sectors.

Technologies that can be utilized on a small to medium scale and integrated into small-scale plants are being considered in this scenario. These technologies are transportable if required and are capable of producing 1-100 kg per day of ammonia (kg/d). To ensure portability, these devices will be equipped with photovoltaic panels to harness solar energy in a sustainable manner. This kind of device should possess the capability to be utilized in situations where the construction of a physical plant is not feasible and/or due to the necessity of on-site ammonia production[16].

Electrocatalysis (aqueous) and Hybrid EC-PC are well-suited for this objective as they offer convenience and operate under mild conditions (room temperature and ambient pressure), eliminating the need for additional electrolysis equipment to produce H_2 on-site. EC and HPE may require occasional replenishment of the electrolyte to maintain the pH balance, as charges and electrons are consumed during electrochemical processes to sustain the charge. The TP-SOEC could also be suitable for this scenario.

In this scenario the proposed technologies, such as EC in aqueous environment, which have a current energy consumption of 135 GJ/t and a theoretical one of 27-29 GJ/t, the process efficiency currently can reach 25% in some cases, Hybrid

Plasma-Electrocatalysis (HPE) and TP-SOEC can also lend themselves well to this application the energy consumptions (referring to the reactor) reported are 253 kWh/kg_{NH3} and 605 MJ/mol_{NH3} respectively, with efficiencies of 55-85% and 10% respectively.

Aqueous EC and HPE work at ambient temperature and pressures, while TP-SOEC being an all-in-one device requires high operating temperatures for both TP and SOEC (400-650°C) and atmospheric pressure.

5.8.3 | Scenario 2: Ammonia produced by small to medium-sized plants

In this scenario, the plant being considered is a larger plant compared to the one examined in the previous instance, and thus not able to be transported. This can be combined with various renewable energy sources such as Wind, Solar, and hydroelectric power[17].

For a plant possessing these theoretical dimensions of 100-500 t/y, the implementation of NTP and TP would be feasible as there are no spatial restrictions. By utilizing electrolyzers, the technique becomes more favourable in terms of performance compared to using non-thermal plasma. The usage of thermal plasma entails high temperatures along with the utilization of argon as a carrier gas or plasma gas. NTP/TP needs Hydrogen and Nitrogen as feed gas both compressed. With adequate safety levels, electrocatalysis in an organic environment and electrocatalysis with ionic liquids could also be considered, with the drawback that the organic solvent must be purified from the ammonia produced and the proton source must be restored. In this scenario, having taken into consideration all the pros and cons, the best choice could be the NTP, given the better productivity, and start-up/shut-down speed, at the expense of greater energy consumption. Substituting hydrogen and compressed nitrogen with air would produce nitrogen oxides, which could later be transformed into the corresponding acids (nitric, nitrous) and subsequently converted into NH_3/NH_4^+.

This principle is exploited in HPE where a plasma jet is generated by feeding air to it in batches, and then catalyses the reduction reaction on the activated nitrogen molecule (NO_x^-). Electrocatalytic conversion from nitrate or nitrite, to ammonia is around 80-97%[18]. Therefore, this technology can also be used in this type of production.

Generally, many renewable energy sources should be used to overcome the problem of energy intermittency. Especially if we consider that the irradiation during the hours when the sun is at its zenith is maximum, and also considering that as latitude increases it decreases. Thus, the excess energy that is not stored, can be better harnessed by plasma catalysis, which has a higher energy demand.

Non-thermal plasma and thermal plasma have energy consumptions of 120-155 GJ/t (theoretical of 60-70 GJ/t) and 58.8-211 GJ/g_{NH3} relative to the reactor, respectively, with efficiencies ranging up to 20%[19,20] for NTP and 30%[21] for TP with arc torch. NTP works in self-heating conditions (tendentially cold plasma is around R.T. to 180°C) and ambient pressure, on the other hand, TP with an arc torch, reaches a considerably higher temperature (800 < T < 3'000 °C).

5.8.4 | Scenario 3: Large facilities

In this specific scenario, the requirement arises for a substantial ammonia production, implementing electrification systems, specifically magnetic induction heating, to the existing HB green plants with necessary adjustments made to the reactor in terms of the heating mechanism.

The suggested scenarios are forecasts or suggestions for the potential of scaling up the systems from a small facility to an industrial-scale one, even though the current technologies are not highly advanced and currently only allow for this conceptually. The shared characteristic among electrochemical technologies is that the byproduct of producing hydrogen can be utilized in instances when the renewable energy source is not accessible, as the hydrogen storage and oxygen

storage at the anode can be employed in a fuel cell to generate electricity using H_2 and O_2.

The diverse technologies pertinent to sub-case 1 encapsulate the aforementioned aspects. This is juxtaposed with sub-case number two, wherein the existing plant remains unchanged, except for the variation in the mode of power supply, notably the adoption of magnetic induction heating. The scarcity of data in the existing literature about this specific technology is notable; however, a patent outlines its implementation to transition extant gas-based reactors to units heated through this novel induction heating method[22].

5.9 | Discussion

In scenario 1, the most cost-effective technologies in terms of size, performance, and safety are (EC) electrochemical technologies, TP-SOEC (Thermal Plasma – Solid Oxide Electrolysis Cell) given its compactness and HPE (Hybrid Plasma Electrocatalysis) reactor given its versatility. TP-SOEC and HPE are relatively new technologies compared to the electrocatalytic approach. Because based on electrical input, it is possible to see that TP-SOEC is still a fairly immature technology with few literature references (first published in 2021), while electrocatalysis in an aqueous environment dates back to 1983[]. In fact, with the assumptions and information previously gathered, the electrical demand of TP-SOEC turns out to be 98.8 GWh, compared to 32.6 MWh of aqueous EC, and 29.8-46.0 MWh of HPE.

Electrocatalysis in an organic environment than EC with ionic liquids (29.6 and 15.8 MWh respectively) may lend themselves well for this purpose. But in the case of organic EC with lithium cycle, would increase the controls related to safety since operating with Li and organic solvents could be risky. Then also EC with ionic liquids, the purification of ILs would require extra equipment. Whereas EC and HPE would only have the aqueous electrolyte to monitor or add.

HPE can still be perfected, since as a versatile and scalable technique it can be scaled up, certainly research is moving in that direction as well. Aqueous EC, abundantly studied, has many limitations because of the competitive reaction of hydrogen production (HER). Thus, for this technology the ideal candidates might be EC and HPE.

In scenario 2, the possibility of a larger plant to produce ammonia in a delocalized manner is considered. In this scenario we could recall all technologies, where comparing the energy demands of individual reactors, the lowest electrical consumption is shown by TP (Thermal Plasma) technology with a relative consumption per single reactor of 83-310 kWh, EC-ILs in second place and NTP in third (15.8 and 26.9 MWh). in this case, plasma technologies could be very competitive as they have very fast uptime compared to EC. HPE being currently under development, and having the activation of N_2 to NO_x^-, by plasma and then in solution electrocatalysis by copper nanowires, could also be competitive although requiring a higher electrical demand (29.8-46.0 MWh). Thus, for this scenario, the technologies that best suited are TP, NTP, and HPE.

In scenario 3, heating by magnetic induction is a method of electrification as an alternative to steam methane reforming (SMR), to heat the HB reactor in a controlled and more efficient manner and with less energy expenditure. In addition to reducing its environmental impact, the scalability of the electrification process would also allow for greater modulability, offering flexibility to production. On the other hand, only ferromagnetic materials can be scaled up by this technology, so one has to think about whether to put coils inside the reactor or make the reactor transparent to magnetic induction, always trying not to exceed the Curie temperature (the temperature at which materials lose their ferromagnetic properties).

The use of magnetic induction may require further study and testing to demonstrate its effectiveness and reliability in the specific context of Haber-Bosch processes.

5.10 | Conclusions

To conclude this extensive section, further information should be collected, processed, and additional boundary conditions should be formulated. Currently, ammonia production primarily occurs through the Haber-Bosch process (both traditional, blue HB with Carbon capture, or Green), as described in scenario 0.

The technologies presented here are potential candidates to achieve global goals, both in reducing CO_2 emissions related to traditional HB (grey HB) and in sustainable ammonia production leveraging renewable energies. These technologies also serve as a vector for green hydrogen production through ammonia decomposition, which could reduce hydrogen transportation costs.

This thesis aims to study the behaviour of various catalysts examined in Chapters 3 and 4 for the production of ammonia via electrocatalysis and plasma-catalysis. In this chapter, these technologies (along with others available in the literature) have been analysed from an economic standpoint, assuming specific requirements represented by scenarios. Solutions have been suggested leveraging the strengths and weaknesses of the different technologies. Looking ahead in the long term, in 10 years the current energetic scenario could change due to the increased need to transition to renewable energies. We could witness greater integration of these technologies, leading to a more efficient and sustainable ammonia production due to enhancements in productivity resulting from catalyst optimization (increased conversion and yields on laboratory scale). After consolidating the process on a laboratory scale (TRL 4), optimization of electrochemical and plasma reactors followed by industrial-scale scale-up, will be necessary before the technology could be used in this proposed scenarios. Moreover, the adoption of favourable policies and incentives for sustainable production could accelerate this transition.

For this reason, scenarios 1, 2, and 3 could work synergistically, cooperating to close the production gaps between small, medium, and large scales, respectively. As the first scenario operates as a stand-alone device, it might enhance the potential for relocating plants, delivering ammonia where needed and producing it on-site. The second scenario acts as an intermediary between the HB and scenario 1, bridging the gap between large and small scale. Scenario 3 has been considered to indicate the potential for making the HB process more sustainable. Therefore, a synergistic collaboration among these three scenarios could be the subject of further studies.

A first step towards creating stand-alone devices could involve developing an artificial leaf, as described in **Chapter 6**, supported by a photovoltaic module but dedicated to producing ammonia, and in a scale-up perspective, the creation of artificial trees[23].

5.11 | Supporting Information

A - Table of technology readiness level meaning
B - Energy Consumption
C- Spider charts parameters value meaning
D- Spider charts parameters evaluation
E- Definitions

A - Table of technology readiness level

Technology Readiness Level (TRL) for the previously mentioned technology, means the *technology maturity grade* and is a value from 1 ("*Observed fundamental principle"* to 9 (*"Real system tested in an operative environment (competitive production, commercialization)"*). For the traditional HB, process TRL is equal to 9; TRL for the EC and for NTP is around 2-4; TP processes for producing NH_3 have a level of 1-2, reach TRL of 4-7 for NO_x removal and 3-5 for NO_x synthesis, Magnetic Induction heating applied on catalysis reach also the laboratory scale value (TRL 1-3), the meaning of all values are expressed in Table 1.

TRL	Description
1	Considered fundamental principles
2	Formulated the technology concept
3	Experimental proof of concept
4	Technology validated in the laboratory
5	Technology validated in an industrially relevant environment
6	Technology demonstrated in an industrially relevant environment
7	Prototype system demonstrated in an operational environment
8	Complete and qualified system
9	Real system tested in an operational environment (competitive production, commercialization)

Table S5.1 *- Technology Readiness Level (TRL) from the European Community* [24]

B - Energy Consumption

When examining the total energy consumption, it is evident that the traditional Haber-Bosch (HB) process currently has an energy consumption of 33 GJ per ton. The calculated theoretical energy consumption for HB ranges from 22 to 26 GJ per ton. Conversely, the green Haber-Bosch process has an energy consumption of 46 to 50 GJ per ton, with a theoretical range of 30 to 35 GJ per ton.

With the introduction of new technologies in the preliminary stages, it becomes apparent that the energy consumption increases significantly. Electrocatalytic processes, for example, exhibit an overall energy consumption of 135 GJ per ton, with a calculated theoretical consumption of 27 to 29 GJ per ton. Non-thermal plasma catalytic processes, on the other hand, display a range of 120 to 155 GJ per ton, with a theoretical range of 60 to 70 GJ per ton. The higher theoretical consumption is a result of the inherent energy requirements of the process.

Thermal plasma processes have an energy consumption (calculated value) on the actual reactor ranging from 58.8 to 211 GJ per gram of NH_3. In comparison, TP-SOEC has a reactor energy consumption of 605 MJ per mole of N. The hybrid plasma electrocatalysis process is another noteworthy development in this field.

C- Spider charts parameters value meaning

The evaluation was made by assigning a value from 1 to 5, where 1 is the worst value and 5 is the best, relative to the parameters, if it is not possible to have a rating of five, the rating is reduced to three values (1 worst, 3 average, 5 best) or two (1 worst, 5 best).

- Electrical efficiency (Higher efficiency is evaluated with a higher number):

1: up to 20%, 2: up to 30%, 3: up to 40%, 4: up to 50% 5: more than 50 %

- Operational temperature (Lower operative temperature is evaluated with a higher number):

1: 800+°C, 2: 800-500°C, 3:500-300°C, 4: 300-50°C 5: RT

- Operational pressure (Lower operative pressure is evaluated with a higher number):

1: 100+ bar, 5: 1 bar

- Scalability (A scalable plant is evaluated with a higher number):

5: Large (High possibility to scale up the system, a large plant could be built in dimensional terms, no critical limitation) 3: Medium (average dimension of the plant, modularity of reactor and size, some limitation) 1: Small (Critical limitation in the facility of increasing the dimensions of the reactor)

- Safety Level (A Safer plant is evaluated with a higher number):

1: High risk (process works with high risk for health or environment; restrictions are applied; bypasses are highly penalizing or difficult; Block by technology limitation) 3: Moderate risk (restricting solutions are preferred; limitation to technology development but not blocking the activities) 5: Low risk (restricting solutions unlikely to be preferred; restricting specific process layouts that have many bypasses)

- Adaptability to renewable energy (better adaptability is evaluated with a higher value):

5: High adaptability (the system can work with renewable energy, does not depend on energy discontinuity and requires less energy) 3: Medium adaptability (The system manages to work with the energy produced by renewable energies, the process does not depend on the continuity of the process, but the process involves high energy demand) 1: Low adaptability (the technology is strongly affected by the intermittency due to renewable energy, the process is strongly linked to energy continuity. the process works continuously without interruptions or possibility of interruption. low energy demand)

- Critical raw material dependence (Lower dependence is evaluated with a higher number):

1: High (Strong dependence from critical material (raw or not), without technology, is not working; no possibility to substitute the material(s) in object) 2: Medium (case of critical materials that works better than other but non block the process, possibility to substitute the material with non-crit ones) 3: Low (No critical material needed, the using of critical material is indifferent respect another one)

- Readiness Level Technology (higher RLT is evaluated with a higher value):

1: RLT (1) 2: RLT (2-3), 3: RLT (3-4), 4 RLT (5-6), 5: RLT (7-9)

- Plant Size (Larger plant size is evaluated with a higher value):

1: 1 mg/d, 2: 0.01-0.09 g/d, 3: 0.1-0.9 g/d, 4: 1-10 g/d , 5: up to 6000 t/d

- Estimated lifetime plant:

1: 1-5y , 5: 20-25y

- Estimated lifetime catalyst:

1: 1000h, 5: 20-25y

- Startup/shutdown (lower startup/shutdown time is evaluated with a higher value):

1: 1 week 3: 0.5-1 hour 5: 1-10 minutes

D- Spider charts parameters evaluation

Operational Parameters	gHB	EC aq	EC org	EC ILs	TP	TP-SOEC	NTP	HPE
Efficiency	5	2	3	5	2	1	1	5
Op. Temperature	3	5	5	5	1	2	5-4	5
Op. Pressure	1	5	5	5	5	5	5	5
Scalability	5	3	3	3	3	1	3	3
Safety level	1	5	1	3	1	3	3	3
Adaptability to renewable energy	1	5	5	5	3	3	3	3

Table S5.2 *– Spider chart parameter evaluation for Operational Parameters.*

Plant Parameters	gHB	EC aq	EC org	EC ILs	TP	TP-SOEC	NTP	HPE
Readiness Level Technology	5	3	3	3	3	3	3	3
Plant Size	5	1	1	3	1	1	4	3
Estimated lifetime plant	5	1	1	1	1	1	1	1
Estimated lifetime catalyst	5	1	1	1	5	1	1	1
Startup/shutdown	1	3	3	3	5	5	5	3

Critical Raw Materials dependence	5	5	1	5	5	1	5	5

Table S5.3 *– Radar chart parameter evaluation for Plant Parameters.*

E- Definitions

- **Electrical efficiency:** $\frac{\boldsymbol{Electricity\ converted\ into\ ammonia}}{\boldsymbol{input\ electricity}} \boldsymbol{x100}$
- **Plant Size**: mass of ammonia produced per day
- **Estimated lifetime plant**: Lifetime of the plant in year(s)
- **Estimated lifetime catalyst**: Lifetime of catalyst expressed in year(s) or operative hour
- **Energy Consumption**: Energy consumption of process (if not specified is relative to the whole plant)
- **Theoretical Energy Consumption**: Relative Energy consumption is theoretically achievable
- **Startup/Shutdown:** time employed by the system to reach a steady state of production
- **Specific NH_3 Production:** normalized mass of ammonia produced per mass of catalyst per hour
- **Op. Temperature**: Operative temperature of the main reactor in Celsius
- **Op. Pressure:** Operative pressure of the main reactor in bar
- **CapEx:** capital expenditure, starting investments
- **OpEx:** operative expenditure value per mass product, chemical, electrical and consumables

5.12 | References

[1] D'Angelo, S. C., Cobo, S., Tulus, V., Nabera, A., Martín, A. J., Pérez-Ramírez, J., & Guillén-Gosálbez, G. (2021). Planetary boundaries analysis of low-carbon ammonia production routes. *ACS Sustainable Chemistry & Engineering*, *9*(29), 9740–9749.

[2] Dechany, A., Van Geem, K., & Proost, J. (2023). Process implications of electrifying ammonia production. *Current Opinion in Chemical Engineering*, *40*, 100915.

[3] Sharma, R. K., Patel, H., Mushtaq, U., Kyriakou, V., Zafeiropoulos, G., Peeters, F., Welzel, S., van de Sanden, M. C., & Tsampas, M. N. (2020). Plasma activated electrochemical ammonia synthesis from nitrogen and water. *ACS Energy Letters*, *6*(2), 313–319.

[4] Sun, J., Alam, D., Daiyan, R., Masood, H., Zhang, T., Zhou, R., Cullen, P. J., Lovell, E. C., Jalili, A. (Rouhollah), & Amal, R. (2021). A hybrid plasma electrocatalytic process for sustainable ammonia production. *Energy & Environmental Science*, *14*(2), 865–872.

[5] Ofori-Bah, C. O., & Amanor-Boadu, V. (2023). Directing the wind: Techno-economic feasibility of green ammonia for farmers and community economic viability. *Frontiers in Environmental Science*, *10*.

[6] Zhang, H., Wang, L., Van herle, J., Maréchal, F., & Desideri, U. (2020). Techno-economic comparison of green ammonia production processes. *Applied Energy*, *259*, 114135.

[7] Ponikvar, Ž., Likozar, B., & Gyergyek, S. (2022). Electrification of catalytic ammonia production and decomposition reactions: From resistance, induction, and dielectric reactor heating to electrolysis. *ACS Applied Energy Materials*, *5*(5), 5457–5472.

[8] Fernandez, C. A., & Hatzell, M. C. (2020). Editors' choice—economic considerations for low-temperature electrochemical ammonia production: Achieving Haber-Bosch parity. *Journal of The Electrochemical Society*, *167*(14), 143504.

[9] Rouwenhorst, K. H. R., Krzywda, P. M., Benes, N. E., Mul, G., & Lefferts, L. (2021). Ammonia Production Technologies. Techno-Economic Challenges of Green Ammonia as an Energy Vector, 41–83.

[10] Verleysen, K., Parente, A., & Contino, F. (2023). How does a resilient, flexible ammonia process look? robust design optimization of a Haber-Bosch process with Optimal Dynamic Control powered by wind. *Proceedings of the Combustion Institute*, *39*(4), 5511–5520.

[11] Zhang, S., Yuan, X., Wang, H., Merida, W., Zhu, H., Shen, J., Wu, S., & Zhang, J. (2009). A review of accelerated stress tests of mea durability in PEM fuel cells. *International Journal of Hydrogen Energy*, *34*(1), 388–404.

[12] Ammonia process A6000. (n.d.). Casale SA. https://www.casale.ch/new-plants/ammonia-new-plants/ammonia-process-a6000

[13] Kato, N., Takeda, Y., Kawai, Y., Nojiri, N., Shiozawa, M., Mizuno, S., Yamanaka, K., Morikawa, T., & Hamaguchi, T. (2021). Solar Fuel Production from CO_2 Using a 1 m-Square-Sized Reactor with a Solar-to-Formate Conversion Efficiency of 10.5%. ACS Sustainable Chemistry & Engineering, 9(48), 16031–16037.

[14] Xie, D., Sun, Y., Zhu, T., Fan, X., Hong, X., & Yang, W. (2016). Ammonia synthesis and by-product formation from H_2O, H_2 and N_2 by dielectric barrier discharge combined with an Ru/Al_2O_3 catalyst. *RSC Advances*, *6*(107), 105338–105346.

[15] Power to Ammonia - Gasoline synthesis from H_2 and N_2 by using water electrolysis and Air Separation. (n.d.). https://ease-storage.eu/wp-content/uploads/2018/09/2018.08_TVAC_WG1_TD-Power-to-Ammonia.pdf

[16] D'Angelo, Sebastiano C., Martín, A. J., Cobo, S., Ordóñez, D. F., Guillén-Gosálbez, G., & Pérez-Ramírez, J. (2023). Environmental and economic potential of decentralised electrocatalytic ammonia synthesis powered by solar energy. *Energy & Environmental Science*, *16*(8), 3314–3330.

[17] Ikäheimo, J., Kiviluoma, J., Weiss, R., & Holttinen, H. (2018). Power-to-ammonia in future North European 100 % renewable power and heat system. *International Journal of Hydrogen Energy*, *43*(36), 17295–17308.

[18] Song, W., Yue, L., Fan, X., Luo, Y., Ying, B., Sun, S., Zheng, D., Liu, Q., Hamdy, M. S., & Sun, X. (2023). Recent progress and strategies on the design of catalysts for electrochemical ammonia synthesis from nitrate reduction. *Inorganic Chemistry Frontiers*, *10*(12), 3489–3514.

[19] Bogaerts, A., Tu, X., Whitehead, J. C., Centi, G., Lefferts, L., Guaitella, O., Azzolina-Jury, F., Kim, H.-H., Murphy, A. B., Schneider, W. F., Nozaki, T., Hicks, J. C., Rousseau, A., Thevenet, F., Khacef, A., & Carreon, M. (2020). The 2020 plasma catalysis roadmap. *Journal of Physics D: Applied Physics*, *53*(44), 443001.

[20] Akay, G., & Zhang, K. (2017). Process intensification in ammonia synthesis using novel coassembled supported microporous catalysts promoted by Nonthermal Plasma. *Industrial & Engineering Chemistry Research*, *56*(2), 457–468.

[21] van Helden, J. H., Wagemans, W., Yagci, G., Zijlmans, R. A., Schram, D. C., Engeln, R., Lombardi, G., Stancu, G. D., & Röpcke, J. (2007). Detailed study of the plasma-activated catalytic generation of ammonia in N_2-H_2 plasmas. Journal of Applied Physics, 101(4).

[22] Højlund Nielsen, P. E. (2017). Method for Start-up Heating of an Ammonia Synthesis Converter (Patent No. WO2017186613A1). Retrieved from https://patents.google.com/patent/WO2017186613A1/en

[23] *Finanziato dal MUR il progetto SCOOP di UniMe per lo sviluppo di un albero artificiale che produca H_2 dall'aria con la luce solare*. Università degli Studi di Messina. (2024). https://www.unime.it/notizie/finanziato-dal-mur-il-progetto-scoop-di-unime-lo-sviluppo-di-un-albero-artificiale-che

[24] Technology readiness levels (TRL), HORIZON 2020 – WORK PROGRAMME 2018-2020 General Annexes, Extract from Part 19 - Commission Decision C (2017) 7124

6. | Coupling PV-EC for CO_2RR to fuels

Adapted from "Ampelli, C., Giusi, D., Miceli, M., Merdzhanova, T., Smirnov, V., Chime, U., Astakhov, O., Martín, A. J., Veenstra, F. L., Pineda, F. A., González-Cobos, J., García-Tecedor, M., Giménez, S., Jaegermann, W., Centi, G., Pérez-Ramírez, J., Galán-Mascarós, J. R., & Perathoner, S. (2023). An artificial leaf device built with Earth-abundant materials for combined H_2 production and storage as formate with efficiency > 10%. *Energy & Environmental Science*, *16*(4), 1644–1661."

6.1 | Preface

The integration of renewable energy with electrochemical systems has sparked significant interest, particularly in the coupling of electrochemical (EC) reactors with photovoltaic (PV) cells. The resulting coupled device is usually defined as an "artificial leaf", which is a system that mimics what nature does by converting carbon dioxide (CO_2) and water into valuable products directly using sunlight. Thinking about the industrial importance of ammonia and its strong dependence on fossil resources (as extensively discussed in chapter 1), a parallelism can be made between the photosynthetic process (to convert CO_2) and the alternative ammonia production (starting from air and water by renewable energy). In this direction, the term "ammonia artificial leaf" was recently proposed in the literature [1]. From a technical point of view, this approach extends beyond solely optimizing the cathode compartment and includes the entire cell, encompassing the anode compartment, electrolyte, exchange membrane, and distances between electrodes.

Within this chapter, we will thus explore the potential of a photovoltaic-electrochemical (PV-EC) coupling approach. However, we preferred to start from the study of CO_2 reduction reaction, because this process currently represents a more mature technology that provides much higher productivity than Nitrogen Reduction Reaction (NRR), but in principle all these results can be extrapolated and addressed to ammonia production.

6.2 | State-of-the-art

One of the challenges that scientific research is actively addressing to limit global warming caused by CO_2 accumulation [2,3,4] in the environment is the conversion of carbon dioxide (CO_2) and water directly into chemicals with higher added value through artificial photosynthesis. At present, two of the hottest topics are Carbon Dioxide Reduction Reaction (CO_2RR) and Nitrogen Reduction Reaction (NRR).

A monolithic photoelectrochemical-photovoltaic device integrated with rare earth electrode materials (i.e. $GaInP_2$/GaAs) with a Faradaic hydrogen efficiency of 12.4% was reported by Khalselev et al.[5]. Another pioneering approach was undertaken by *Nocera et al.*[6] with their cell operating at 11 SUN, under neutral pH conditions. This research was focused on water splitting and aimed to achieve a solar efficiency of 5%. The photo-electrocatalytic (PEC) pathway yields valuable fuels and chemicals, such as carbon monoxide (CO), formate (HCOO-), methanol (CH_3OH), ethylene (C_2H_4), and other alcohols, hydrocarbons, and C_2+ acids. It is noteworthy that carbon monoxide and formate are the easiest intermediates to achieve, as their reduction involves a 2-electron step, resulting in the highest Faradaic efficiencies (FEs). *Urbain et al.*[7] reported a reduction process with Zinc electrodeposited on Copper foam as the working electrode, supported photo-electro reduction with a 1-sun photoanode (Si heterojunction connected with Nickel foam), producing syngas at a H_2:CO ratio of 5 to 0.5, with the highest FE for CO of 85% and *solar-to-syngas* conversion of 4.3%. Furthermore, *Piao et al.*[8] synthesized an efficient electrocatalyst for the selective conversion of CO_2 to formate using multilayered porous Bismuth dendrite electrodes, that exhibited an exceptional FE of nearly 100% for formate production. By utilizing photovoltaic-cell-assisted electrocatalysis, an approximate FE of 95% and a solar conversion efficiency of 8.5% ($_{at}$ a current density of10 mA cm^{-2}) were achieved for formate production. The activity of the Bi electrodes remained unchanged for 360 hours, indicating their long-term stability. Recently, *Kato et al.* reported a large cell for solar-guided CO_2 reduction

with 7.2% solar-to-formate conversion[9]. The cell operated in stacks of eight and achieved a 1 m^2 irradiation area. By using ruthenium-based catalysts with a low-resistive substrate, large formate production rates of 93.5 mmol h^{-1} were achieved; subsequently, solar-to-fuel (STF) efficiency was increased up to a 10.3% conversion and 1167 mmol/h production rate[10].

Numerous strategies have been developed to enhance the activity of Cu in CO_2RR, involving the creation of nanostructures and control of morphology. In order to find the optimal catalyst for CO_2RR, in a complex space of optimizations, one must move toward the top of the volcano plot as shown in **Figure 6.1**.

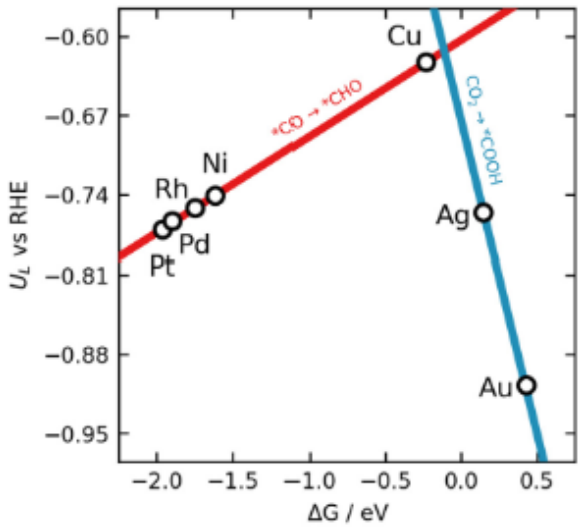

***Figure 6.1** - Scaling-relations-based volcano plot for CO_2RR on seven transition metal surfaces, reprinted from [11]*

Preliminary studies on CO_2 reduction have been carried out as reported by Jaramillo et al., where a large variety of products were detected following CO_2RR, understanding that Copper based on catalyst structure, pH, applied voltage, and current density, generates a whole series of products[12,11].

As reported by *Shinagawa et al.*[13], copper modified by sulfur in the structure favours the reaction towards the formation of formate, synthesizing Cu-S by solvothermal synthesis, and tested in an aqueous environment in a customized two-compartment leak-proof glass electrochemical cell in two-electrode mode. The best performance for the formate was obtained at an applied potential of -0.8V vs RHE, and ~80% of FE.

6.3 | Aim of chapter

Few devices in the literature work without noble metals and at high current densities, nor have studies of the co-production of formate and hydrogen been investigated. In this Chapter, without going into too much detail on the reduction reaction to fuel and specifically formate (which is not the topic of this thesis), the approach to develop and optimize a PV-EC coupling, applicable to nitrogen reduction reaction (NRR), will be discussed, since the issues to be addressed are the same, thus allowing an analogy to be made.

This work was carried out in the framework of a European H2020 Project (*A-LEAF – An Artificial Leaf: a photo-electro-catalytic cell from earth-abundant materials for sustainable solar production of CO_2-based chemicals and fuels"*, ID: 732840). A solar-to-fuel (STF) conversion of 10.1% was achieved by i) operating at a current density of 17 mA cm^{-2} and a cell potential of 2.5 V; ii) providing for a formate productivity of 193 μmol h^{-1} cm^{-2}; iii) exploiting materials abundant on the earth; iv) coupling a silicon heterojunction (SHJ) four-cell module used to absorb sunlight and provide electricity. Here we will discuss how to approach and optimize the electrochemical cell using non-critical raw materials, thus opening the door for further studies and improvements in this direction.

6.4 | Electrochemical setup

***Figure 6.2** - Exploded view of the electrochemical (EC) – photovoltaic (PV) device and related electrodes, including O-rings and gaskets*

The electrochemical (EC) cell, constructed with transparent Plexiglas to allow easy visual observation of its internal processes (**Figure 6.2**), operates as a lab-scale electrochemical flow cell with carefully optimized gas and liquid flow pathways. Within this setup, a gas diffusion layer (GDL) separates a gas chamber, supplied with pure CO_2, from a liquid catholyte consisting of a 0.1 M $KHCO_3$ aqueous solution saturated with CO_2 at a pH of 6.8. The active catalytic material responsible for CO_2 reduction, specifically Cu–S, is oriented toward the liquid side. The gas diffusion electrode (GDE) and the gas chamber play a crucial role in promoting efficient gas-liquid interaction near the electrode, enhancing the transport of gaseous substances through the carbon fibre support by leveraging hydrophobic repulsion against the liquid phase.

The counter anodic process, i.e. the Oxygen Evolution Reaction (OER), takes place over an electrode based on Ni–Fe–Zn oxide in a 1 M KOH aqueous solution with a pH of approximately 14. The utilization of different electrolytes in the cathode and anode compartments stems from the need to individually optimize the electrocatalytic performance of Cu–S and Ni–Fe–Zn oxide, which operate at distinct pH levels. Additionally, this choice is influenced by the stability of the electrodes under the specified conditions and working potential. To maintain the

pH difference during electrocatalytic tests, a commercial proton exchange membrane (PTFE-reinforced Nafion, N-324) is employed, facilitating efficient charge transfer between the catholyte and anolyte solutions while minimizing the crossover of intermediate or product species.

In the absence of solar irradiation, electrochemical testing is conducted in the aforementioned EC device using a three-electrode configuration. An electrical bias ranging from -0.4 to -1.0 V vs. RHE is applied to the cathode. A thin capillary Ag/AgCl (3 M KCl) electrode serves as the reference electrode and is positioned near the Cu–S/GDL interface.

The cell was engineered with a compact design, adhering to optimization criteria centred around minimizing overpotential, resistances, and fine-tuning parameters such as electrolyte volumes, electrode spacings, and gas-liquid phase configurations. These optimizations were aimed at facilitating the appropriate diffusion of carbon dioxide through the gas diffusion layer (GDL) while preventing any undesired leakage into the gas chamber. Additionally, a continuous recirculation system was implemented for the electrolytes, maintaining a consistent flow from their respective containers into the designated half-cells, as depicted in **Figure 6.3a**, while **Figure 6.3b** shows a picture of the the full prototype.

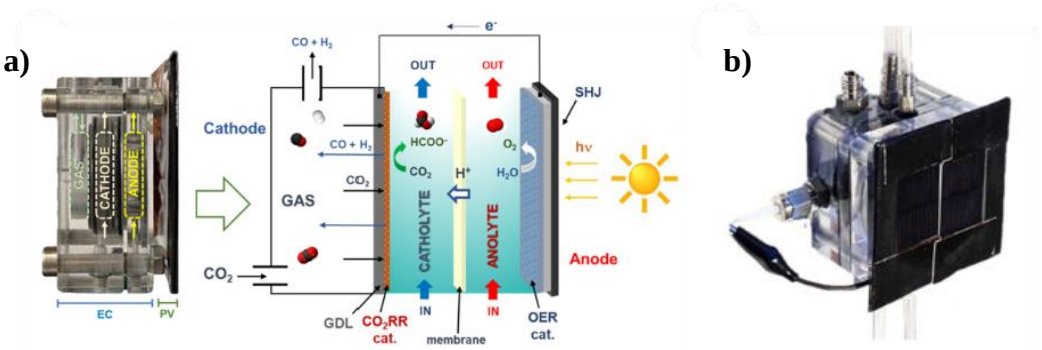

Figure 6.3 *- (a) representative scheme of the working principle of the artificial leaf (a side picture is also provided on the left). The CO_2 Reduction Reaction (CO_2RR) occurs in a liquid electrolyte*

(catholyte) at the cathode side. A gas chamber enhances the local concentration of gaseous CO_2 (directly on the electrode surface) flowing through a Gas Diffusion Layer (GDL). The counter-reaction is the Oxygen Evolution Reaction (OER) by water oxidation. ''cat.'' represents the catalyst; (b) picture of the full PV/EC device

The cathodic reactions involve half-cell processes concerning CO_2 reduction leading to the formation of formate and CO (according to equations (1) and (2)), and proton reduction yielding H_2 (equation (3)), expressed as:

$$CO_2 + 2e^- + H^+ \rightarrow HCOO^- \quad \text{(eq. 6.1)}$$

$$CO_2 + 2e^- + 2H^+ \rightarrow CO + H_2O \quad \text{(eq. 6.2)}$$

$$2H^+ + 2e^- \rightarrow H_2 \quad \text{(eq. 6.3)}$$

Conversely, the anodic side initiates the Oxygen Evolution Reaction (OER) as follows:

$$2OH^- \rightarrow \frac{1}{2}O_2 + 2e^- + H_2O \quad \text{(eq. 6.4)}$$

It is significant that the gaseous products (CO and H_2) from reactions (2) and (3), respectively, are exclusively collected at the outlet of the gas chamber, diffusing back through the gas diffusion layer (GDL). Importantly, these gases do not dissolve in the liquid catholyte due to the gas chamber operating under atmospheric pressure.

6.5 | PV module and coupling

A small photovoltaic (PV) device comprises four silicon heterojunction solar cells, with a total area of 12.71 cm^2, interconnected in a shingled arrangement[14] and enclosed within a structure consisting of glass, thermoplastic polyolefin (TPO), module material, and TPO back sheet (**Figure 6.4**).

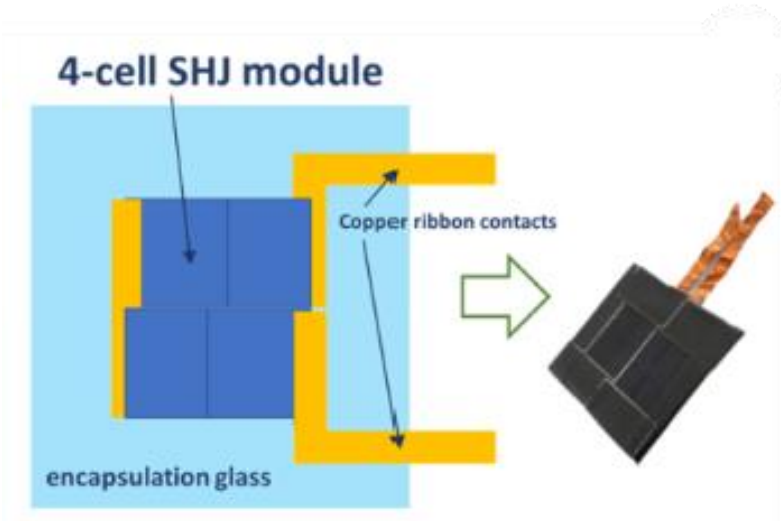

Figure 6.4 *- scheme and picture of the silicon heterojunction (SHJ) four-cell module used to absorb sunlight and provide electricity.*

This PV module is positioned externally in proximity to the anode side of the EC cell, ensuring it does not come into direct contact with the liquid anolyte. Short electrical wires connect the PV module to the EC section, enabling it to harness solar energy and supply the necessary electrical power for the electrocatalytic processes. The connection process between the Electrochemical Cell and the PV module was conducted using a 300 W Xenon arc lamp equipped with a 1.5 Global Air-Mass filter. The module was calibrated to operate at 1 SUN, which is equivalent to 100 mW cm^{-2}, by carefully adjusting the distance between the device and the light source (18.1 cm = 1 SUN). The temperature of the module during the operational phases (31.5°C) was measured using a thermocouple. By plotting the polarization curve of the cell along with the IV graph of the PV panel, which provides the maximum power point (MPP) at 2.303 V, it can be observed that the cell, after optimization, achieved a cell potential of 2.5 V, thus very close to the MPP (**Figure 6.5**). Furthermore, the higher temperature reduces the conversion efficiency of the PV module from 20.3 to 19.7%.

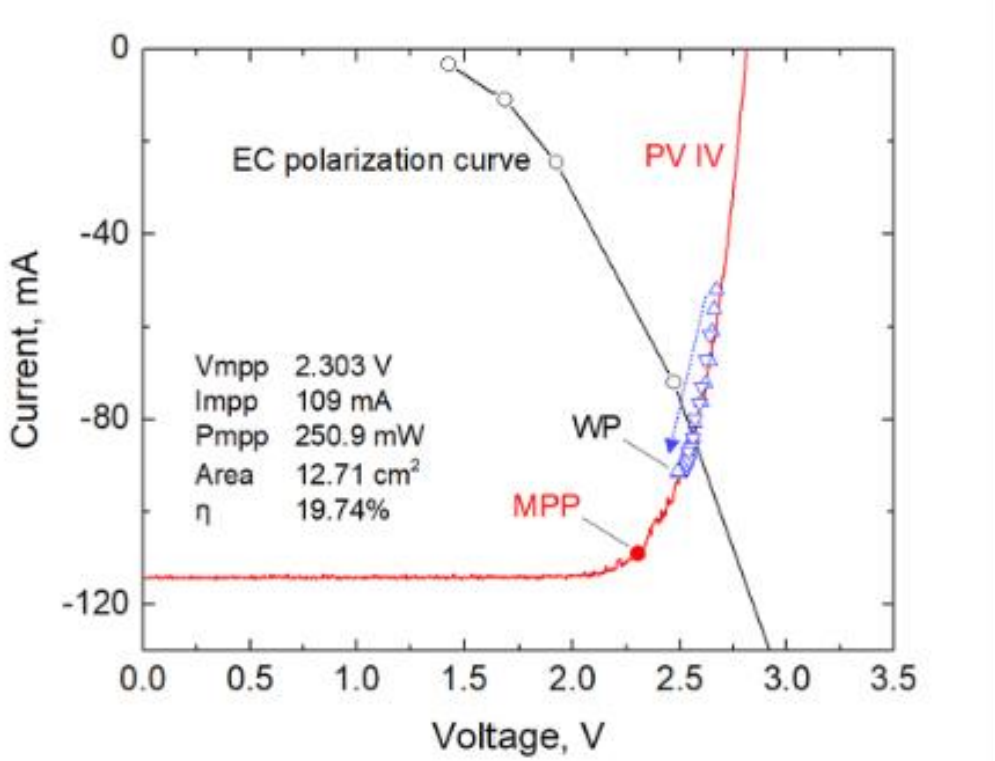

Figure 6.5 *– Coupling photovoltaic module and electrochemical devices. The IV curve of SHJ photovoltaic (PV) module (red line) and the polarization curve (black dot-line) of the electrochemical cell (EC). The blue triangles indicate the evolution of the WPs (in the direction indicated by the arrow*

6.6 | Results

6.6.1 | Preliminary electrochemical tests

The outcomes derived from the electrocatalytic assessments are depicted in **Figure 6.6**, where the applied potential (in V vs. RHE) is plotted on the X-axis. The left Y-axis represents the Faradaic Efficiency (FE), while the right Y-axis indicates the current density. Notably, at -1.0 V, formate exhibits its peak performance, reaching a maximum value of 62.2%, accompanied by a current density of 15.1 mA cm^{-2}. Conversely, hydrogen production experiences a reduction with escalating potential, declining to 33%. Simultaneously, a presence

of carbon monoxide (CO) is observed at this particular potential, albeit in a relatively lower concentration of 4.2%.

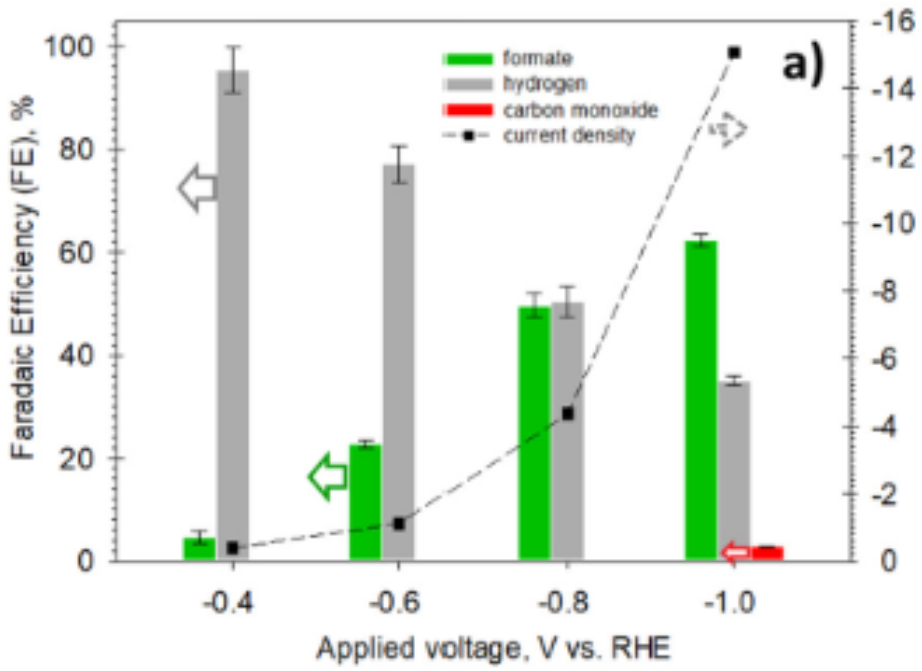

Figure 6.6 *– Performance of Electrochemical cell during tests in three-electrode configuration at different applied potentials*

As part of additional validation, a test was executed in galvanostatic mode employing a two-electrode configuration. A set-point of 10 mA cm^{-2} current density was applied, enabling concurrent measurement of both cell voltage and reference voltage. As illustrated in **Figure 6.7**, the system demonstrates notable stability during a sustained steady-state, evident over a 1.5-hour operational period, with a recorded cell potential of 2.5 V. Such findings have relevance for the next PV-EC coupling step.

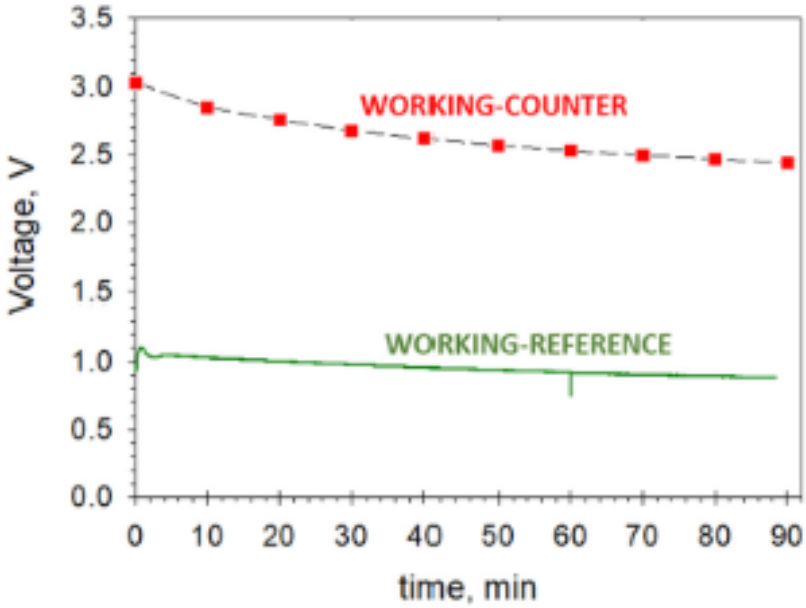

Figure 6.7 *– Working-Counter Electrode (Cell Voltage) measurements and working-reference (vs RHE) voltage profile versus time obtained at applied 10 mA cm^{-2}*

6.6.2 | Validation of the device

The coupling was validated by using a certified solar simulator under standard irradiation conditions, using the AM1.5G filter, and adopting the two-electrode cell configuration. The cell was tested with two sets of photo-electrochemical tests of 5h each (10h total) to indicate the robustness of the system. In the first validation test (0-5h) liquid products were taken every hour, while in the second test (5-10h) every two hours; gaseous products were sampled during the test, at constant time interval of 10 min. The electrolyte solution was restored and the second 5h test was performed.

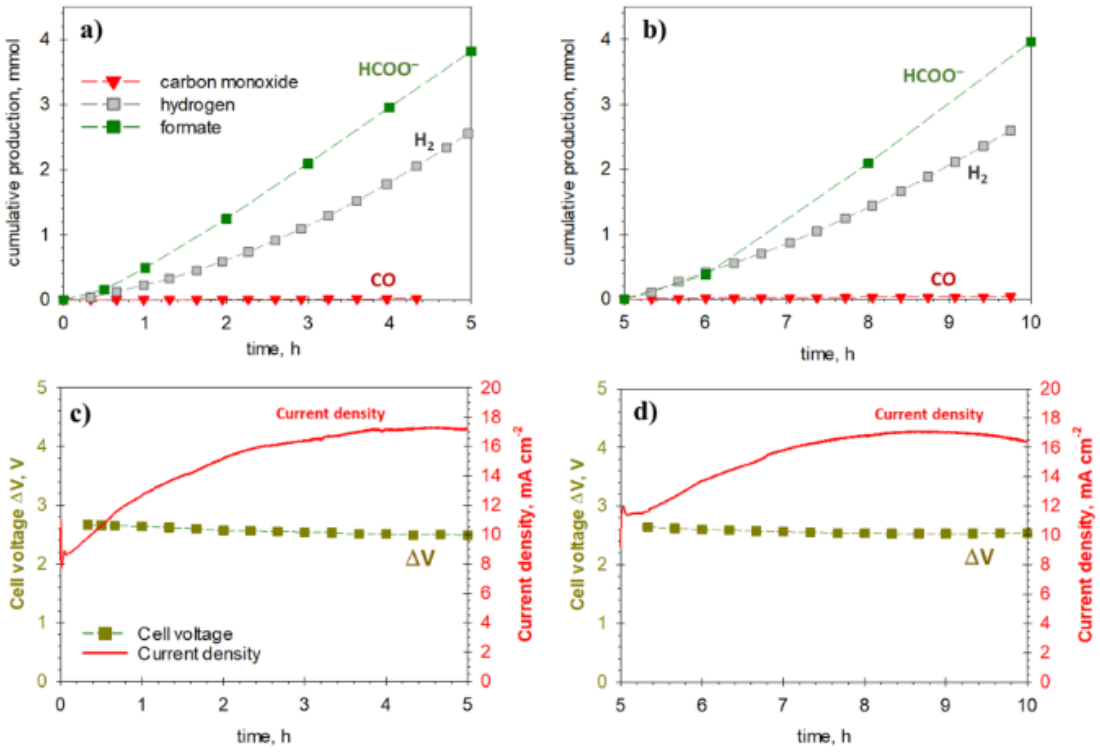

Figure 6.8 *– Performance of photo-electrochemical device a) Cumulative production ($HCOO^-$, CO and H_2) in the first 5h and b) in the consecutive 5h of irradiation. c) Current density profile and Cell Voltage during first 5h and d) during the last 5h*

After two hours from the test initiation, both formate and hydrogen production stabilized, demonstrating sustained performance without any discernible deterioration. Notably, **Figures 6.8a** and **6.8b** illustrate this stability, showcasing consistent results between the 1-5h and 6-10h tests, indicating excellent reproducibility without notable electrode transformations. Throughout the initial 2-3 hours of testing, a gradual increase in current density was observed, eventually stabilizing around 16-17 mA cm^{-2}. Simultaneously, the cell voltage settled at 2.5 V after starting at 2.7 V. The progression of the cell potential is graphically represented by blue triangles in **Figure 6.5**. Additionally, it is noteworthy that the FE to formate remained consistently ~60% during these validation tests.

6.7 | Conclusion

The feasibility of integrating an electrochemical cell and a photovoltaic module in a wired configuration, utilizing earth-abundant materials, has been demonstrated. This configuration achieved a solar-to-formate (STF) conversion rate of 6.2%, which increased to 10.1% when considering H_2 + formate. These results were realized through the optimization of the electrochemical reactor to minimize energy losses. Furthermore, the comprehensive validation of the entire PV+EC system over an extended operational period revealed consistent electrode performance without discernible decay.

6.8 | Supporting Informations

A- Electrochemical Protocol
B- Copper-sulfide synthesis
C- Ni-Zn-Fe oxide synthesis
D- Electrodes Preparation
E- Solar-to-electricity calculation
F- Solar-to-fuel (STF) calculation

A- Electrochemical Protocol

The electrochemical assessments were meticulously conducted following a systematic procedure. Initially, the open circuit voltage (OCP) was measured, succeeded by an initial cyclic voltammetry (CV) analysis aimed at stabilizing the electrocatalyst from +0.2 V (vs. RHE) to the desired potential at a scan voltage rate of 20 mV s^{-1}. Subsequent chronoamperometry (CA) tests were executed for 1.5h at different potential. Achieving a consistent behaviour required multiple CV cycles, typically around 20-30, until a steady state was established prompting the cessation of the CV analysis. Upon stabilization and a subsequent OCP measurement after a brief interval, the assessment of capacitance was performed using the double-layer technique. This method involved conducting a series of CV cycles at progressively increasing voltage rates, ranging from 2 to 50 mV s^{-1}, within a narrowly defined voltage range centred around the OCP (± 0.016 V).

In the experimental procedure, a consistent approach was employed to evaluate the same catalyst across a voltage range from -0.4 V to -0.8 V. Between each voltage setting, the electrolyte was modified, and the system underwent thorough rinsing. The comprehensive testing protocol, involving pre-CVs, CA, and post-CVs, was rigorously followed for each distinct voltage level.

Throughout the CA assessments, both gaseous and liquid products underwent meticulous analysis. Gas products were detected by Gas Chromatography (microGC-TCD, Pollution GCX), calibrated for H_2, methane, ethylene, ethane, propylene, and propane, with the outlet gas stream sampled at regular intervals of 10 minutes. In contrast, liquid products were gathered within the catholyte and later analysed via Gas Cromatography-Mass Spectroscopy (GC-MS, Thermo Fisher Trace 1310 and TSQ8000 EVO triple quadrupole mass spectrometer) for methanol, ethanol, methyl formate, propane-2-ol, acetone. Ionic Chromatography (MetrOhm 940 Professional IC Vario – 944 Professional UV/Vis detector equipped with organic acid column 250/7.8) for formic acid, acetic acid, and oxalic acid post-CA testing. Subsequently, the identical CV analysis cycles were

repeated after the completion of the CA examination to ensure consistency and thorough assessment of the catalyst's performance across the voltage range.

B- Copper-sulphide synthesis

Copper sulphide (Cu–S) was synthesized using a solvothermal method, following procedures detailed elsewhere[15,16]. In a nutshell, a mixture of 4 mmol of $Cu(NO_3)_2 \bullet 3H_2O$ and 0.067 mmol of elemental sulfur (Sigma-Aldrich, >95%) was combined in 40 mL of ethylene glycol (Sigma-Aldrich, 99%) and stirred at room temperature for 30 minutes. The resulting mixture was then transferred into a 50 mL Teflon-lined autoclave and subjected to heat treatment at 140°C for ten hours (with a heating rate of 5°C min^{-1}), followed by gradual cooling to room temperature. The resultant mixture underwent thorough washing with ultrapure water through centrifugation (6000 rpm, 10 minutes), and the resulting powder was subsequently dried under vacuum overnight at 80°C.

C- Ni-Zn-Fe oxide synthesis

The synthesis of the metal oxide $NiZnFeO_x$ employed a hydrothermal method. Initially, equimolar quantities of metal nitrates dissolved in water (metal concentration: 50 mM) underwent hydrolysis through the addition of diluted aqueous ammonia until achieving a pH of 8.5. Subsequently, this solution was introduced into a Teflon cup within an autoclave and subjected to a temperature of 140°C for a duration of 2 hours. Following the hydrothermal treatment, the pressure vessel was gradually cooled in ambient air. The resulting product underwent sequential washing steps with H_2O and CH_3CH_2OH. The subsequent collection of nanoparticles was achieved through centrifugation, culminating in a final particle size estimation of approximately 8 nm.

D- Electrodes Preparation

Cu–S or Ni–Fe–Zn oxide powders were applied onto carbon-based substrates for electrode preparation. Specifically, a measured quantity of catalyst, aiming for a final loading of 1.0 mg cm^{-2}, was mixed with 4 mL of water, 4 mL of isopropanol, and 50 mL of 10% Nafion® perfluorate. This mixture underwent sonication until a stable suspension formed, a process lasting approximately 15 minutes. The resulting ink was then spray-coated onto a preheated porous carbon-based gas-diffusion layer (GDL, Sigracet 39BCE from Ion Power), serving as the substrate. Subsequently, the solvent was allowed to evaporate, ensuring uniform fixation of the powder onto the electrode surface.

E- Solar-to-electricity calculation

The artificial leaf works at a current density j = 17.3 ± 0.5 mA cm^{-2} , with a cell potential of 2.5 V (V_{WP}) and an electrode area of A_e = 5.31 ± 0.05 (cm^2). With these parameters, we can estimate the ratio of solar to electrical power conversion (i.e., the photovoltaic conversion efficiency) as:

$$Solar - to - electricity\ (\%) = \frac{V_{WP} \times j \times A_e}{P \times A_{PV}} \times 100 = 18.1\% \qquad \text{(eq. S6.1)}$$

where P is the incident irradiation power (in W cm^{-2}), and A_{PV} is the irradiated surface area of the PV module (in cm^2), accounting for the solar irradiation power.

F- Solar-to-fuel (STF) calculation

$$STF_i\ (\%) = \frac{E_i \times j \times A_e \times FE_i}{P \times A_{PV}} \times 100 \qquad \text{(eq. S6.2)}$$

where E_i corresponds to the energy stored in each product I ($E_{formate}$ = 1.43 V and $E_{hydrogen}$ = 1.23 V), and FE_i is the Faradaic efficiency to the i-reduction product. The STF efficiency to formate is calculated as 6.2 ± 0.4%. The additional STF efficiency to hydrogen, as collected from the gas chamber, is 3.9 ± 0.3%. The overall STF efficiency combining these two major products is 10.1 ± 0.5%.

6.9 | References

[1] Martín, A. J., Shinagawa, T., & Pérez-Ramírez, J. (2019). Electrocatalytic reduction of nitrogen: From Haber-Bosch to ammonia artificial leaf. *Chem, 5*(2), 263–283.

[2] Li, X., Yu, J., Jaroniec, M., & Chen, X. (2019). Cocatalysts for selective photoreduction of CO_2 into solar fuels. *Chemical Reviews, 119*(6), 3962–4179.

[3] Galan-Mascaros, J. R. (2020). Photoelectrochemical solar fuels from carbon dioxide, water and sunlight. *Catalysis Science & Technology, 10*(7), 1967–1974.

[4] Ampelli, C., Centi, G., Passalacqua, R., & Perathoner, S. (2010). Synthesis of solar fuels by a novel photoelectrocatalytic approach. *Energy & Environmental Science, 3*(3), 292.

[5] Khaselev, O., & Turner, J. A. (1998). A monolithic photovoltaic-photoelectrochemical device for hydrogen production via water splitting. *Science, 280*(5362), 425–427.

[6] Reece, S. Y., Hamel, J. A., Sung, K., Jarvi, T. D., Esswein, A. J., Pijpers, J. J., & Nocera, D. G. (2011). Wireless solar water splitting using silicon-based semiconductors and earth-abundant catalysts. *Science, 334*(6056), 645–648.

[7] Urbain, F., Tang, P., Carretero, N. M., Andreu, T., Gerling, L. G., Voz, C., Arbiol, J., & Morante, J. R. (2017). A prototype reactor for highly selective solar-driven CO_2 reduction to synthesis gas using nanosized earth-abundant catalysts and silicon photovoltaics. *Energy & Environmental Science, 10*(10), 2256–2266.

[8] Piao, G., Yoon, S. H., Han, D. S., & Park, H. (2019). Ion-Enhanced Conversion of CO_2 into formate on porous dendritic bismuth electrodes with high efficiency and durability. *ChemSusChem, 13*(4), 698–706.

[9] Kato, N., Mizuno, S., Shiozawa, M., Nojiri, N., Kawai, Y., Fukumoto, K., Morikawa, T., & Takeda, Y. (2021). A large-sized cell for solar-driven CO_2 conversion with a solar-to-formate conversion efficiency of 7.2%. *Joule, 5*(3), 687–705.

[10] Kato, N., Takeda, Y., Kawai, Y., Nojiri, N., Shiozawa, M., Mizuno, S., Yamanaka, K., Morikawa, T., & Hamaguchi, T. (2021). Solar fuel production from CO_2 using a 1 M-square-sized reactor with a solar-to-formate conversion

efficiency of 10.5%. ACS *Sustainable Chemistry & Engineering, 9*(48), 16031–16037.

[11] Rendón-Calle, A., Builes, S., & Calle-Vallejo, F. (2018). A brief review of the computational modeling of CO_2 electroreduction on Cu Electrodes. *Current Opinion in Electrochemistry, 9*, 158–165.

[12] Kuhl, K. P., Cave, E. R., Abram, D. N., & Jaramillo, T. F. (2012). New insights into the electrochemical reduction of carbon dioxide on metallic copper surfaces. *Energy & Environmental Science, 5*(5), 7050.

[13] Shinagawa, T., Larrazábal, G. O., Martín, A. J., Krumeich, F., & Pérez-Ramírez, J. (2018). Sulfur-modified copper catalysts for the electrochemical reduction of carbon dioxide to formate. *ACS Catalysis, 8*(2), 837–844.

[14] Lee, M., Ding, X., Banerjee, S., Krause, F., Smirnov, V., Astakhov, O., Merdzhanova, T., Klingebiel, B., Kirchartz, T., Finger, F., Rau, U., & Haas, S. (2020). Bifunctional Cofevox catalyst for solar water splitting by using multijunction and heterojunction silicon solar cells. *Advanced Materials Technologies, 5*(12).

[15] Larrazábal, G. O., Martín, A. J., Krumeich, F., Hauert, R., & Pérez-Ramírez, J. (2017). Solvothermally-prepared Cu_2O electrocatalysts for CO_2 reduction with tunable selectivity by the introduction of p-block elements. *ChemSusChem, 10*(6), 1255–1265.

[16] Wu, C., Yu, S.-H., & Antonietti, M. (2006). Complex concaved cuboctahedrons of copper sulfide crystals with highly geometrical symmetry created by a solution process. *Chemistry of Materials, 18*(16), 3599–3601.

7. | General Conclusions

In this dissertation, different chemical approaches have been investigated for the activation of dinitrogen molecule (N_2) and its conversion to ammonia, i.e. the process of Nitrogen Reduction Reaction (NRR). The study started from the synthesis of the catalysts, which were prepared by wet impregnation, varying the metals used (i.e. Ru, Fe, and Ru-Fe co-doped) on different supports (functionalized carbon nanotubes -CNTs- and alumina -Al_2O_3). The as prepared electrocatalytic materials were fully characterized for the evaluation of their crystalline, morphological, surface, and porosity properties, as well as by advanced electrochemical techniques.

Then, their behavior was evaluated in **electrochemical environment (EC)**, in combination with a gas-diffusion layer (GDL) as the substrate, using custom reactors of advanced design, working both in gas phase (i.e. electrolyte-less conditions) and in liquid phase in the case of Electrochemical Impedance Spectroscopy (EIS). All operations were done to i) minimize intra- and out-system contaminations; ii) increase conversion by using the gas phase to overcome the low solubility of nitrogen in aqueous media; iii) unearth potentials where NRR is preferred over the Hydrogen Evolution Reaction (HER), which is the main competitive reaction; iv) bring beneficial aspects to the reaction by co-doping the electrode materials with a noble metal (Ru) and/or an earth-abundant metal (Fe). A wide range of potentials (from -0.1 to -0.8 V vs RHE) was investigated, by evaluating the behaviour of NRR, in relation to the competitive HER. Notably, the investigation revealed the prevalence of NRR at potentials approximately within the range from -0.2 to -0.4 V vs RHE, exhibiting enhanced Faradaic efficiency (FE) and productivity. Conversely, the dominance of HER emerged notably at applied potentials exceeding -0.5 V vs RHE. In the case of catalysts based on carbon nanotubes (CNTs), they showed similar activity, such

as Fe_2O_3 in comparison to Ru and Ru-Fe co-doped variants. On the contrary, alumina-based catalysts showcased distinctive trends. Specifically, doping with Ru provided higher catalytic performance compared to Fe_2O_3, while the substitution of Fe with Ru in a co-doped configuration (Ru-Fe/Al_2O_3) yielded the highest observed catalytic performance of 1.047 μg mg_{cat}^{-1} h^{-1}, with a FE of 0.5% and a current density of 294 μA cm^{-2} at -0.3 V vs RHE. It is evident in this case that, partially replacing un expensive metal (such as Ru) with a less expensive one (Fe) brings benefits, although many aspects of NRR need to be studied to make significant progress in this field. Among all the samples, Fe_2O_3/CNTs showed the best performance of 0.63 μg mg_{cat}^{-1} h^{-1} with a FE of 1.5% and a current density 40 μA cm^{-2} at -0.3 V vs RHE. Moreover, a direct comparison between two cell setups (gas-phase and gas-liquid-phase), showed that the gas phase promotes ammonia formation due to the presence of the Membrane Electrode Assembly, which in contrast is more fragile in terms of mechanical stability.

The same catalysts were also tested under **plasma catalytic environment (PC)**, in a tubular alumina barrier dielectric discharge reactor. In this case, i) the influence of the ratio of hydrogen and nitrogen in the feed-gas was evaluated; ii) the flowrates were optimized iii) the plasma discharge paths on the respective support materials were studied by high-speed recording camera. The power input and frequency (in the main tests) were kept constant at 27 W and 20 kHz, respectively, and the variable value was the peak-to-peak voltage. The combination of metal and support used to increase the performance of the substrate plays a key role in the case of alumina, where the performance follows the order Ru/Al_2O_3 >Ru-Fe/Al_2O_3 > Fe_2O_3/Al_2O_3 >> Fe_2O_3 /CNTs > Ru/CNTs. The difference in productivity between the two supports may also be influenced by mesopore size and surface area, in addition to the fact that CNTs conduct more than alumina. Further, the metal distribution on the surface and the plasma path in a packed reactor, which is commonly known as a surface streamer, may contribute to the difference in productivity. There is a strong correlation between

surface propagation and catalytic performance. CNTs, being more conductive have shown an opposite trend with respect to alumina catalysts, where metal-doped catalysts have lower productivity than the support alone. Furthermore, because of porosity, the metal exposed to plasma is less than the metal on alumina. Modifying the flowrate, on the other hand, results in a decline in ammonia productivity in parts per million, and a subsequent decrease in Specific Energy Input (SEI), which demonstrates a linear relationship. The overall calculation, which considers not only the parts per million (volumetric) of ammonia produced but also the flow of reactant gas, reveals that as the flowrate increases, the overall value also increases, except for CNTs, which exhibit the highest overall value at 160 mL min^{-1}. Moreover, by observing the change in slopes of cumulative graphs, one can also discern the affinity of the reactant gases for the catalyst. Stability tests have shown also that CNTs alone require plasma treatment to activate, while CNTs doped with metals do not require a period of activation. Furthermore, a high-speed camera was used to capture the plasma discharge behaviour during a discharge test session, and an IR camera was also used to detect the temperature reached on the external surface of the reactor. The comparison evinced that the ruthenium-based catalyst doped on alumina (Ru/Al_2O_3) achieved the best performance of 4725.7 ppm (22.7 μmol min^{-1}) with an N_2:H_2 ratio of 2:1 and an energy consumption of 70.1 MJ mol^{-1}. The value, unbalanced toward higher nitrogen contents shifts the reaction ratio from 1:3 to 2:1.

Testing results were very promising. As mentioned before, in EC conditions, described in **Chapter 3**, after assembling the membrane electrode, the best performance was observed for the Ru-Fe catalyst co-doped on alumina. On the other hand, in PC conditions, after packing the tubular reactor described in **Chapter 4**, the best performance was achieved by Ru/Al_2O_3, as schematically reported in the Table 7.1.

	Input	Catalyst	Productivity ($\mu g\ mg_{cat}^{-1}\ h^{-1}$)	Energy Consumption ($MJ\ mol^{-1}$)	Efficiency (%)
Electro-Catalysis	N_2/H_2O/Electricity	Ru-Fe/Al_2O_3	1.05	159	0.5
	N_2/H_2O/Electricity	Fe_2O_3/CNTs	0.63	-	1.5
Plasma-Catalysis	N_2/H_2/Electricity	Ru/Al_2O_3	13.6	70.1	-

(-) no calculation available

Table 7.1 *- Comparison of the best catalyst results for electrochemical and Plasma-catalytic approach*

After obtaining these results and comparing them with the literature, the **Chapter 5** aims to provide a comprehensive and objective view of ammonia production technologies, comparing the advantages and disadvantages of different technologies and the challenges each methodology brings. The search for sustainable and innovative solutions is the key to shaping a future in which the chemical industry can ensure efficient and environmentally friendly ammonia production that meets global needs. For this reason, an extensive literature search was conducted to study the techno-economic aspects of conventional and unconventional techniques for ammonia production, taking both the conventional and green Haber-Bosh processes as references. The information gathered at this stage was used to develop a techno-economic evaluation (TEA) of the various technologies currently being developed, although on a laboratory scale (TRL 4). Afterwards, the boundary conditions and based scenarios, aiming to close the production gap between small, medium, and large scale (*i.e* scenario 1, 2 , and 3 respectively), have been defined. The scenario 2 acts as an intermediary between the HB and scenario 1, bridging the gap between large and small scale. Scenario 3 has been considered to indicate the potential for making the HB process more sustainable. Therefore, a synergistic collaboration among these three scenarios could be the subject of further studies. In scenario 1, the most cost-effective technologies in terms of size, performance, and safety are (EC) electrochemical technologies, TP-SOEC (Thermal Plasma – Solid Oxide Electrolysis Cell) given

its compactness and HPE (Hybrid Plasma Electrocatalysis) reactor given its versatility. TP-SOEC and HPE are relatively new technologies compared to the electrocatalytic approach. Electrocatalysis in an organic environment than EC with ionic liquids (29.6 and 15.8 MWh respectively) may lend themselves well for this purpose. But in the case of organic EC with lithium cycle, would increase the controls related to safety since operating with Li and organic solvents could be risky. On the contraty, EC in aqueous environment requires 32.6 MWh. Then, in term of security and stability EC could be the right technology for this scenario. For the Scenario 2, TP (Thermal Plasma) technology with a relative consumption per single reactor of 83-310 kWh could provide ammonia in a medium scale, using different renewable energy with respect to the stand-alone-device discussed in scenario 1. Finally for scenario three, in order to maintain large scale production, the electrification system by magnetic induction heating applied to the current HB was considered. the other technologies mentioned in **Chapter 5** are immature to be used in series and reach current HB levels. Thus, in the future when these technologies are more established (TRL > 4) the implementation of these scenarios could be validated. For example, as described in **Chapter 6**, the problem of coupling electrocatalytic cell with photovoltaic module has been addressed, which although adapted to CO_2 reduction, the concept is also applicable to nitrogen reduction or other solar-driven electrocatalytic reactions.

Despite remaining far from industrial standards, many more efforts need to be made to make significant improvements to NRR, such as i) increase the current maximum of the state-of-the-art in ammonia production (e.g. Efficiency, Yield, Conversion), ii) enhance the mechanical and chemical stability of catalysts over time, iii) increase the size of reactors, iv) improve the energy efficiency of processes, v) implement greater process automation, vi) reduce the use of critical raw materials, vii) prioritize sustainability, viii) enhance communication and collaboration between universities and industry. Progressing the current situation requires not only a meticulous analysis of the existing limitations, but also a

dedicated commitment to research and development, incorporating innovative methodologies and technologies that can open the routes for a substantial enhancement in NRR performance.

List of activities carried out

List of activities carried out

First Year

- ERC Synergy SCOPE online meeting (18/02/21)
- ERC Synergy SCOPE online meeting (18/03/21)
- ERC Synergy SCOPE online meeting (06/07/21)
- ERC Synergy SCOPE online meeting (31/08/21)
- Webinar “Horizon Europe: scenario e prospettive del nuovo programma europeo per la ricerca e l'innovazione” (25/02/21)
- Panel discussion COST ACTIONS - Operational Issues (16/04/21)
- SunCOChem Project Webinar conference on "Photocatalytic synthesis for a carbon-neutral production of fuels and chemicals" (28/04/21)
- Webinar “Towards Zero Pollution in the Production of Green Fuels and Chemicals” (04/06/21)
- Laboratorio Partecipativo “La tutela dell’ambiente per il futuro dell’Europa” virtual event (15/06/21)
- A-leaf 54M meeting (30/06/21)
- 3° Workshop on Innovative materials for Energy (30/09/21 – 01/10/21)

Second Year

- Corso di formazione in materia di salute e sicurezza sui luoghi di lavoro – art. 37 del DLgs 81/08 e s.m.i. (21/02/2022)
- eCCU³ Workshop (30/03/2022)
- SOLAR2CHEM X SEAFUEL Symposium (01/04/2022)
- NMR course (09-10-12/05/2022)
- Radiation Protection Training Analytical x-ray equipment (10/05/22)
- Mini Symposium Chemical Engineering and Chemistry with Klavs Jensen (11/05/2022)
- SunCoChem Towards the implementation of the EU Green Deal through the production of sustainable fuels and chemicals (31/05/2022)
- SEMINAR: "Brevetti per invenzioni industriali: strumenti per la tutela delle invenzioni nascenti dalla ricerca universitaria" Dr. Paolo Patanè U. OP. Tutela proprietà Industriale- Università degli Studi di Messina (27/06/2022)

- Primo seminario Horizon Europe fornirà un focus specifico su come scrivere una proposta di successo nell'ambito del Pillar II Cluster 1 HEALTH e Cluster 5 CLIMATE ENERGY AND MOBILITY, fornendo una panoramica teorica e pratica sulle diverse questioni da considerare; (09/11/2022)
- "Fotosintesi artificiale. Produzione di idrogeno e riduzione di anidride carbonica tramite luce solare" (PGR2021) Plasma surface modification for interfacial design of hybrid photocatalyst, Dr. Noritaka Sakakibara (11/11/2022)
- CAS SciFinder-n Training - AS SciFinder-n workshop Università di Messina (1h) (23/11/2022)
- III conferenza di dipartimento (06/12/2022)
- Avogadro Colloquia - From Water to Chemicals: Vision and Opportunities of a Sustainable Hydrogen Society (15-16/12/2022)
- Cerimonia di Conferimento del Dottorato Honoris Causa In ACCESS al Prof. Robert Schogl, Direttore e membro scientifico del Fritz Haber Institute della Max Planck Society di Berlino e del Max Planck Institute for Chemical Energy Conversion di Mulheim an der Ruhr (30-31/01/2022)

Third year

- Webinar "EIS on Battery Research" Metrohm. (12/04/2023)
- Kick-off meeting Project PRIN2022 HYDREAM – Turin (24/11/2023)

Research periods abroad

1st February 2022- 31st July 2022 (6 months)
Eindhoven University of Technology, Eindhoven, North Brabant, Netherlands.
Local tutor: Prof. Fausto Gallucci, Dr. Sirui Li.
• Ammonia production through plasma-catalytic tests, with different catalysts in a coaxial Dielectric Barrier Discharge.

1st July 2023 – 31st December 2023 (6 months)
CASALE SA, Lugano, Canton Ticino, Swiss.
Local tutor: Dr. Pierdomenico Biasi, Dr. Alberto Garbujo.
• Technical-economic evaluation of conventional and unconventional technologies conventional for ammonia production.

Articles in preparation

1. *M. Miceli, C. Ampelli, P. Biasi, A. Garbujo, G. Centi, S. Perathoner*. A Technical economical evaluation of conventional and non-conventional techniques for ammonia synthesis: A review (**in preparation**)

2. *M. Miceli, C. Ampelli, G. Centi, S. Perathoner*. A simplified methodology for minimizing critical raw material doping in supported catalysts for sustainable electroreduction of N_2 to NH_3 under mild conditions (**in preparation**)

3. *M. Miceli, C. Ampelli, F. Gallucci, S. Li, G. Centi, S. Perathoner*. Exploring Iron-Ruthenium catalysts and their mixtures supported on carbon nanofiber and alumina for plasma catalytic nitrogen fixation in a dielectric barrier discharge reactor (**in preparation**)

Published papers (in ISI Web of Science/Scopus)

1. *D. Giusi, F. Tavella, M. Miceli, C. Ampelli, G. Centi, D. Cosio, C. Genovese, S. Perathoner*. Synergetic Electrocatalytic Effects of Cu_2O-TiO_2 Heterostructures in a Solar Driven PEC Device for CO_2 Reduction to >C1 Chemicals, **Chemical Engineering Transactions,** Vol. 86 (**2021**), AIDIC Servizi S.r.l. (Milano, Italy), ISSN: 2283-9216, ISBN: 978-88-95608-84-6, DOI: 10.3303/CET2186235, published: 15 June 2021.

2. *D. Giusi, M. Miceli, C. Genovese, G. Centi, S. Perathoner, C. Ampelli*. In situ electrochemical characterization of Cu_xO-based gas-diffusion electrodes (GDEs) for CO_2 electrocatalytic reduction in presence and absence of liquid electrolyte and relationship with C_{2+} products formation, **Applied Catalysis B: Environmental (IF=22.1)**, vol. 318 (**2022**), Article number 121845, doi: 10.1016/j.apcatb.2022.121845

3. *C. Ampelli, D. Giusi, M. Miceli, T. Merdzhanova, V. Smirnov, U. Chime, O. Astakhov, A. Martin Fernandez, F. Veenstra, F. Garcés-Pineda, J. Gonzalez-Cobos, M. García-Tecedor, S. Gimenez, W. Jaegermann, G. Centi, J. Pérez-Ramírez, J. Galan-Mascaros, &, S. Perathoner* (**2023**). An artificial leaf device built with Earth-abundant materials for combined H2 production and storage as formate with efficiency > 10%. **Energy & Environmental Science (IF=32.5),** doi: 10.1039/d2ee03215e

4. *D. Giusi, F. Tavella, M. Miceli, A. M. Ronsisvalle, V. Costantino, C. Ampelli*. Copper Oxide onto Gas Diffusion Electrodes to Enhance Selectivity towards >C1 Chemicals in Gas-phase CO2 Electrocatalytic Reduction, **Chemical Engineering Transactions,** Vol. 100 (**2023**), AIDIC Servizi S.r.l. (Milano, Italy), ISSN: 2283-9216, ISBN: 979-12-81206-03-8, DOI: 10.3303/CET23100108, published: 30 June 2023.

Oral communications at national and international conferences

1. *M. Miceli, F. Tavella, S. Perathoner, G. Centi, C. Ampelli*. Activation of N_2 over Fe(and/or Ru)-based electrocatalysts in unconventional electrochemical reactors for ammonia production, 18th International Congress on Catalysis (ICC 2024), Lyon (France), 14-19 July 2024, **abstract submitted for oral presentation**.

2. "Iron/Metal-Organic Framework (Fe-MOF)-based electrodes for direct nitrogen reduction reaction to ammonia in mild conditions", Claudio Ampelli, Hua Wei, Matteo Miceli*, Daniele Giusi, Jérome Canivet, Elsje A. Quadrelli, Gabriele Centi, Siglinda Perathoner, "FEZA2021 Virtual conference", 5th -7th July 2021 **oral presentation**

Proceedings in national and international conferences

1. *C. Ampelli, F. Tavella, D. Giusi, M. Miceli, A.M. Ronsisvalle, S. Perathoner, G. Centi*. Engineering of an artificial leaf-type device for the continuous production of hydrogen, 14th European Congress of Chemical Engineering and 7th European Congress of Applied Biotechnology (ECCE 14 & ECAB 7), Berlin (Germany), 17-21 September 2023.

2. *D. Giusi, A.M. Ronsisvalle, C. Genovese, M. Miceli, G. Centi, S. Perathoner, C. Ampelli*. Electrocatalytic behaviour of CuS_x-Bi nanocrystals in CO_2 reduction using new engineered artificial leaf-type devices, 15th European Congress on Catalysis (EuropaCat2023), Prague (Czech Republic), *Book of Abstracts*, CO2-OL-20, 27 August – 1 September 2023.

3. *M. Miceli, C. Genovese, C. Ampelli, G. Centi*. Green H_2 beyond electrolysis, XXIII National Catalysis Congress (GIC 2023), Genova, 14-16 June 2023.

4. *D. Giusi, F. Tavella, M. Miceli, A.M. Ronsisvalle, V. Costantino, C. Ampelli*. Copper oxide onto gas diffusion electrodes to enhance selectivity towards >C1 chemicals in gas-phase CO_2 electrocatalytic reduction, 16th International Conference on Chemical & Process Engineering (ICheaP-16), *Book of Abstracts*, ASI-Mo 11:40\3, Naples (Italy), 21-24 May 2023.

5. *D. Giusi, M. Miceli, C. Ampelli, F. Tavella, C. Genovese, S. Perathoner, G. Centi*. Engineering of gas diffusion electrodes to improve selectivity towards >C1 chemicals in gas-phase CO_2 electrocatalytic reduction, 13th European Congress of Chemical Engineering and 6th European Congress of Applied Biotechnology (ECCE 13 & ECAB 6), *Book of Abstracts*, *virtual event*, 20-23 September 2021.

6. *C. Ampelli, H. Wei, M. Miceli, D. Giusi, J. Canivet, A. Quadrelli, G. Centi, S. Perathoner*. Iron/Metal-Organic Framework (Fe-MOF)-based electrodes for direct nitrogen reduction reaction to ammonia in mild conditions, 8th Conference of the Federation of European Zeolite Associations (FEZA 2021), *Book of Abstracts*, *virtual event*, 5-9 July 2021.

7. *D. Giusi, F. Tavella, M. Miceli, C. Ampelli, G. Centi, D. Cosio, C. Genovese, S. Perathoner*. Synergetic Electrocatalytic Effects of Cu_2O-TiO_2 Heterostructures in a

Solar Driven PEC Device for CO_2 Reduction to >C1 Chemicals, 15th International Conference on Chemical & Process Engineering (ICheaP-15), *Book of Abstracts*, MAR-Mo 16:40\2, *virtual event*, 23-26 May 2021.

Acknowledgments

I would like to thank **Prof. Gabriele Centi** and **Prof. Siglinda Perathoner** for the opportunity I received through this *Advanced Catalytic Processes for Using Renewable Energy Sources* Ph.D. course. My tutor, **Prof. Claudio Ampelli**, for supporting and coordinating my research activities. **My research group and colleagues** in Messina. **Prof. Fausto Gallucci** and his research group for hosting me in the Netherlands at the TU/e. The **O'Sheas** group. **Dr. Pierdomenico Biasi**, **Dr. Alberto Garbujo**, and all the employees of Casale SA for always being helpful during my time at the company. My closest friends **Alessandro**, **Alberto**, **Chiara**, **Emanuele**, **Francesco**, **Giulia**, **Nipun** and **Walter**, who have put up with me over the years, my lovely cat, and **all** those who have made me the person I am, enriching me professionally and personally.

Last but not least, I would like to thank my family for raising me with sound principles and providing me with everything I need to be able to pursue my dreams.

With love,

Matteo Miceli